Elucidating oxygen electrocatalysis with synchrotron X-rays: PEM fuel cells and electrolyzers

An experimental study

Pedersen, Anders Filsøe

Publication date:
2016

Document Version
Publisher's PDF, also known as Version of record

Ph.D. Thesis
Doctor of Philosophy

DTU Physics
Department of Physics

Elucidating oxygen electrocatalysis with synchrotron X-rays: PEM fuel cells and electrolyzers

An experimental study

Anders Filsøe Pedersen

Kongens Lyngby 2016

DTU

DTU Physics
Department of Physics
Technical University of Denmark

Fysikvej
Building 312
2800 Kongens Lyngby, Denmark
Phone +45 4525 3344
info@fysik.dtu.dk
www.fysik.dtu.dk

Abstract

In this thesis electrocatalysts for the oxygen reduction reaction (ORR) and the oxygen evolution reaction (OER) have been investigated using synchrotron based X-ray diffraction and X-ray absorption spectroscopy methods. The catalysts are based on Pt alloys and RuO_2 for ORR and OER, respectively.

For ORR model systems of Pt_xGd and Pt_xY alloys were fabricated. EXAFS were measured on a range of size-selected Pt_xGd nanoparticles to determine the interatomic Pt-Pt distances. The larger particles with a diameter of 8 nm were most active with a mass activity of 3.5 A/mg_{Pt}, and these particles also showed the greatest compression of the Pt-Pt nearest neighbor distance. This is consistent with the formation of a pure Pt overlayer that is compressed relative to bulk Pt, which explains the increase in activity purely due to strain effects. The activity of the different sized nanoparticles was correlated to the compression; the smaller particles are less active and has a lower degree of compression.

To get more insight into the Pt overlayer single crystal model systems of Gd/Pt(111) and Y/Pt(111) were fabricated by depositing films of Gd or Y on a Pt(111) single crystal at high temperatures in UHV. XRD measurements on both model systems showed the formation of an FCC-like overlayer about 3 atomic layers thick on Y/Pt(111) and about 5 layers thick on Gd/Pt(111). The average in-plane compression on the two systems were 1.4% and 0.31% respectively. The XRD analysis also revealed a possible high degree of micro-strain, which can explain why both model systems have similar ORR activity despite their large difference in average compression.

An in-situ XRD study of Gd/Pt(111) showed that the overlayer forms immediately upon exposure to acidic electrolyte at open circuit potential. Furthermore stability measurements showed that the in-plane compression relaxes during the first 2000-3000 cycles, explaining the loss of activity primarily in this range of cycling.

For OER mass-selected nanoparticles of metallic Ru and thermally oxidized RuO_2 were fabricated. Both materials are highly active for OER, although the metallic Ru nanoparticles exceptionally so. However this comes as a trade-off in stability, as the metallic particles dissolves rapidly at OER conditions. In an in-situ XAS experiment the oxidation state of the nanoparticles were tracked as a function of potential. It was found that the metallic nanoparticles strongly oxidize around 1.1 V vs. RHE. Furthermore, from the measurements of both types of nanoparticles we hypothesize that RuO_2 binds O too strongly, as an increase in potential leads to further oxidation of Ru. As a consequence of too strong binding of O, the oxidation state of Ru

decrease during OER as the coverage of O intermediates are no longer based on thermodynamics but rather kinetics.

Finally an IrO_2 protection layer on a RuO_2 thin film catalyst was investigated using high resolution XAS. It was found that the stability of the RuO_2 thin film could be improved by adding small amounts of IrO_2 on the surface. With in-situ XAS measurements we were able to measure the oxidation state of Ir as a function of applied potential. It was found that the IrO_2 does not participate in the OER, but sits at the surface and takes up oxygen by increasing its oxidation state.

Resumé

I denne afhandling er elektrokatalysatorer til iltreduktion (ORR) og iltudvikling (OER) blevet undersøgt ved hjælp af synkrotronbaseret røntgendiffraktion og røntgenabsorbtionsspektroskopi. Katalysatorerne er baseret på henholdsvis platin og ruthendioxid til iltreduktion og iltudvikling.

Til ORR er modelsystemer bestående af Pt_xGd og Pt_xY legeringer blevet fremstillet. EXAFS er blevet målt på en række størrelseudvalgte Pt_xGd nanopartikler for at bestemme deres interatomare Pt-Pt afstande. De største partikler med en diameter på 8 nm var mest aktive med en masseaktivitet på 3.5 A/mg_{Pt}, og disse partikler viste den kraftigste kompression af den nærmeste nabo Pt-Pt afstand. Det stemmer overens med dannelsen af et rent Pt overlag, som er komprimeret i forhold til massivt Pt, hvilket forklarer forbedringen i aktivitet udelukkende på baggrund af tøjningseffekter. Aktiviteten af nanopartikler med foskellige størrelse var korreleret med tøjningen, jo mindre partiklerne var jo mindre aktive var de, samt de havde en mindre grad af komprimering.

For at få mere indsigt i overlagets struktur fabrikerede vi enkeltkrystal modelsystemer af Gd/Pt(111) og Y/Pt(111) ved deponering af tyndfilm af Gd eller Y på en Pt(111) enkeltkrystal ved høj temperatur under vakuum (UHV). XRD målinger af begge modelsystemer viste dannelsen af et FCC-lignende overlag der er omkring 3 atomlag tykt på Y/Pt(111) og omkring 5 atomlag tykt på Gd/Pt(111). Den gennemsnitlige kompression i overfladeplanen på de to systemer var på henholdvis 1.4% og 0.31%. Analysen af XRD resultaterne viste en høj spredning af tøjning i materialerne, hvilket kan forklare hvorfor de to katalysatorer har næsten samme katalytiske aktivitet på trods af den store forskel i gennemsnitlig kompression.

Et in-situ studie af Gd/Pt(111) afslørede at overlaget dannes med det samme ved eksponering til sur elektrolyt under åbent kredsløb. Stabilitetsmålinger viste at tøjningen i overfladeplanen relakserer gennem de første 2000-3000 cykler, hvilket forklarer at faldet i aktivitet primært sker i dette område.

Til undersøgelse af iltudvikling fremstillede vi størrelsesudvalgte nanopartikler af metallisk Ru og termisk oxiderede RuO_2. Begge materialer er meget katalytisk aktive til iltudvikling, og de metalliske partikler er exceptionelt aktive. Denne forøgelse sker på bekostning af stabiliteten, hvilket ses ved at de metalliske partikler hurtigt går i opløsning under de kemiske forhold ved iltudvikling. I et in-situ XAS eksperiment kunne vi følge oxidationstrinnet af Ru som funktion af spænding. Vi observerede at de metalliske partikler oxiderede kraftigt ved 1.1 V i forhold til RHE. Udfra

målingerne på begge typer nanopartikler fremstiller vi en hypotese at RuO_2 binder ilt for kraftigt, idet en forøgelse i spændingen medførte et højere oxidationstrin af Ru. Som en konsekvens af den for stærke oxygenbinding vil oxidationstrinnet af Ru falde under iltudvikling, idet dækningsgraden af iltmolekyler ikke længere er bestemt af termodynamik, men i stedet er bestemt af kinetiske barrierer.

Til sidst har vi undersøgt et beskyttende lag af IrO_2 på en tyndfilm af RuO_2 ved hjælp af høj-opløsning XAS. Målinger viste at stabiliteten af RuO_2 kunne forbedres ved blot at tilføje små mængder IrO_2 på overfladen. In-situ målinger muliggjorde at måle oxidationstrinnet af Ir som funktion af spænding. Vi fandt ud af at IrO_2 ikke indgår i iltudvikling, men i stedet sidder på katalysatoroverfladen og optager ilt, og dermed øger sit oxidationstrin.

Preface

This PhD thesis was prepared at the Department of Physics at the Technical University of Denmark in fulfillment of the requirements for acquiring a PhD degree in physics. The project carried out as a long term collaboration between the Center for Individual Nanoparticle Functionality (CINF) at DTU and SUNCAT at Stanford University and SLAC National Laboratory in California, USA. The project was supervised by Ib Chorkendorff and Ifan E. L. Stephens from DTU and Anders Nilsson from SLAC and Stockholm University. The PhD project was funded by an DTU institute stipend as well as from the NACORR project, supported partly be Innovation Fund Denmark project number 12-132695.

Most of the results presented in chapters 8 and 9 are collected at beam times at SSRL. I have played a large role at all these beam times, but of course I could not have collected the data without all the people mentioned in the acknowledgments. However, I have completed the data analysis for all the experiments presented in those two chapters, and unless otherwise stated, I have collected and analyzed the data.

Kongens Lyngby, November 8, 2016

Anders Pedersen

Anders Filsøe Pedersen

Acknowledgements

I would like to thank my supervisors for allowing me to help tackle some of the great challenges facing our modern energy concerns and climate change. Furthermore they have guided me into the great world of catalysis and X-rays.

I would like to thank my colleagues at DTU for their great help in realizing these very difficult experiments, both in preparing the samples and participating in beam time. Especially I would like to thank Elisabeth Ulrikkeholm, Maria Escudero-Escribano, Amado Velazquez-Palenzuela, Bela Sebok, Anders Bodin, Rasmus Frydendal, and Elisa Paoli.

I also have great thanks to people on the other side of the Atlantic, especially Daniel Friebel has welcomed me and trained me to work in the world of synchrotron X-rays. From the SUNCAT experimentalist group I would like to thank Lin Li, André Eilert, Filippo Cavalca, Hirohito Ogasawara, and Sloan Roberts. Thanks are also given to the Tom Jaramillo group at Stanford to helping with lab equipment. Furthermore, the staff at SSRL have gone above and beyond to help making experiments succeed, and extra thanks goes to Ryan Davis and Chad Miller. Also from SSRL, Apurva Mehta has been an invaluable help during countless beam times and for the following complex data analysis, as well as discussion of science and everything else.

Special thanks also go to the additional funding from the Ministry of Higher Education and Science from granting me the EliteForsk travel grant, as well as the Danish Agency for Science, Technology and Innovation (DASTI) for also granting funds for traveling.

Finally my family deserves great thanks for supporting me during my physics studies for many years, and continuing to support me while living far from home in California. And Ena gets tremendous credit for coping with me during beam times and especially the last part of the project.

List of papers

Papers appended to this thesis

The enhanced activity of mass-selected Pt_xGd nanoparticles for oxygen electroreduction
Amado Velázquez-Palenzuela, Federico Masini, Anders F. Pedersen, María Escudero-Escribano, Davide Deiana, Paolo Malacrida, Thomas W. Hansen, Daniel Friebel, Anders Nilsson, Ifan E.L. Stephens, Ib Chorkendorff
Journal of Catalysis, 2015, volume 328, pages 297-307

Probing the nanoscale structure of the catalytically active overlayer on Pt alloys with rare earths
Anders F. Pedersen, Elisabeth T. Ulrikkeholm, María Escudero-Escribano, Tobias P. Johansson, Paolo Malacrida, Christoffer M. Pedersen, Martin H. Hansen, Kim D. Jensen, Jan Rossmeisl, Daniel Friebel, Anders Nilsson, Ib Chorkendorff, Ifan E.L. Stephens
Nano Energy, 2016, *in press*

Pt_xGd alloy formation on Pt(111): Preparation and structural characterization
Elisabeth T. Ulrikkeholm, Anders F. Pedersen, Ulrik G. Vej-Hansen, María Escudero-Escribano, Ifan E.L. Stephens, Daniel Friebel, Apurva Mehta, Jakob Schiøtz, Robert K. Feidenhansl', Anders Nilsson, Ib Chorkendorff
Surface Science, 2016, volume 652, pages 114-122

Formation and evolution of the Pt overlayer on Gd/Pt(111) single crystals
Anders F. Pedersen, María Escudero-Escribano, Elisabeth T. Ulrikkeholm, Daniel Friebel, Ifan E. L. Stephens, Ib Chorkendorff
In preparation

Papers not appended

Oxygen evolution on RuO_2: An in-situ XAS study
Anders F. Pedersen, Bela Sebok, Anders Bodin, María Escudero-Escribano, Daniel Friebel, Jan Rossmeisl, Ifan E. L. Stephens, Anders Nilsson, Ib Chorkendorff
In preparation

Selective IrO_x protection of RuO_2 for oxygen evolution
Anders F. Pedersen, Elisa Paoli, Rasmus Frydendal, Daniel Friebel, Jan Rossmeisl, Ifan E. L. Stephens, Anders Nilsson, Ib Chorkendorff
In preparation

List of acronyms

ALS - Advanced light source

AR-XPS - Angle resolved X-ray photoelectron spectroscopy

CE - Counter electrode

CV - Cyclic voltammogram

DFT - Density functional theory

DOS - Density of states

DSA - Dimensionally stable anode®

EXAFS - Extended X-ray absorption fine spectrum

HDI - Human development index

HERFD-XAS - High energy resolution fluorescence detected X-ray absorption spectroscopy

ID - Insertion device

NHE - Normal hydrogen electrode

OCV - Open circuit potential

OER - Oxygen evolution reaction

ORR - Oxygen reduction reaction

PEM - Proton exchange membrane

PEMFC - Proton exchange membrane fuel cell

RE - Reference electrode

RHE - Reversible hydrogen electrode

RIXS - Resonant inelastic X-ray scattering

SAXS - Small angle X-ray scattering

SHE - Standard hydrogen electrode

SLAC - Stanford linear accelerator center

SPEAR - Stanford positron electron asymmetric ring

SSRL - Stanford synchrotron radiation lightsource

SSRP - Stanford synchrotron radiation project

STM - Scanning tunneling microscope

TEM - Transmission electron microscope

WE - Working electrode

XANES - X-ray absorption near edge spectrum

XAS - X-ray absorption spectroscopy

XPS - X-ray photoelectron spectroscopy

XRD - X-ray diffraction

Contents

CHAPTER 1

Introduction

Our modern society has developed tremendously since the beginning of the industrial revolution, providing better living standards and vastly progressing technology to improve living standards for the majority of the population. Many of these new technologies rely on energy to function, and most humans are to a large extent reliant on readily available energy.

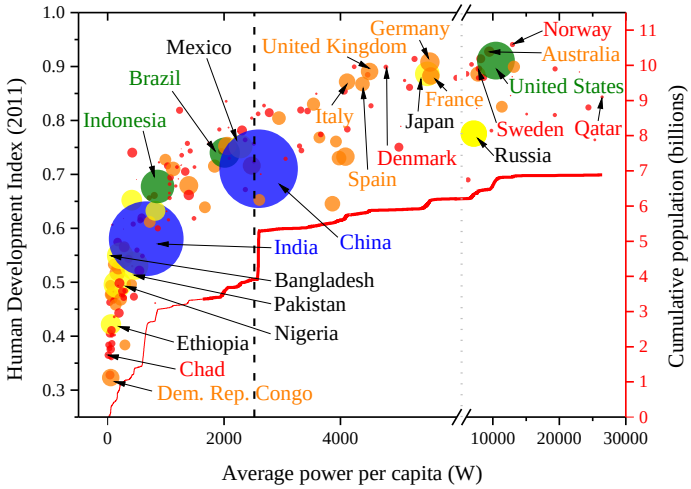

Figure 1.1: The figure shows the human development index (HDI), a United Nations metric for living standard, as a function of energy consumption per capita. The circle size and color represent the population of each country, and the red line shows the cumulative population. The Western countries with high HDI all have a high energy consumption, and as large countries such as China and India are moving towards higher HDI the global energy demand will increase significantly. The HDI data is from the UN [1], energy consumption is from the U.S. Energy Information Administration [2], and the population numbers are from the World Bank [3].

1.1 World energy consumption

In the Western world we are relying on energy for transportation of both persons and goods, electricity for heating and cooling, and in general a higher living standard requires a higher energy consumption. Figure 1.1 shows the human development index (HDI), a United Nations metric for living standard, as a function of the energy consumption per capita for most countries in the world in 2011. The size and color of the circles for each country represent the population of the country. The red line shows the cumulative population as a function of the energy consumption per capita, and it is seen that the majority of the world population uses much less energy than the Western countries. As expected the Western countries have a high HDI, and as large countries such as China and India move towards higher HDI the global energy demand will rise significantly over the next decades.

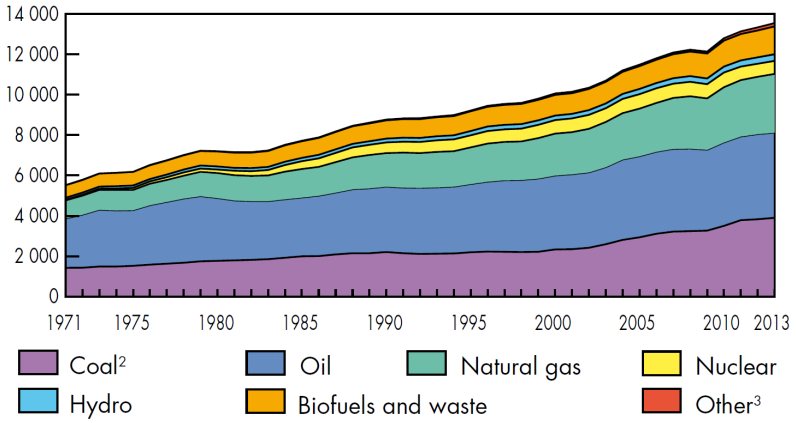

Figure 1.2: The figure shows the world's total primary energy supply from 1971 to 2013 by fuel type. In general the energy supply has doubled in the 40 year period covered here, and most of the growth has been covered by increasing coal and natural gas production. In total the fossil fuels (oil, coal, and natural gas) covers 80% of the energy supply in 2013. The figure is from [4], ([2]) peat and oil shale is included with coal, ([3]) 'other' includes geothermal, solar, wind, heat, and other energy sources.

As the global population has become very large and the energy demand is growing, an important aspect of energy consumption is its sources. Figure 1.2 shows the evolution of the total primary energy supply for the world by fuel type from 1971 to 2013. Coal, oil, and natural gas are all fossil fuels, and from the graph it is clear that about 80% of our energy is produced from these non-sustainable sources. The sustainability of nuclear energy may be questioned, but if we here include it as sustainable only 20% of our energy demand is provided by sustainable sources. Figure 1.3 shows the detailed distribution of energy sources for 1973 and 2013, and what is

typically known as 'green' energy (hydro and 'other') only makes out 1.9% and 3.6% of our energy production, respectively.

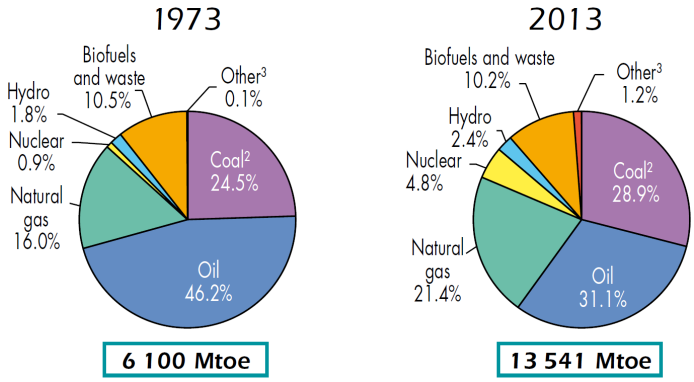

Figure 1.3: The figure shows the world's total primary energy supply in 1973 to 2013 detailed by fuel type. The traditional 'green' energy sources consist of hydro and 'other', and only makes out 3.6% of the energy supply in 2013. The figure is from [4], ([2]) peat and oil shale is included with coal, ([3]) 'other' includes geothermal, solar, wind, heat, and other energy sources.

1.2 Carbon emissions

Burning off fossil fuels release CO_2 into the atmosphere, and because of the rate at which fossil fuels are burnt and have been burnt since the start of the industrial revolution, the atmospheric CO_2 concentration is rising significantly. Figure 1.4 shows the atmospheric concentration of CO_2 in the past 50 years, and it is seen to rise at an ever increasing rate as the time goes by. The graph shows both the annual deviations in the CO_2 concentration as well as the seasonally averaged level. Furthermore, the present CO_2 levels are much higher than anything observed in the last 400,000 years. Figure 1.5 shows the CO_2 concentration on a geographical time scale, and the present day increase in CO_2 is unprecedented.

CO_2 is a naturally occurring greenhouse gas in Earth's atmosphere, among e.g. water vapor, methane, and nitrous oxide. These gases all absorb light in the thermal infrared spectrum, effectively trapping some of the thermal heat emitted from the surface of the Earth. When human activities significantly increase the concentration of these greenhouse gases more heat gets trapped, leading to an increase in the global surface temperature. This rise in temperature is seen in figure 1.6 showing the change in global temperatures over the last 130 years. Rising temperatures are problematic as more ice melts raising the sea level, as well as possible changes in weather patterns. Rising sea levels pose an immediate threat to humans as most people live at or

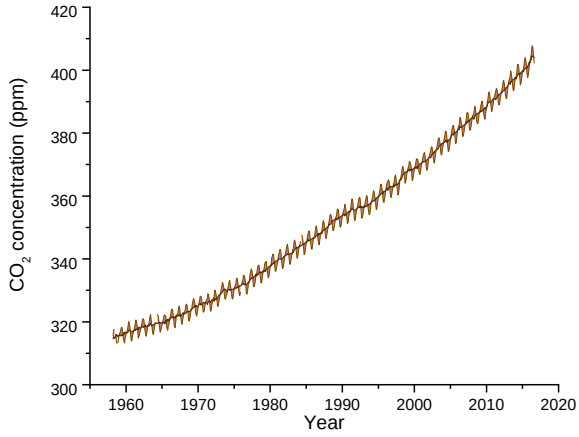

Figure 1.4: The figure shows the atmospheric CO_2 concentration over time, as it is increasing at faster rates as time goes by. The increase in concentration is much larger than the seasonal variations also shown in the graph. The data is from [5].

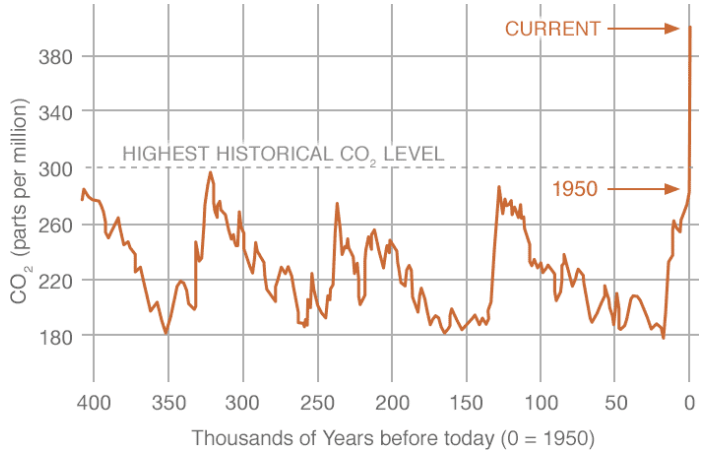

Figure 1.5: The figure shows the atmospheric CO_2 concentration on a geographic time scale. The increase in CO_2 concentration observed in modern time is unprecedented. The figure is from [5].

near coast lines, and some countries have large fraction of their land below current sea levels (e.g. Holland and Bangladesh). Changing weather patterns pose a more indirect threat as it can impact agriculture, and the food supply can be severely limited if certain areas become more arid.

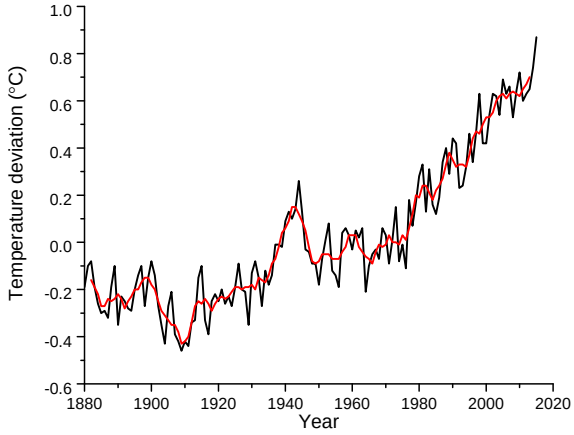

Figure 1.6: The figure shows the change in the global temperature over the last 130 years. The black line shows the yearly temperature average and the red line shows a 5-year average. The temperature has been steadily rising since the 1970's. The data is from [6].

To avoid global scale catastrophic weather changes and sea level rise, the use of fossil fuels must be phased out and replaced by sustainable energy sources. Sustainable energy sources harvest their energy from the sun, and typically convert it into electricity, e.g. solar, wind, hydro, and wave energy. With the exception of hydro electricity, these sources are all intermittent, solar cells only produce electricity during the day and windmills produce electricity as the wind blows. So in order for these technologies to be adopted widespread it is crucial to enable energy storage. One option for energy storage is chemical bonds, which requires the use of energy conversion devices that can convert excess electricity into fuels, and convert the fuels back to electricity when needed [7].

1.3 Energy conversion devices

Fuels present the option to store energy with a high gravimetric and volumetric density, and are therefore attractive for use in the transportation sector [8]. Especially

since the transportation requires high energy density fuels, it is difficult to find alternatives to combustion engines. And as seen in figure 1.7 more than half of the world's oil products are used for transportation, and are thus a significant and growing contributor to the overall energy consumption.

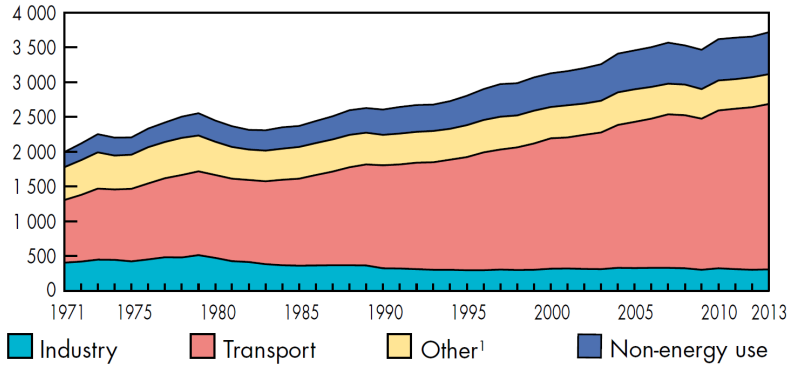

Figure 1.7: The figure shows the consumption of oil products among different sectors. It is clear that the transportation sector takes up more than half of the global oil use, and its demand keeps increasing. The figure is from [4].

The proton exchange membrane (PEM) technology is a fairly mature technology allowing electrochemical energy transformation at room temperature [10]. The central part in a PEM device is a membrane that conducts protons but not electrons, and Nafion is often used (®by Dupont), a polymer based on sulfonated tetrafluoroethylene. For example a hydrogen fuel cell can be realized using this membrane, and a sketch of such a device is shown in figure 1.8.

Depending on the catalyst materials a PEM device may be optimized as either a fuel cell producing electricity from fuel, or an electrolyzer generating fuel from electricity.

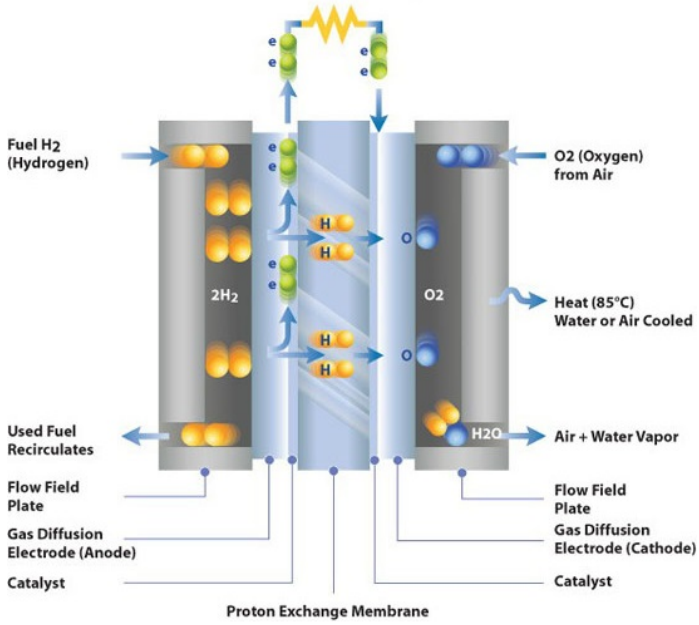

Figure 1.8: The figure shows a sketch of a hydrogen PEM fuel cell. The hydrogen is supplied at the anode at the left where it is oxidized. The protons migrate through the membrane while the electrons pass through an external circuit performing electric work. The protons, electrons, and oxygen combine at the cathode to form water. The figure is from [9].

1.3.1 PEM fuel cell

In the fuel cell case the simplest fuel is hydrogen gas (H_2), which is combined with oxygen to form water,

$$2H_2 + O_2 \rightarrow 2H_2O\,. \tag{1.1}$$

For this device Pt may be used on both the anode and cathode to make the reaction run. The electrical performance of a modern fuel cell based on Pt is seen in figure 1.9. This plot shows the fuel cell voltage as a function of the current density drawn. Ideally the cell should give a constant potential of 1.16 V as indicated, as this is the thermodynamic potential for the energy obtained in reaction (1.1) at 80 °C [11]. The losses have been indicated, and as expected one can find ohmic losses (ΔE_Ω) and mass transport losses (η_{tx}), however by far the greatest loss is associated with the oxygen reduction reaction (ORR) at the cathode (η_{ORR}). The losses associated with ORR are entirely due to intrinsic properties of the materials used in the fuel cell, and developing better materials for ORR is highly important for the improvement of fuel

cells [8, 11, 12].

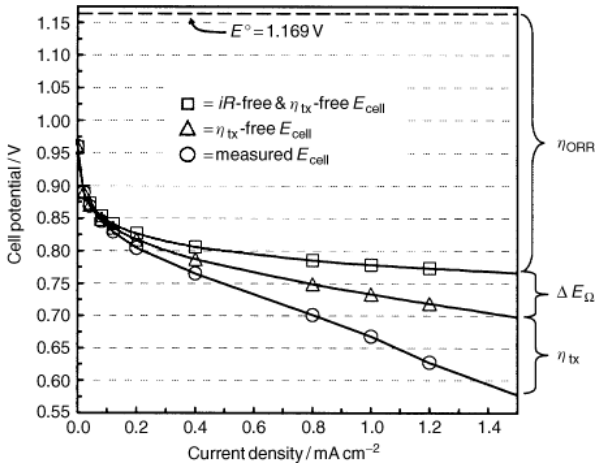

Figure 1.9: The figure shows the cell voltage of a PEMFC with Pt at both the anode and cathode as a function of the current density drawn. Ideally the potential should be 1.16 V, however large losses are seen, most of which is attributed to the oxygen reduction reaction at the cathode. The figure is from [11].

Fuel cells do not only operate with hydrogen as fuel, it can in principle be made with any fuel that can deliver hydrogen, another example is direct methanol fuel cells [13, 14]. Using a different fuel presents several challenges, e.g. finding a good material for the anode. But for all PEM fuel cells the cathode will do the oxygen reduction reaction, and improvements in ORR performance will benefit all PEM fuel cells.

1.3.2 PEM electrolyzer

Simply using a hydrogen fuel cells does not guarantee sustainability, unless the hydrogen is produced in a sustainable way. One way of doing so it to perform water splitting in an electrolyzer,

$$2H_2O \rightarrow 2H_2 + O_2\,. \tag{1.2}$$

The PEM electrolyzer is designed in a very similar way to the PEM fuel cell, but instead the electricity is put into the cell to provide the energy to split the water. In a typical PEM electrolyzer the cathode (that does hydrogen evolution) is based on Pt, whereas the anode (that does the oxygen evolution) is based on Ir. The performance of a modern PEM electrolyzer is seen in figure 1.10 and shows the potential required to run the water splitting at a given current density. This cell is run at 80 °C like the fuel cell above, and so the potential to run water splitting should ideally be 1.16

V. However, the potentials are much higher, which cannot be accounted for by ohmic resistance and mass transport limitations alone. In this case the oxygen evolution reaction (OER) is severely limiting the efficiency of the device, in the same way as ORR limits the fuel cell.

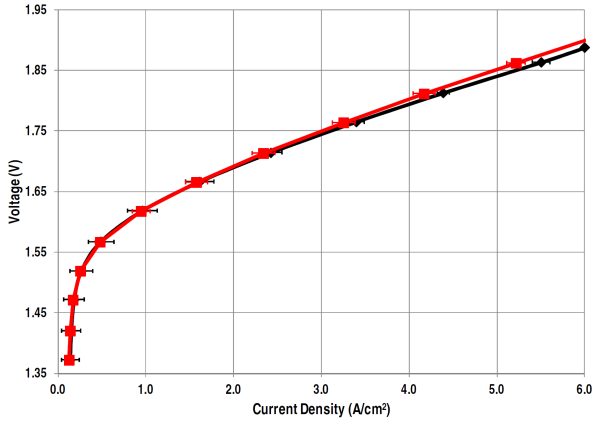

Figure 1.10: The figure shows the supplied cell voltage of a series of modern PEM electrolyzers with a Pt-based cathode and an Ir-based anode as a function of the current density. Ideally the potential should be 1.16 V, however large losses are again seen, most of which is attributed to the oxygen evolution reaction at the cathode. The figure is from [15].

Due to difficulties of storing hydrogen at high volumetric densities, it is attractive to form liquid fuels directly by electrochemical methods. One such example is CO_2 reduction, in which CO_2 is converted into fuels like methanol or higher hydrocarbons [16, 17]. In the reduction of chemicals into fuels a source of hydrogen is needed, and as long as the hydrogen source is water, the oxygen evolution reaction will limit the efficiency of the device.

CHAPTER 2

Oxygen electrocatalysis

For the PEM fuel cell and electrolyzer the noble metals platinum, iridium, and ruthenium are often used at the anode and cathode. These materials are expensive [18, 19], but are used because they act as catalysts for the chemical reactions at each side of the cell. A catalyst basically helps to facilitate a chemical reaction without being consumed, by lowering the energy barriers needed for the reaction to proceed. This is indicated in the scheme in figure 2.1, in which two reactants X and Y react to form the product Z. The difference in free energy between the reactants and product is labeled ΔG, and it is important to note that the catalyst does not change the thermodynamics of the reaction, and a negative change in free energy is still required for the reaction to occur.

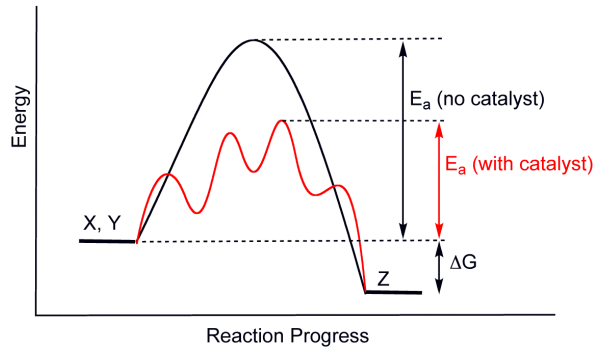

Figure 2.1: The figure shows a sketch of how a catalyst changes the activation energy for a chemical reaction. The difference in free energy (ΔG) between the reactants (X and Y) and the product (Z) must be negative for the reaction to proceed, the catalyst only impacts the activation barriers. The figure is from [20].

Using Pt, Ir, and Ru presents challenges both in terms of the sheer price of these materials, e.g. in a mass-produced fuel cell based on Pt, the price of Pt will make out

about half of the cost of the entire fuel cell stack [21]. But even more challenging is the scarcity of these metals, which are among the most scarce naturally occurring elements in Earth's crust. Figure 2.2 shows the global annual production of the elements. Here Pt, Ir, and Ru are found towards the bottom, and the annual production of Pt is about 200 tons, while Ir and Ru are side products from Pt mining and only about 10 tons of Ir and 20 tons of Ru are produced annually. Pt has a higher price than Ir despite its higher production, but Ir has very few applications and so the demand is quite low.

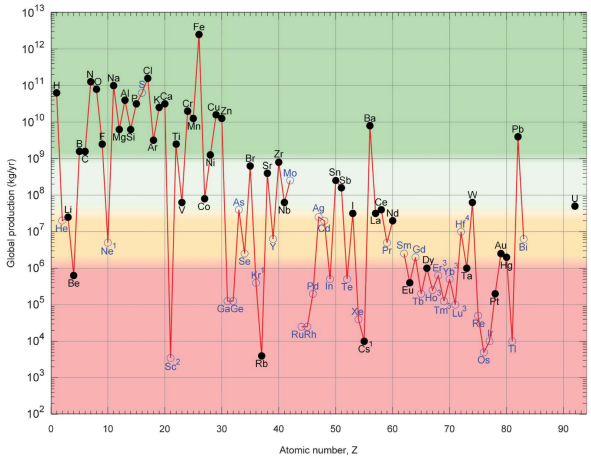

Figure 2.2: The figure shows a the global annual production of the elements in 2010. The noble metals Pt and Ir are towards the bottom with a very low production. The figure is from [22].

Using current PEM fuel cell technology based on Pt, a 100 kW fuel cell stack suitable for a personal vehicle requires about 80 g of Pt [22]. Assuming that all Pt is used to make fuel cells for cars this would limit the annual production of cars to 2.5 million, which is far below the 90 million vehicles produced in 2015 [23]. The problem is similar for water splitting and Ir, but the supply of Ir is even more constrained.

The scarcity of these materials combined with the desire to reduce fossil fuel usage strongly motivates the development of better catalyst materials for both ORR and OER. In this work the focus is on improving Pt based ORR catalysts, so that less Pt is required for the same or better fuel cell performance. In the case of OER the focus is on understanding Ir and Ru better so that more active catalysts can be developed with no or extremely small amounts of Ir. Efforts to replace the Pt for ORR catalysts [24, 25] and Ir of OER catalysts [26] by more abundant materials are being investigated in other groups [27, 28].

2.1 Scaling relations

Having discussed the role of catalysts and seen the big losses in oxygen catalysis, one may ask why oxygen is so difficult?

Part of the answer is that oxygen reduction/evolution is a complex chemical reaction. It is generally accepted that ORR in acidic electrolyte proceeds in the following steps [29–31],

$$\begin{aligned}
\mathrm{O_2} + {}^* &\rightarrow {}^*\mathrm{O_2}\,, && (2.1)\\
{}^*\mathrm{O_2} + \mathrm{H^+} + \mathrm{e^-} &\rightarrow {}^*\mathrm{OOH}\,, && (2.2)\\
{}^*\mathrm{OOH} + \mathrm{H^+} + \mathrm{e^-} &\rightarrow \mathrm{H_2O} + {}^*\mathrm{O}\,, && (2.3)\\
{}^*\mathrm{O} + \mathrm{H^+} + \mathrm{e^-} &\rightarrow {}^*\mathrm{OH}\,, && (2.4)\\
{}^*\mathrm{OH} + \mathrm{H^+} + \mathrm{e^-} &\rightarrow \mathrm{H_2O} + {}^*\,, && (2.5)
\end{aligned}$$

where * indicates an adsorption site on the catalyst surface. For OER in acidic electrolyte the reaction steps are reverse of the above [32]. This reaction is complex in the sense that 4 coupled proton/electron transfers are required for a single oxygen molecule. The difference in free energy in between these intermediates is defined as,

$$\begin{aligned}
\Delta G_1 &= G_{\mathrm{O_2}} - G_{\mathrm{OOH}}\,, && (2.6)\\
\Delta G_2 &= G_{\mathrm{OOH}} - G_{\mathrm{O}}\,, && (2.7)\\
\Delta G_3 &= G_{\mathrm{O}} - G_{\mathrm{OH}}\,, && (2.8)\\
\Delta G_4 &= G_{\mathrm{OH}}\,, && (2.9)
\end{aligned}$$

where G_X is the free energy of intermediate X adsorbed on the catalyst surface. In order for the reaction to proceed all these free energy differences must be negative, which can be controlled by an external potential. So in the case of ORR the limiting potential will be the smallest step, i.e.

$$U_{\mathrm{ORR}} = \min(\Delta G_1, \Delta G_2, \Delta G_3, \Delta G_4)/e\,. \tag{2.10}$$

But in the case of OER the potential we provide to split water must be greater than the largest step,

$$U_{\mathrm{OER}} = \max(\Delta G_1, \Delta G_2, \Delta G_3, \Delta G_4)/e\,. \tag{2.11}$$

From this it is seen that the optimal catalyst is found when all steps are equal, resulting in an individual step height of 1.23 eV (at room temperature [32]) and a total change in free energy of 4.92 eV. Any deviation from equal steps results in a penalty in the potential, known as the overpotential.

On many metal and oxide surfaces it turns out that $\Delta G_3 = \Delta G_4$ [32, 33]. With this constraint we can assume that ΔG_1 and ΔG_3 are free parameters with $\Delta G_2 =$

$4.92\text{eV} - \Delta G_1 - 2\Delta G_3$. From the two free parameters the potential for ORR and OER may be calculated, and are shown in figure 2.3. Here two volcanos are seen, the blue for ORR and the green for OER. The volcanoes illustrate Sabatier's principle; the optimum catalyst should not bind the intermediates too strong nor too weak. And by tuning ΔG_1 and ΔG_3 freely a point may be achieved in which there is no overpotential for ORR or OER.

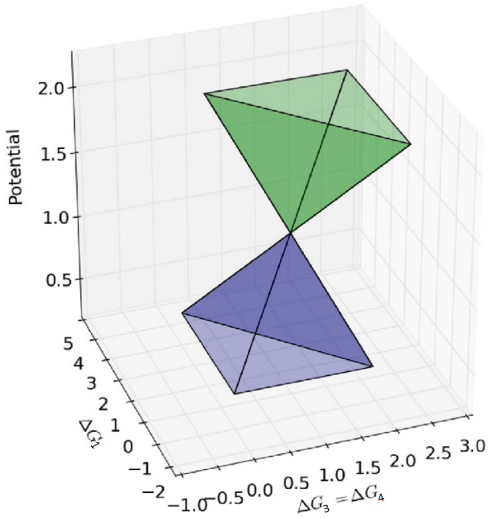

Figure 2.3: The figure shows the theoretical overpotential for ORR (blue) and OER (green) as ΔG_1 and ΔG_3 are varied freely. The figure is adapted from [32].

Unfortunately nature does not allow the binding energy of the reaction intermediates to be varied independently so easily. In fact it is found from density functional theory (DFT) calculations that on transition metal surfaces the *OH, *O, and *OOH binding energies are all correlated so that $G_{\text{O}} = 2G_{\text{OH}}$ and $G_{\text{OOH}} = G_{\text{OH}} + 3.2$ eV [32, 33]. The calculated binding energies of these three reaction intermediates are plotted in figure 2.4 as a function of the *OH binding energy.

The correlation of the binding energies are called scaling relations. The calculations have been made for a range of transition metal surfaces with different terminations, and all data points follow the scaling, showing the universality of the scaling relations on flat surfaces. On one hand the scaling relations makes the description of a catalyst simpler, as only one binding energy determines the activity of a catalyst. On the other hand it also limits the activity of catalysts as the difference between G_{OOH} and G_{OH} of 3.2 eV does not match 2×1.23 eV, meaning that an overpotential cannot be avoided. Figure 2.5 shows the same 3D volcano as before, but with the scaling relation shown as a red plane.

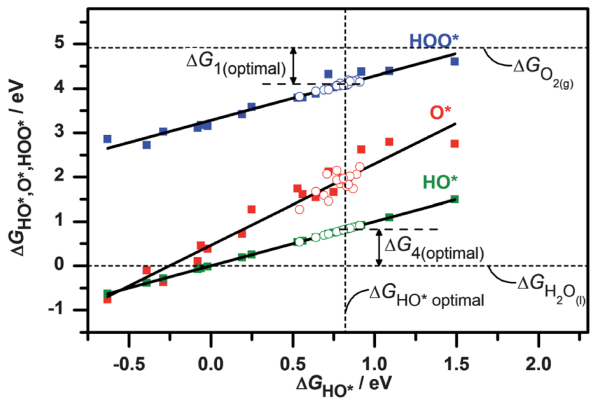

Figure 2.4: The figure shows the calculated binding energy of the *OH, *O, and *OOH reaction intermediates as a function of the *OH binding energy. These calculations have been done for a range of transition metal surfaces with different terminations, and shows the universality of scaling relations. The figure is from [33].

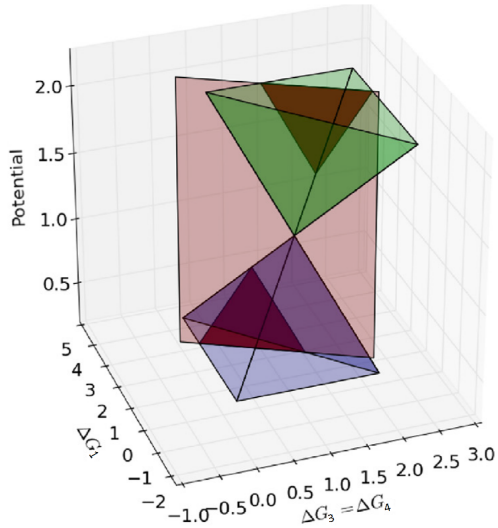

Figure 2.5: The figure shows the theoretical overpotential for ORR (blue) and OER (green) as ΔG_1 and ΔG_3 are varied freely. Additionally the $G_{\mathrm{OOH}} = G_{\mathrm{OH}} + 3.2$ eV scaling relation has been shown by the red plane. The figure is adapted from [32].

The scaling relations trap us on the red plane when the catalyst is a flat surface, resulting in unavoidable overpotentials. Furthermore, the two 1D volcanoes for ORR and OER does not line up, meaning that the optimal catalyst for ORR will not be a good catalyst for OER and vice versa. This is more clearly seen in figure 2.6 that shows the theoretical volcanoes for ORR and OER obtained from the intersection of the two 3D volcanoes with the red plane.

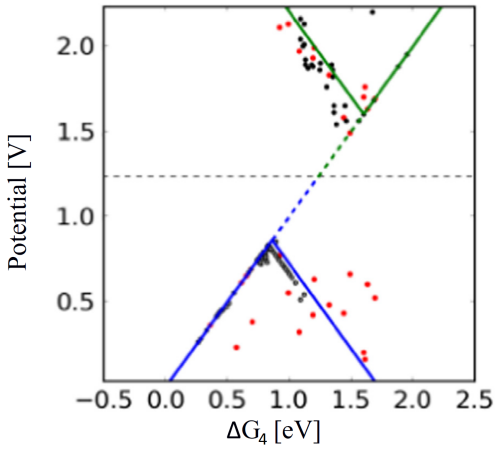

Figure 2.6: The figure shows the theoretical overpotential for ORR (blue) and OER (green) as a function of ΔG_4. Here it is seen that an overpotential cannot be avoided, and that the optimal catalyst for ORR is not a good OER catalyst as the volcanoes are misaligned. The figure is adapted from [32].

Using the scaling relations we can calculate all the 4 changes in free energy as a function of G_{OH} (which is equal to ΔG_4),

$$\Delta G_1 = 1.72\,\mathrm{eV} - G_{\mathrm{OH}}\,, \tag{2.12}$$
$$\Delta G_2 = 3.2\,\mathrm{eV} - G_{\mathrm{OH}}\,, \tag{2.13}$$
$$\Delta G_3 = G_{\mathrm{OH}}\,, \tag{2.14}$$
$$\Delta G_4 = G_{\mathrm{OH}}\,. \tag{2.15}$$

From these equations it is seen that the maximum potential obtainable for ORR is 0.86 V, which happens when $\Delta G_1 = \Delta G_4$ [33]. For OER the smallest potential required for water splitting is 1.60 V, which is when $\Delta G_2 = \Delta G_4$. As the equilibrium potential is 1.23 V these two best cases both have an overpotential of 0.37 V.

Even though the coupled proton/electron transfers are somewhat complicated this model is still a great simplification of a realistic system. Not only in ORR

and OER systems, but any system in aqueous electrolyte, has liquid water present which shows non-trivial interactions with the surface. In-situ investigations of the catalyst/electrolyte interface is also an important challenge [34, 35].

In the following two sections the path to reaching the top of both the ORR and OER volcanoes will be discussed.

2.2 Pt alloys for ORR

As mentioned in previous sections Pt is often used as an ORR catalyst, however pure Pt is not at the top of the ORR volcano, clearly demonstrated by figure 2.7. In this figure the theoretical volcano both shows the potential at which the reaction starts as well as the activity enhancement at a fixed potential (0.9 V) relative to Pt. Furthermore, the figure also shows an experimental volcano plotting the activity enhancement over pure Pt as a function of the calculated OH binding energy. The experimental volcano is close to the theoretical one, and supports that the optimum catalyst binds OH about 0.1 eV weaker than pure Pt [36, 37].

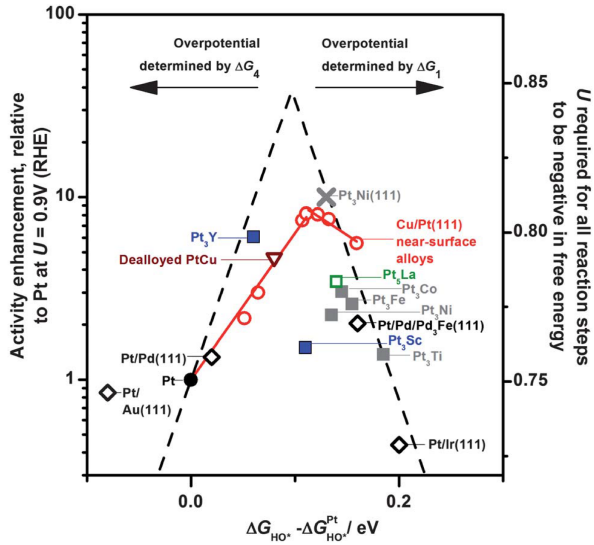

Figure 2.7: The figure shows both the calculated thermodynamic volcano as well as an experimental volcano showing the activity enhancement over pure Pt as a function of the calculated OH binding energy. The figure is from [33], diamond symbol data are from [38–40], gray squares data are from [41–43], crosses data are from [44], blue squares data are from [45], inverted triangles data are from [46, 47], red circles data are from [48], and the theoretical volcano is from [29, 49].

A frequently used path towards tuning the OH binding energy is through alloying. By introducing a second element with Pt the alloy may take on a new crystal structure, which contributes to electronic structure changes (strain effects) along with direct electronic structure changes from having a different element (ligand effect) [46, 50–53]. On transition metals the bonding of surface intermediates to the metal surface can often be understood within the d-band model [54–59]. For transition metals the partially filled d-band at the Fermi level is quite narrow in energy with a high density of states, which allows it to form bonding and anti-bonding states with an adsorbed molecule much in the same way bonding and anti-bonding molecular orbitals are formed when atoms form molecules. For O based intermediates the bonding forms mostly through the O 2p orbital [60, 61]. Figure 2.8 shows a sketch of this process, in which the separate bonding and anti-bonding states between the absorbed atom and the transition metal surface form. Within this framework one is able to predict the strength of the bonding to the adsorbed molecule by the filling of the d-band. The strongest bond is formed when all the bonding states are occupied and all the anti-bonding states are unoccupied, which is half-filling of all the states. By going to more noble metals the d-band is pulled down, and the anti-bonding states get filled, thus weakening the bond.

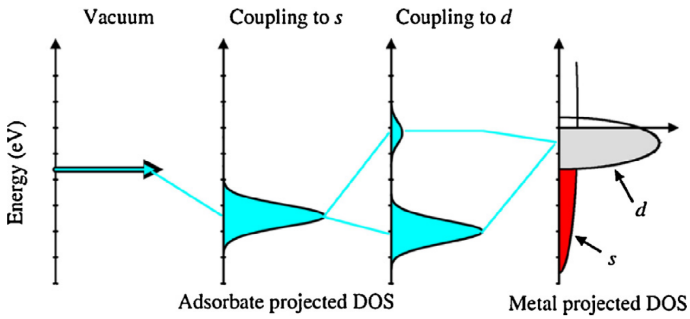

Figure 2.8: The figure shows a sketch of the formation of the bonding and anti-bonding states between the d-band of a transition metal and an absorbed molecule. The figure is from [61].

This model can also be applied to Pt and ORR, since we know that the OH binding energy should be weakened by 0.1 eV. This can be achieved by alloying with 3d transition metals, and figure 2.9 shows the volcano forming as the d-band center is tuned by adding different 3d transition metals to Pt. And indeed a significant enhancement in activity over pure Pt is found.

When alloying the noble metal Pt with a less noble element the catalyst surface may experience significant restructuring when exposed to the chemically harsh acidic environment in a PEM fuel cell. This causes dealloying and leaching of the less noble element into the electrolyte, which may lead to drastically decreased performance of the alloy catalyst [63–66]. The leaching of the second element may leave behind a

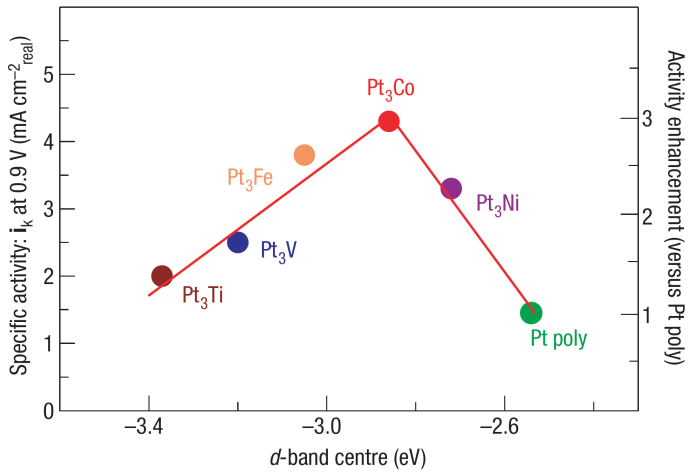

Figure 2.9: The figure shows the activity enhancement of Pt alloys over pure Pt by tuning the d-band center by choosing different ligands for alloying. The figure is from [62].

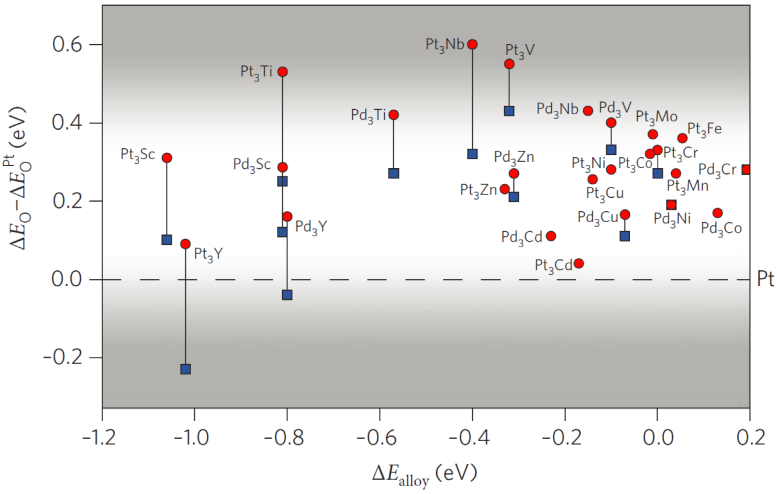

Figure 2.10: The figure shows the results from a DFT screening study. Two new alloys with a negative alloy formation energy and a reasonable O binding energy were identified: Pt_3Y and Pt_3Sc. For some alloys the binding energy was calculated with either 50% (red circles) or 25% (blue squares) of the alloying element in the second layer from the surface. The figure is from [45].

porous so-called skeleton structure, which could be less stable than a smooth surface [62, 67]. Alternatively certain systems and catalyst preparations may result in an atomically smooth surface with just a single Pt layer on the alloy surface, know as a Pt skin [62, 67]. Especially the Pt skin structure has shown incredibly high activity both as extended single crystal surface [44] as well as nanoparticles [68].

So far most of the alloys discussed have been Pt and late 3d transition metals. However, these alloys have a small alloy formation energy [45], which could explain the generally low stability [69]. There are exceptions to this trend, and as just discussed some materials with Pt_xNi and a Pt skin are stable [44, 68]. This started a theoretical DFT screening study to find binary Pt and Pd alloys that have a more negative alloy formation energy while providing a 0.2 eV weaker O binding energy [45]. One of the main findings of the paper is shown in figure 2.10, showing the surface O binding energy as a function of the alloy formation energy. As just discussed most of the Pt_3M alloys, with M being a 3d transition metal, do show promising O binding energy for ORR, however their alloy formation energy is quite high (or even positive). Two new alloys were identified as promising candidates as a stable and active ORR catalyst: Pt_3Y and Pt_3Sc.

These two newly identified Pt alloys were tested for ORR activity in the form of bulk polycrystalline alloys. The results are seen in figure 2.11, and shows that both alloys are indeed more active than pure Pt, but Pt_3Y especially so.

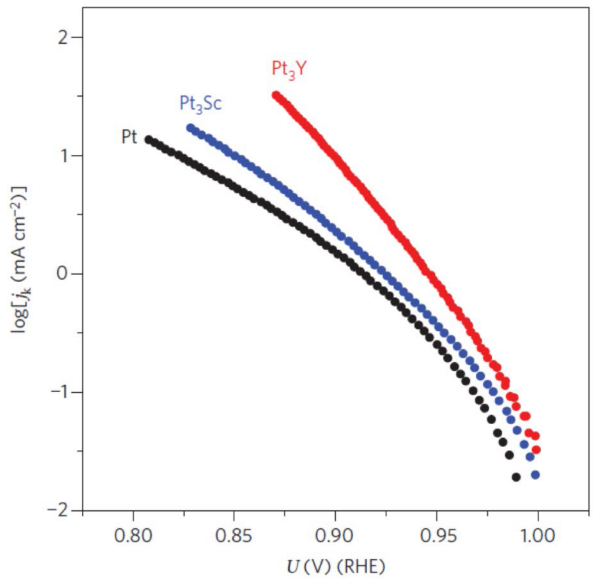

Figure 2.11: The figure shows the ORR activity of polycrystalline bulk alloys of Pt_3Y and Pt_3Sc compared to polycrystalline Pt. Both alloys are more active than pure Pt, but Pt_3Y especially so. The figure is from [45].

In [45, 70] it was found the Pt_3Y and Pt_5Y form a thick skeleton-like Pt overlayer. This overlayer suggests a different mechanism for enhancing the ORR activity, as the DFT screening study assumed a Pt-skin structure with Y content in the second layer from the surface. Further studies of polycrystalline Pt_5La, Pt_5Ce, and Pt_5Gd showed enhanced activity over pure Pt as well as the formation of a thick Pt overlayer [71, 72]. Angle-resolved X-ray photoelectron spectroscopy (AR-XPS) results in figure 2.12 shows the formation of a ∼1 nm thick Pt overlayer on a polycrystalline Pt_5Gd sample after electrochemical measurements. Not only are these alloys more active than pure Pt, Pt_5Gd also shows a high stability, making it attractive in PEM fuel cell use [72].

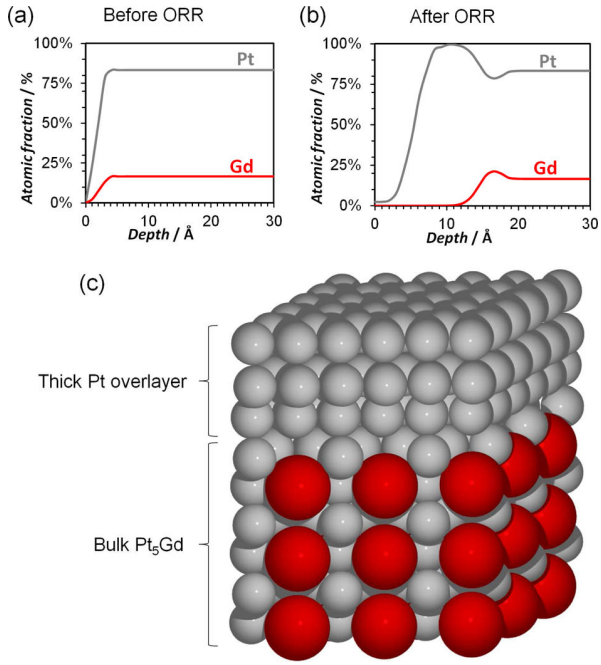

Figure 2.12: The figure shows elemental depth-profiles on polycrystalline Pt_5Gd obtained from AR-XPS. This shows that a ∼1 nm thick overlayer of pure Pt forms at the surface after ORR activity has been measured. The figure is from [72].

To gain further insight into the mechanism for the enhancement of ORR activity of these Pt alloys a more well-defined model system was desired. Single crystals of Pt_xY and Pt_xGd were impossible to acquire, but instead simulated single crystal surfaces may be fabricated from Pt(111) single crystals. Such crystals were prepared in ultra-high vacuum (UHV). The basic procedure is to evaporate Y or Gd onto the Pt(111) single crystal at elevated temperature, which forms the alloy instantaneously, and by depositing a thick layer, a reasonably thick alloy film may be formed. This yields a

single crystal labeled Y/Pt(111) or Gd/Pt(111), and the atomic ratio is consistent with the formation of a Pt_5Y or Pt_5Gd alloy, respectively. The detailed description of the alloy formation and its characterization is found in [73–76]. These single crystals are also active for ORR, as seen in figure 2.13, and both single crystal systems form overlayers after electrolyte exposure [77].

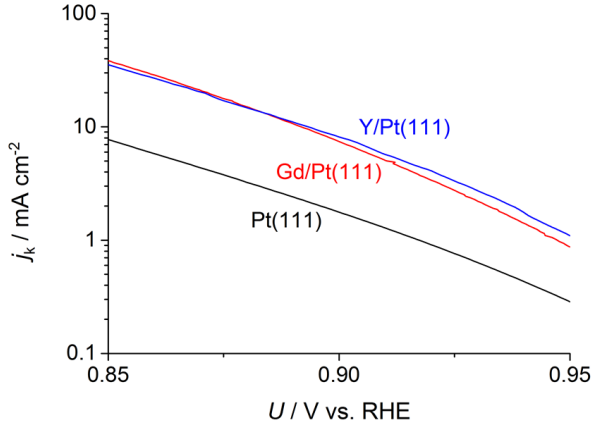

Figure 2.13: The figure shows a Tafel plot of the ORR activity of Pt(111), Y/Pt(111), and Gd/Pt(111), which a plot of the current density on a logarithmic scale versus the applied potential. It is seen that both the Y and Gd modified Pt(111) surfaces are much more active than pure Pt(111). The figure is from [77].

From the single crystal studies it was found that the alloys produce a compression of the Pt-Pt distance relative to bulk Pt. With these systems it seemed that the compression of the alloy could be responsible for the compression of the Pt overlayer. Further studies with Pt_5Ln (Ln = lanthanide) showed that the degree of compression of the alloy could be tuned by the lanthanide contraction [78]. And furthermore a volcano-like relation was found between the activity and the alloy compression, as seen in figure 2.14.

All the Pt_xY and Pt_xGd studies have involved extended surfaces, either as bulk polycrystalline sample or as single crystal alloy thin films. So studying nanoparticles of these Pt alloys was of great interest. However, due to the extreme oxofilicity of Y, Gd, and other lanthanides, a chemical synthesis of nanoparticles is very difficult [80, 81]. But instead a magnetron cluster source enabled the production of size-selected nanoparticles of Pt, Pt_xY, and Pt_xGd via physical methods.

Initial studies on Pt_xY nanoparticles revealed that they are indeed more active than pure Pt nanoparticles fabricated in the same way, and the mass-activity was enhanced by a factor of 3 over pure Pt [79]. Furthermore extended X-ray absorption fine structure (EXAFS) analysis was used for structural analysis, showing a correla-

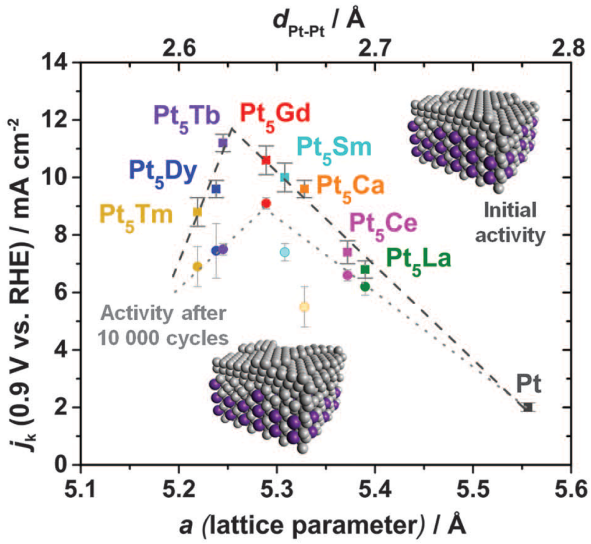

Figure 2.14: The figure shows the ORR activity as a function of the Pt-Pt compression in Pt_5Ln (Ln = lanthanide) alloys. A volcano is formed with the maximum initial activity (squares) for Pt_5Tb, whereas after 10000 cycles (circles) Pt_5Gd has the highest activity. The figure is from [78].

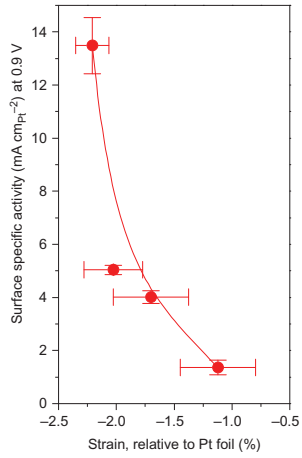

Figure 2.15: The figure shows the surface specific activity of Pt_xY nanoparticles as a function of the average Pt-Pt compression relative to bulk Pt. It is seen that the higher compression, the higher the ORR activity. The figure is from [79].

tion with the average Pt-Pt distance compression and the ORR activity, see figure 2.15.

Inspired by the success of the Pt_xY nanoparticles, a second experiment was carried out with Pt_xGd nanoparticles. First of all, the nanoparticles showed high activity towards ORR both in terms of surface specific and and mass activity, as shown in figure 2.16. The activity results are compared to that of both pure Pt and Pt_xY, and in terms of mass activity the 8 nm Pt_xGd nanoparticles have a slightly higher activity than the Pt_xY nanoparticles, and are a factor of 3.5 more active than pure Pt. The stability of the particles was investigated by electrochemically cycling the potential, and as seen in figure 2.17 only some of the activity is lost over time. Other measurements have shown that the intensity loss is due to intrinsic changes in the nanoparticles, rather than a simple loss of the nanoparticles from the substrate [82].

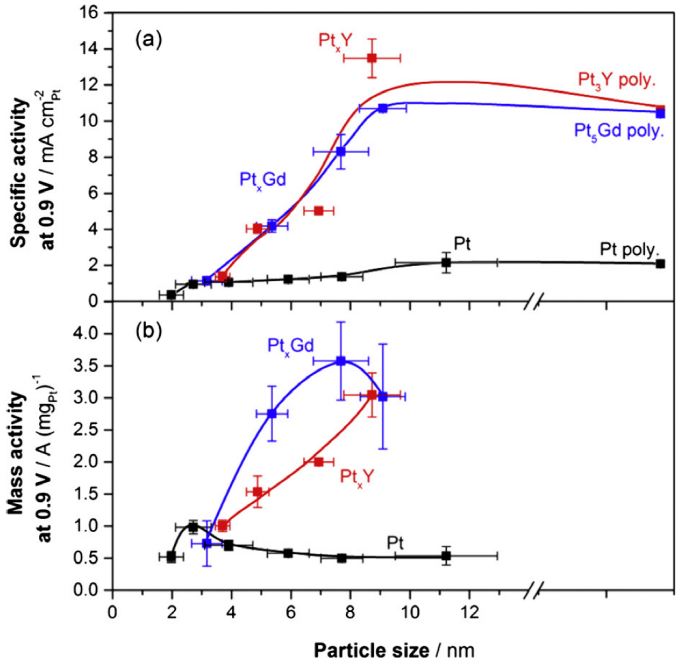

Figure 2.16: The figure shows the measured surface specific and mass activity for ORR of Pt_xGd, Pt_xY, and pure Pt nanoparticles, and for the surface activity also extended surface polycrystalline samples are compared. The two alloys show similar surface activity, which increases with particle size, and the mass activity is also highest for rather large nanoparticles. The enhancement in mass activity for Pt_xGd nanoparticles over pure Pt nanoparticles is about a factor of 3.5. The figure shows data from [79, 82], and it is from [82].

The structural analysis is shown and discussed in section 8.1.

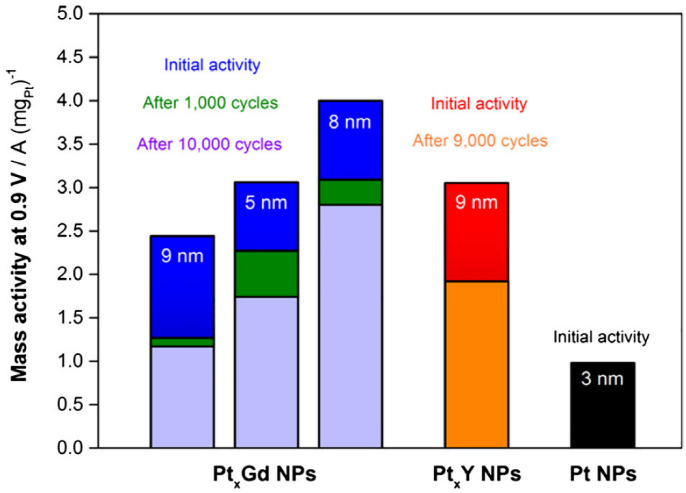

Figure 2.17: The figure shows the stability of the nanoparticles, as the activity is compared before and after extended cycling of the electrochemical potential. For the most active 8 nm Pt_xGd nanoparticles about 20-25% of the mass activity is lost. The figure shows data from [79, 82], and it is from [82].

On a side note it is also worth mentioning the structure of the alloy. In order to understand and control the overlayer it is also important to understand the structure of the underlying alloy. However, the structure of Pt_5Gd and Pt_5Y has remained elusive. Early attempts [83, 84] on powders indicated that the Pt_5Gd structure is related to the Cu_5Ca structure, but it was not identical to that structure, as more diffraction peaks were present. Attempts at measuring the structure of a polycrystalline Pt_5Gd crystal at our lab revealed a similar pattern, it has the peaks expected from the Cu_5Ca structure plus additional peaks. The situation is similar for Pt_5Y as a single stable crystal phase has not been found [85].

The goal of this thesis is to investigate the overlayer further, using different X-ray structural tools to elucidate both the structure of the overlayer itself, as well as the underlying alloy structure. Especially investigating the single crystals after electrochemical measurements is of high interest, since it is not possible to use the typical surface science techniques due to contamination of the surface.

2.3 Precious metals for OER

When doing water splitting the electrochemical potential is significantly higher than during ORR, and especially in acid the conditions are highly oxidizing. For this reason most effort towards OER catalyst are focused on oxides, as a metallic surface would oxidize under operating conditions [86]. But in acidic electrolyte like the PEM electrolyzer only very few materials are active for OER and stable [87]. This is seen in figure 2.18, which shows the overpotential at initial operation and the overpotential after a stability test, and a stable material will fall on the marked line. In the case of acid electrolyte the only material that does not immediately disintegrate and has a reasonable overpotential is IrO_x. In alkaline electrolyte there are more materials to choose from, and they do not contain precious metals, but the overpotential is still fairly high and the alkaline electrolyte is not compatible with the PEM membrane.

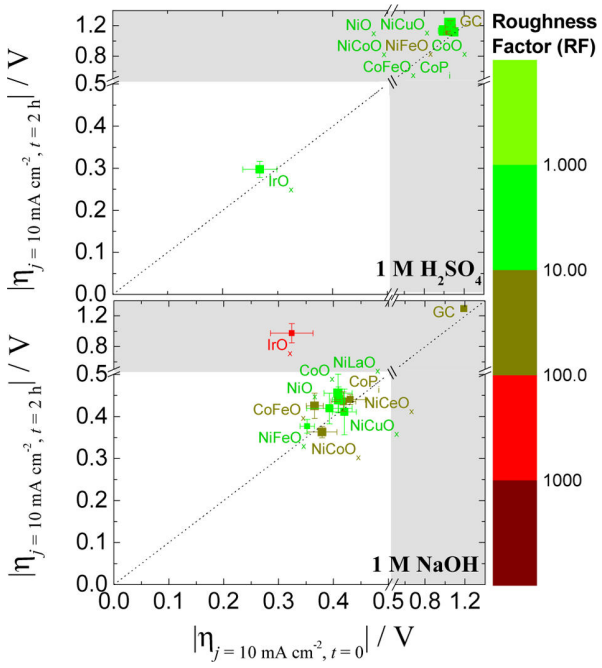

Figure 2.18: The figure shows the overpotential and stability of some transition metal oxides for OER. The overpotential after 2 hours of testing is shown as a function of the initial overpotential, and a stable material will have the same overpotential at both times. In acid only a single stable and active material is present: IrO_x. The figure is from [87].

Another promising material for OER in acid not shown in figure 2.18 is RuO_2, which has been investigated along with IrO_2 as effective OER catalysts since the

1970's [88–90]. RuO_2 shows improved performance over IrO_2 [91–93], see figure 2.19. However, it is not as stable as IrO_2 [94], which is a big issue in terms of making commercial electrolyzers. These two oxides are also very good for chlorine evolution [95, 96], and advances in the industry led to the development of the dimensionally stable anode®(DSA) in 1980 [97]. This material consists of a mixture of Ir/Ru/Ti oxides, and proves to be a stable and active anode for both chlorine evolution and OER, and is still considered state-of-the-art in modern water splitting [98–100]. Other studies from the same time period again shows that Ru/Ir mixtures are active and stable for OER [101, 102].

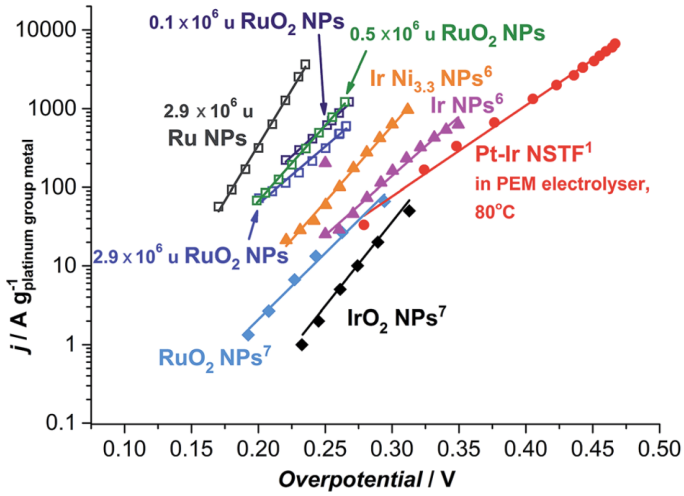

Figure 2.19: The figure shows the current density as a function of overpotential for the OER for nanoparticles and thin films of RuO_2, IrO_2, and alloys thereof. The current has been normalized to the mass of precious metals in the catalyst. The figure and measurements of the mass-selected Ru-based nanoparticles are from [92], the RuO_2 and IrO_2 nanoparticle data are from [93], the Ir and IrNi nanoparticle data are from [103], and the PtIr nano-structured thin film data is from [104].

Efforts are still being put into making new stable Ir/Ru combinations [105, 106], and it is suggested that there is an intrinsic inverse relation between activity and stability for OER catalysts, and so the optimal catalyst will have to be a compromise between the two [106, 107]. These experimental findings are backed up by thermodynamic considerations [108]. However, other studies seem to suggest that the OER activity is highly dependent on structure and catalyst preparation, and that a trade-off in activity with increased stability is rather complex [109].

This concept has been explored theoretically using DFT calculations, in which the electrode was RuO_2 with Ir decorating the under-coordinated sites [110]. More specif-

ically the model consisted of a stepped $RuO_2(110)$ surface with Ir atoms replacing the Ru atoms at the under-coordinated step sites. The idea is that this catalyst will have the activity of RuO_2, assuming that the active sites are the $RuO_2(110)$ terrace sites, and it will be more stable as the step sites that are most prone to dissolution are covered by the more stable IrO_2. This approach does not violate the inherent thermodynamic stability discussed above, but as the dissolution potential for IrO_2 is higher than for RuO_2 [86], the presence of IrO_x at the surface introduces a kinetic barrier against dissolution. In these calculations it was found that the Ir atoms on the step sites are indeed more stable than the Ru atoms on the same site.

Inspired by these results our group fabricated thin films of RuO_2 covered by either 2 Å or 4 Å of IrO_2, equivalent to a half and a whole monolayer assuming an ideally flat film, respectively. They were deposited by reactive sputtering on a polycrystalline Au electrode. The thin films were tested electrochemically, and it was verified that the stability of the electrode is improved while cycling the potential. Figure 2.20 shows the average corrosion rate of the thin films after 150 cycles between 1.23 and 1.80 V vs. RHE at 20 mV/s in 0.05 M H_2SO_4.

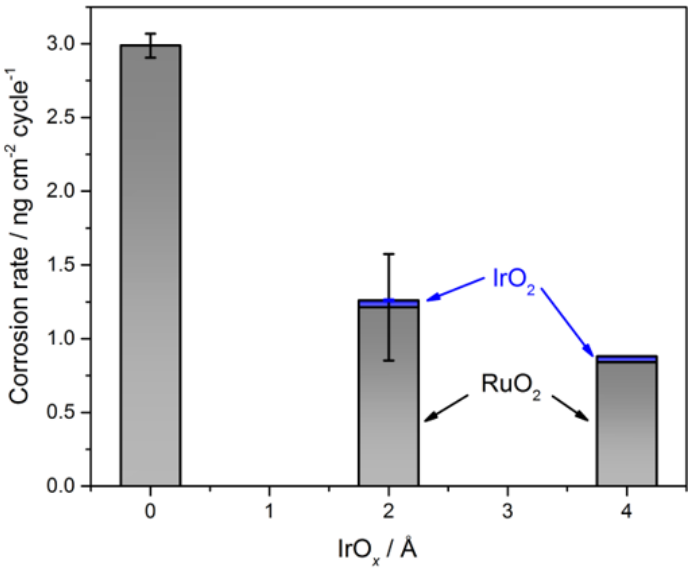

Figure 2.20: The figure shows the corrosion rate of thin films of RuO_2 with none, 2, or 4 Å of IrO_2 deposited on top. These amounts of IrO_2 correspond to none, half, and a whole monolayer of oxide assuming ideally flat films. It is seen that by covering the RuO_2 thin film by half a monolayer of IrO_2 the corrosion rate is less than half as high as the unprotected film.

This system may provide insight into the protection mechanism of IrO_2 on RuO_2,

as well as provide guiding to designing new stable anode materials with extremely low Ir and Ru loadings. Other groups have used in-situ X-ray techniques (XAS) to investigate pure IrO_2 [111] as well as novel alloys of Ru/Ir oxides [105] under OER conditions. For pure IrO_2 it was found that during OER Ir exists both in the +3 and +5 oxidation states [111], whereas for the Ir/Ru alloy Ir did get an increased oxidation state, but Ru did most of the work as a much larger change in Ru oxidation state was observed [105]. In our experiments we will use the more advanced HERFD-XAS technique to study the Ir on this hybrid IrO_x/RuO_2 thin film, and with the enhanced energy resolution offered by this technique any band structure of the valence band should be visible. In the rutile crystal structure the oxygen makes a crystal field that is octahedral with a slight distortion, splitting the d-orbitals into a low energy component, t_{2g}, and a high energy component, e_g. The t_{2g} band is formed by the d_{xy}, d_{yz}, and d_{zx} orbitals, whereas the e_g band is formed by the d_{z^2} and $d_{x^2-y^2}$ orbitals.

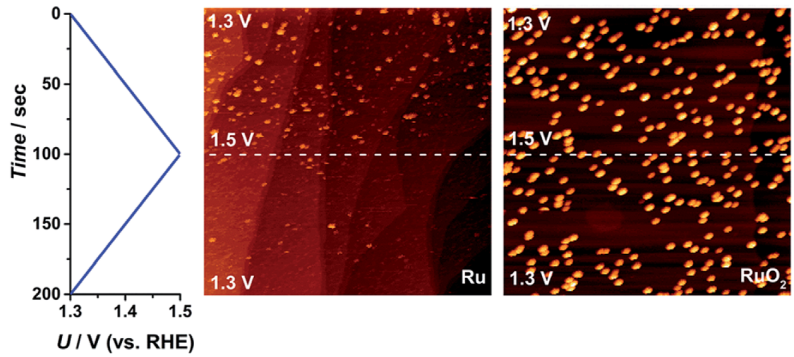

Figure 2.21: The figure shows electrochemical STM images of metallic and thermally oxidized Ru nanoparticles while the potential is being scanned. As the potential reaches 1.5 V vs. RHE the metallic Ru particles disappear immediately, whereas the thermally oxidized nanoparticles remain stable. The figure is from [92].

Coming back to the intrinsic stability, the preparation conditions have great influence on both the activity and stability [109]. To gain more insight into the fundamentals of activity and stability of RuO_2 our group fabricated and tested size-selected Ru nanoparticles for OER. Some of these metallic nanoparticles were oxidized thermally to form a thermal oxide, whereas others were left metallic, and supposedly forms an electrochemical oxide under OER conditions [92]. The activity of these nanoparticles are also included in figure 2.19. However, the high activity comes at a price in terms of stability, as the metallic particles disappear almost instantaneously when exposed to potentials above 1.5 V vs. RHE. One might hypothesize that the electrochemically derived oxide is more disordered or maybe amorphous, as it is formed at low temperature [112]. A more amorphous structure may allow each Ru atom to coordinate more O at defects, which may explain the lower stability. Figure 2.21 shows

an electrochemical scanning tunneling microscope (STM) image, which images the nanoparticles under operating conditions. It is seen that the metallic particles disappear immediately after being exposed to 1.5 V vs. RHE. This trend that a thermal oxide is more stable than an electrochemical oxide based on the same metal has been observed for both Ru and other transition metals [107, 113, 114]. The theory is that the electrochemical oxide has more defects, which may be involved in the metal ions to oxidize beyond the +4 state and become unstable [107].

In order to examine the Ru/RuO_2 nanoparticle systems further to get more insight into the OER activity on Ru we decided to use XAS to examine the oxidation states of both types of well-defined catalysts during in-situ OER operation.

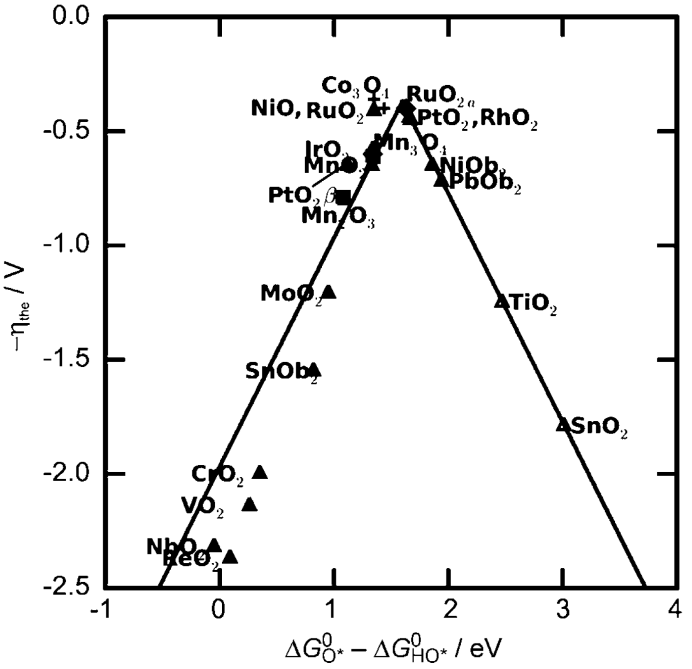

Figure 2.22: The figure shows a theoretical volcano of OER of various oxides in acidic electrolyte, using ΔG_3 as a descriptor. The figure is from [115].

In designing better catalysts an accurate theoretical description of the chemical process can help direct experimental research. Therefore much effort has been put into understanding the fundamentals of OER. The first successful volcano relationship was constructed in 1980 on the basis of transitions between oxidation states for a range of materials [90], and the new approach in this case was to look at the oxide material properties itself rather than properties of the metallic element. Since then tremendous advances have been made in DFT calculation techniques, and with the theory of intermediate steps outlined in section 2.1 a volcano relation can be calcu-

lated for oxides in acidic media, see figure 2.22. Despite advances in DFT calculation techniques, oxide materials still present a major challenge, and getting reliable computational results is not always possible [116]. Especially RuO_2 presents challenges for DFT [116, 117], and as seen in figure 2.22 RuO_2 can be on either side of the volcano, depending on what surface structure is considered.

Determining what side of the volcano that RuO_2 falls on is important, since it affects what the potential limiting step is. If the material is on the strong binding side (left side) of the volcano the most difficult step is to go from an $^*O$ to $^*OOH$, whereas on the weak binding side (right side) adsorbing $^*OH$ or going from $^*OH$ to $^*O$ will be potential limiting. The in-situ XAS measurements performed on the RuO_2 nanoparticles may also give hints towards this question.

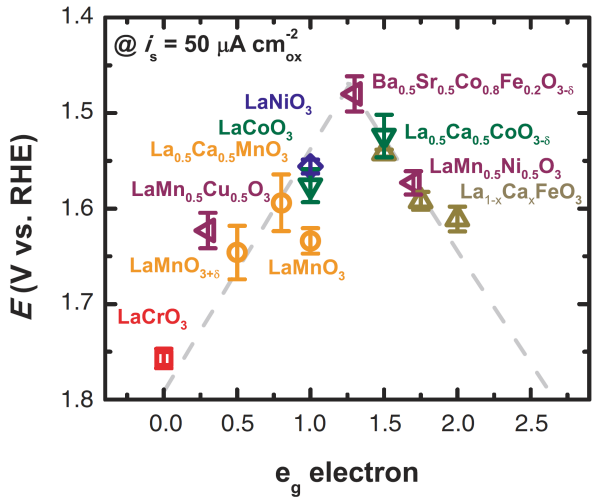

Figure 2.23: The figure shows the OER overpotential in alkaline electrolyte for a series of perovskite materials with varying electron filling of the valence e_g band. As the filling of the e_g band governs the binding to the surface oxygen intermediates a parallel may be drawn to the d-band model for transition metals. The figure is from [118].

Most discussion so far has dealt with acidic electrolyte, but more classes of materials are stable in alkaline electrolyte. And in alkaline electrolyte a descriptor similar to the d-band filling for the transition metals has been found by studying perovskites [118]. In the perovskite crystal structures the transition metal elements experience an octahedral crystal field from the surrounding oxygen atoms, leading to a splitting of the valence band into the t_{2g} and e_g bands due to the spatial symmetry of the d-orbitals. In these perovskite materials the OER activity has been correlated to the filling of the e_g band, as it effects the bonding to the intermediate oxygen species. Figure 2.23 shows the experimental OER activity volcano obtained by plotting the

OER overpotential as a function of the surface e_g band filling. In this study it is alluded to that the OER mechanism may be more complex than ORR, as O is also part of the catalyst itself, but it may take part in the reaction [118]. Therefore understanding the oxide materials and their OER performance better is necessary in order to design better catalyst that can avoid or minimize the usage of the scarce Ir and Ru.

CHAPTER 3

X-rays from electrons

In a synchrotron storage ring highly relativistic electrons circulate in an orbit comprised of small straight sections with bending magnets in between. Whenever charged particles are accelerated they emit radiation, and this is the underlying principle of synchrotron radiation.

3.1 Bending magnets

The most simple X-ray source at the synchrotron is the bending magnet. As the name suggests this device's purpose is to bend the electron orbit keeping it in the large ring. During this bending motion the electron emits broadband radiation from visible light all the way up to X-rays. Because of the relativistic speed of the electrons the emitted radiation is affected by the Doppler effect, effectively only emitting radiation in a narrow cone tangentially to the electron orbit. The angle of this radiation cone is approximately $1/\gamma$, where γ is the electron energy in units of rest mass energy,

$$\gamma \equiv \frac{E_e}{m_e c^2}\,, \tag{3.1}$$

and E_e is the electron energy, m_e is the electron rest mass, and c is the speed of light [119]. The relativistic energy of an electron is given as

$$E_e = \frac{m_e c^2}{\sqrt{1-(\frac{v}{c})^2}}\,, \tag{3.2}$$

where v is the speed of the electron. Combining this with the relative speed, $\beta \equiv v/c$, the expression from γ may be given as

$$\gamma = \frac{1}{\sqrt{1-\beta^2}}\,. \tag{3.3}$$

As the electron speed approaches the speed of light γ becomes very large, and the light emission cone becomes very narrow. For the SPEAR3 storage ring with an electron energy of 3 GeV, $\gamma = 5871$ and $1/\gamma = 0.17$ mrad.

The radius, R, of the circular motion of the electron in a magnetic field can be calculated from the momentum of the electron, $p = ReB$, where p is the momentum,

e is the electron charge, and B is the magnetic field strength. For a highly relativistic particle the momentum is approximately $p = \gamma mc$, since $v \approx c$. This gives the following relation

$$\gamma mc = ReB \Leftrightarrow R = \frac{\gamma mc}{eB}\,. \tag{3.4}$$

For typical bending magnet at SSRL with a strength of 1.3 T, the radius is $R = 7.7$ m.

Another parameter for describing the radiation from a bending magnet is the characteristic energy,

$$\hbar\omega_c = \frac{3}{2}\gamma^3\frac{c}{R} = \frac{3}{2}\frac{e\gamma^2 B}{m} = \frac{3}{2}\frac{e}{m^3c^4}BE_e^2\,, \tag{3.5}$$

which describes the peak energy in the energy distribution of the X-rays [119].

The figure of merit for describing the beam quality is the brilliance, which is the number of photons per second divided by the divergence of the beam (in mrad), divided by the area of the source (in mm^2), integrated over a relative bandwidth of 0.1% [119]. The brilliance is a function of the photon energy, and figure 3.1 shows the normalized brilliance as a function of photon energy relative to the characteristic energy. The brilliance is normalized by E_e^2 in GeV and the storage ring current in A. For a typical bending magnet at SSRL the characteristic energy is 7.8 keV and the brilliance at this energy is $8.7 \times 10^{13}\ \frac{\text{photons/sec}}{\text{mrad}^2\text{mm}^2}$.

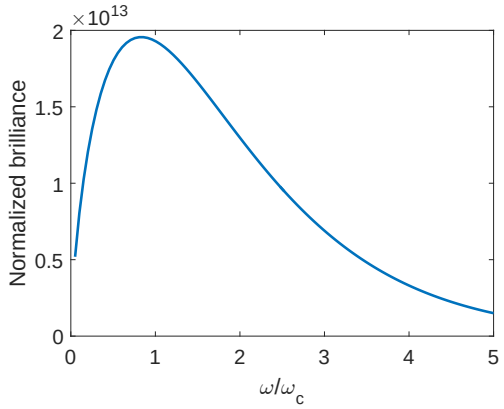

Figure 3.1: The figure shows the normalized brilliance from a bending magnet as a function of normalized photon energy. The photon energy is normalized to the characteristic energy, $x = \hbar\omega/\hbar\omega_c$, and the brilliance is normalized by E_e^2 in GeV and the storage ring current in A. The formula for this curve is $1.327 \times 10^{13}x^2K_{2/3}^2(x/2)$, where K is the modified Bessel function of the second kind.

The X-rays are strongly polarized, and in the plane of the storage ring they are horizontally polarized (assuming the synchrotron is horizontal). Above and below the accelerator plane the X-rays are circularly polarized, with opposite helicity, respectively.

3.2 Wigglers

In an effort to increase the intensity of the radiation from a synchrotron a class of new sources were developed, called insertion devices (IDs). These devices are inserted into the straight section of the electron path in between the bending magnets. One of the first kinds of insertion devices was the wiggler, which consists of an array of permanent magnets with alternating directions. In this manner the electrons are "wiggled" in a horizontal sinusoidal motion, and at each bend X-rays are emitted and the intensity is added each time. The X-ray spectrum from a wiggler is the same as for a bending magnet, but the intensity is multiplied by $2N$, where N is the number of periods of sinusoidal motion. This increases the intensity many-fold, typically more than an order of magnitude. The total energy radiated is typically on the order of kW [119], and care must be taken when designing optical components that can deal with the high broadband heat load. A further price to pay for the increased intensity is also an increase in horizontal divergence of the beam. Because of the large oscillations of the electron path, a significant amount of radiation is spread out horizontally. The maximum angle of the electron path from the wiggler axis is given as K/γ, and K parameter is given as [119],

$$K = \frac{eB_0}{mck_u} = 0.934\lambda_u[\mathrm{cm}]B_0[\mathrm{T}]\,, \tag{3.6}$$

where B_0 is the mean magnetic field and $k_u = 2\pi/\lambda_u$ is the spatial frequency of the magnetic field variations. The radiation cone from a wiggler has the same vertical angle as the bending magnet, γ^{-1}, but the horizontal angle is K/γ. For a wiggler K is typically around 20, so a significant spread of the beam is expected. At SSRL the beam lines at wiggler insertion devices are often arranged such that three end stations utilize the radiation from a single wiggler, the central of which will receive the highest intensity.

3.3 Undulators

The undulator is based on the same principle as the wiggler with an array of alternating permanent magnets. However, the period of the array is designed in such a way that it matches the period of the emitted radiation, meaning that the emitted radiation at every turn is in phase with the radiation from the previous turns. This results in much brighter x-rays, but also a very different spectrum of emitted radiation. Because only a single frequency is promoted, undulator radiation is much more

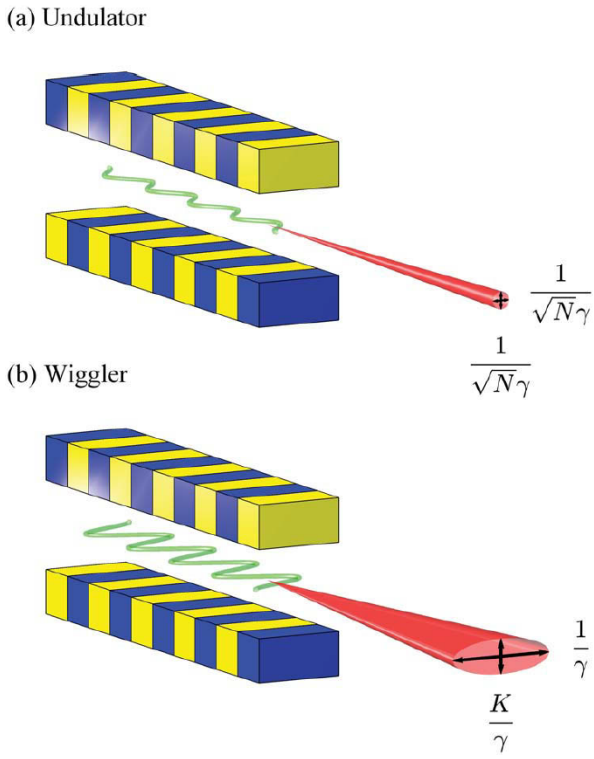

Figure 3.2: The figure summarizes the X-ray beam divergence from an undulator (a) and a wiggler (b). The figure is from [119].

monochromatic than wigglers and bending magnets. Furthermore, the radiation cone angle also gets smaller the more periods the undulator has, and scales both horizontally and vertically as $(\sqrt{N}\gamma)^{-1}$. The increase in flux from having multiple bends, almost monochromatic radiation, and low emission angle all increase the brilliance of undulator sources, and they can reach brilliances several orders of magnitude higher than wigglers. Figure 3.2 shows the X-ray beam divergence from an undulator (a) and a wiggler (b), the figure is from [119].

Because of the electrons being relativistic, the electron pathway is not purely sinusoidal, but becomes more triangular with increasing magnetic field strength (achieved by decreasing the undulator gap, thus increasing the K parameter), which leads to the spectral distribution to also contain significant intensity in higher odd orders of the basic frequency. Figure 3.3 shows the intensity spectrum for two different gap settings (and therefore K-values) of a given undulator. Figure 3.4 shows the brilliance of the first, third, and fifth harmonics of a soft X-ray undulator at the Advanced Light Source (ALS) at Lawrence Berkeley National Laboratory, CA, USA. This brilliance

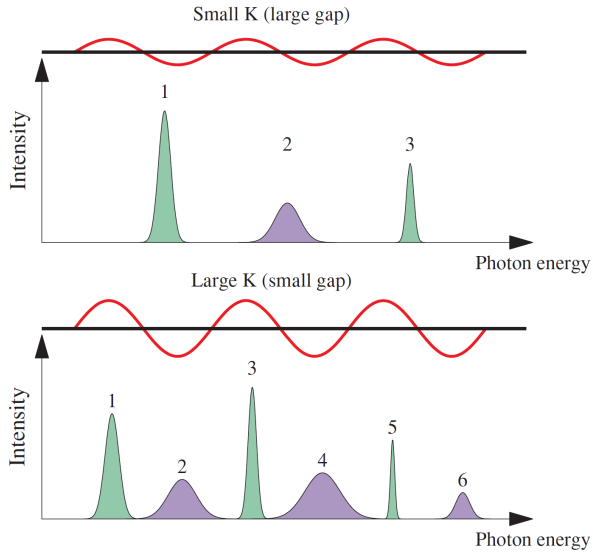

Figure 3.3: The figure shows the intensity as a function of photon energy for two different gap (K) settings the the same undulator. It is seen that the spectrum is dominated by the odd harmonics of the fundamental frequency, which can be shifted by changing the gap size (K-value). The figure is from [119].

shape is obtained by scanning the undulator gap, so as to align the first, third, or fifth harmonic to the desired energy. This particular device is an elliptically polarizing undulator, which has four independent magnetic arrays, that allows the electron path to vary vertically as well as horizontally, which can produce an array of elliptical polarizations, linear polarization being a special case. When the polarization is set to circular, the electron trajectory is helical and has a constant angle from the undulator axis, and the Doppler shift is therefore constant, leading to all power being emitted in the fundamental frequency only. The derivation of these results is beyond the scope of this text, and the results presented here can be found in [119].

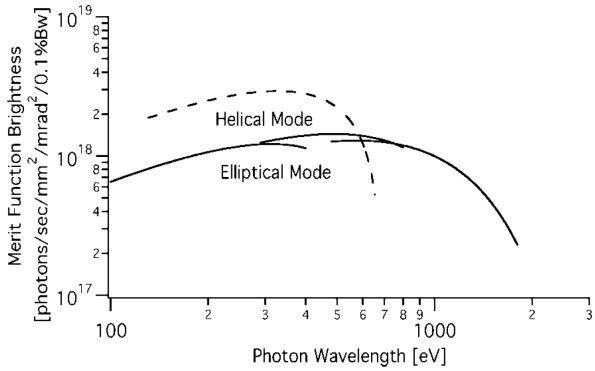

Figure 3.4: The figure shows the brilliance of the first, third, and fifth harmonics of an elliptically polarizing undulator at the Advanced Light Source (ALS) at Lawrence Berkeley National Laboratory, CA, USA. This soft X-ray source reaches a brilliance of $>10^{18}$, which is orders of magnitude higher than a wiggler can achieve. The figure is from [120].

CHAPTER 4

X-ray absorption spectroscopy

X-ray absorption spectroscopy (XAS) is a very powerful technique, since it is an element-specific technique able to provide both structural and chemical information. The element specificity arises from the fact that the X-rays interact with the core-level electrons, which have specific energy levels unique to each element. Furthermore, X-rays interact weakly with the samples compared to other probes, such as electrons, and it is therefore often possible to have highly complex sample environments, and operate the sample material close to realistic conditions. The basis for XAS is the interaction of X-rays photons and atoms.

X-rays interact with matter much like other photons, but because of their high energy they are able to eject core electrons when absorbed by atoms, see figure 4.1(a). This generates a short-lived core-hole that relaxes either by emitting another X-ray photon (fluorescence), see figure 4.1(b), or an Auger electron, see figure 4.1(c).

The core levels are labeled alphabetically starting with K for the first shell, L for the second shell, and so on. Within higher shells there are several sub-levels, one for the s-orbital and two for each of the spin-orbit split p-, d-, and f-orbitals, and these sub-levels are numbered. For example the L-level is split into the 2s orbital, named L_1, the $2p^{1/2}$, named L_2, and $2p^{3/2}$, named L_3. The particular energies associated with fluorescence emission are similarly labeled with the letter of the shell that has the core-hole, followed by a combination of a Greek letter and a number, see figure 4.2 for an overview of the emission line names.

From the emission lines shown in figure 4.2 it is seen that not all transitions are shown, and for example there are no transitions from L_1, M_1, or N_1 states to the K-level. This is because these transitions are not allowed due to the dipole selection rules, coming from the fact that the final quantum state must overlap with the initial state multiplied by the dipole operator. This requires that the l quantum number must change by $+1$ or -1 and the m quantum number can remain constant or change by $+1$ or -1 [122],

$$\Delta l = -1, +1\,,\ \Delta m = -1, 0, +1\,. \tag{4.1}$$

So for example an s-electron can only transition to a $p^{1/2}$ or $p^{3/2}$ state. This is

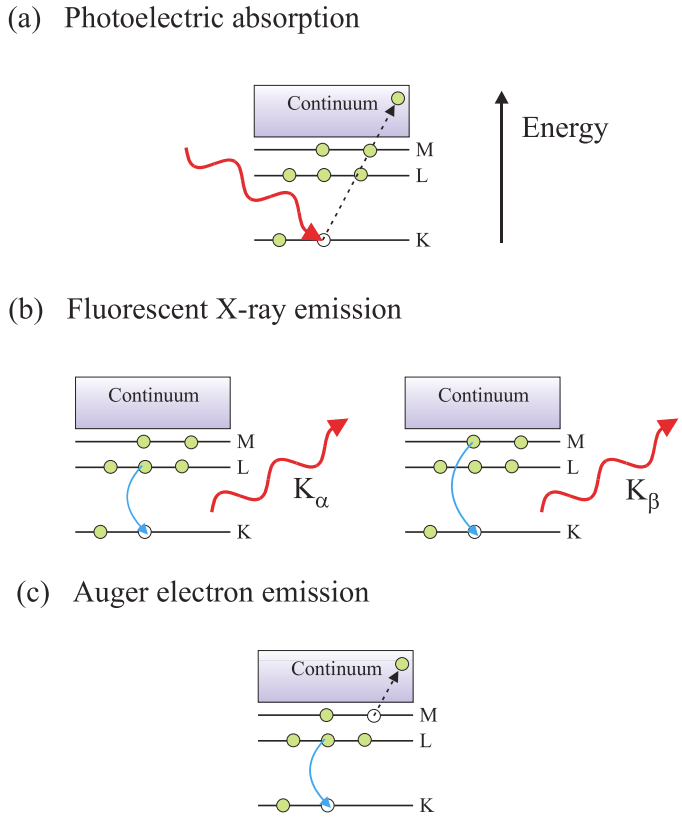

Figure 4.1: The figure shows an atom absorbing an X-ray photon and ejecting a core electron (a). The core-hole may be filled by emission of a fluorescence X-ray photon (b) or an Auger electron (c). The figure is from [119].

why the L_1, M_1, and N_1 states cannot decay to the K-level; they are all s-states.

Absorption through a material is described by the linear absorption coefficient, μ, and the absorption of a slice of material of thickness dx is given by μdx. This means that the change in the beam intensity at depth x into the material is proportional to the intensity at this depth,

$$dI = -I(x)\mu dx\,. \tag{4.2}$$

The differential equation leads to the Beer-Lambert law, which has the following solution,

$$\frac{dI}{dx} = -\mu I(x) \;\Leftrightarrow\; I(x) = I_0 e^{-\mu x}\,. \tag{4.3}$$

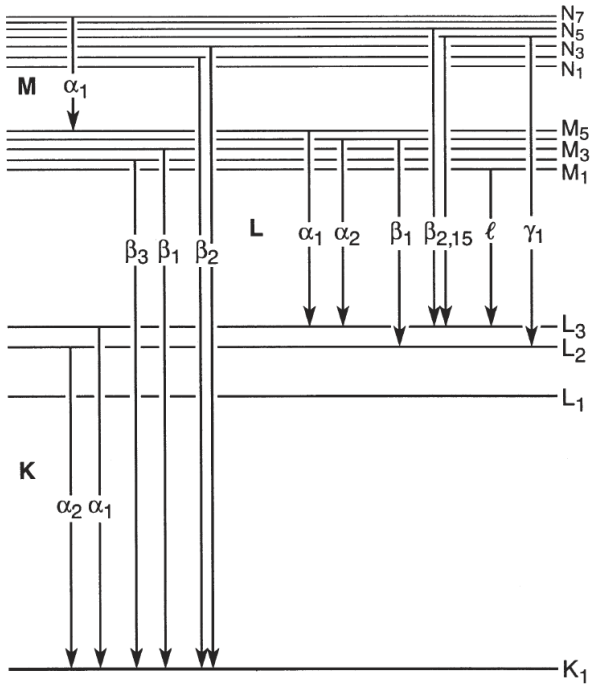

Figure 4.2: The figure shows the nomenclature naming the X-ray fluorescence emission lines. The figure is from [121].

In the solution of the differential equation the incoming intensity at the surface of the material is set to I_0. The linear absorption coefficient, μ, can be decomposed into the atomic density, ρ_{at}, and the absorption cross section, σ_a, of the given atom,

$$\mu = \rho_{at}\sigma_a \,. \tag{4.4}$$

If a material consists of different kinds of atoms, the total absorption coefficient is calculated as follows,

$$\mu = \sum_j \rho_{at,j}\sigma_{a,j} \,. \tag{4.5}$$

The linear absorption coefficient can easily be measured by how much intensity is absorbed as a function of incoming X-ray photon energy, and this is the basis of X-ray absorption spectroscopy (XAS). In most samples the atomic density remains constant, and the changes in the spectrum is then determined by the absorption cross section. In general the cross section decrease with increasing photon energy, however at certain energies there are almost discontinuous increases in the absorption coefficient. As an example the absorption coefficient for Fe is shown over a large energy span in figure

4.3. The abrupt jumps in absorption are called absorption edges, and they occur when the incoming photon energy exceeds the binding energy a lower lying electron shell, increasing the number of electrons that can be ejected into the continuum, thus increasing the absorption cross section. The XAS method is an element specific probe since absorption edges of different elements are at different energies, which helps make it a very powerful tool.

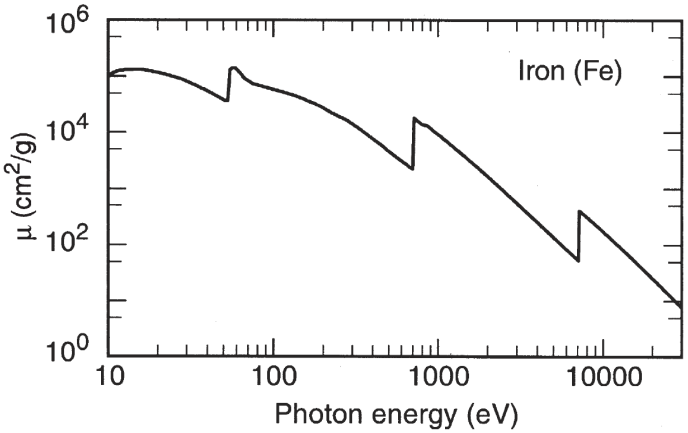

Figure 4.3: The figure shows the absorption coefficient of Fe over a large energy range, and in general the absorption coefficient is decreasing with increasing photon energy. However, there are almost discontinuous jumps at specific energies, which is particular to the element. These jumps are called absorption edges, and occur at energies where the photon energy exceeds the binding energy of a lower electron shell, thus enabling more electrons to be ejected into the continuum, increasing the absorption cross section. The absorption edge with the highest energy is the K-edge (∼7000 eV), followed by the L-edges (∼700 eV, the three edges are too close to distinguish in this plot), and the M-edges at even lower energies (∼60 eV). The figure is from [121].

In an XAS experiment the goal is to measure the absorption coefficient, and this can be done in two ways; either by detecting the attenuation directly by measuring the intensity lost from transmission though the sample, or by measuring the intensity of the fluorescence photons from the sample.

In the case of a transmission the experiment the intensity is measured before the sample, I_0, and after the sample, I_1. From equation (4.3) the absorption coefficient may be determined from these two intensities,

$$I_1 = I_0 e^{-\mu t} \Leftrightarrow \mu = \frac{1}{t} \ln\left(\frac{I_0}{I_1}\right) , \tag{4.6}$$

where t is the thickness of the sample. In order for the transmission experiment to work the sample must be homogeneous and have a uniform thickness across the area of the X-ray footprint. Furthermore, the sample must be thick enough to absorb a significant amount of the X-rays, and not be too thick so that I_1 becomes difficult to detect. One rule of thumb is that μt should be in the range 1-3, so that between 37% and 5% of the incoming beam is transmitted.

In case of fluorescence the emitted intensity is proportional to absorption coefficient,

$$I_f \propto \mu I_0 \,, \tag{4.7}$$

and so the absorption coefficient can be determined by dividing the fluorescence intensity by the direct beam intensity,

$$\mu \propto \frac{I_f}{I_0} \,, \tag{4.8}$$

where I_f is the fluorescence intensity. There are also some sample requirements, since both the incoming beam and the outgoing fluorescence are attenuated by the sample. In order to show these requirements a more detailed consideration of the experimental setup is required. In a general fluorescence XAS experiment the incoming beam makes an angle θ with the sample surface, and the fluorescence photons going into the detector makes an angle ϕ with the sample surface, as shown in figure 4.4.

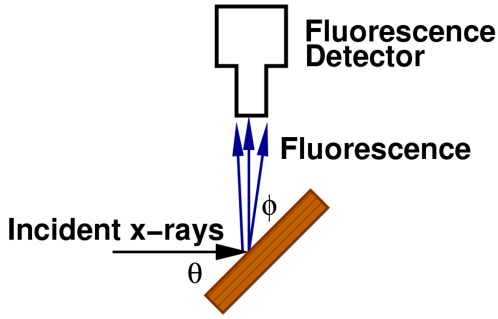

Figure 4.4: The figure shows a general fluorescence XAS setup, in which the incoming beam makes an angle θ with the sample surface and the detected fluorescence photons exit the surface at an angle ϕ. The figure is from [123].

In this setup the intensity of the detected fluorescence signal can be written as [123],

$$I_f = I_0 \frac{\epsilon \Delta\Omega}{4\pi} \frac{\mu_{el}(E)\left[1 - e^{-[\mu_{tot}(E)/\sin(\theta) + \mu_{tot}(E_f)/\sin(\phi)]t}\right]}{\mu_{tot}(E)/\sin(\theta) + \mu_{tot}(E_f)/\sin(\phi)} \,, \tag{4.9}$$

where ϵ is the fluorescence yield, $\Delta\Omega$ is the solid angle covered by the detector, μ_{el} is the absorption coefficient by the element whose edge is being probed, and μ_{tot} is the total absorption coefficient, E is the incoming photon energy, and E_f is the fluorescence photon energy. The total absorption coefficient consists of a sum of the absorption coefficient from the element that is probed and all other elements,

$$\mu_{tot}(E) = \mu_{el}(E) + \mu_{other}(E)\,. \tag{4.10}$$

In the general case determining μ_{el} is more difficult to separate from the measurement of just I_0 and I_f. But for the special case that the sample is very thin compared to the absorption coefficient, $\mu t \ll 1$, doing a first order Taylor expansion of the exponential function yields a much simpler relation,

$$I_f \approx \frac{\epsilon\Delta\Omega}{4\pi}\mu_{el}(E)t\,. \tag{4.11}$$

For this sample the simple extraction of μ is possible. A second case that gives a simple relation is a very thick dilute sample, in which $\mu_{tot}t \gg 1$ and $\mu_{tot} \approx \mu_{other}$. Here the exponential function goes to 0, leaving the following expression,

$$I_f \approx I_0\frac{\epsilon\Delta\Omega}{4\pi}\frac{\mu_{el}(E)}{\mu_{other}(E)/\sin(\theta) + \mu_{other}(E_f)/\sin(\phi)}\,. \tag{4.12}$$

Here the energy dependence of μ_{other} is smooth, since the energy is around the absorption edge of the element el, and therefore it can be ignored. When designing an XAS experiment one should be careful if neither of these two sample conditions are fulfilled, a very thin or very dilute sample. In the extreme case of a thick and concentrated sample, $\mu_{tot}t \gg 1$ and $\mu_{tot} \approx \mu_{el}$, the fluorescence intensity becomes,

$$I_f \approx I_0\frac{\epsilon\Delta\Omega}{4\pi}\frac{\mu_{el}(E)}{\mu_{el}(E)/\sin(\theta) + \mu_{el}(E_f)/\sin(\phi)}\,. \tag{4.13}$$

Here $\mu_{el}(E)$ is in both the numerator and denominator, and any changes in $\mu_{el}(E)$ will be reduced. In certain choices of incident and exit angles the fluorescence intensity can become constant! This is called self-absorption, and it is best to avoid. However, if it is not too bad, and both the fluorescence and transmission intensity is measured it can be corrected using the full equation (4.9). A different way to get around self-absorption in a thick concentrated sample is to have the incidence angle close to 90° and the exit angle very shallow. In that case,

$$I_f \approx I_0\frac{\epsilon\Delta\Omega}{4\pi}\frac{\mu_{el}(E)}{\mu_{el}(E_f)/\sin(\phi)}\,, \tag{4.14}$$

and since the fluorescence photon energy, E_f, remains constant, the full XAS without dampening can be achieved.

The fluorescence yield, ϵ, depends on the element number, and the heavier the element, the higher the yield. Figure 4.5 shows the calculated fluorescence yield for elements 3-110. The absorbed photons not resulting in fluorescence are mostly

emitted as Auger electrons, and the relations for the Auger electron intensity is the same as for fluorescence photons [123]. Therefore Auger electron intensity can be used to measure XAS as well, but since electrons have a much shorter mean free path in solids and require vacuum to be measured, they are only rarely used to measure XAS.

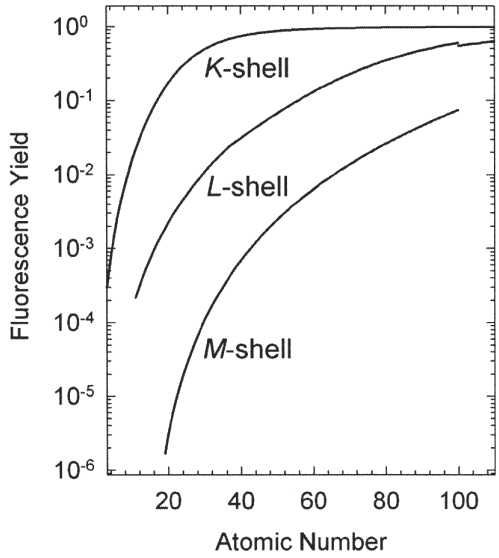

Figure 4.5: The figure shows the calculated fluorescence yield as a function of atomic number for the K-, L-, and M- absorption edges for element number 3-110. The absorbed photons note emitted as fluorescence photons are mostly emitted as Auger electrons. The figure is from [121] with data from [124] and [125].

4.1 Detectors

In order to measure X-ray absorption spectra it is essential to measure the intensity of the direct beam as well as the intensities transmitted and/or fluorescence beams. Here two detectors typically used are presented; the ion chamber and semiconductor detector.

4.1.1 Ion chamber

The ion chamber is a closed volume of gas with two parallel metal plates providing a strong electric field across the gas. When the X-rays pass through the chamber,

some of the X-rays will interact with the gas molecules and generate high energy photoelectrons, Auger electrons, or fluorescence photons. These highly energetic particles resulting from the initial interaction will interact with other gas molecules and generate a larger number of ions in the gas. The electrons and ions are then collected at each metal plate, and the current in the external circuit connecting the two metal plates is proportional to the intensity of the incoming beam [121].

The ion chamber is typically equipped with X-ray windows in either end where the beam enters and exits the chamber to minimize absorption of the incoming beam. These detectors let most of the X-ray beam pass through, and at most hard and tender X-ray beam lines they are used to measure the incoming X-ray intensity before the sample. Furthermore, when measuring XAS in transmission mode they are typically used to measure the intensity of the transmitted beam as well.

4.1.2 Semiconductor detector

Semiconductor detectors made from silicon or germanium work as energy discriminating single photon counters. These detectors are based on pn-junction diodes, and when an X-ray passes through the detector a cascade of electron-hole pairs are generated, and in the depletion region of the diode they are split up and migrates to the connections. An electronic circuit registers and counts the current pulses for each X-ray photon, and furthermore registers the potential of the electron-hole pair, which provides the energy discrimination [121].

Modern detectors, such as the Vortex detector, can read up to about 1 million counts per second, although a linear response is only maintained up until about 100,000 counts per second. The energy resolution is about 150 eV at 5.9 keV X-rays, which allows the distinction of fluorescence lines from neighboring elements, as well as separating fluorescence from elastically scattered photons when measuring XAS [126]. To get more signal some detectors consists of an array of diode detectors, so that they cover a larger solid angle.

4.2 EXAFS

When XAS was first measured of solid state systems it was quickly noted that the absorption coefficient just above the absorption edge was not a smooth function as expected, but rather showed oscillations that slowly decayed going to higher energy. The oscillations are part of fine structure of the X-ray absorption coefficient, and the regular oscillations above the absorption edge are known as the Extended X-ray Absorption Fine Spectrum (EXAFS).

This fine structure originates from the interaction between the absorbing atom and neighboring atoms, and monatomic gases do not show the fine structure. One such example is Kr gas versus Kr arranged in a 2D lattice, and the XAS spectra of these two samples are seen in figure 4.6, the Kr gas on the left and 2D crystalline Kr on the right.

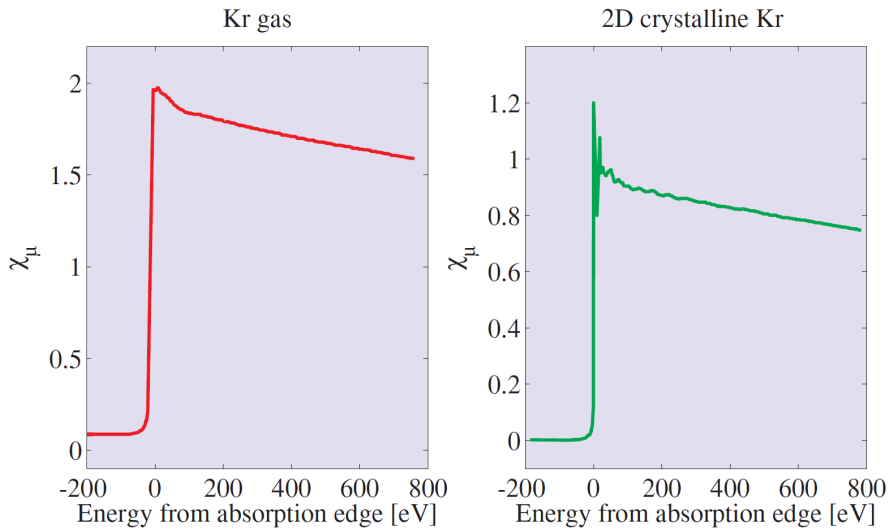

Figure 4.6: The figure shows measured XAS spectra of Kr gas on the left and 2D crystalline Kr on the right. The figure is from [123].

More precisely the EXAFS oscillations arise from the free photo-electron backscattering from neighboring atoms and interfering with itself. In order to analyze the fine structure of the absorption coefficient the oscillations are separated from the smooth absorption coefficient from a lone atom, and the EXAFS oscillation function is typically labeled χ [123],

$$\chi(E) = \frac{\mu(E) - \mu_0(E)}{\Delta\mu_0}\,, \tag{4.15}$$

where $\mu(E)$ is the total absorption coefficient, $\mu_0(E)$ is the smooth absorption coefficient from a lone atom, and the $\chi(E)$ function is normalized by the absorption edge height, $\Delta\mu_0$. See figure 4.7 for a sketch of the separation of the EXAFS function. In the quantitative treatment of EXAFS it is more useful to use the wavenumber of the photo-electron than the energy, which can be calculated from the dispersion relation of a free electron,

$$E_{pe} = (E - E_0) = \frac{\hbar^2 k^2}{2m} \Leftrightarrow k = \sqrt{\frac{2m(E - E_0)}{\hbar^2}}\,, \tag{4.16}$$

where E_{pe} is the photo-electron energy, which is equal to the photon energy, E, minus the absorption edge energy, E_0, k is the electron wave number, and m is the electron mass.

A detailed description of the EXAFS oscillations may be derived from Fermi's golden rule, as they stem from the modification of the final state of the atom. A

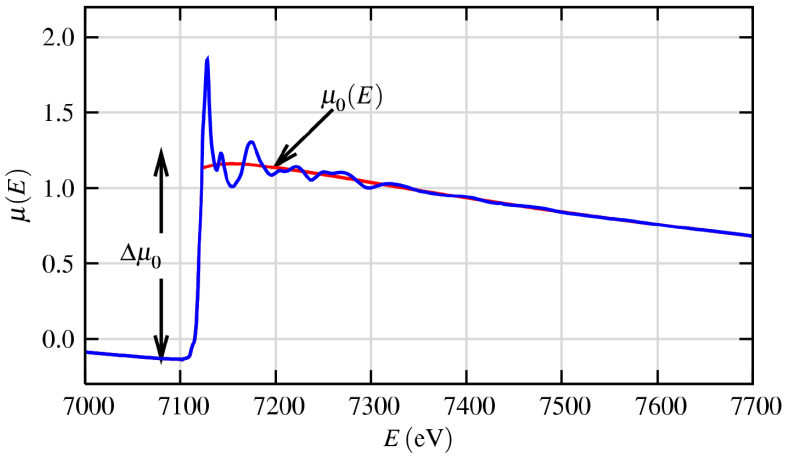

Figure 4.7: The figure shows a sketch of an absorption spectrum, where the absorption edge height, $\Delta\mu_0$, and the smooth atomic absorption coefficient, $\mu_0(E)$, are indicated. The absorption edge is the Fe K-edge and the material is FeO. The figure is from [123].

walk-through of the derivation is included in appendix B.1, but here we simply state the governing equation for the EXAFS oscillations [123],

$$\chi(k) = \sum_j \frac{S_0^2 N_j e^{-2k^2\sigma_j^2} e^{-2R_j/\lambda(k)} f_j(k)}{kR_j^2} \sin(2kR_j + \phi_j(k)) \,. \tag{4.17}$$

Here S_0 is the amplitude reduction factor, including the the effect of other electrons relaxing into the core hole. This parameter is correlated with N, the number of neighboring atoms, and is often set as a constant in the range 0.7-1.0. σ is the Debye-Waller factor, including the effects of amplitude damping from thermal vibrations. R is the neighboring atom distance. $\lambda(k)$ is a interaction dampening term that includes the effects of limited mean free path of the photo-electron and the limited lifetime of the excited absorber atom. Finally $f(k)$ and $\phi(k)$ are the amplitude and phase of the backscattered photo-electron. The parameters labeled with j are calculated or fitted to each combination of neighboring element and distances. From this equation it is seen that EXAFS is inherently a local probe, since the signal is dampened by the R_j^2 term as well as the dampening term $e^{-2R/\lambda(k)}$. In practice atomic distances up to 6 Å may be measured in favorable cases, but for more disordered samples the maximum atomic distances observed may be 4 Å.

The distances and number of neighboring atoms are determined by fitting equation (4.17) to the experimentally obtained spectrum. The type of neighboring atoms cannot be determined accurately, so knowledge of the sample composition is required, in order to calculate the relevant backscattering properties for the neighboring atoms.

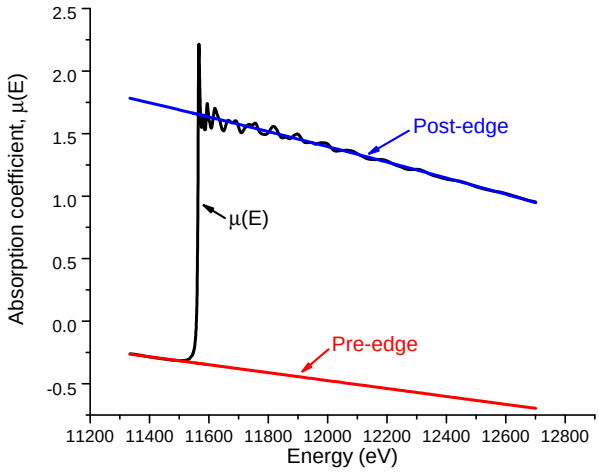

Figure 4.8: The figure shows the measured absorption coefficient of a Pt foil in transmission mode. To normalize the spectrum a linear function is fitted to the pre-edge region, and a quadratic function is fitted to the post-edge region.

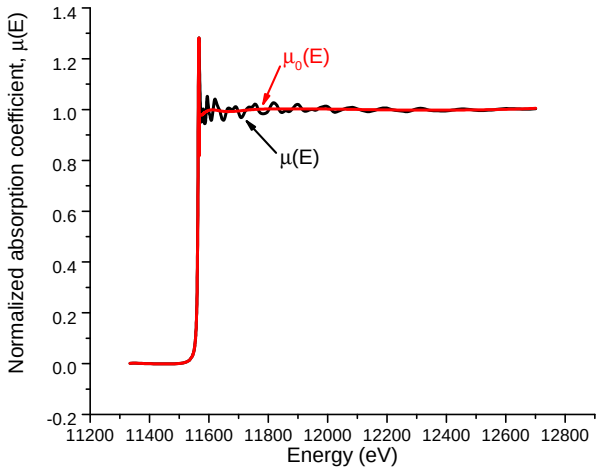

Figure 4.9: The figure shows the normalized absorption coefficient of a Pt foil. To approximate the atomic absorption coefficient, $\mu_0(E)$, a spline function is fitted to the post-edge region, and in the process it is important that the spline does not remove any of the fine structure.

This equation is very sensitive to R_j, so the neighboring distances can be determined very accurately, typically within a fraction of an Å, even if the sample is not crystalline.

The EXAFS equation (4.17) is built up as a sum of different frequencies for each absorber-neighbor distance. Therefore a Fourier transform yields a distance distribution function, however the distances are typically shorter than the actual interatomic distances due to the phase term in $\sin(2kR_j+\phi_j(k))$ part of the EXAFS equation. The Fourier analysis is very useful in the initial analysis as one can see which interatomic distances have most neighbors.

Before the data can be fitted the EXAFS function $\chi(E)$ must be extracted. This is done by first normalizing the measured absorption coefficient, so that the intensity before the absorption edge (pre-edge) is flat at the value 0, and the step height of the absorption edge is 1. Figure 4.8 shows the fitting of the pre-edge and post-edge regions used to normalize the absorption spectrum.

The next step is to separate the EXAFS oscillations, $\chi(E)$, from the smooth atomic part of the absorption coefficient, $\mu_0(E)$. This is done by fitting a spline to the post-edge region, however care must be taken that the spline remains smooth and does not remove any of the fine structure oscillations. Figure 4.9 shows the normalized absorption coefficient along with a fitted spline approximating the atomic absorption coefficient, $\mu_0(E)$.

When the EXAFS function has been extracted, the x-axis is changed to electron wavenumber, k, rather than incoming X-ray energy by using equation (4.16). The absorption edge, E_0, is usually taken as the inflection point of the absorption edge, i.e. the steepest part of the absorption coefficient, but this parameter may be corrected during the fitting procedure. Figure 4.10 shows the extracted $\chi(k)$ function, along with a window function used when Fourier transforming the data. The high k region is typically cut off since it is noisy, and the abrupt ending of the data will give artifacts in the Fourier transform. At low k the spline is often not very accurate, and the absorption coefficient is dominated by excitations into the empty conduction band and the oscillations are strongly influenced by multiple scattering (due to high mean-free path of the photo-electron), and is typically omitted in the EXAFS analysis.

As can be seen from figure 4.10 the EXAFS oscillations die down quickly, and in order to give higher weight to the high k values, $\chi(k)$ is often multiplied by k^2 or k^3. The case of $k^2\chi(k)$ for the same data is shown in figure 4.11, where the same Fourier transform window is shown.

Finally one may Fourier transform the EXAFS function to get the pseudo radial distribution function, as seen in figure 4.12. When Fourier transforming $\chi(k)$ a complex function is obtained, and the magnitude represents the atomic density. But there is of course information in the phase of the complex signal, and when fitting in real space it is important to fit the complex value. When checking the fit it is important to verify that not only the magnitude, but also the phase of the complex function matches $\chi(R)$. The figure also shows the local nature of the EXAFS probe; the data is from a Pt foil which has 12 nearest neighbors, 6 atoms in the second coordination shell, and 24 atoms in the third shell. However, it is clearly seen from the figure that

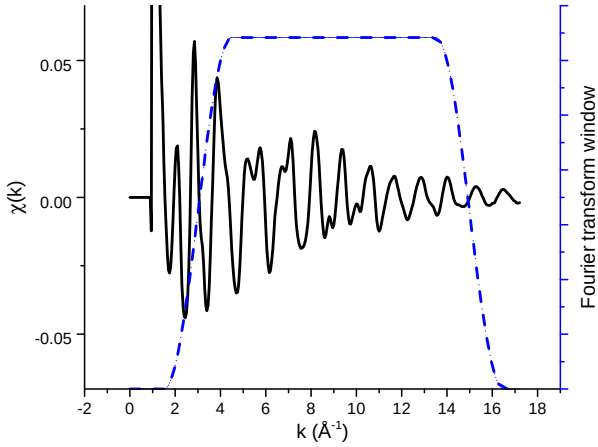

Figure 4.10: The figure shows the extracted EXAFS function, $\chi(k)$, for a Pt foil as a function of the photo-electron wave number, k. Furthermore, an appropriate Fourier transform window is shown, which is multiplied onto $\chi(k)$ when making a Fourier transform to real space.

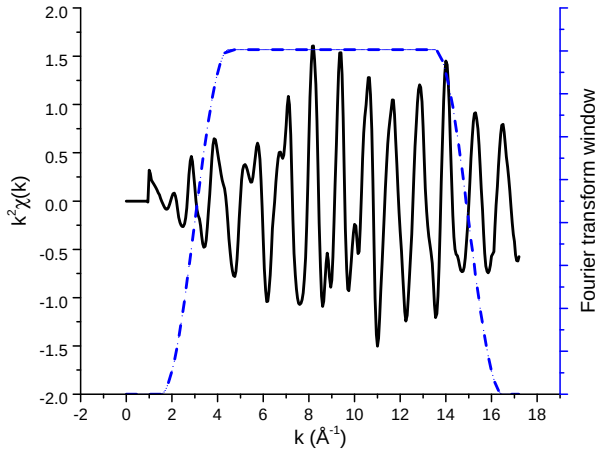

Figure 4.11: The EXAFS function $\chi(k)$ is often multiplied by k^2 or k^3 to give higher weight to the oscillations at higher k. In this graph the same $\chi(k)$ data as in figure 4.10 has been multiplied by k^2.

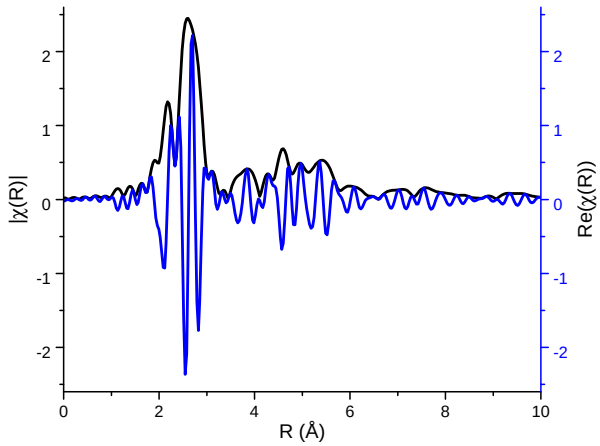

Figure 4.12: The figure shows the magnitude, $|\chi(R)|$, and the real part, $\mathrm{Re}(\chi(R))$, of the Fourier transform of $k^{\chi}(k)$ shown in figure 4.11. The magnitude $|\chi(R)|$ shows the pseudo radial distribution, and this example highlights the local nature of the EXAFS probe. The Pt foil sample has 12 nearest neighboring atoms at 2.5 Å and 24 atoms in the third shell at 4.5 Å, although the intensity is much lower at 4.5 Å. Above 6 Å only noise is left.

the $|\chi(R)|$ is much smaller at the third shell at 4.5 Å than at the first shell at 2.5 Å, even though there are twice as many atoms in the third shell. Furthermore, above a distance of 6 Å only noise remains. This demonstrates the local nature of EXAFS discussed earlier.

When the fitting procedure is complete, information about the structure can be extracted. The information can reveal details of the nearest neighbors; what distance they are at, how many of them there are, and how ordered the material is. If a material contains multiple elements this analysis can be done for multiple elements in the same sample, giving a detailed structural model.

EXAFS measurements presented in this thesis have all been done at beam line 11-2, see appendix E.4 for the detailed setup of this beam line.

4.3 XANES

XANES stand for X-ray Absorption Near Edge Spectrum, and this analysis deals with the XAS features at energies just above the absorption edge. This analysis provides some information about changes in structure, but it also provides chemical and electronic structure information of the absorbing atom.

In the XANES region the photo-electron generated upon absorption has a very low

kinetic energy, and therefore a somewhat longer mean free path than photo-electrons generated in the EXAFS region. This means that the fine structure oscillations are often dominated by multiple scattering paths, in which the photo-electron scatters off multiple nearby atoms before returning to the absorber. This process cannot be fitted in the same way as EXAFS due to the many paths involved, and so can rarely give quantitative structures. However, changes in the XANES structure relative to a reference material or upon conditioning of the sample is an indication of structural changes, which can then be investigated with EXAFS or other structural techniques. Modern first principles computer codes, such as version 9 of FEFF are getting better at reproducing measured XAS spectra also in the XANES region, and in some cases simulating different structures may give an idea of what structural changes might be happening [127].

More often the XANES analysis is used to get chemical information about the absorbing atom, since the absorption edge position is sensitive to the oxidation state of the absorbing atom. When an atom becomes more oxidized the core electrons shield the nucleus, and thus becomes slightly stronger bound, increasing the absorption edge energy. The response in absorption edge energy is not always linear, and in order to quantify oxidation state changes it is necessary to compare the edge position to reference materials with known oxidation states.

The shape of the XAS spectrum close to the absorption edge reflects the density of states (DOS) of the unoccupied states just above the Fermi level, as the absorption probability is proportional to the density of the final state. Due to the dipole selection rules, only DOS of a certain orbital symmetry is probed, so for example K-edge spectroscopy will probe the unoccupied p-states and L_3-edge spectroscopy will probe unoccupied s- and d-states. For most transition elements the L_3 absorption edge shows a strong peak right at the edge, which is due to the high DOS of the narrow d-band, whereas the often much wider s- and p-bands do not give sharp peaks [128]. Historically the sharp peaks at the transition element L_3 absorption edges are known as "white lines". This name comes from the fact XAS spectra used to be recorded on photographic film, and the large absorption coefficient right at the edge shows up as a white line on the negative of the photographic film. Figure 4.13 shows the XANES region of an XAS spectrum of the L_3 edge of Pt along with the calculated DOS of the Pt 5d states. The energy of the XAS spectrum has been aligned at the absorption edge, and the DOS is aligned at the Fermi level, meaning that the states below 0 are occupied, and the ones above are empty. The atomic absorption edge is indicated by an arctan function [122], and it is seen that the white line feature in the XAS spectrum is aligned with the unoccupied part of the DOS.

It is seen in figure 4.13 that the white line feature is much broader than the unoccupied DOS, which is due to lifetime broadening. This effect is due to the very short lifetime of the core-hole excited atom generated when absorbing the X-ray photon. According to Heisenberg uncertainty principle, there is a relation between the energy- and time-resolution achievable,

$$\Delta E \Delta t \geq \hbar \,, \tag{4.18}$$

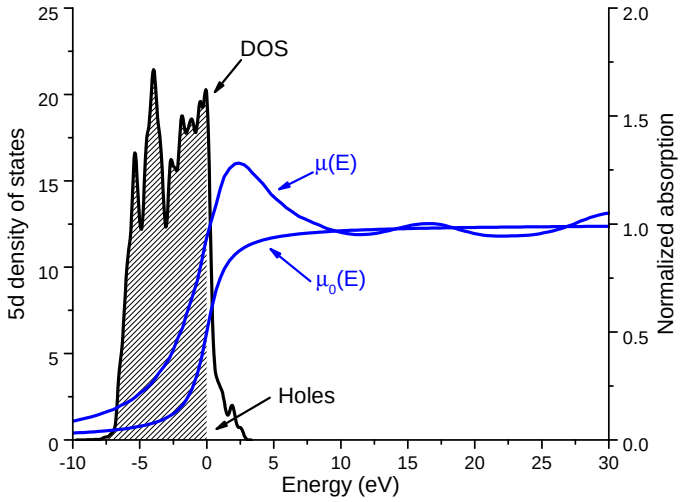

Figure 4.13: The normalized absorption coefficient for the Pt L_3 edge is shown along with the 5d-band electronic density of states (DOS). The energy for the absorption edge has been shifted to show the energy relative to the absorption edge, and for the DOS the energy is relative to the Fermi energy. The hatched part of the DOS is the part below the Fermi edge, which is occupied by electrons. The atomic absorption coefficient has been indicated by an arctan function centered at the absorption edge. It is seen that the absorption white line is aligned with the unoccupied states (holes) in the 5d band.

where ΔE is the energy resolution and Δt is the lifetime of the excited absorber-atom. The peak shape of an ideally sharp final state will be Lorentzian, whereas in the case of a band structure final state(s) the peak is broader, and the shape may be distorted or asymmetric [128]. For example the calculated line broadening at the Pt L_3 absorption edge is 5.31 eV, and tabulations for line widths of most elements can be found [129].

The XANES data presented in this thesis have been measured at beam line 14-3, see appendix E.5 for the setup used at this beam line.

The more advanced HERFD-XAS techniques, that can provide XANES spectra with better energy resolution has also been used. The detailed description of this technique is found in appendix B.2. XANES measurements with this technique were carried out at beam line 6-2, see appendix E.2 for a description of the beam line setup.

CHAPTER 5

X-ray refraction

X-rays are electromagnetic radiation just as visible light, and therefore refraction phenomena are expected to occur. For optical wavelengths the refractive index, n, of many transparent solids such as glass is around 1.5. According to Snell's law[1] total internal reflection may occur when going from a high index material to a lower density material. However, for X-rays the refractive index of solids is slightly less than 1, and therefore total *external* reflection may occur instead. The refractive index of a solid at X-ray wavelengths is typically given as,

$$n = 1 - \delta \,, \tag{5.1}$$

where,

$$\delta = \frac{2\pi\rho r_0}{k^2} \,, \tag{5.2}$$

and here ρ is the electronic density, r_0 is the Thompson scattering length, and k is the X-ray wave number [119]. For solids and X-rays the δ parameter is typically on the order of 10^{-5} [119], and so the critical angle for total external reflection is indeed very small.

Formulating Snell's equation with a grazing incidence angle (see figure 5.1), α, in vacuum and a grazing exit angle, α_o, in a solid gives,

$$\cos(\alpha) = n\cos(\alpha_o) \,. \tag{5.3}$$

At the critical angle for total external reflection $\alpha = \alpha_c$ and $\alpha_o = 0$, and since α_c is very small the cosine may be expanded to second order, giving the following relation,

$$1 - \frac{\alpha_c^2}{2} = 1 - \delta \;\Leftrightarrow\; \alpha_c = \sqrt{2\delta} \,. \tag{5.4}$$

For a typical value of $\delta = 10^{-5}$, $\alpha_c = 0.25°$.

The concept of a refractive index less than 1 may seem impossible, since this implies the speed of the X-rays inside the material exceeds the speed of light. However,

[1] Snell's law is often formulated as $n_1 \sin\theta_1 = n_2 \sin\theta_2$, where the angles are defined from interface normal.

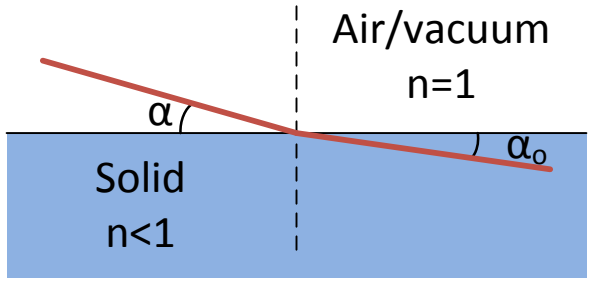

Figure 5.1: The figure shows an interface between air or vacuum and a sold material. The incidence angle relative to the interface is α, and the refracted beam exits at a smaller angle α_o as the index of refraction is smaller in the solid.

it is only the phase velocity of the X-rays that is faster than the light, the group velocity remains slower.

Absorption of a material may also be included in the refractive index by allowing an imaginary component,

$$n = 1 - \delta + i\beta\,. \tag{5.5}$$

The parameter β may is related to the linear absorption coefficient, μ, discussed in the previous section,

$$\beta = \frac{\mu}{2k}\,. \tag{5.6}$$

At incidence angles below the critical angle the intensity of the transmitted beam drops off exponentially inside the material, while a so-called evanescent wave runs parallel to the solid surface. This provides a unique way to achieve highly surface sensitive measurements, however in the case of XAS one must keep self-absorption effects in mind, since the incoming X-rays may only penetrate a few nanometers into the solid. At an incident angle equal to the critical angle the reflected X-ray beam is in phase with the incoming beam, in effect doubling the X-ray amplitude and quadrupling the X-ray intensity of the evanescent wave. Figure 5.2 shows the reflectivity, penetration depth, evanescent wave intensity, and phase shift of the reflected beam as a function of the incoming beam angle close to the critical angle.

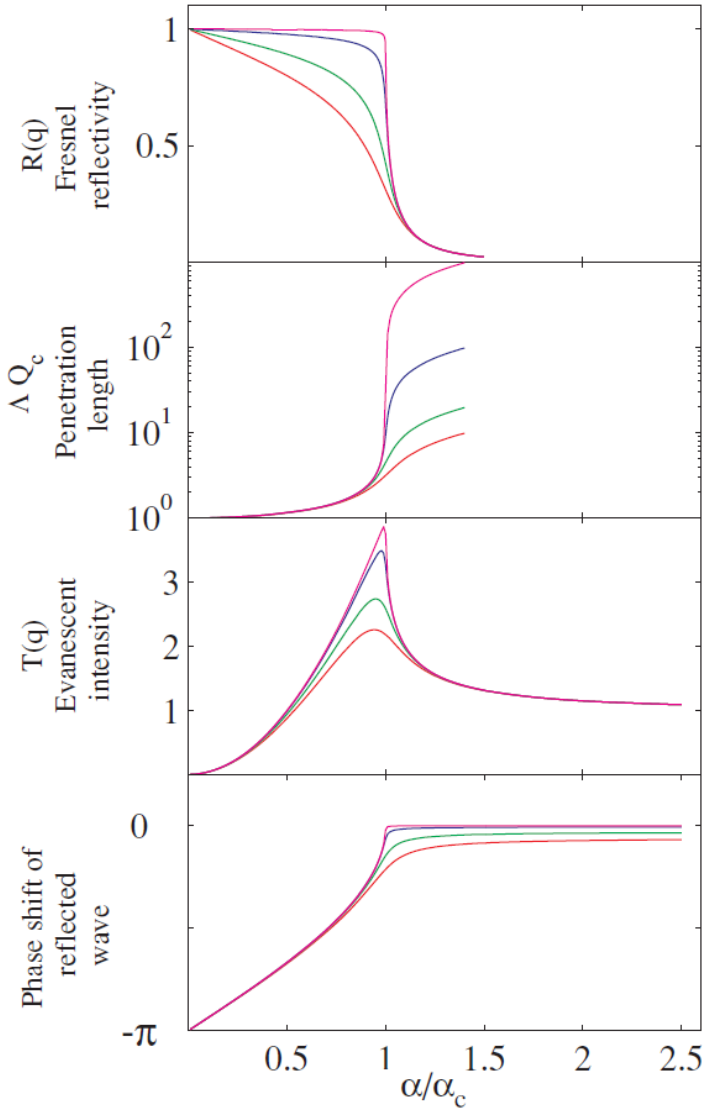

Figure 5.2: The figure shows the reflectivity, penetration depth, evanescent wave intensity, and reflected beam phase shift as a function of the incoming beam angle close to the critical angle. The incoming angle has been normalized to the critical angle. The refraction properties have been plotted for different absorption coefficients, and the higher the absorption is the more smooth the functions are. It is seen that the evanescent wave intensity is up to 4 times the incident beam intensity at the critical angle, which can be used to enhance surface sensitivity. The figure is adapted from [119].

CHAPTER 6

X-ray diffraction

As seen in the previous section X-rays interact with electrons in matter, which can cause the X-ray photon to be absorbed. Alternatively an X-ray photon may also interact elastically with an electron, exchanging momentum so that the direction of the photon is changed, but its energy is conserved. This is the basis of X-ray diffraction, and when atoms are arranged in periodic crystal structures the scattered X-rays from each atom interfere causing a particular pattern of X-ray intensity to be emitted. This was realized early on in the history of X-rays, and diffraction has been used to determine structures very accurately of countless materials since then. This technique is also used on biological samples, in which a crystal of a particular molecule is been grown, which allows the molecular structure to be determined. A famous example was the discovery of the helical structure of DNA in 1953 [130], which prompted the award of the Nobel Prize in Medicine and Physiology in 1962.

6.1 Scattering from a single electron

Treating the scattering from a single electron classically offers results in terms of intensity and polarization in good agreement with Thompson scattering obtained from a full non-classical description. But the inelastic Compton scattering is only described through the non-classical treatment, however this scattering process is not treated here, and the reader is instead referred to [119, 131].

Classically X-ray scattering from an electron occurs because the electric field of the X-ray waves accelerate the electron, giving rise to scattered electromagnetic waves at the same wavelength. Typically synchrotron radiation is horizontally polarized, causing the electron to oscillate horizontally perpendicular to the direction of the X-rays. This is indicated in figure 6.1 where the X-rays propagate along z and are horizontally polarized along x.

Assuming the observer sits at the point X, the electric field generated by the oscillating electron depends on the projected acceleration of the electron,

$$E = \frac{qa\sin(\Psi)}{4\pi\varepsilon_0 c^2 R}\,, \tag{6.1}$$

where q is the charge, $a\sin(\Psi)$ is the projected acceleration, ε_0 is the vacuum permittivity, and R is the distance to the observer [131]. The acceleration is due

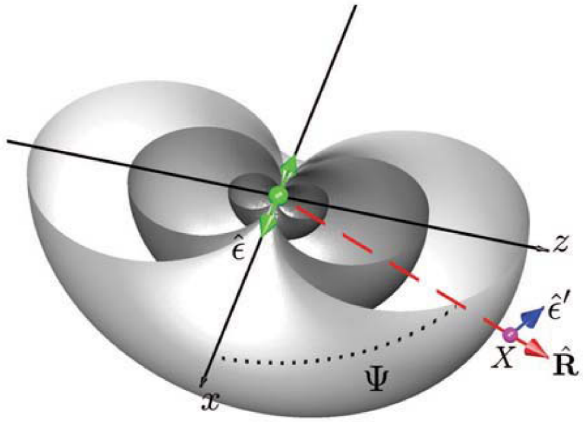

Figure 6.1: The figure shows an oscillating electron when subjected to an X-ray traveling along z and polarized along x. The observer sits at the point X, and it is seen that the projected acceleration of the electron decreases as the angle Ψ is decreased. The figure is from [119].

to the X-ray electric field with amplitude E_0, and the electric field amplitude thus becomes,

$$E = \frac{E_0 e^2}{4\pi\varepsilon_0 mc^2 R}\sin(\Psi) = r_0\frac{E_0}{R}\sin(\Psi)\,, \tag{6.2}$$

where $r_0 = 2.82 \times 10^{-5}$ Å is known as the Thompson scattering length. The intensity is proportional to the square of the electric field [131],

$$I \propto E^2 = r_0^2\frac{E_0^2}{R^2}\sin^2(\Psi)\,. \tag{6.3}$$

This intensity distribution is also indicated in figure 6.1 and it is seen that the intensity is constant in the vertical yz-plane, whereas the intensity drops to 0 at 90° scattering angle in the horizontal xz-plane. This is the reason why fluorescence detectors for XAS measurements most often are placed at 90° in the horizontal plane from the sample, as the elastically scattered intensity is maximally suppressed.

6.2 Scattering from a single atom

When X-rays scatter off from multiple electrons, the intensity is determined by interference between the scattered X-rays. The phase difference between the different scattered X-rays therefore becomes the important parameter, and so the complex notation of the electric field becomes more convenient,

$$E = E_0 e^{i\mathbf{k}\cdot\mathbf{r}} e^{-i\omega t}\,, \tag{6.4}$$

where $\mathbf{k}$ is the wave vector that has the magnitude of the wave number, $2\pi/\lambda$, and point in the direction of the X-ray travel direction, $\mathbf{r}$ is a vector pointing to a point in space, and ω is the angular frequency of the X-ray.

In a scattering event momentum is transferred from the electron to the X-ray photon, and this momentum transfer vector, $\mathbf{Q}$, is a very important concept in scattering. The momentum transfer vector is defined as $\mathbf{Q} = \mathbf{k}_f - \mathbf{k}_i$, and is illustrated in figure 6.2. Applying this only to elastic scattering $k_i = k_f = k$, and the magnitude of the momentum transfer vector is related to the X-ray wave number and the scattering angle,

$$Q = 2k\sin(\theta) = \frac{4\pi}{\lambda}\sin(\theta)\,. \tag{6.5}$$

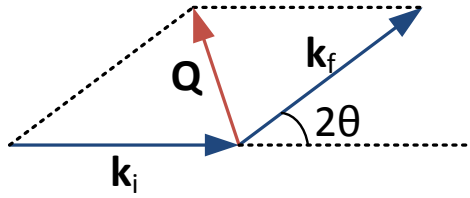

Figure 6.2: The figure shows the incoming X-ray with wave vector $\mathbf{k}_i$ and the scattered X-ray with wave vector $\mathbf{k}_f$. The momentum transfer vector is then defined as $\mathbf{Q} = \mathbf{k}_f - \mathbf{k}_i$. The length of $\mathbf{Q}$ can be found from k and the scattering angle 2θ.

An atom has a collection of electrons, that are all able to scatter X-rays, and assuming that the observer is far away from an atom with point-like electrons, the electric field amplitude at a distance R from the atom becomes [131],

$$E = \frac{r_0 E_0}{R} e^{i(kR-\omega t)} \sum_n e^{i\mathbf{Q}\cdot\mathbf{r}_n}\,, \tag{6.6}$$

where the electrons are positioned at $\mathbf{r}_n$ relative to the atomic center. In an atom the electrons are not point-like, but rather spread out with density ρ, and by replacing the sum by an integral the electric field from a single electron around an atom becomes [131],

$$E = \frac{r_0 E_0}{R} e^{i(kR-\omega t)} \int e^{i\mathbf{Q}\cdot\mathbf{r}} \rho\, dV\,. \tag{6.7}$$

Here the integral is known as the electronic form factor,

$$f_e(\mathbf{Q}) = \int e^{i\mathbf{Q}\cdot\mathbf{r}} \rho \, dV \,. \tag{6.8}$$

It is seen that this is simply the Fourier transform of the electronic density. For the whole atom, an *atomic* form factor may be defined as well, which is simply a sum of the individual electronic form factors,

$$f(\mathbf{Q}) = \sum_n f_e(\mathbf{Q})_n \,. \tag{6.9}$$

In general the atomic form factor cannot be calculated analytically, except in the case of hydrogen [119],

$$f_H(Q) = \frac{1}{\left[1 + \left(\frac{Qa_0}{2}\right)^2\right]^2} \,, \tag{6.10}$$

where $a_0 = 0.53$ Å is the Bohr radius. In this case only the magnitude of $\mathbf{Q}$ in included due to the spherical symmetry of the 1s orbital. Calculated atomic form factors are tabulated for most elements. However, these tables are typically based on a single atom in vacuum, and the form factor is spherically averaged assuming a spherical electron density. For heavy elements this assumption most often holds well as most electrons are core electrons, however there are some cases with light elements in which the non-spherical distribution of charge become significant.

This concept can be extended to collections of atoms, and for example a molecular form factor may be calculated by adding the individual atomic form factors multiplied by the correct phase term [119],

$$F(\mathbf{Q}) = \sum_n f_n(Q) e^{i\mathbf{Q}\cdot\mathbf{r}_n} \,. \tag{6.11}$$

The electric field is proportional to the form factor, which is in general a complex function, and so the measured intensity is proportional to the squared modulus of the form factor,

$$I(\mathbf{Q}) \propto |F(\mathbf{Q})|^2 \,. \tag{6.12}$$

6.3 Reciprocal space

In crystals atoms are arranged on a lattice, in which an atom (or collection of atoms) are repeated to form a 3-dimensional structure. A more rigorous description of crystals is provided in appendix C.1. In this section the concept of the reciprocal lattice is introduced. This construction is extremely helpful in treating diffraction theory as we will see in the next section.

The real space lattices vectors $\mathbf{a}_1$, $\mathbf{a}_2$, and $\mathbf{a}_3$ construct the 3D lattice, and now a set of reciprocal lattice vectors are defined by [119],

$$\mathbf{a}_i \cdot \mathbf{b}_j = 2\pi\delta_{ij}\,, \tag{6.13}$$

where $\mathbf{b}_j$ are the reciprocal lattice vectors and δ_{ij} is the Kronecker delta. It is seen that the units of the reciprocal lattice vectors are inverse distance, giving rise to the name reciprocal lattice. In 3D the reciprocal lattice vectors can be constructed from the real space lattice vectors, fulfilling the requirement above [131],

$$\mathbf{b}_1 = \frac{2\pi}{V}\mathbf{a}_2 \times \mathbf{a}_3\,, \tag{6.14}$$

$$\mathbf{b}_2 = \frac{2\pi}{V}\mathbf{a}_3 \times \mathbf{a}_1\,, \tag{6.15}$$

$$\mathbf{b}_3 = \frac{2\pi}{V}\mathbf{a}_1 \times \mathbf{a}_2\,, \tag{6.16}$$

where $V = \mathbf{a}_1 \cdot \mathbf{a}_2 \times \mathbf{a}_3$ is the unit cell volume. In the same way as the real space lattice is constructed from the lattice vectors, the reciprocal space lattice is built from the reciprocal lattice vectors,

$$\mathbf{G} = h\mathbf{b}_1 + k\mathbf{b}_2 + l\mathbf{b}_3\,, \tag{6.17}$$

where h, k, and l are integers. These integers also define crystal planes in the real space crystal, which are defined as the plane going through the points $\mathbf{a}_1/h$, $\mathbf{a}_2/k$, and $\mathbf{a}_3/l$. The distance between these crystal planes is [131],

$$d_{hkl} = \frac{1}{|\mathbf{G}_{hkl}|}\,. \tag{6.18}$$

6.4 Scattering from crystals

As we saw earlier with atoms and molecules the diffraction intensity can be calculated as a function of $\mathbf{Q}$ by use of the form factor. The same approach can be used for crystals. The following results are only valid within the kinematical (or weak) scattering limit, in which it is assumed that the X-rays are interacting weakly with the crystal so that a photon is scattered maximally one time. If X-rays scatter multiple times the following theory framework is no longer valid in the dynamical scattering regime. The dynamical regime is approached for large single crystal (domains) and for heavier elements, and care has to be taken when the domains are on the order of the attenuation length of the material. In this section only kinematical scattering will be covered, and the reader is referred to [119, 131] for dynamical scattering theory.

Using the same approach for a crystal as with a molecule the crystal form factor can be calculated,

$$F_{\text{crystal}}(\mathbf{Q}) = \sum_{j}^{\text{All atoms}} f_j(Q) e^{i\mathbf{Q}\cdot\mathbf{r}_j} \,, \tag{6.19}$$

where $f_j(\mathbf{Q})$ is the atomic form factor for atom j and $\mathbf{r}_j$ is the position vector for atom j. It is worth noting that just like the atomic form factor is the Fourier transform of the electron distribution within the atom, the crystal form factor is also the Fourier transform of the crystal. But now by using the knowledge of crystalline order this sum can be split into two sums, one summing all the unit cells, and one summing over the atoms within the unit cell [119],

$$F_{\text{crystal}}(\mathbf{Q}) = \sum_{n}^{N} e^{i\mathbf{Q}\cdot\mathbf{R}_n} \sum_{j} f_j(Q) e^{i\mathbf{Q}\cdot\mathbf{r}_j} \,, \tag{6.20}$$

assuming there are N unit cells in the whole crystal. The second sum is really the parameter unique for a given structure, since it carries information about the positions and types of atoms within the unit cell, and is known as the structure factor,

$$F(\mathbf{Q}) = \sum_{j} f_j(Q) e^{i\mathbf{Q}\cdot\mathbf{r}_j} \,, \tag{6.21}$$

and again noticing that this sum only runs over the atoms within a single unit cell. When calculating the intensity the first sum in the crystal form factor can be evaluated as a geometric series,

$$I \propto |F_{\text{crystal}}(\mathbf{Q})|^2 \propto \left| \frac{1 - e^{iN\mathbf{Q}\cdot\mathbf{R}}}{1 - e^{i\mathbf{Q}\cdot\mathbf{R}}} \right|^2 |F(\mathbf{Q})|^2 = \frac{\sin^2(N\mathbf{Q}\cdot\mathbf{R}/2)}{\sin^2(\mathbf{Q}\cdot\mathbf{R}/2)} |F(\mathbf{Q})|^2 \,. \tag{6.22}$$

This is not strictly correct, as the sum over unit cells should have been split into 3 sums along the direction of each of the lattice vector directions, but keeping the vector notation here we arrive at the same realization. The function $\sin^2(Nx)/\sin^2(x)$ has a value of N^2 when x is an integer multiple of π and a low value everywhere else when N is large, see figure 6.3. In the case of a real crystal the number of unit cells can easily exceed 10^4 in each direction, and this function basically becomes a delta-function. This shows that there is only non-zero intensity when $\mathbf{Q}\cdot\mathbf{R}$ is an integer, and the intensity is then very large. This requirement is fulfilled exactly when the momentum transfer vector, $\mathbf{Q}$, is equal to a reciprocal lattice point, $\mathbf{G}$, which is known as the Laue diffraction condition [119],

$$\mathbf{Q} = \mathbf{G}_{hkl} \,. \tag{6.23}$$

This can be shown from the definition of the reciprocal lattice requiring that $\mathbf{a}_i \cdot \mathbf{b}_j = 2\pi\delta_{ij}$,

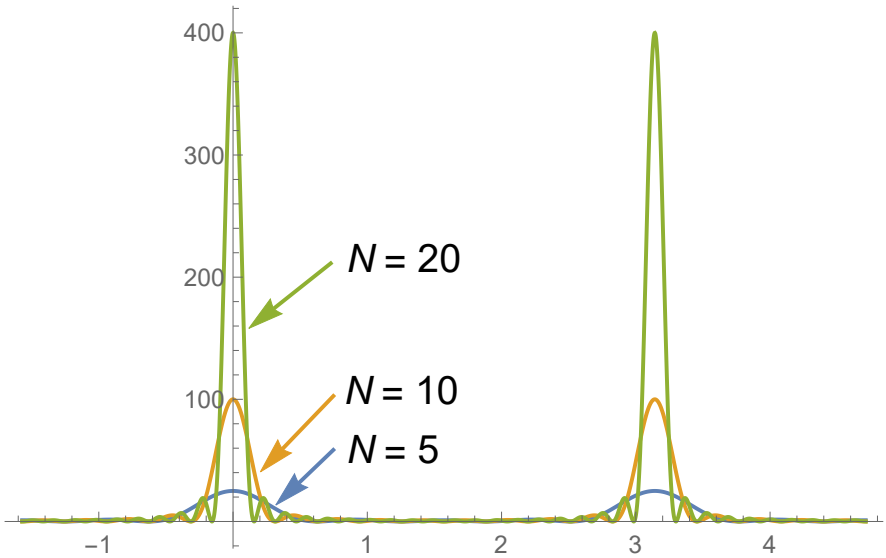

Figure 6.3: The figure shows a plot of the function $\sin^2(Nx)/\sin^2(x)$ for a few values of N. The height of the peaks when x is a multiple of π quickly sharpens when N becomes larger, and the height of the peak is N^2. A macroscopic crystal may contain on the order of 10^4 unit cells in each direction. But for example a 4 nm Pt nanoparticle only has 10 unit cells in each direction, giving rise to significant broadening as seen here.

$$\mathbf{G}_{hkl} \cdot \mathbf{R} = 2\pi(h+k+l)\,. \tag{6.24}$$

When solving an unknown crystal structure from an X-ray diffraction pattern the unit cell can be determined from the position of diffraction spots, since they are only allowed on the reciprocal lattice points. The intensity is measured at these points, and their relative intensity ratios are determined by the types and positions of the atoms in the unit cell.

One example is Pt, which has the FCC structure. In a simple cubic unit cell there are 4 Pt atoms at (0,0,0), (1/2,1/2,0), (1/2,0,1/2), and (0,1/2,1/2), and the structure factor can be calculated,

$$F = \sum_{j=1}^{4} f_{\mathrm{Pt}}(Q) e^{i\mathbf{Q}\cdot\mathbf{r}_j} = f_{\mathrm{Pt}}(Q)\left(1 + e^{i\pi(h+k)} + e^{i\pi(h+l)} + e^{i\pi(k+l)}\right)\,. \tag{6.25}$$

This structure factor becomes $4f_{\mathrm{Pt}}(Q)$ in the case that h, k, and l are all even or all odd, otherwise it is 0. This is known as a general reflection condition, and holds true for all crystals with this space group.

6.5 Solving structures

The goal in XRD is to measure the structure factors, so that the structure may be determined. This is not trivial, and in appendix C.2 a new approach is introduced, in which the entire measured reciprocal space is obtained from an Ewald sphere construction. This technique is very useful when determining structures in complex samples, where multiple structures may be present, as the reciprocal space data is represented in Cartesian coordinates.

The first step when analyzing single crystal diffraction data is to determine the type of unit cell by observing the symmetry of the location of the diffraction peaks, e.g. cubic or hexagonal. Then from the distance in between the reciprocal space lattice points the reciprocal lattice vectors may be determined, from which the real space lattice parameters may be calculated. When the reciprocal lattice vectors are known each diffraction peak may have their *hkl* index assigned, and the intensity is integrated and associated with that particular reciprocal lattice index.

Now before leaving the diffraction peaks completely it is worth noting that the diffraction peaks have finite widths. There are both experimental and intrinsic factors impacting the width. Some external effects depend on the beam, such as a finite divergence, while other depend on the detector, for example finite pixel/slit angular resolution. As for intrinsic effects imperfections and finite size of the crystal are the main contributors, and imperfections could be impurities, lattice defects, or strain. For very small crystals, typically less than 100 nm [131] the finite size broadening may become the primary component of the peak width. As shown back in figure 6.3 it is seen that the peaks, corresponding to diffraction peaks, have finite widths when the crystal consists of only a few unit cells in a particular direction. The width of the peak in 3 dimensions reflects the number of unit cells in 3 dimensions, which may be different. So for example a thin film may give elongated diffraction peaks, since there are much fewer unit cells in the thickness direction than within the film plane. The diffraction peaks are often approximation by a Gaussian, Voigt (convolution of Gaussian and Lorentizian peaks), or pseudo-Voigt (linear combination of Gaussian and Lorentzian peaks) line shapes, and the full width at half maximum (FWHM) may be extracted. To quantify crystal size the Scherrer equation is used with the FWHM, ΔQ, of the peak [131–133],

$$D = \frac{2\pi K}{\Delta Q}\,, \tag{6.26}$$

where D is the crystallite size and K is the shape parameter, which is on the order of 1. For a perfect sphere the shape parameter is $K = 1$, but for example for a thin film the shape factor is $K = 0.886$ [133].

Now the unit cell has been found and the crystallite size has been determined, and so the next step is to determine the structure, i.e. the atomic arrangement within the unit cell. This can be found from the structure factor, which is related to the integrated intensity of the diffraction spots. However, the relation between intensity and structure factor is not linear [119],

$$I_{\text{meas}} \propto I_0 NPL|F|^2 \,, \tag{6.27}$$

where I_{meas} is the measured intensity, I_0 is the incoming X-ray beam intensity, N is the total number of unit cells illuminated, P is the polarization factor, L is the Lorentz factor, and F is the structure factor. Here the explicit **Q**-dependence has been left out as most of these parameters depend on the scattering geometry. The incoming X-ray beam intensity is typically measured by an ion chamber and can easily be used to normalize the scattered intensity at each recorded frame. The number of unit cells illuminated depends strongly on both the sample and scattering geometry. The illuminated volume of a thin film for example depends on the incidence angle only because the size of the X-ray beam is constant, but the scattering geometry may be chosen as to fix the incidence angle, thus removing any variations in N. The polarization factor comes from the fact that the scattered intensity depends on the angle relative to the polarization direction, as discussed in section 6.1. So for the 6-circle diffractometer used here the polarization factor depends on the detector angles only,

$$P = p_h \cos^2(\nu) + (1 - p_h)\cos^2(\delta) \,, \tag{6.28}$$

where p_h is the fraction of horizontally polarized X-rays in the main beam, which is typically around 95% for bending magnet and wiggler beam lines. The Lorentz factor depends on the type of scan being done, and essentially arises from the amount of overlap between the reciprocal lattice and the Ewald sphere shell (which has a finite thickness due to the energy resolution of the monochromator). When a survey scan is performed at small steps of ϕ rotation the ϕ motor is rocked during the scan, so that intensity at all ϕ-angles are recorded. This changes the Lorentz factor, since the speed with which the lattice points move through the Ewald sphere affects the intensity. For this type of rocking scan the Lorentz factor becomes [134, 135],

$$L = \frac{1}{\sin(\delta)\cos(\alpha)} \,. \tag{6.29}$$

Calculating these factors the intensities may be converted to structure factors squared. The structure factor is the Fourier transform of the real space lattice, and so an inverse Fourier transform would yield the real space crystal structure. However, the Fourier transform is complex, and when measuring the intensity the phase is lost, and a simple inverse Fourier transform will not produce the crystal structure. However, the inverse Fourier transform of the magnitudes of the structure factors do contain information about the structure, and it is called the Patterson function [136]. The Patterson function gives a map of all the interatomic distances, which may be used to come up with an initial guess for the actual structure. The Patterson function is a 'direct' method of solving crystal structures, since the structure produced requires no other input than the measured structure factors. Other direct methods include phase retrieval, which is an iterative method to attempt to recover the phase of the structure factors [137–139]. The algorithm works as follows,

1. Initially random phases may be used for the known magnitudes $|F|$.
2. The complex structure factors are inverse Fourier transformed to produce a real space charge density.
3. Physical constraints are applied to the charge density, e.g. any negative density can be set to 0.
4. The updated charge density is Fourier transformed to reciprocal space.
5. The calculated magnitudes of the structure factors are replaced by the measured structure factor magnitudes.
6. Return to step 2, and repeat until change is less than a set threshold.

This technique has not been mathematically proven to converge, and the method is somewhat sensitive to errors in the measured structure factors. There are also certain problems with mirror images appearing, but further treatment of this technique is beyond the scope of this text.

A software package often used in protein crystallography is SHELX [140]. In this program the user provides a list of the indexed structure factor magnitudes, the unit cell, and any symmetry observed on the basis of the reciprocal lattice. The program has multiple extensions, and the one called SHELXT has a direct method built in, so it tries to find the space group as well as the unique atomic positions within the unit cell. The initial guess of the crystal structure may then be refined by fitting with the SHELXL extension, which merges the measured intensities according to the symmetry of the space group, so that a more accurate value is found and an error may be estimated for the structure factor. This extension also allows the user to fit thermal vibrations, either isotropic or anisotropic vibrations.

Thermal vibrations in crystals reduce the intensity of the diffraction peaks, since the atoms are no longer lined up perfectly. In the case of isotropic thermal motion the atomic scattering factor is damped by the Debye-Waller factor [119, 131],

$$f(\mathbf{Q})_{\text{thermal}} = f(\mathbf{Q})e^{-\frac{1}{2}Q^2\langle u^2\rangle}\,, \tag{6.30}$$

where $\langle u^2\rangle$ is the mean squared displacement of the atom. This may be extended to anisotropic displacements, in which u becomes a matrix, but this is beyond the scope of this text.

Finally after measuring the scattered intensity and converted the integrated intensities to structure factors, the structure has been determined.

CHAPTER 7

Electrochemical measurements

The field of electrochemistry covers chemical reactions driven by charge transfers, such as electrons and protons, and are typically done on a catalyst to aid the reaction. This leads to inherently complicated reaction environment that involves the studied catalyst/electrode, the solid or liquid electrolyte, and charge carriers (e.g. electrons). The reactions are then studied by applying an electric potential and monitoring the current. The electronic circuit of such an experiment must make a closed loop, which means that there will always be two electrochemical reactions taking place, since two contacts must be made to the electrolyte. This makes it difficult to study a single reaction, since the current and voltage characteristics with just two electrodes will reflect the properties of both reactions at the same time. This problem can be alleviated by a 3-electrode setup which can be used to study a half-cell reaction, i.e. only one of the two reactions happening at the electrodes.

The standard 3-electrode setup contains the working electrode, which is where the reaction under study takes place, a counter electrode, where the counter-reaction takes place, and a reference electrode. The need for the reference electrode comes from the fact that electronic potential is a relative quantity, and as argued above the counter electrode potential is not suitable as a reference. See figure 7.1 for a sketch of a typical 3-electrode electrochemical setup. The reference electrode is typically housed in a separate enclosure, so that the electrolyte does not contaminate the sample chamber electrolyte with other anions, such as Cl^- and SO_4^{2-}. And in order for the reference electrode to work it is connected to the main compartment by a ceramic frit that minimizes the exchange of the electrolyte in the two compartments, but still allows the reference electrode to sense the chemical potential.

The potentials and currents applied to the 3 electrodes are typically controlled by a potentiostat. When the user requests a specific voltage for the working electrode it is with respect to the reference electrode, so the potentiostat adjusts the voltage between the working electrode and counter electrode, so that the working electrode achieves the correct voltage. The current is monitored in between the working and counter electrodes.

The counter electrode material is not so important in this setup, since the potential of the working electrode is always relative to the well-defined reference electrode.

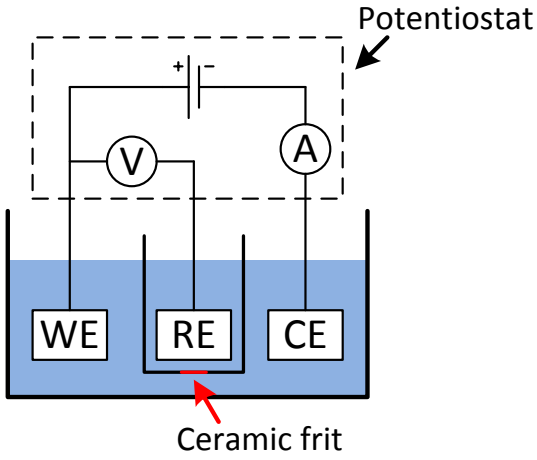

Figure 7.1: The figure shows a sketch of a typical 3-electrode electrochemical setup, which has the working electrode (sample), reference electrode, and counter electrode. The reference electrode is typically housed in a separate compartment so that contamination from the reference electrode is avoided. They are connected by a ceramic frit that minimizes transfer of electrolyte between the two compartments, while still allowing the reference electrode to sense the chemical potential of the solution. The potential is measured between the working electrode and reference electrode and the current is measured between the working and counter electrode. The potentials and current are controlled by the potentiostat, applying potentials/currents specified by the user.

However, the counter electrode must remain stable in the solution, and should not be a limiting factor if a high current is required. Therefore a Pt wire or mesh is often the choice in aqueous electrolyte due to its high inertness and high activity for hydrogen evolution/oxidation.

In aqueous electrolyte the choice of reference is often the hydrogen electrode, which is defined by the equilibrium of the hydrogen oxidation/reduction reaction,

$$\mathrm{H}^+ + e^- \rightleftharpoons 1/2\mathrm{H}_2\,. \tag{7.1}$$

One definition of this potential is the theoretical standard hydrogen electrode (SHE), in which this equilibrium potential is defined as 0 V in an ideal solution (activity of H^+ is 1) on a Pt electrode. A practical approximation of the SHE is the normal hydrogen electrode (NHE), in which the same potential is defined as 0 V in a 1M nitric acid solution also on a Pt electrode. These reference electrodes are both defined in acid at $pH = 0$, and so their potentials will change according to changes

in the electrolyte pH. To get a stable reference in different electrolytes the reversible hydrogen electrode (RHE) has been defined as 0 V at any pH. The relation between RHE and SHE is linear in pH,

$$E_{\mathrm{RHE}} = E_{\mathrm{SHE}} + 0.059\,\mathrm{V} \times pH\,. \tag{7.2}$$

Practically these hydrogen electrodes are not so easy to use as reference electrodes directly, so a different well-defined reference potential must be chosen. Often the Ag/AgCl or Hg/Hg_2SO_4 electrodes are used, which consist of a Ag or Hg electrode in a solution of KCl or K_2SO_4. These electrodes simply have a constant offset from the SHE, and so to convert a potential measured in an experiment relative to the Ag/AgCl electrode can be converted to a potential versus RHE,

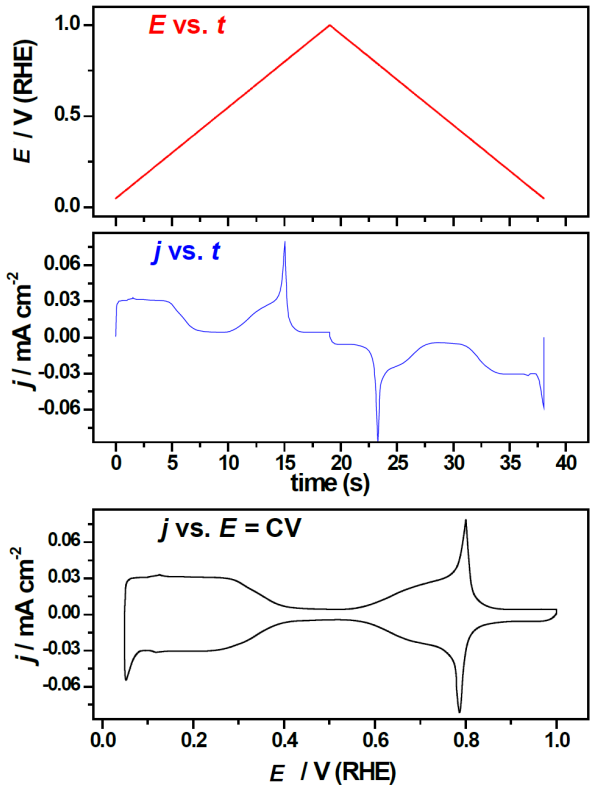

Figure 7.2: The figure shows how a cyclic voltammogram (CV) is measured. The potential is scanned linearly up and down between two given potentials, and the current is measured in response. For analysis the current density is plotted against the potential, as shown here for a Pt(111) single crystal in an N_2-saturated electrolyte.

$$E_{\mathrm{RHE}} = E_{\mathrm{Ag/AgCl}} + 0.199\,\mathrm{V} + 0.059\,\mathrm{V} \times pH\,. \tag{7.3}$$

A modern potentiostat has many characterization techniques from simply applying a constant potential or current up to sophisticated spectroscopies, which can all give different information about the working electrode. One of the most used techniques is cyclic voltammetry (CV), in which the potential is scanned linearly in time between two set vertex potentials, and the current is recorded in response. When analyzed the current density is plotted as a function of the applied potential, as shown in figure 7.2.

The shape of the CV can indicate the reactivity of the surface, and it is seen at which potentials certain redox reactions occur. An example of how the CV can change is seen in figure 7.3 which shows a CV of a Pt(111) single crystal, Pt_xY alloy, and Pt_xGd alloy [77]. These CVs were obtained in N_2-saturated 0.1 M $HClO_4$ with a scan rate of 50 mV/s. The perchloric acid is chosen because the ClO_4^- ion does not adsorb strongly on the sample surface, and it is saturated with N_2 to suppress the oxygen reduction reaction which would otherwise interfere with the shape of the CV. Finally the scan rate can have an impact on the CV shape as well, and 50 mV/s is a standard scan rate used for extended surfaces.

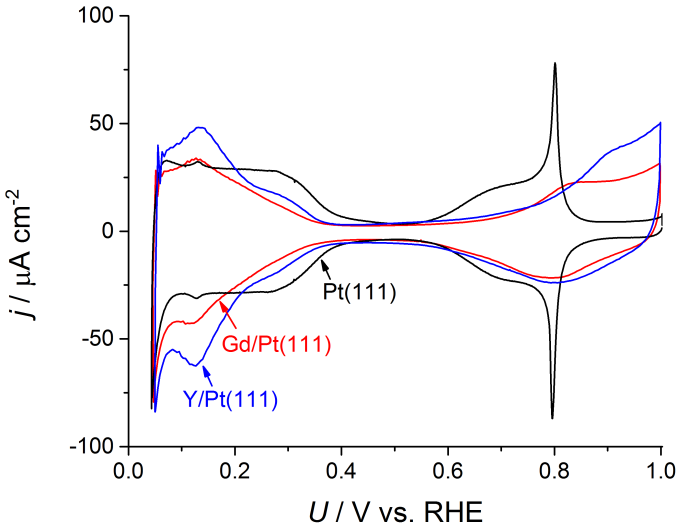

Figure 7.3: The figure shows the CV of Pt(111), Pt_xY alloy, and Pt_xGd alloy. Although the different samples have similar surfaces, even the small change are seen to have a great impact on the shape of the CV. These CVs were all acquired in N_2-saturated 0.1M $HClO_4$ electrolyte, and it taken from [77].

It is also worth mentioning that applying a constant potential (chronoamperometry, CA) or constant current (chronopotentiometry, CP) are useful techniques when studying how the sample activity for a certain reaction changes over time, i.e. stability measurements. Further techniques and analysis of electrochemical methods is beyond the scope of this text.

CHAPTER 8

Platinum alloys for ORR

In this chapter a series of results regarding the structure of Pt-alloy catalysts will be presented, as they have proven highly active for the oxygen reduction reaction. Most experiments have involved Pt_xGd alloys, but the Pt_xY alloy has also been investigated. The overarching goal of these studies were to understand the structure of the Pt overlayer and the underlying alloy structure, as this helps explain the activity and stability of this class of alloys.

8.1 Pt_xGd nanoparticles

As outline in section 2.2 the Pt_xGd nanoparticles are highly active for ORR. Furthermore previous structural studies on Pt_xY nanoparticles motivated us to do structural studies on Pt_xGd nanoparticles as well using EXAFS.

The EXAFS measurements were carried out at BL11-2 at SSRL, using a grazing incidence geometry. The nanoparticles were deposited on a flat glassy carbon disk 5 mm in diameter, and the grazing incidence geometry maximize the number of particles illuminated as well as provide an enhancement in intensity from the evanescent wave. In this experiment the nanoparticles were measured ex-situ, and we had samples as-prepared, after initial activity measurement, and after stability test. Due to time constraints and with the main focus being the Pt structure, only the Pt L_3 edge was measured, which is at 11,564 eV. The setup utilizes the advanced fluorescence detector at the beam line, and the L_α fluorescence line at 9,442 eV (as well as the much weaker L_{α_2} line at 9362 eV) was recorded.

The incident photon energy was scanned in the range 11,334 eV to 12,289 eV, equivalent to a k-range of 0-13.8 $Å^{-1}$. The point spacing was chosen as to be equidistant in k, and the time recording at each point was scaled by k^2, giving more even signal-to-noise ratio across the k-range. This was measured on 8 samples, 5 nm, 8 nm, and 9 nm as-prepared (AP), 3 nm, 5 nm, 8 nm, and 9 nm after electrochemical measurements (EC), and finally 9 nm after stability test (ST). To get a reasonable data quality, between 6 and 16 scans were made on each sample.

The XAS data was processed using the program SIXPack (Sam's Interface for XAS analysis Package) [141], which is based on the IFEFFIT code [142]. In this program the data was first averaged, since multiple scans had been made, as well as averaging the signal from the functioning channels of the 100-element fluorescence

detector (about 20 channels were dead). The second step was to normalize the data by fitting an exponential tail to the pre-edge region and a quadratic or linear function to the post-edge region. Within the same part of the SIXPack program the $\chi(k)$ function is extracted by fitting a spline to the normalized absorption spectrum.

Before fitting the EXAFS data a structural model was needed, however no structure of a Pt rich Pt_xGd alloy had been published at the time [83]. However, the structure of Pt_5Gd seems to be related to the Cu_5Ca structure, which our own measurements on our polycrystalline Pt_5Gd sample had also indicated. Therefore this structure was chosen as a model, which is a hexagonal unit cell with the lattice parameters $a = 5.297$ Å and $c = 4.414$ Å. The unit cell is shown in figure 8.1, and two crystallographically different Pt sites are shown in white and blue, whereas the Gd is green. The shortest inter-atomic distances from a Pt absorber and their average coordination is shown in table 8.1. The two nearest neighboring Pt atoms are at almost the same distance, only 0.037 Å apart, which are very difficult to separate, and even more so if the structure is disordered. Therefore it is worth considering the first and second shell as a single shell with coordination number 7.2.

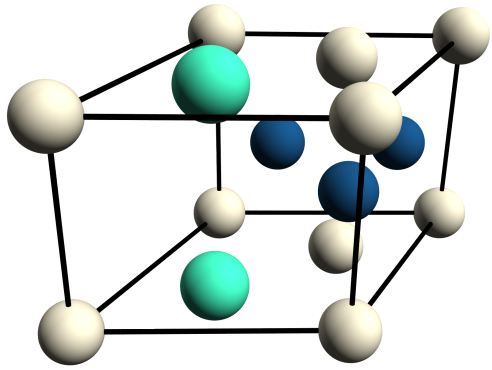

Figure 8.1: The figure shows a Pt_5Gd unit cell in the Cu_5Ca structure, which is a hexagonal cell with lattice parameters $a = 5.297$ Å and $c = 4.414$ Å. In this structure there are two different Pt sites, which are shown as white and blue, and a single Gd site shown as green.

Neighbor	Pt	Pt	Pt	Gd	Gd
Distance (Å)	2.648	2.685	3.058	3.058	3.447
Avg. coordination	2.4	4.8	1.2	1.2	2.4

Table 8.1: The table shows the nearest neighboring atoms from a Pt absorber, their distances, and average coordination number. The average coordination are not integers because there are two different Pt sites.

The nearest neighbor paths were simulated in FEFF6, which calculates the backscattering amplitude and phases. This could be used to complete the fitting of the EXAFS data in SIXPack. In all cases the $\chi(k)$ function was weighted by k^2, which seemed to give the most even weighting across the k-range, which was chosen as 3-11 $Å^{-1}$. All the fitting was done in R-space. The resulting plots of the fits are shown in figures 8.2 and 8.3, in which both $k^2\chi(k)$ and $|\chi(R)|$ are plotted for both the data and the fit. The further distance shells above 3 Å was not seen in the data, and therefore all data was fitted as a single Pt shell. It was not possible to get a reasonable fit having two Pt neighbors at very close distances, and as discussed above it proved more reliable to treat them as a single Pt neighbor with a higher degree of disorder.

Sample	Particle size (nm)	$R_{\mathrm{Pt-Pt}}$ (Å)	$N_{\mathrm{Pt-Pt}}$	$\sigma^2 \times 10^{-3}$ ($Å^2$)	ΔE_0 (eV)	R-factor
3 nm EC	3.2 ± 0.5	2.75 ± 0.01	8.2 ± 0.4	7.1	5.8 ± 1.0	0.010
5 nm AP	5.4 ± 0.5	2.66 ± 0.01	6.4 ± 0.5	8.8	1.2 ± 1.5	0.023
5 nm EC	5.4 ± 0.5	2.72 ± 0.01	8.1 ± 0.5	10.0	4.3 ± 1.0	0.013
8 nm AP	7.7 ± 0.9	2.67 ± 0.01	6.0 ± 0.5	9.0	2.6 ± 1.5	0.027
8 nm EC	7.7 ± 0.9	2.71 ± 0.01	7.7 ± 0.5	9.7	4.2 ± 1.1	0.015
9 nm AP	9.1 ± 0.8	2.67 ± 0.01	5.5 ± 0.4	8.0	3.4 ± 1.4	0.015
9 nm EC	9.1 ± 0.8	2.70 ± 0.01	6.4 ± 0.4	8.0	4.3 ± 1.3	0.017
9 nm ST	9.1 ± 0.8	2.72 ± 0.01	8.2 ± 0.4	11.0	5.4 ± 0.8	0.009

Table 8.2: The table shows the EXAFS fitting results for the 8 samples and the detailed size distributions. The Debye-Waller factor, σ^2, shows no error estimates since it was fixed during the fitting procedure to avoid an unstable fit due to its strong correlation with the coordination number, N.

All the fitting parameters are shown in table 8.2, which also has the more accurate estimates of particle sizes. The Debye-Waller factor, σ^2, was fixed and optimized by hand during the fitting procedure, since it has a tendency to have a strong correlation with the coordination number, N. The estimated errors on the fitting parameters come from the fitting program.

The interatomic Pt-Pt distances obtained from the EXAFS analysis are shown in figure 8.4, both plotted as a function of particle size and as a function of the Gd:Pt

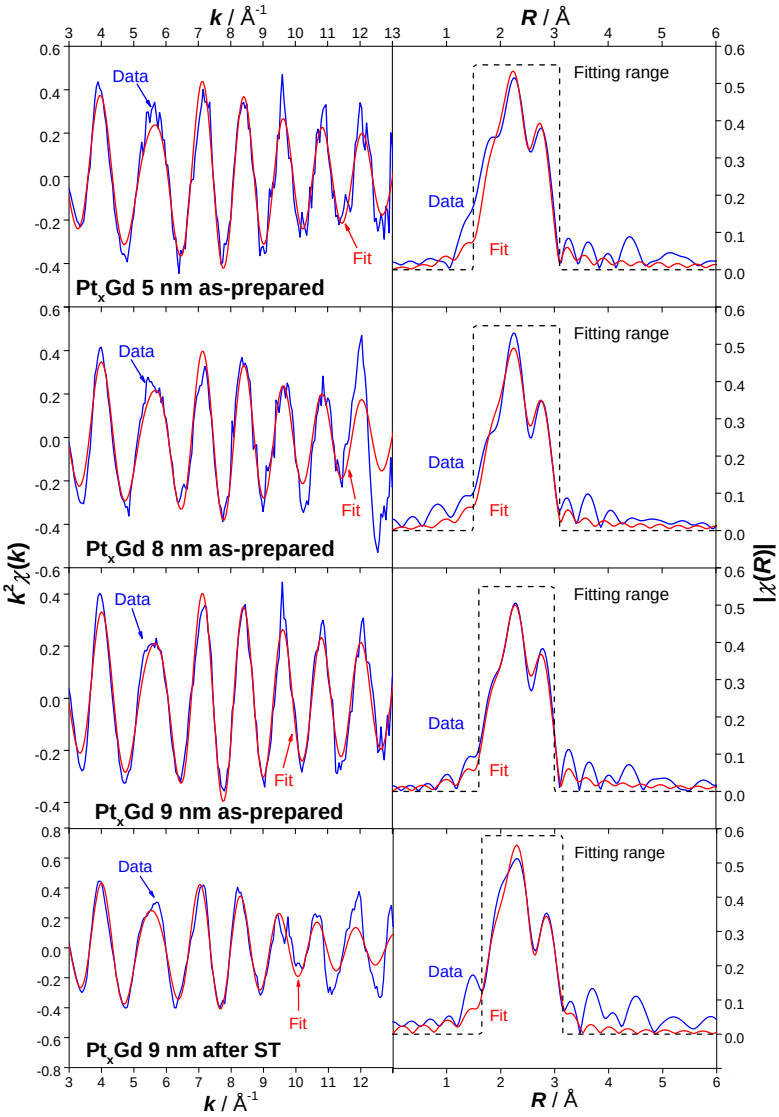

Figure 8.2: The figure shows $k^2\chi(k)$ and $|\chi(R)|$ for both the measured data and the fit for the as-prepared 5 nm, 8 nm, and 9 nm samples as well as the 9 nm sample after stability test. The range used in fitting in the R-space is indicated, and the range of data taken from k-space is 3-11 Å^{-1}. Only a single Pt neighbor was fitted with a high degree of disorder.

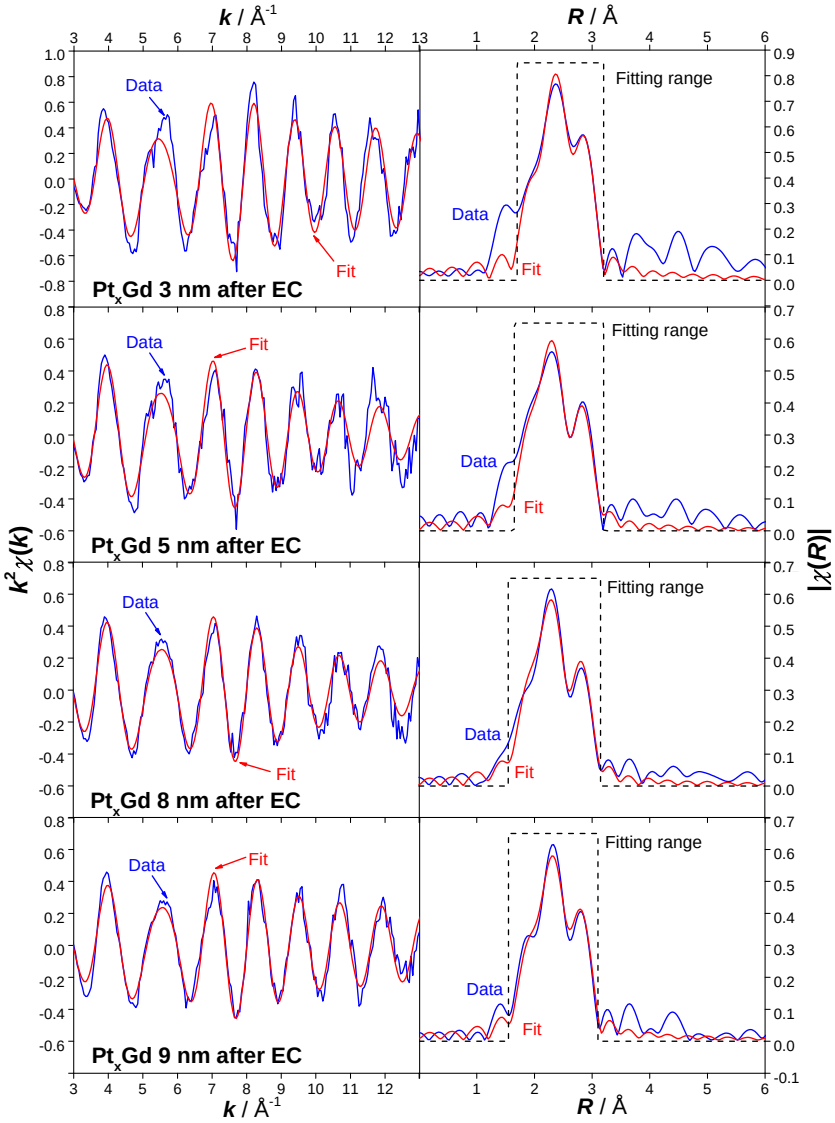

Figure 8.3: The figure shows $k^2\chi(k)$ and $|\chi(R)|$ for both the measured data and the fit for the 3 nm, 5 nm, 8 nm, and 9 nm particles after electrochemical testing. The range used in fitting in the R-space is indicated, and the range of data taken from k-space is 3-11 $Å^{-1}$. Only a single Pt neighbor was fitted with a high degree of disorder.

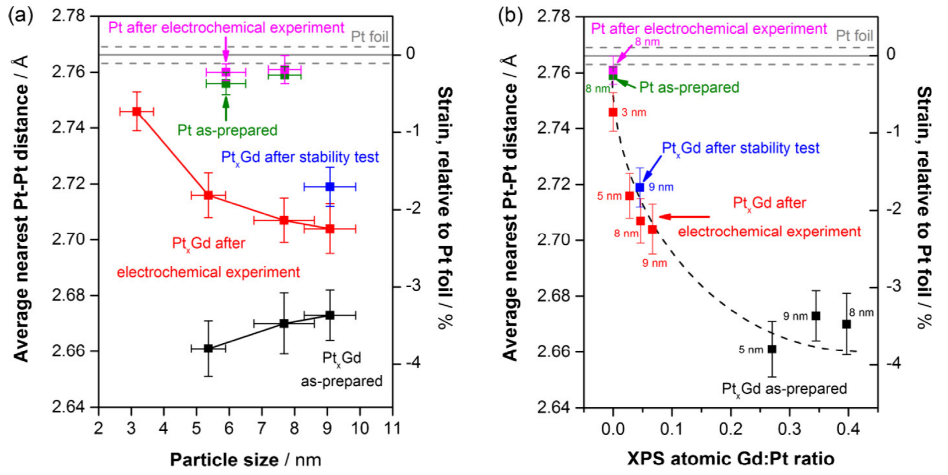

Figure 8.4: The figure shows the average Pt-Pt distance obtained from the EXAFS analysis (a) as a function of the particle size and (b) as a function of the Gd:Pt ratio measured by XPS. It is seen that all the as-prepared samples have a similar compressed Pt-Pt distance and atomic ratios, suggesting uniform particles of a Pt_xGd alloy. After electrochemical measurements Gd leeches out from the surface and presumably forms a ∼1 nm thick Pt overlayer that relaxes towards the bulk Pt lattice constant. The smaller particles have a larger volume fraction of overlayer, and so shows an average Pt-Pt distance closer to bulk Pt. The figure is from [82], *the XPS measurements were done by Paolo Malacrida.*

ratio measured by XPS. It is seen that the as-prepared particles all have the same Pt-Pt distance, indicating that they consist of an alloy from the core all the way to the surface. This is also backed up by the coordination numbers, which are similar for all 3 as-prepared samples and only a bit lower than the 7.2 neighbors calculated from the Pt_5Gd structure. When exposed to electrochemical measurements some Gd leeches out as seen in the XPS ratio, which produces a difference in Pt-Pt distances among the different particle sizes. Presumably a Pt ∼1 nm overlayer forms when Gd is leeched out, which will try to relax back to the bulk Pt lattice constant, and so the larger volume fraction the overlayer occupies, the closer to bulk Pt the Pt-Pt distances will become. This interpretation is once again backed up by the coordination numbers, which have all increased compared to the as-prepared nanoparticles, and it is seen that the smaller nanoparticles with a larger volume fraction of overlayer has a higher Pt-Pt coordination number, which is 12 for bulk Pt.

For the samples that have had their electrochemical activity measured we can plot the activity as a function of the average strain relative to bulk Pt, as seen in figure 8.5, which also includes data for the Pt_xY of pure Pt nanoparticles from [79]. It is seen

that the activity scales with the average strain of the nanoparticles independently of the particle alloy and treatment. For example the 9 nm Pt_xGd sample that has endured stability test shows lower activity than the fresh 9 nm particles, but it also shows a lower degree of compression, falling on the same trend line.

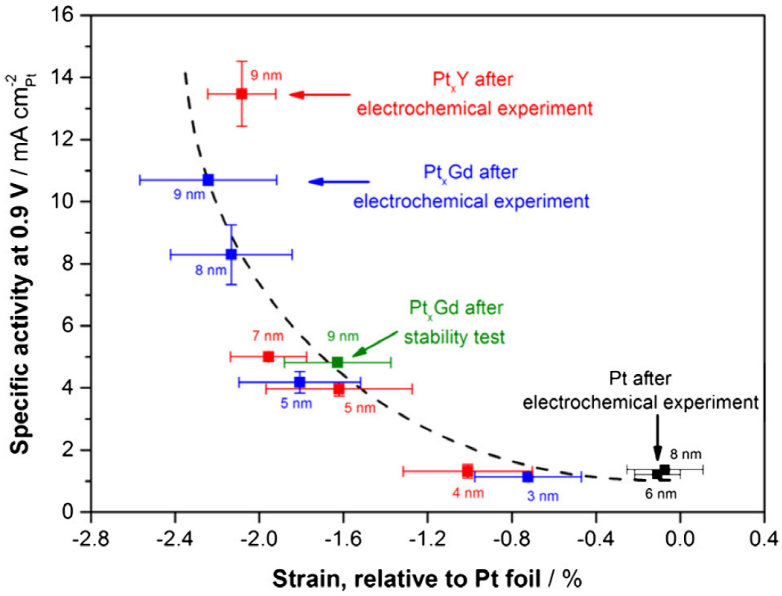

Figure 8.5: The figure shows the surface specific ORR activity as a function of the average strain of the Pt-Pt distance relative to bulk Pt. The plots includes data from both the Pt_xGd nanoparticles described here, Pt_xY nanoparticles investigated earlier [79], and pure Pt nanoparticles produced in the same way [79]. It is seen that the activity scales with the average strain of the nanoparticles independently of the particle alloy and treatment. For example the 9 nm Pt_xGd sample that has endured stability test shows lower activity than the fresh 9nm particles, but it also shows a lower degree of compression, falling on the same trend line. The figure has data from [79, 82], and it is from [82], *the activity measurements were done by Amado Velazquez-Palenzuela.*

These measured interatomic Pt-Pt distances are averaged over each entire particle, and is not representative of the local structure at the surface where the reaction is taking place. The surface is expected to be more relaxed, showing significantly smaller strain than what is plotted here, however the trend is expected to remain the same.

8.2 Pt overlayer on Y/Pt(111) model system

The results obtained from the nanoparticle studies lead to a clear question; what is the structure of the overlayer? This is very difficult to answer for the nanoparticles as they comprise a very complex system, and even the polycrystalline samples are too complex, as they show multiple facets with many possible orientations.

At this point the detailed structure of the overlayer was the goal in constructing the single crystal alloy, and by having a single crystal X-ray diffraction is a very powerful tool to investigate even highly complex structures. And this technique is in general used to study surface on a many different classes of materials [143]. But measuring such a thin overlayer is challenging, and so it was decided to do the measurements ex-situ, since all the previous AR-XPS measurements have been done ex-situ (in UHV actually).

The XRD on the Y/Pt(111) single crystal was measured at BL1-5 at SSRL, equipped with a simple goniometer and a large imaging plate, and using 11 keV photon energy. In order to optimize the surface sensitivity the incidence angle was set to 0.2°, after aligning the sample surface normal to the ϕ rotation axis with a laser. By rotating the sample a full 360° around the ϕ axis during a single exposure of the detector, a full overview of all the allowed diffraction spots is made. This image is shown in figure 8.6, in which the pixel values have been converted to in-plane, $Q_{\parallel}$, and out-of-plane, $Q_{\perp}$, components of the momentum transfer vector. The 'horizon' is shown by a dashed line, which marks the surface of the sample, and no diffracted intensity is seen below as the sample has absorbed the X-rays. The diffraction spots from the Pt(111) substrate is indicated by the 6 circles, and the rest of the diffraction peaks are all from the Pt_5Y alloy. This image was recorded on the as-prepared sample, and the overlayer has not been formed yet.

To get a more detailed measurement of the diffraction pattern the sample was rotated 120° in steps of 0.5°. The Y/Pt(111) crystal was brought to the beam line as-prepared, and when the survey measurement had been completed the sample was mounted in an electrochemical cell to be conditioned. This conditioning process involved 175 cycles between -0.1 and 0.8 V vs. RHE and 189 cycles between 0.05 and 1.05 V vs. RHE, which forms the overlayer. The sample was dried and remounted at the beam line to complete another survey scan. This process was repeated one more time, in which the potential was cycled 261 times between 0.05 and 1.20 V vs. RHE and 202 cycles from 0.05 to 1.30 V vs. RHE.

In these measurements we are separating the in-plane and out-of-plane components of the scattering vector, and so it is more convenient to define a new unit cell for the Pt(111) substrate, which has one lattice vector normal to the sample surface and two lattice vectors parallel to the surface. This construction can be made using a hexagonal unit cell with the lattice parameters $a = 2.775$ Å and $c = 6.797$ Å, which are $a_{\text{cubic}}/\sqrt{2}$ and $a_{\text{cubic}}\sqrt{3}$ respectively. Using the new hexagonal unit cell, the allowed reflections in the region of Q-space that has been recorded are (1,0,1), (1,0,4), and (0,1,2), and 120° rotations of these. The complete list of allowed reflection is shown in table 8.3.

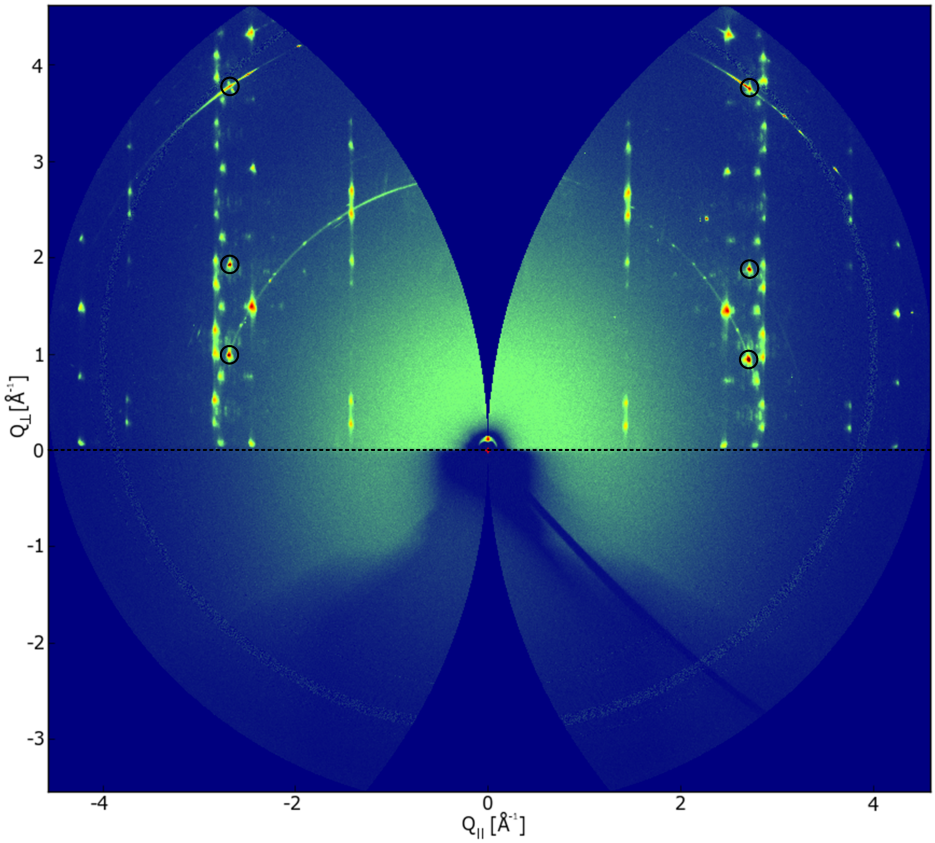

Figure 8.6: The figure shows an overview of the diffraction pattern from the Y/Pt(111) single crystal. The image has been acquired by rotating the sample a full 360° around the ϕ axis during a single exposure of the detector. The image has subsequently been processed to show the intensity as a function of the in-plane, $Q_{\parallel}$, and out-of-plane, $Q_{\perp}$, components of the momentum transfer vector. The X-rays are incident at 0.2°, meaning they are almost parallel to the sample surface. This is seen as a 'horizon' on the detector, as indicated by the dashed line, and there are no diffracted X-ray intensity below since it will be absorbed by the Pt substrate. The six circles indicate diffraction spots from the Pt(111) substrate; the rest is from the Pt_5Y alloy. The sample was as-prepared when this diffraction pattern was recorded, and so the overlayer has not been formed yet.

Hexagonal	Cubic
(1,0,1)	(1,1,-1)
(-1,1,1)	(-1,1,1)
(0,-1,1)	(1,-1,1)
(0,1,2)	(0,2,0)
(-1,0,2)	(0,0,2)
(1,-1,2)	(2,0,0)
(1,0,4)	(2,2,0)
(-1,1,4)	(0,2,2)
(0,-1,4)	(2,0,2)

Table 8.3: The table shows the allowed reflections in the volume of Q-space measured by the survey scan. The indices are shown for both the hexagonal and cubic unit cells, where the hexagonal cell is more intuitive for the Pt(111) surface.

Upon examining the survey data after electrochemical conditioning we found weak scattering peaks from the overlayer. It was seen that some part of the overlayer has the same orientation as the Pt(111) substrate and another part is rotated by 30° around the ϕ axis. Seeing a rotated overlayer was not completely surprising, since the alloy itself is sometimes rotated by 30°, and it happened about half the times the alloy was made. However, having both a rotated and unrotated overlayer was a surprising complexity.

Figure 8.7 shows the evolution of the diffraction peaks from the not rotated overlayer in a small section of Q-space only integrated over 4° rotation. The structure of the overlayer is FCC like bulk Pt(111) structure, however the overlayer has domains that are rotated 60° from each other, resulting in diffraction peaks at $L = 1$, 2, and 4 at the same H and K indices. The diffraction peaks are elongated in the out-of-plane direction, indicating a very thin overlayer as expected. The overlayer peaks are indicated by the dashed ellipses, and since the overlayer is not rotated the Pt(111) reflection (0,1,2) is indicated by the red circle. The remaining columns of diffraction peaks are from the Pt_5Y alloy. In the as-prepared state there is no diffraction from the overlayer as expected, after the first electrochemical conditioning the overlayer peaks have appeared, and after the second conditioning the peaks are still present, although seemingly narrower peaks in the out-of-plane direction.

The diffraction from the rotated overlayer is seen in figure 8.8. The rotated overlayer shows the same structure, just rotated by 30°. However, one notices that these peaks are much wider in the out-plane-direction, indicating an even thinner overlayer. It also appears after the first electrochemical conditioning, but it disappears again after the second electrochemical treatment.

After the second electrochemical conditioning cycling from 0.05 to 1.30 V vs. RHE a third kind of overlayer appeared rotated ±5° from the substrate. This region is shown in figure 8.9, where it is noticed that this overlayer only appears after the

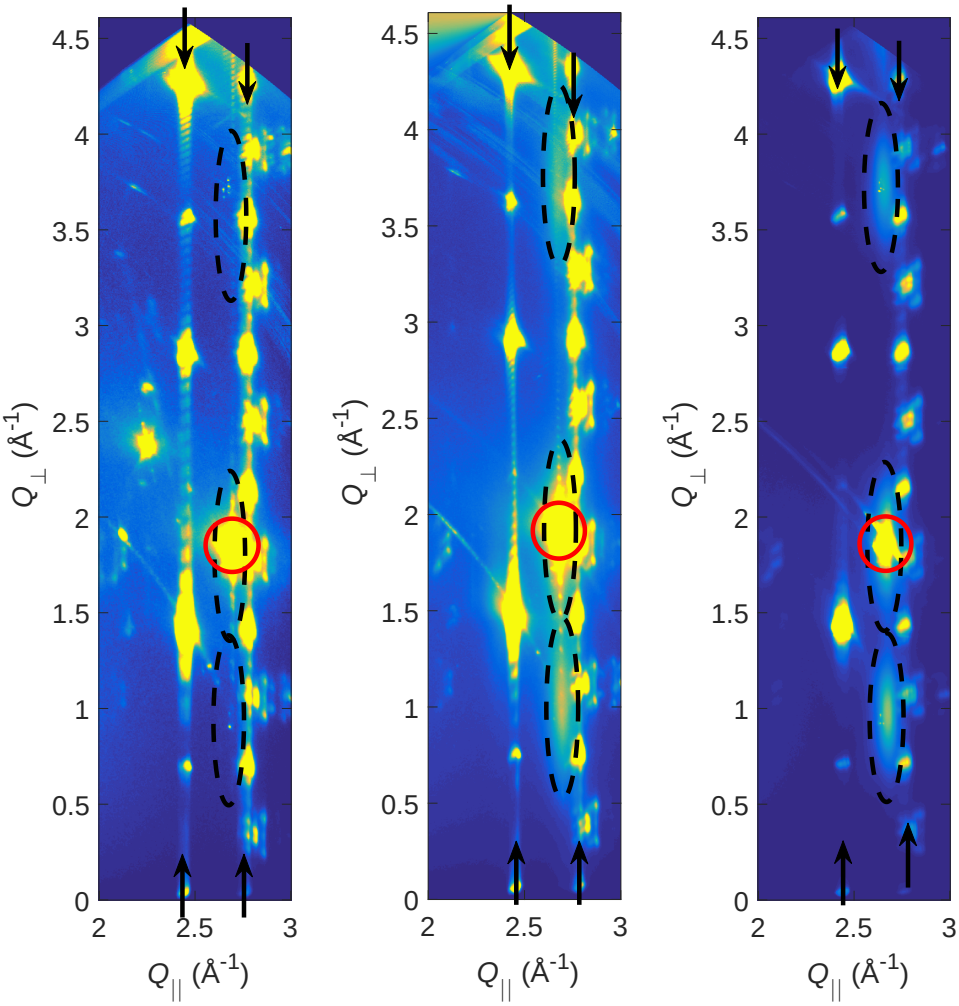

(a) As-prepared.

(b) Electrochemical conditioning 0.05-1.05 V vs. RHE.

(c) Electrochemical conditioning 0.05-1.30 V vs. RHE.

Figure 8.7: The figure shows a small section of Q-space with the not rotated overlayer diffraction spots. To obtain these images the intensity was integrated over ϕ_c=−2°-2°. Besides the overlayer diffraction peaks indicated by the ellipses the images show the Pt(111) substrate (0,1,2) diffraction peak in the red circle and two columns of peaks from the Pt_5Y alloy. On the as-prepared sample there is no overlayer, but after both electrochemical conditionings the not rotated overlayer remains visible.

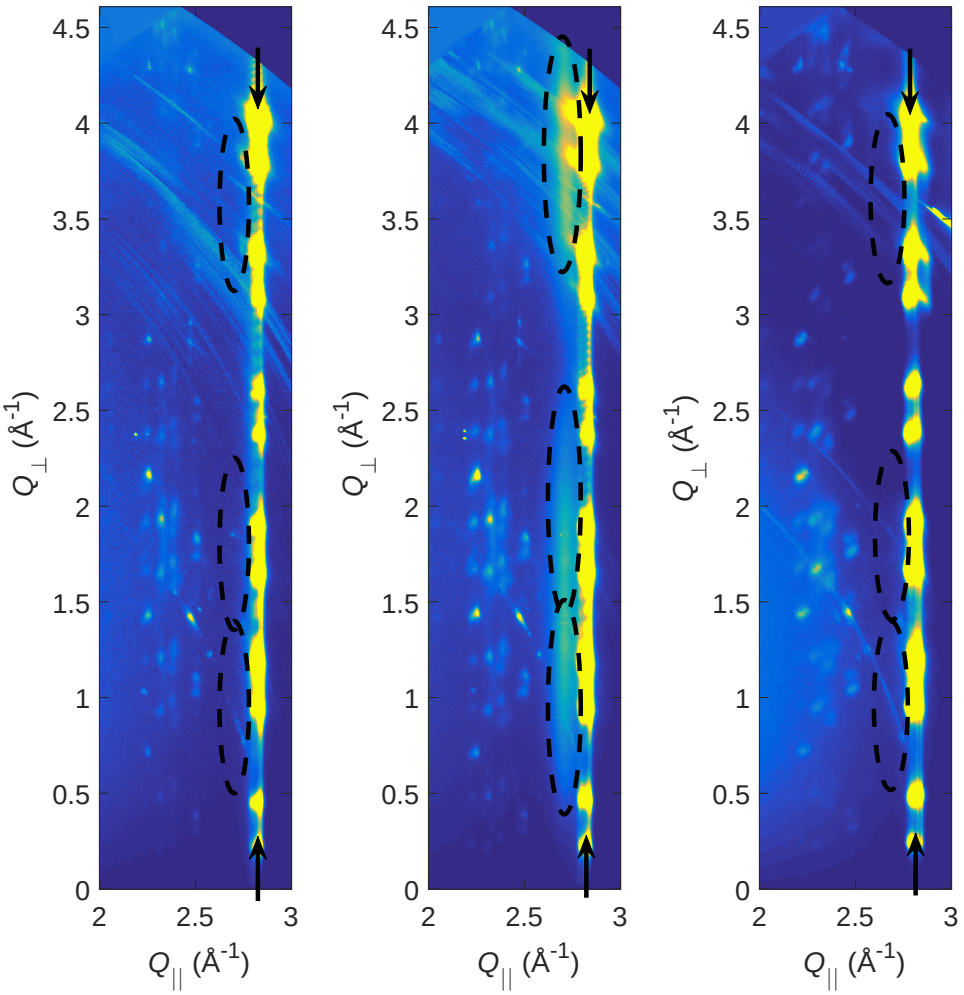

(a) As-prepared.

(b) Electrochemical conditioning 0.05-1.05 V vs. RHE.

(c) Electrochemical conditioning 0.05-1.30 V vs. RHE.

Figure 8.8: The figure shows a small section of Q-space with the rotated overlayer diffraction spots. To obtain these images the intensity was integrated over ϕ_c=28°-32°. Besides the overlayer diffraction peaks indicated by the ellipses the images show a column of peaks from the Pt_5Y alloy. On the as-prepared sample there is no overlayer, but after the first electrochemical conditioning the rotated overlayer forms, but disappears again after the second conditioning.

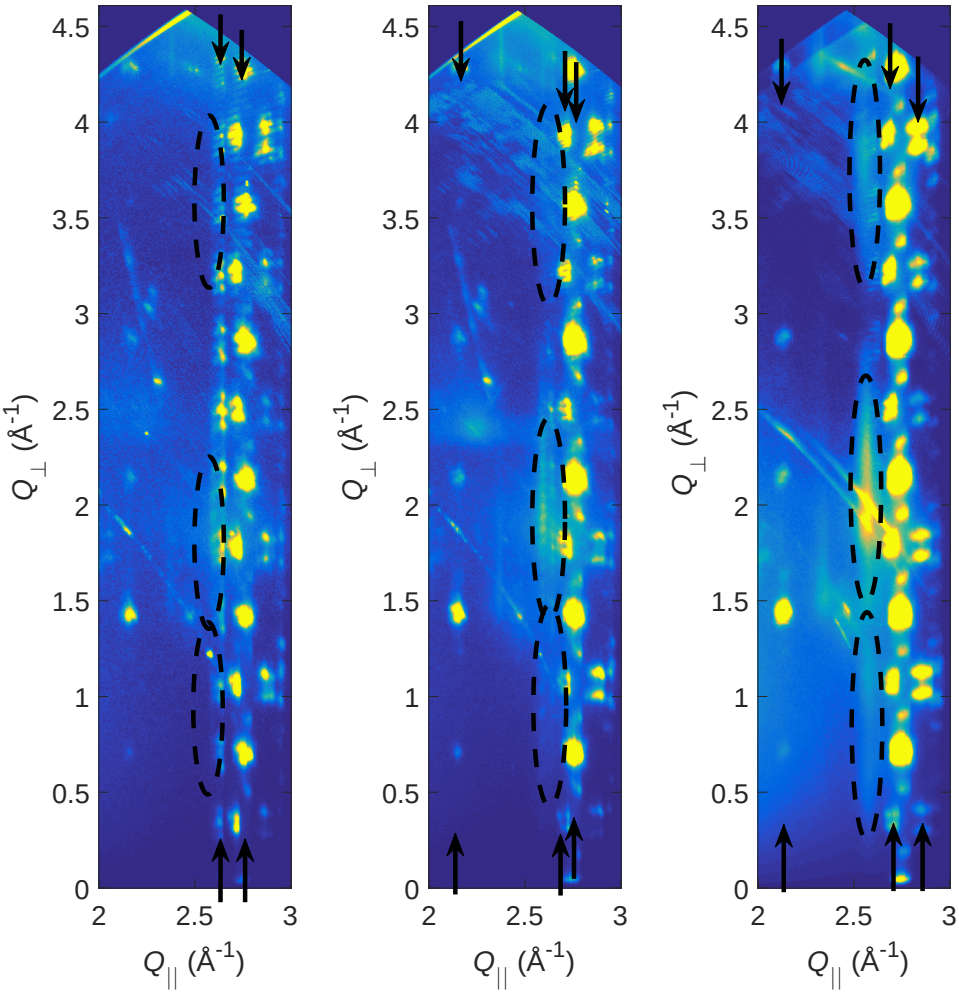

(a) As-prepared.

(b) Electrochemical conditioning 0.05-1.05 V vs. RHE.

(c) Electrochemical conditioning 0.05-1.30 V vs. RHE.

Figure 8.9: The figure shows a small section of Q-space with the $\pm 5°$ rotated overlayer diffraction spots. To obtain these images the intensity was integrated over ϕ_c=3°-7°. Besides the overlayer diffraction peaks indicated by the ellipses the images show columns of peaks from the Pt_5Y alloy. This overlayer only appears after the second electrochemical conditioning.

second conditioning, although it is very weak.

30° rotated	V_{max} = 1.05 V vs. RHE	V_{max} = 1.30 V vs. RHE
Strain ∥ (%)	-1.4±0.2	-
Strain ⊥ (%)	-2.3±0.9	-
D ∥ (Å)	42±3	-
D ⊥ (Å)	5.1±0.1	-
Not rotated		
Strain ∥ (%)	-0.5±0.2	0.2±0.5
Strain ⊥ (%)	-3±4	-1.4±2.6
D ∥ (Å)	61±1	75±5
D ⊥ (Å)	9.7±0.1	16±0.6

Table 8.4: The table shows the in-plane and out-of-plane strain of the overlayer relative to bulk Pt, as well as the crystallite size of the of the overlayer. These parameters have been calculated from the fitting parameters of 2D Gaussian and Lorentzian peak shapes to the overlayer diffraction peaks. The strain has been calculated from the center position of the diffraction peaks relative to that of the Pt(111) substrate, and the crystallite size have been calculated from the full width at half max (FWHM) using Scherrer's formula (equation (6.26)).

The rotated and not rotated overlayers were quantified by fitting 2D Gaussian and

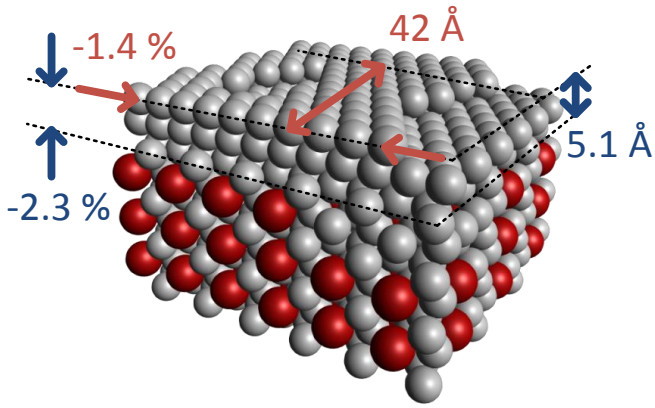

Figure 8.10: The figure shows the unit cell parameters and crystallite dimensions obtained for the rotated overlayer after the first electrochemical conditioning. It is seen that there is a strong in-plane and out-of-plane compression. The figure is adapted from [77].

Lorentzian peak shapes to all the overlayer peaks, where the position gives the unit cell parameters and the widths give the crystallite dimension through the Scherrer equation (equation (6.26)). For a thin platelet a shape factor of $K = 0.886$ is used [133]. The $\pm 5°$ rotated overlayer was too weak to fit properly, and so it cannot be quantified. The fitting results for the rotated overlayer after the first conditioning is shown in figure 8.10. The full quantification for both overlayers is seen in table 8.4.

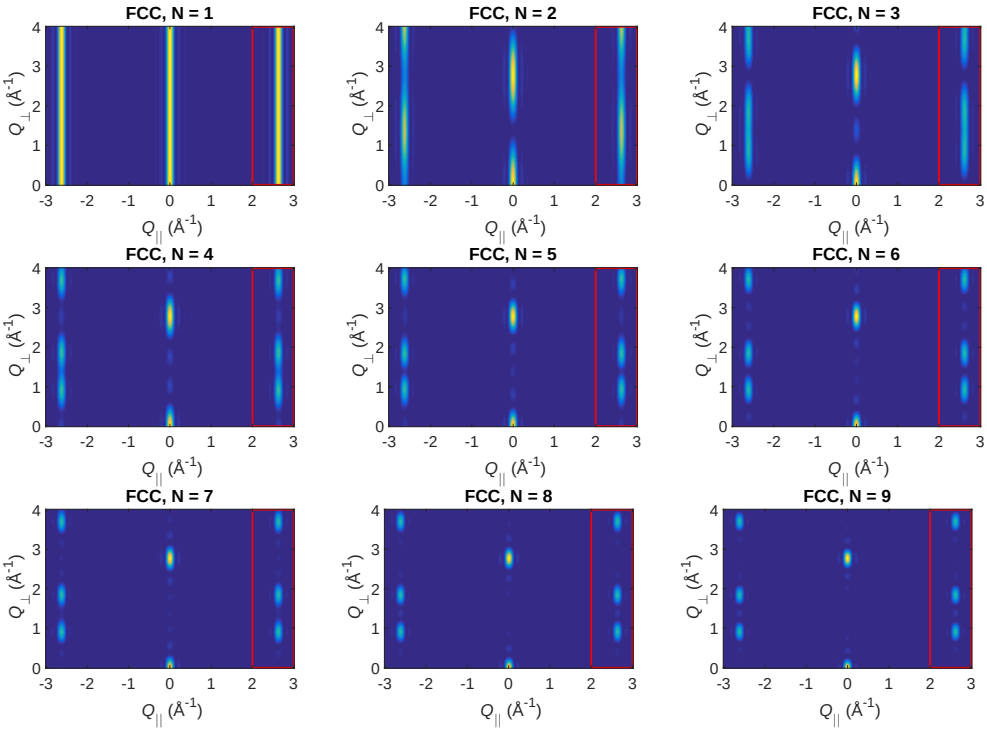

Figure 8.11: The figure shows a simulation of the diffraction peaks from a Pt overlayer with the FCC structure, while varying the number of atomic layers from 1 to 9. In the simulation it is assumed that there are 60° rotated domains like the sample has. A wide range of scattering vector components are shown, but in the images from the measurements above only the section in the red rectangle is shown.

The rotated overlayer shows a strong compression both in-plane and out-of-plane, and this is perhaps why it is less stable than the not rotated overlayer and does not withstand the harsh conditions when going to higher potentials. This high in-plane strain explains why this alloy is active for the ORR, and in that case it is clear that the catalytic improvement over pure Pt completely disappears when exposing the sample to very high potentials. The out-of-plane crystallite size can be interpreted

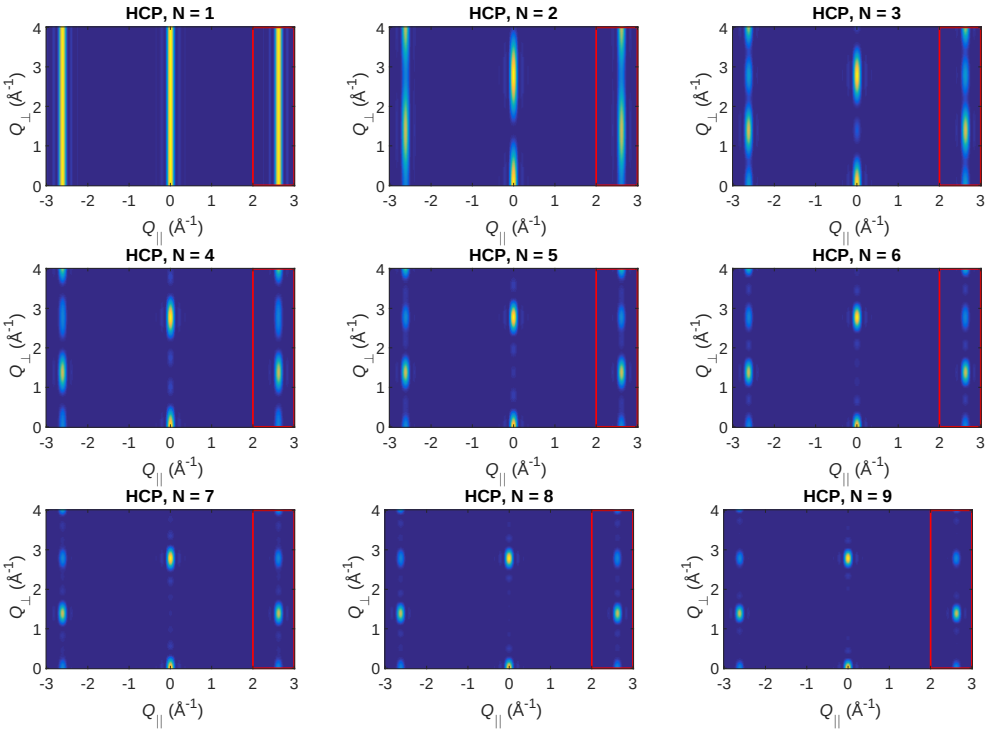

Figure 8.12: The figure shows a simulation of the diffraction peaks from a Pt overlayer with the HCP structure, while varying the number of atomic layers from 1 to 9. In the simulation it is assumed that there are 60° rotated domains like the sample has. A wide range of scattering vector components are shown, but in the images from the measurements above only the section in the red rectangle is shown.

as the thickness of the overlayer, assuming there are no non-epitaxial or amorphous atomic layers in the overlayer as well. Under these assumptions the rotated overlayer is about 3 atomic layers thick, whereas the not rotated layer is 5 atomic layers thick. Upon cycling to higher potentials the not rotated layer grows in thickness up to 8-9 layers. The number of layers in the overlayer can also be estimated from a visual comparison with a simulation of the diffraction peaks from the overlayer only, as seen in figure 8.11 that shows the simulation of an FCC structured Pt overlayer with 1 to 9 atomic layers.

With simulations we can also verify that the overlayer does not have the hexagonal close packing (HCP), which only differs from FCC in the stacking order. A similar simulation series of a thin Pt overlayer with 1 to 9 atomic layers with the HCP stacking order is seen in figure 8.12. It is immediately clear that the FCC structure

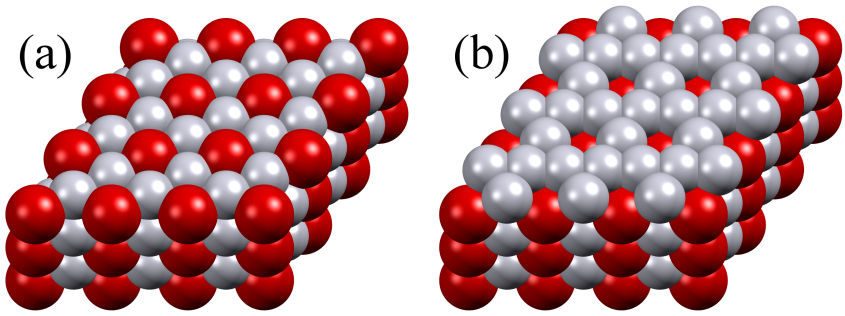

Figure 8.13: The figure shows the two layers of the Cu_5Ca structure, of which the pure Pt layer displays a kagome type pattern. It is quite possible that when the Y leeches out during the formation of the overlayer one or more of the layers maintain this kagome structure. (a) shows the mixed hexagonal layer and (b) shows the pure Cu (Pt) layer with a kagome type structure.

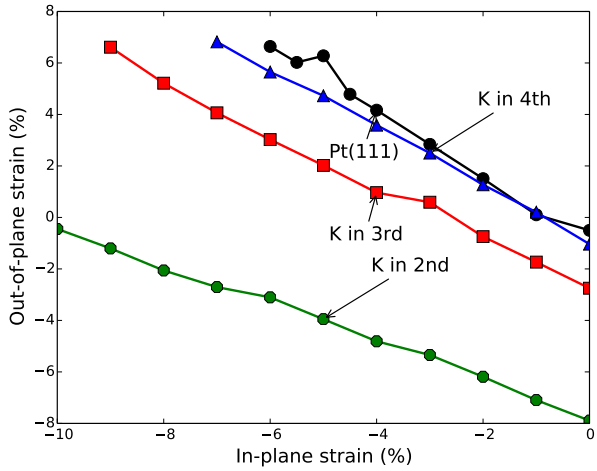

Figure 8.14: The figure shows the calculated out-of-plane strain as a function of in-plane strain for a range of structures. It is clearly seen that if the second or third layer from the top is a kagome layer it is possibly to have a reduction of the unit cell volume. K is for kagome. The figure is from [144], *these calculations have been done by Martin Hangaard Hansen.*

matches the measurements much better.

For both the rotated and not rotated overlayer it is seen that both the in-plane and out-of-plane components show compression. This may seen counterintuitive as such a large change in unit cell volume is unfeasible. The alloy structures of Pt_5Y and Pt_5Gd are closely related [83], and as discussed above they are related to the Cu_5Ca structure. This structure has layers of so-called kagome lattices as shown in figure 8.13. It is possible that when the Y leeches out from the surface the remaining structure could contain such a layer. And DFT calculations [144] show that it is indeed favorable to have a contraction both in-plane and out-of-plane if the second or third layer from the surface is a kagome layer, as seen in figure 8.14.

Having kagome layers in the overlayer changes the structure, and therefore changes the diffraction pattern. We have simulated 64 different overlayer configurations, and about half of them show diffraction patterns similar to the FCC pattern that was measured. There are additional features in the diffraction pattern from these overlayers, but they are much weaker than the main peaks, and so we are unable to detect them. Some selected diffraction patterns are shown in figure 8.15, but here the color scale is logarithmic spanning 4 orders of magnitude in intensity, and most features are 3 orders of magnitude lower intensity than the main peaks.

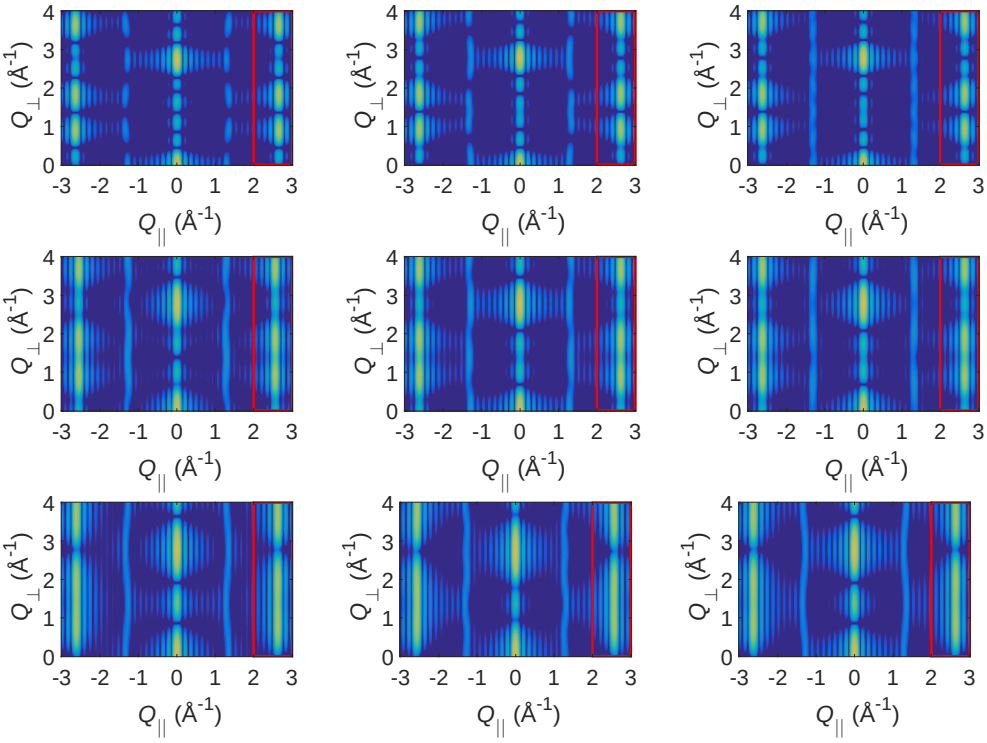

Figure 8.15: The figure shows a simulation of the diffraction peaks from a Pt overlayer including one or more kagome layers. In the simulation it is assumed that there are 60° rotated domains like the sample has. A wide range of scattering vector components are shown, but in the images from the measurements above only the section in the red rectangle is shown. The color scale is logarithmic and spans 4 order of magnitude of intensity, and most features are 3 orders of magnitude weaker than the main peaks.

8.3 Pt overlayer on Gd/Pt(111) model system

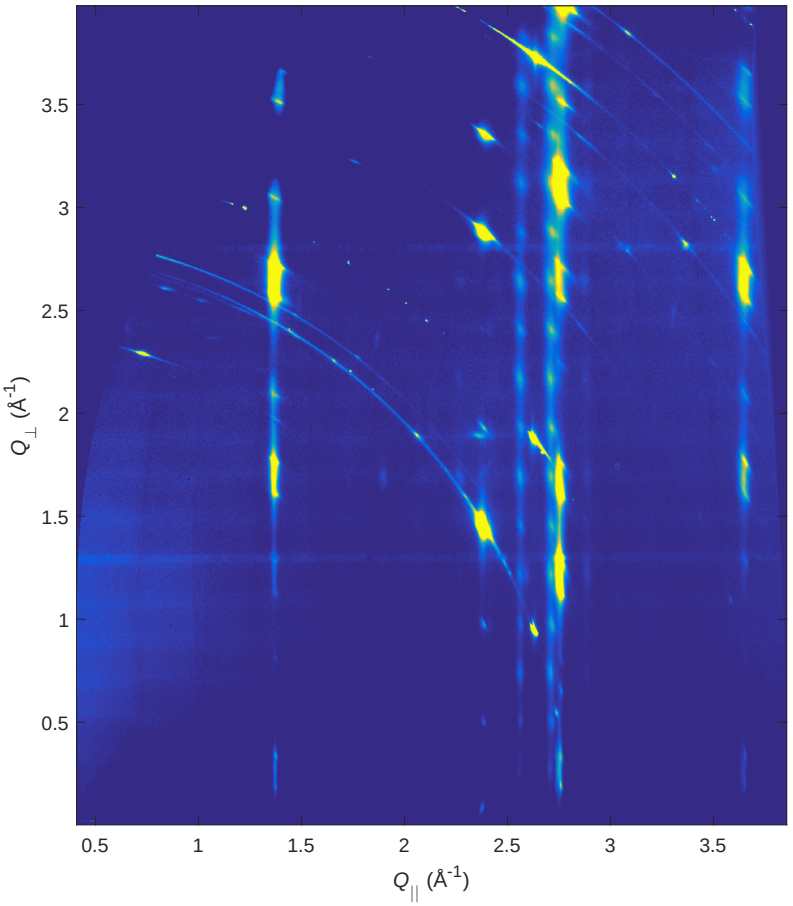

Figure 8.16: The figure shows an overview of the diffraction pattern from the as-prepared Gd/Pt(111) sample. The image is obtained by rotating the crystal 360° around the ϕ axis during a single exposure. Since the detector is narrow this image has been stitched together from 6 exposures with different detector position. The black circles indicate the Pt(111) substrate diffraction spots, and they are (1,0,1), (0,1,2), and (1,0,4) or symmetrically equivalent, using the hexagonal surface unit cell. All the remaining peaks are from the Pt_5Gd alloy phase.

The Gd/Pt(111) sample was also measured ex-situ, but this time at BL7-2 equipped with a Pilatus 300K detector. The much faster detector allowed the collection of full 360° survey data sets in reasonable time. Again a laser was used to align the crystal

surface normal to the ϕ rotation axis. And to maintain a high surface sensitivity the incidence angle was fixed at 0.2°. An overview of the the diffraction when the sample is rotated 360° in a single exposure is seen in figure 8.16.

The crystal was brought to the beam line as-prepared and measured, and conditioned in an electrochemical cell next to the beam line. The first round of conditioning consisted of 1461 cycles between -0.1 and 0.8 V vs. RHE and 125 cycles from 0.0 to 1.00 V vs. RHE. After measuring a second XRD survey data set the second electrochemical conditioning was 106 cycles from 0.0 to 1.10 V vs. RHE and 98 cycles from 0.0 to 1.20 V Vs. RHE.

Upon the first conditioning up to 1.00 V vs. RHE the overlayer was observed. On this sample only a single overlayer appeared, and it was rotated by 30°, just as the alloy was rotated by 30° on this sample. This model system also shows a 50/50 chance of whether the alloy is rotated or not after Gd deposition. After the second electrochemical conditioning up to 1.20 V vs. RHE the overlayer remained, and no other overlayers formed. As seen in figure 8.17 the diffraction peaks are quite elongated in the out-of-plane direction, again indicating a thin overlayer. In this case from visual comparison the overlayer may be 4-5 atomic layers thick, and does not change thickness after the second conditioning. The structure of the overlayer looks like FCC like on the Y/Pt(111) overlayers, but as discussed above the presence of kagome layers in the overlayer cannot be excluded.

Again the overlayer lattice parameters were quantified, and the results after the first conditioning is shown in figure 8.18. Here it is seen that the overlayer has a small in-plane compression but an out-of-plane expansion. This is more in line with what would be expected for a pure FCC structured overlayer, however kagome layers may still be present in the 4th layer from the surface according to figure 8.14. The fitting results after both electrochemical conditionings are shown in table 8.5.

30° rotated	$V_{\max} = 1.00$ V vs. RHE	$V_{\max} = 1.20$ V vs. RHE
Strain $\parallel$ (%)	-0.31±0.05	-0.07±0.07
Strain $\perp$ (%)	0.2±0.4	1.1±0.7
D $\parallel$ (Å)	96±5	105±3
D $\perp$ (Å)	10.9±0.3	101.8±0.3

Table 8.5: The table shows the in-plane and out-of-plane strain of the overlayer relative to bulk Pt, as well as the crystallite size of the of the overlayer. These parameters have been calculated from the fitting parameters of 2D Gaussian and Lorentzian peak shapes to the overlayer diffraction peaks. The strain has been calculated from the center position of the diffraction peaks relative to that of the Pt(111) substrate, and the crystallite size have been calculated from the full width at half max (FWHM) using Scherrer's formula (equation (6.26)).

For the Gd/Pt(111) overlayer it is also seen that going to higher oxidative potentials the overlayer relaxes completely, having the same lattice parameter as bulk

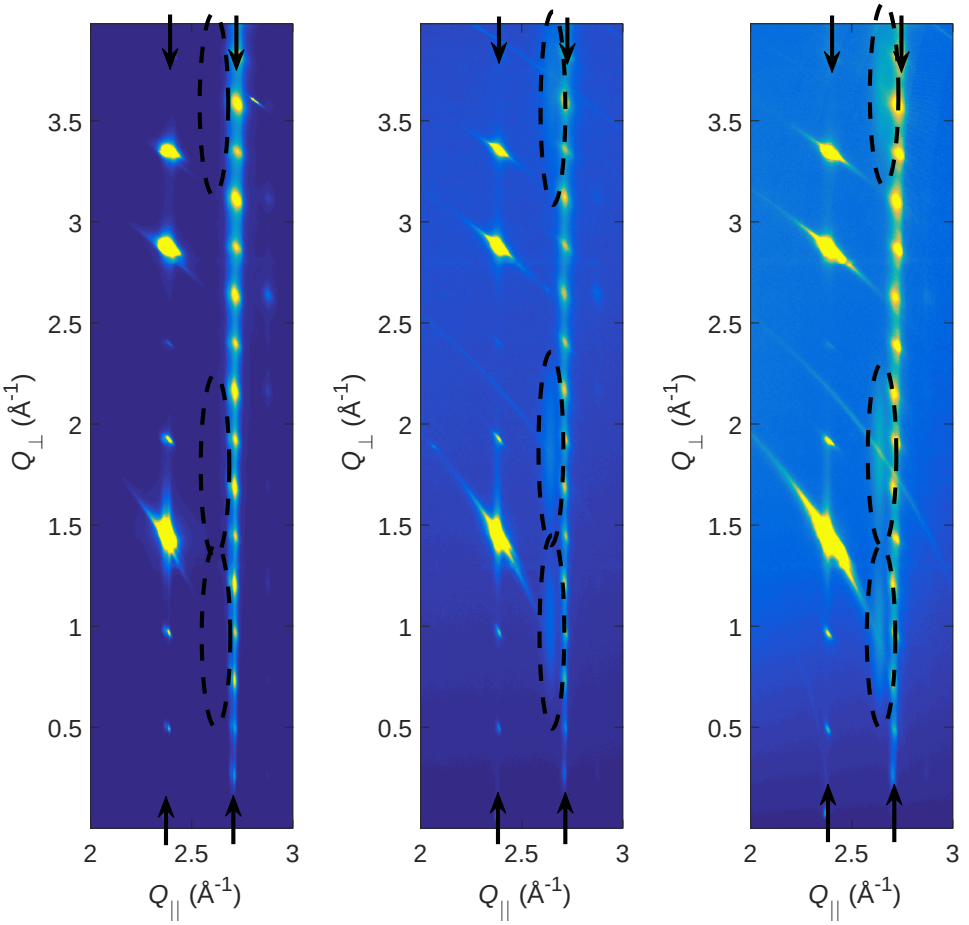

(a) AP **(b)** EC1 **(c)** EC2

Figure 8.17: The figure shows the rotated overlayer diffraction spots before and after the electrochemical conditioning. In these images only the section with the overlayers have been integrated, so ϕ_c =28°-32°. The diffraction from the overlayer is indicated by the ellipses, and the diffraction spots in the other columns are from the Pt_5Gd alloy.

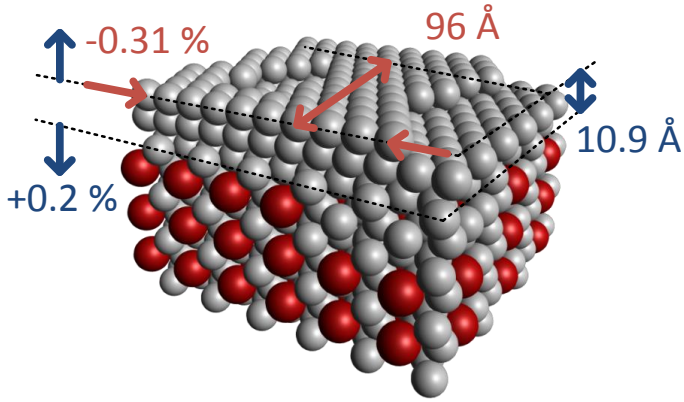

Figure 8.18: The figure shows the fitting results for the rotated overlayer on the Gd/Pt(111) sample after the first conditioning up to 1.0 V vs. RHE. On this sample only a small in-plane compression is observed, whereas there is an out-of-plane expansion. The figure is adapted from [77].

Pt.

It is worth noting that the strain measured on both the Gd/Pt(111) and Y/Pt(111) vary significantly, even though they show the same activity. Here it is important to mention that the strain values reported are the average values for the entire overlayer, and in the peak shape analysis only crystallite size was considered. It is perhaps more realistic to imagine that the width of the diffraction peaks reflect a combination of crystallite size and microstrain, which represents a variation of strain across the different domains. These two effects cannot be distinguished from the data sets collected, but by adding or subtracting half width at half max (HWHM) of the peak width from the peak position the microstrain may be estimated. For the rotated overlayer on Gd/Pt(111) the in-plane strain could range from -1.39% to +0.79% after the first conditioning up to 1.00 V vs. RHE and -1.06% to +0.94% after the second conditioning up to 1.20 V vs. RHE. Similarly the rotated overlayer on Y/Pt(111) could have a strain ranging from -3.78% to +1.02% after conditioning up to 1.05 V vs. RHE, and the unrotated overlayer could range from -2.17% to +1.20% and -1.19% to +1.61% after the first and second conditioning up to 1.05 and 1.30 V vs. RHE, respectively. With these wide ranges of microstrain one might imagine that the activity of the surface is dominated by a part of the surface with a high compression, and the fraction of highly active sites could be the same on both Gd/Pt(111) and Y/Pt(111). Figure 8.19 shows the activity of these model systems as a function of both strain and measured OH binding energy in relation to the theoretical volcano for activity and other Pt(111)-based model systems. It is seen that the average strain

underestimates actual strain that would explain the activity improvement, whereas the OH binding energy measured by cyclic voltammetry overestimates the change in binding energy.

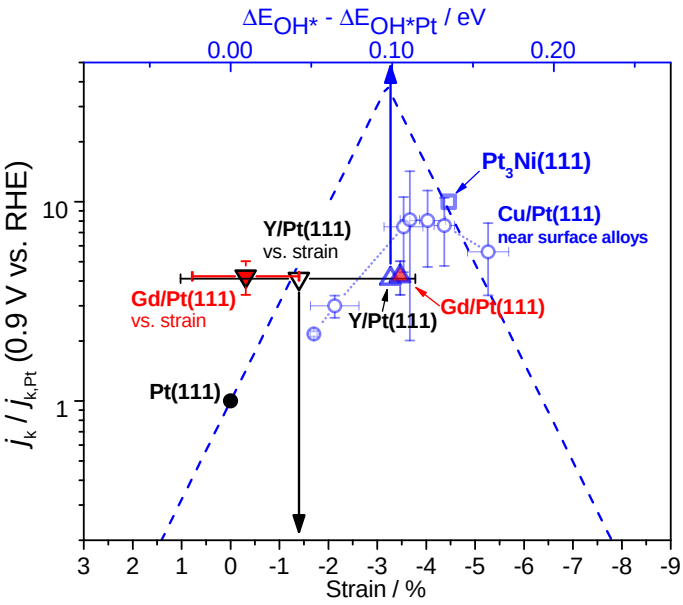

Figure 8.19: The figure shows the thermodynamic volcano plot for ORR as a function of the OH binding energy, neglecting any kinetic barriers, and the volcano is from [145]. The OH binding energy has correlated to the in-plane strain by DFT calculations, and are from [78]. The black triangles show the activity of Gd/Pt(111) and Y/Pt(111) as a function of the rotated overlayer strain, and the strain error bars represent the microstrain. The blue triangles show the activity of Gd/Pt(111) and Y/Pt(111) as a function of the OH binding energy estimated by cyclic voltammetry. The square shows the activity of $Pt_3Ni(111)$ from [146], and the circles show the activity of a series of Cu/Pt(111) near surface alloys [48]. The figure is from [77], *the OH bond energy shift was calculated with DFT by Martin Hangaard Hansen and the experimental bond energy shift was measured by Maria Escudero-Escribano.*

8.4 Pt overlayer formation and evolution on Gd/Pt(111)

After the ex-situ experiments we got to understand the structure of the overlayer better, but questions still remained in terms of which conditions forms the overlayer. Therefore we designed a set of in-situ experiments in which we would selectively monitor the overlayer peaks only, thus allowing the unit cell to be measured under many different conditions. Surface sensitive XRD is also highly applicable for other systems in which surface changes can me tracked in-situ [147].

The experiment was done at BL7-2 with a Pilatus 300K area detector, and we used the hanging meniscus cell described in section D.1. Instead of doing a survey scan the intensity was integrated directly by rocking the ϕ motor in a $\pm 5^\circ$ range at the position of overlayer peaks. But since the ϕ_c angle varies across the detector, this angular range only covered the $L = 1$ or $L = 2$ peaks from the overlayer (using the hexagonal surface unit cell). Figure 8.20 shows a representative image of an overlayer and Pt(111) substrate (1,0,1) peak. The substrate peak is visible here since the overlayer and alloy were not rotated relative to the substrate on this sample.

For this experiment two Gd/Pt(111) single crystal were fabricated and brought to the beam line. On one sample we measured the overlayer diffraction pattern immediately after exposing the sample to the electrolyte under open circuit conditions. We subsequently cycled the potential to gradually higher maximum potentials, recording the diffraction pattern at each step. On this sample both the overlayer and alloy was rotated by 30° from the Pt(111) substrate, as observed in the ex-situ experiment. Figure 8.21 shows the in-plane and out-of-plane strain as a function of cycling potential. As mentioned above the first data point was measured at open circuit conditions, and it is immediately seen that the overlayer has already formed, and the diffraction pattern was the same as observed in the ex-situ experiment. The second measurement was after cycling from 0.0 to 1.0 V vs. RHE, and diffraction measurements were acquired while fixing the potential at 0.1, 0.5, and 0.9 V vs. RHE. This process was repeated after cycling from 0.0 to 1.20 and 1.25 V vs. RHE. Due to time limitations the diffraction measurements were done while cycling the potential in the range 0.0 to 1.3, 1.4, 1.5, and 1.6 V vs. RHE. Figure 8.22 shows the crystallite sizes measured under the same conditions. The crystallite size were estimated from the FWHM of the diffraction peaks, neglecting any broadening from microstrain.

Overall it is noted that the in-plane strain is similar to what was measured ex-situ, whereas the out-of-plane strain is compressive on the sample, indicating the presence of kagome layer(s) in the overlayer. Furthermore, this overlayer is thicker, which could be related to the different structure of the overlayer. The overlayer forms at open circuit conditions, and remains stable while cycling up to 1.0 V vs. RHE. At 1.20 V vs. RHE the strain relaxes, and a large spread is seen in both the strain and crystallite size depending on whether the diffraction was obtained at 0.1, 0.5, or 0.9 V vs. RHE. This behavior might be linked to the relaxation process happening exactly at this potential, since the measurements after cycling up to 1.25 are stable

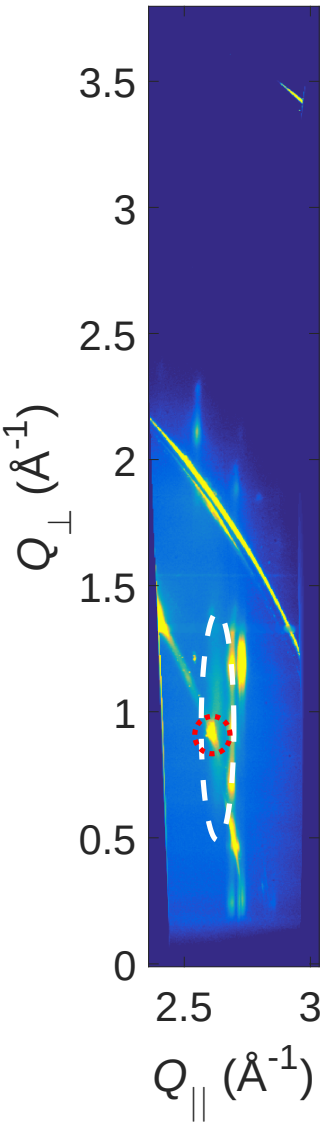

Figure 8.20: The figure shows a representative image from the Pilatus detector when capturing the overlayer peak. The overlayer peak is indicated by the white ellipse and a Pt(111) substrate peak is indicated by the red circle. All the remaining peaks are from the Pt_5Gd alloy phase. Because of the variation in ϕ_c across the detector image, only the $L = 1$ diffraction peaks are visible in the angle range used here.

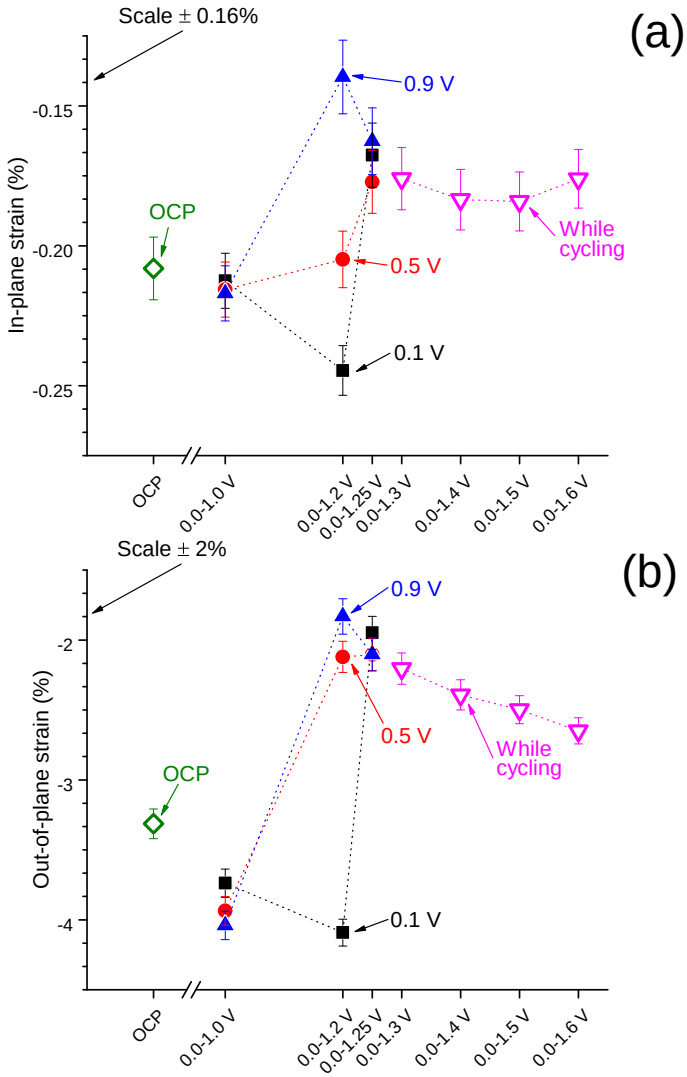

Figure 8.21: The figure shows the in-plane (a) and out-of-plane (b) strain of the Pt overlayer relative to bulk Pt as a function of electrochemical potential cycling conditions. The first measurement was done at open circuit conditions, and it is seen that the overlayer has already formed. The following measurements were done after cycling from 0.0 to 1.0, 1.2, and 1.25 V vs. RHE, and the diffraction patterns were acquired after each cycling procedure while keeping the potential fixed at 0.1, 0.5, and 0.9 V vs. RHE. Due to time limitations the diffraction measurements when cycling 0.0 to 1.3, 1.4, 1.5, and 1.6 V vs. RHE were done while cycling the electrochemical potential.

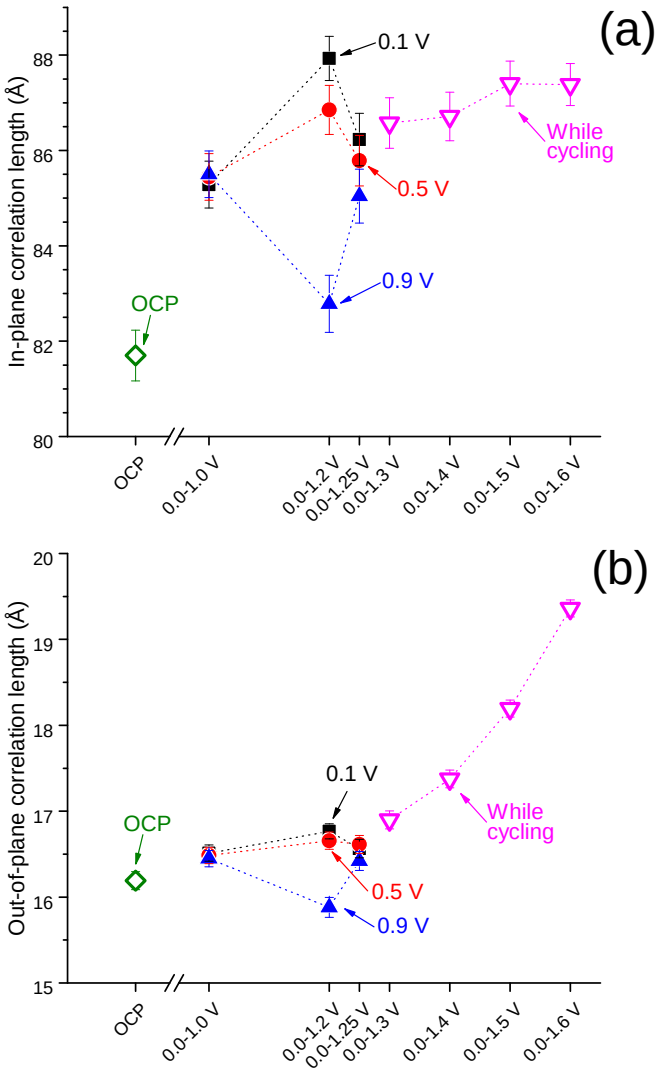

Figure 8.22: The figure shows the in-plane (a) and out-of-plane (b) crystallite size of the Pt overlayer as a function of electrochemical potential cycling conditions. The first measurement was done at open circuit conditions, and it is seen that the overlayer has already formed. The following measurements were done after cycling from 0.0 to 1.0, 1.2, and 1.25 V vs. RHE, and the diffraction patterns were acquired after each cycling procedure while keeping the potential fixed at 0.1, 0.5, and 0.9 V vs. RHE. Due to time limitations the diffraction measurements when cycling 0.0 to 1.3, 1.4, 1.5, and 1.6 V vs. RHE were done while cycling the electrochemical potential.

and shows a more relaxed overlayer. Going to higher potentials the strain and in-plane crystallite size remains constant, whereas the out-of-plane crystallite size, and presumably thickness, increase above 1.3 V vs. RHE.

The other sample that was brought to the beam line turned out to have a non-rotated alloy and overlayer. For this sample the electrochemical potential was cycled in the ranges 0.0 to 0.6, 0.8, and 1.0 V vs. RHE, with the diffraction pattern measured in between each set of cycles. After this point the potential was only cycled in the range 0.6 to 1.0 V vs. RHE for an extended number of cycles, measuring the diffraction at different intervals up to 8000 cycles had been completed. At most points the diffraction was measured at 0.1, 0.5, and 0.9 V vs. RHE, but again because of time restrictions the diffraction was also measured while cycling. In the initial measurements when only cycling up to 0.6 and 0.8 V vs. RHE, the diffraction measurements were not done at 0.9 V vs. RHE, but rather 0.6 and 0.8 V vs. RHE, respectively. The strain during this procedure is seen in figure 8.23 and the crystallite size is shown in figure 8.24. There are no significant changes whether the potential is fixed at 0.1, 0.5, or 0.9 V vs. RHE, and it is therefore assumed that the data points obtained during cycling are no different.

In this experiment we see that the in-plane strain is higher than for the other sample, which could be caused by the overlayer not being rotated. Furthermore, the overlayer is also thinner than on the other two Gd/Pt(111) samples measured, which seems to sustain a higher in-plane strain. The out-of-plane strain is also compressive, again indicating the presence of kagome layer(s). During the cycling the in-plane strain relaxes slightly, with most of the relaxation occurring during the first 2000-3000 cycles. The relaxation of the strain correlates with a decrease in activity observed on the nanoparticles and polycrystalline alloys [78], and in particular the nanoparticles also show the greatest loss of activity with initial cycling. The out-of-plane strain and crystallite sizes remain constant during this cycling procedure. At the end of the experiment the electrolyte in the cell was replaced, exposing the crystal surface to air, and the overlayer seems to be completely stable.

Furthermore, this sample showed a high degree of miscut. The sample was aligned with a laser to the surface normal, and the accuracy is estimated to be within 0.1°. However, the Pt(111) substrate was found to be tilted by 1.10°, the alloy was tilted by 1.28°, and the overlayer was tilted 1.60°. These tilt angles and the angles relative to the Pt(111) substrate is shown in table 8.6. The tilt of the Pt(111) substrate could be caused by an error in the polishing of the crystal, so that the surface is not parallel to the Pt(111) plane. The miscut of the substrate then seems to propagate into the alloy and overlayer, getting an even higher tilt angle in the same direction. Since this tilt has not been observed on any other sample, it is suspected to be related to the initial miscut of the Pt(111) substrate. The tilt of the alloy and overlayer can be a simple further tilt in the same direction, but it could also represent a monoclinic distortion of the hexagonal unit cell, forcing the α and/or β angles to deviate from 90°. The acquired data is insufficient to distinguish these two cases, but either way may be a mechanism for accommodating the strain.

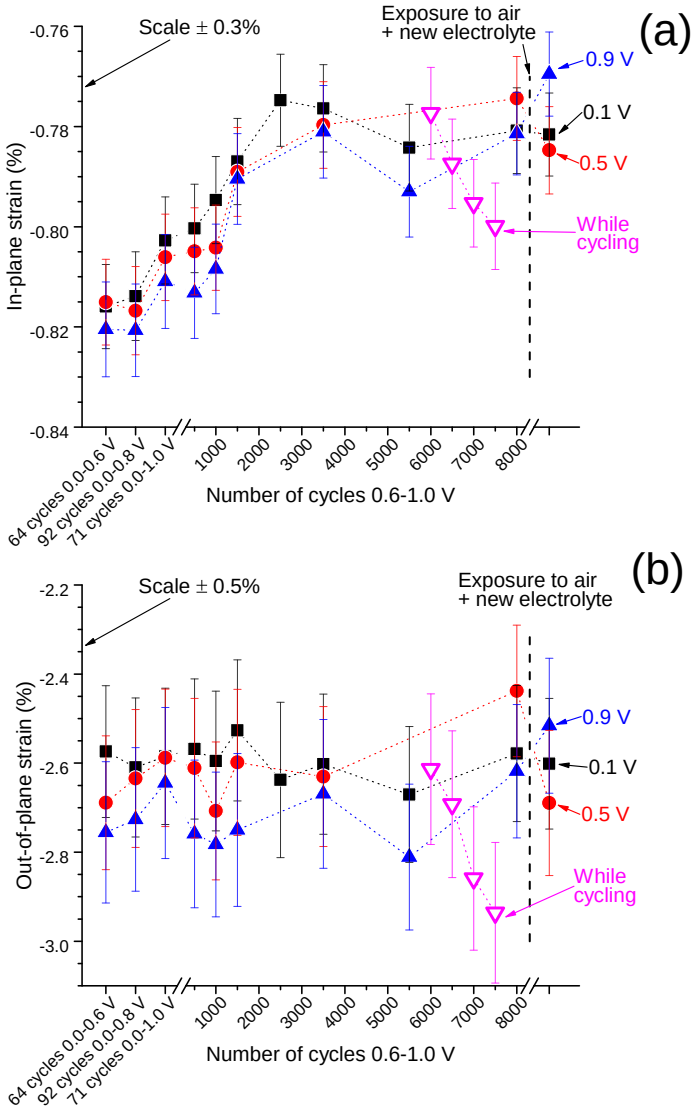

Figure 8.23: The figure shows the in-plane (a) and out-of-plane (b) strain of the Pt overlayer relative to bulk Pt as a function of electrochemical potential cycling conditions. The initial cycles were done from 0.0 to 0.6, 0.8, and 1.0 V vs. RHE, and all the following measurements were done at different number of cycles between 0.6 and 1.0 V vs. RHE. The diffraction measurements were done at certain point up to 8000 cycles.

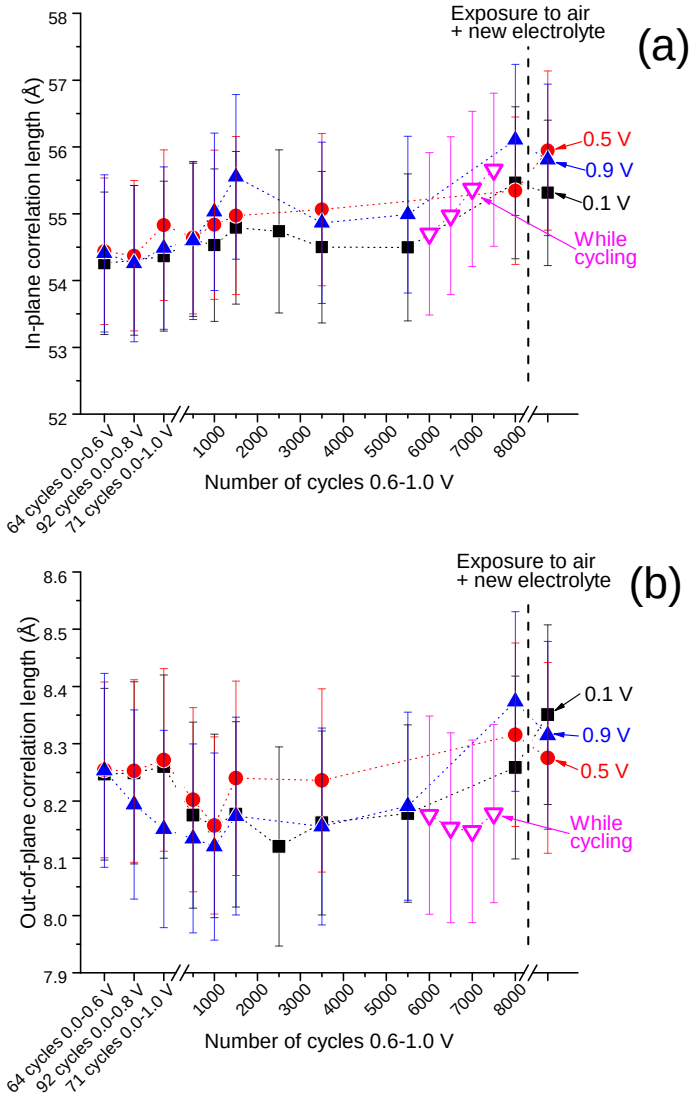

Figure 8.24: The figure shows the in-plane (a) and out-of-plane (b) crystallite size of the Pt overlayer as a function of electrochemical potential cycling conditions. The initial cycles were done from 0.0 to 0.6, 0.8, and 1.0 V vs. RHE, and all the following measurements were done at different number of cycles between 0.6 and 1.0 V vs. RHE. The diffraction measurements were done at certain point up to 8000 cycles.

Layer	Tilt vs. surface normal (±0.1°)	Tilt vs. Pt(111) substrate
Pt(111) substrate	1.10°±0.02°	-
Pt_5Gd alloy	1.28°±0.001°	0.18°±0.02°
Pt overlayer	1.60°±0.05°	0.50°±0.07°

Table 8.6: The table shows the amount of tilt of the Pt(111) substrate, the Pt_5Gd alloy, and the Pt overlayer. The tilt angles are all in the same direction, and are shown both relative to the surface normal and the Pt(111) substrate.

8.5 Gd/Pt(111) alloy crystal structure

In order to understand and control the overlayer it is also important to understand the structure of the underlying alloy. As discussed several times above the structure of Pt_5Gd has remained elusive. Early attempts [83] on powders indicated that the structure is related to the Cu_5Ca structure, but it was not identical to that structure, as more diffraction peaks were present. Attempts at measuring the structure of a polycrystalline Pt_5Gd crystal at our lab revealed a similar pattern, it has the peaks expected from the Cu_5Ca structure plus additional peaks.

Therefore we also used the data collected when measuring the Q-space surveys of the ex-situ Gd/Pt(111) crystal to try to determine the structure. The benefit of having a single crystal over a powder or a polycrystalline sample is the ability to reconstruct the reciprocal lattice in 3 dimensions, rather than only having the magnitude of Q for each peak. A caveat worth mentioning is the fabrication method of this single crystal, which may result in a different crystal structure than the polycrystalline sample.

For the production of a thick alloy approximately 200 Å of Gd was evaporated onto the Pt(111) substrate, forming a Pt_5Gd alloy approximately 63 nm thick. In the following analysis we used the data obtained from the as-prepared sample, although the formation of the overlayer and surface treatment should not have an effect on such a thick alloy film.

The first step in determining the structure was to identify the unit cell. From the 3D reciprocal space map we quickly identified columns of closely spaced diffraction peaks along the z-direction (out-of-plane direction). By integrating the intensity along z we can see the in-plane structure of the reciprocal lattice, as seen in figure 8.25. Immediately a hexagonal symmetry is observed, and shown by red circles, similarly to that of Pt(111), indicated by black circles. The reciprocal lattice vector H and K are shown, whereas the L vector points out of the plane. When studying the low intensity peaks it is seen that a large number of closely spaced peaks are seen around the main hexagonal peaks indicated by red circles. These peaks are interpreted as superspots, indicating a large number of small domains that are twinned by merohedry (overlapping diffraction peaks). Furthermore, it is seen that the main peaks in the

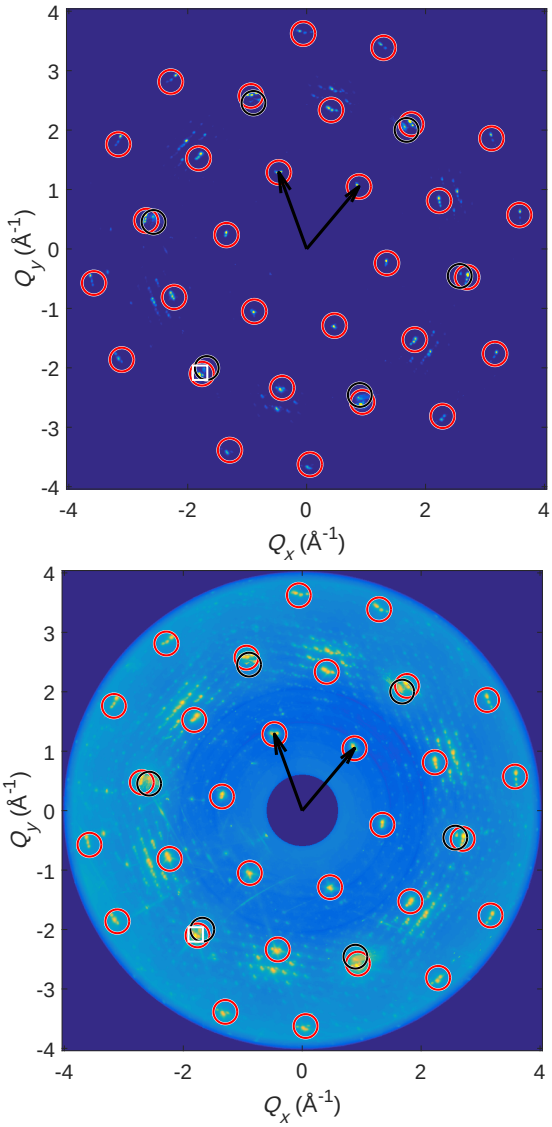

Figure 8.25: The figure shows the reciprocal space integrated along the L direction, which is the surface normal and the z-axis. The in-plane reciprocal vector H and K are shown with the black arrows. The red circles show the main peaks from the Pt_5Gd alloy forming a hexagonal lattice, and the black circles show the Pt(111) substrate peaks. The top and bottom panel show the intensity on a linear and logarithmic color scale, respectively. On the bottom panel a large number of super-spots are seen, indicating the alloy consists of many small domains. The figure is from [74].

red circles are actually split into three peaks very close to each other, showing non-merohedral twinning. Figure 8.26 shows a zoom of the area in the white square, showing the three close peaks from the alloy and a Pt(111) substrate peak that has no splitting. This means that the splitting into slightly rotated domains only takes place inside the alloy.

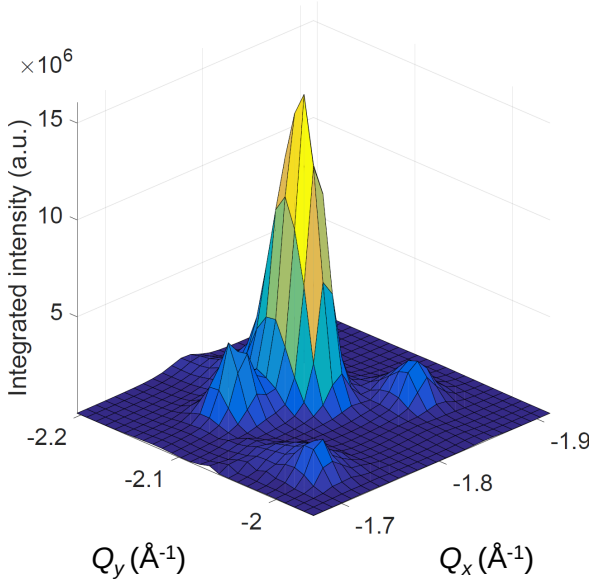

Figure 8.26: The figure shows the diffraction peak indicated by a white square in figure 8.25. The alloy diffraction peak is seen to be split into three peaks, whereas the Pt(111) substrate at lower Q_x and Q_y values is not split. The figure is from [74].

The main alloy peaks were fitted by a pseudo-Voigt profile shape, and the distance between the peaks revealed the hexagonal lattice parameters are $a = 5.3309 \pm 0.0008$ Å and $c = 40.358 \pm 0.012$ Å. Using Scherrer's formula, equation 6.26, with a shape factor of 1, the crystallite size is estimated to be 22 nm in-plane and 12 nm out-of-plane. Here any broadening due to microstrain has been neglected, so these numbers are minimum estimates. This crystallite size is consistent with the super-spots, since the coherence length of the X-ray beam is on the order of 1 µm, and will illuminate a large number of crystallites coherently.

To determine the structure the integrated intensity at each measured reciprocal lattice point is determined. The main alloy peaks are integrated, and because the non-merohedral twins have peaks very close together it was not possible to separate them and they were all integrated as a single peak. During the processing of the data set the background was subtracted, and no further background subtraction was needed

when extracting the integrated intensities. The error of the integrated intensity was estimated from the typical background of 10 counts per second for each voxel. The in-plane reciprocal lattice indices (H and K) ranged from (1,0) to (2,1), and the L index ranged from 1 to 24, although the six columns with the lowest in-plane lattice vector were cut off at 21 or 22 due to the low incidence angle. And due to the fixed incidence angle it was not possible to record the specular diffraction spots, (00L). The total list of integrated intensities has 705 diffraction peaks indexed.

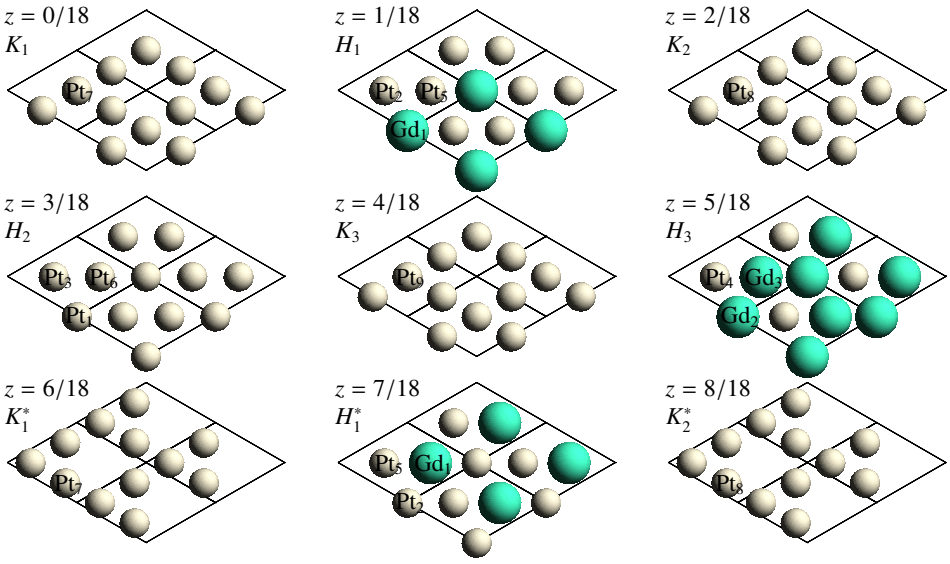

Figure 8.27: The figure shows the initial guess for the structure of Pt_5Gd alloy in the Gd/Pt(111) sample. Because of the symmetry the layers are repeated after 6 layers, which is seen as layer 7 is just a translation of layer 1. This unit cell has 54 atoms, but only 12 are unique, and they have been labeled here. The figure is from [74].

To find the space group and begin to solve the structure the program SHELXT was used [140]. This program finds possible space groups from the list of indexed diffraction peaks, and uses direct methods to try to find the structure. Due to the many small domains we expected 60° rotated twins to be present, which complicates to solution of the structure. Whether inputting information about twinning or not the program consistently found the space group to be R3m (space group number 160), but was unable to place any atoms on meaningful positions in the unit cell. This space group has rhombohedral symmetry, but it is compatible with representation in the more intuitive hexagonal unit cell. When trying to fill the unit cell we got inspiration from the Cu_5Ca structure discussed above, as well as a somewhat similar

structure found at high temperature of Pd_5Ce [148]. The length of the c-axis of the unit cell is equivalent to about 18 Pt(111)-like atomic layers, which fits well with the rhombohedral symmetry that reduces the asymmetric unit cell to just 6 layers. Combining structural features from the two structures mentioned, an initial guess was made, which is seen in figure 8.27. This structure consists of alternating kagome (K) and hexagonal (H) layers. The first 9 of the 18 layers are shown, but only 6 of the layers are unique; the seventh layer (at height $z = 6/18$) is shifted by a third of the unit cell, the eighth layer is also shifted by a third of the unit cell, and so forth. All the kagome layers are similar, whereas the hexagonal layers have different elemental composition; there is a pure Pt layer (H_2), a Pt_2Gd layer (H_1), and a $PtGd_2$ layer (H_3). The Cu_5Ca structure is just a repetition of the first two layers (K_1 and H_1) in figure 8.27, but in this structure the shift of the layers is accompanied by a layer with two large Gd atoms next to each other, which are then displaced in the z-direction into the holes in the kagome layers above and below. The name kagome comes from a traditional woven bamboo basket pattern. Some of the atoms in these first six layers are generated from symmetry, so the 12 unique atoms are labeled in the figure.

Space group	$a(\alpha)$	$b(\beta)$	$c(\gamma)$
R3m	5.3309 Å	5.3309 Å	40.358 Å
160	90°	90°	120°
Atom	x	y	z
Gd_1	0	0	0.0380
Gd_2	0	0	0.2302
Gd_3	0	0	0.9250
Pt_1	0	0	0.1372
Pt_2	0	0	0.3500
Pt_3	0	0	0.4542
Pt_4	0	0	0.5520
Pt_5	0	0	0.6654
Pt_6	0	0	0.7642
Pt_7	0.5039	0.0078	0.9373
Pt_8	0.4983	0.9967	0.0516
Pt_9	0.4735	0.9470	0.1857

Table 8.7: The table shows the space group symbol and number, the unit cell parameters, and the fractional coordinates of the 12 unique atoms in the unit cell of the refined structure. The table is from [74].

To optimize the initial structure the program SHELXL was used [140], which is a least squares refinement based program. This program keeps atoms on their symmetry sites, and for example all the atoms in the hexagonal layers are on a 3a Wyckoff site, restricting motion to $(0, 0, z)$, whereas the kagome layers are generated by a single Wyckoff 9b site in each layer, that are found at $(x, 2x, z)$. Here x and z are fractional coordinates inside the unit cell. These atomic positions leave 12 unique

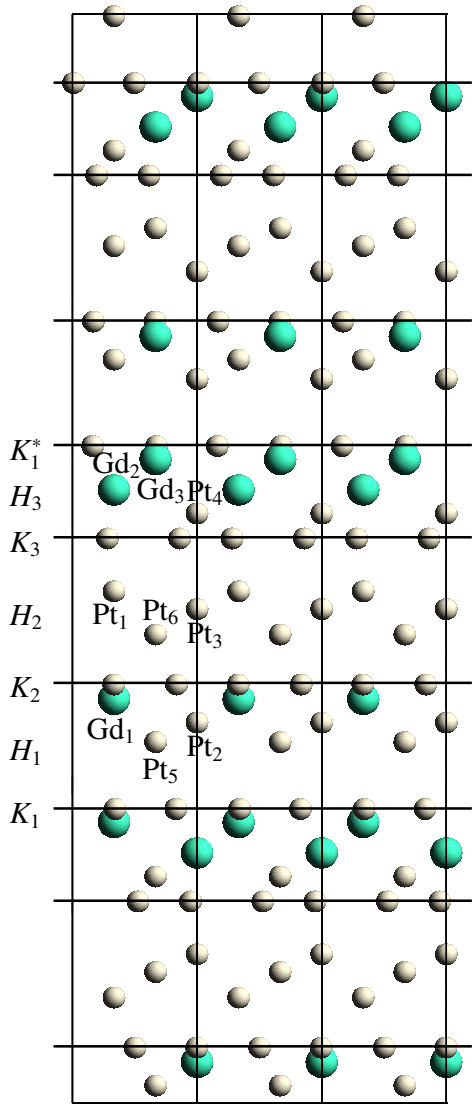

Figure 8.28: The figure shows the refined unit cell along the a-axis. The kagome layers are marked by black lines, and it is seen that the layers from the initial structure are still present, although more disordered. The figure is from [74].

atoms, 15 position parameters, generating 54 atoms in the entire unit cell. Before fitting the data the SHELXL program combines the measured intensities according to the space group symmetry, and in this case the 705 measured peaks are reduced to 55 unique peak intensities. Initial attempts of refinement when entering the twinning information assuming either 60° rotation or obverse/reverse rhombohedral twinning failed. In a second attempt we calculated which indices would have intensity from one of two 60° rotated twins, and removed the indices from the list of peak intensities. This process left a total list of 470 peaks with 47 unique peak intensities. With this data set it was possible to get a stable fit by fixing all the Debye-Waller factors to be isotropic with the value 0.02 $Å^2$, and restricting the Pt-Pt distances to be almost equal. After initial convergence the restriction on the Pt-Pt distances was lifted, giving a stable fit with an R1-parameter of 0.57 (perfect fit is 0). This is not a very good fit though, but we suspect that it is influenced by the low number of unique peaks and large number of domains with possibly different structures. This refined structure is shown in figure 8.28, showing the same layers as discussed above, but it is quite disordered. The figure shows the unit cell along the a-axis, and the kagome layers are indicated by black lines. The atomic positions in the refined unit cell and the unit cell parameters are seen in table 8.7.

In trying to understand the disorder more asymmetric Debye-Waller factors were fitted while fixing the atomic positions found. With the data quality the asymmetric Debye-Waller factors are not representative for the directionality of the atomic vibrations, but more likely show disorder along certain directions. Figure 8.29 shows the asymmetric unit cell along the a-axis, and the ellipsoids represent the disorder. It is seen that some sites have most disorder in the z-direction, like Pt_1, whereas others mostly have it within the layer, such as Pt_7.

Looking closer at the disorder in kagome layer 1 with Pt_7, it is seen that the disorder could be a sign of breaking the symmetry. Figure 8.30 shows kagome layer 1 from above, and from the disorder two possible arrangements of Pt atoms are shown in red and blue, which would break the symmetry of the space group.

Finally it was analyzed which diffraction peaks fitted best with the measured intensities. Figure 8.31 shows the 47 unique peak intensities measured and calculated as a function of the peak index (left) and the magnitude of the scattering vector Q (right). It is seen that many of the weak peaks are described well whereas the more intense peak are not as well fitted.

Some of the high intensity peaks not fitted well by this structure have L-values of 9 and 18, which are exactly the diffraction peaks expected for a pure Cu_5Ca structure. It was not possible to fit, but it is suspected that this alloy contains both the structure found, the Cu_5Ca structure, and potentially others. This structure and the Cu_5Ca structures are closely related to the Laves phases, which are based on a certain geometric size ratio between the two elements. These types of alloy typically exist in different crystal structures only differing in the stacking sequence. Therefore the energy of each crystal phase is close to each other, causing more phases to coexist often [149, 150]. This is could also be the case here, which explains the difficulty in determining the structure of Pt_5Gd.

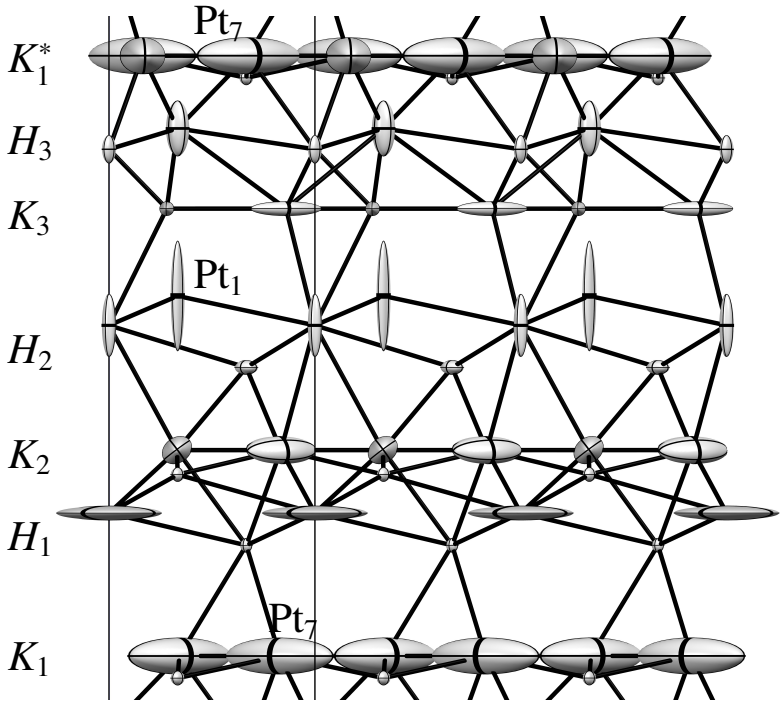

Figure 8.29: The figure shows anisotropic Debye-Waller factors fitted while fixing the atomic positions. With this data quality and disordered structure these are more likely to represent the disorder in the crystal rather than atomic vibrations. Some atoms shows mostly in-plane disorder whereas others show out-of-plane disorder, e.g. Pt_7 and Pt_1, respectively. The figure is from [74].

But coming back to the relation between the overlayer and the alloy, it seems that the important structural motif is the kagome layer forming around the larger Gd atoms. These layers essentially have a vacancy compared to a close-packed layer, and can therefore sustain a shorter Pt-Pt distance than bulk Pt. In the structure we found the Pt-Pt distance in the kagome layers are 3.9% compressed relative to bulk Pt.

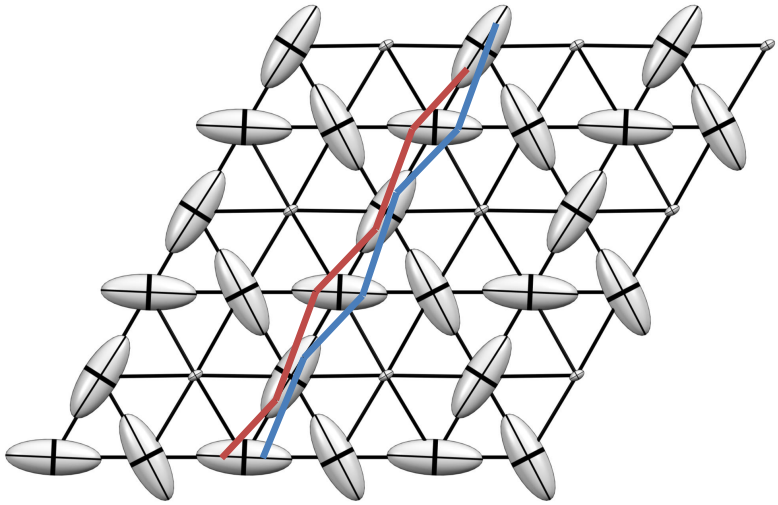

Figure 8.30: The figure shows anisotropic Debye-Waller factors in the plane of kagome layer 1. The disorder in this layer could be an indication of broken symmetry, as the atoms could be arranged as indicated by the blue and red lines. These positions however would violate the symmetry of the space group. The figure is from [74].

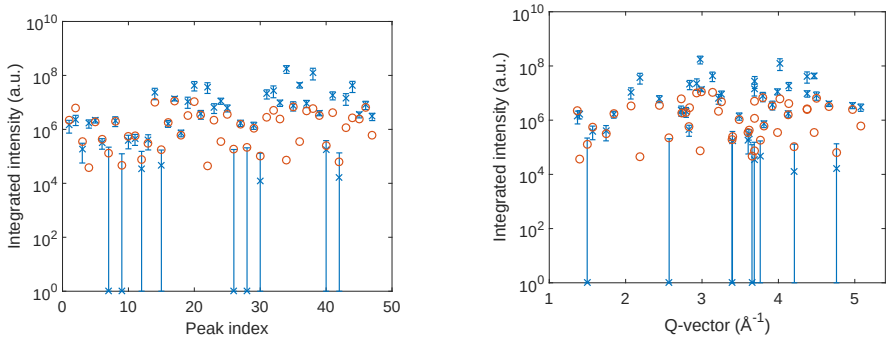

Figure 8.31: The figure shows the measured and calculated intensity of the 47 unique reflections. In the left panel they are plotted against their index, and on the right they are plotted against the magnitude of the scattering vector, Q. The figure is from the supplementary material of [74].

8.6 Conclusion

For the Pt alloy system the overlayer structure has been investigated for both Pt_xY and Pt_xGd. The Pt_xGd nanoparticles showed a very similar trend to the Pt_xY nanoparticles, and the activity scales in the same way with Pt-Pt compression. This is also expected, as both alloy systems form similar Pt overlayers, and so the Gd or Y does not have any direct (ligand) effect of the ORR activity. As discussed in the introduction the loss of activity over time is due to intrinsic changes of the nanoparticles, and the EXAFS measurements have proven that the loss of activity is due to a relaxation in the Pt-Pt compression.

The XRD studies of the single crystal model systems allowed us to examine the overlayer directly. As expected the overlayer was compressed as anticipated, although not as much as expected. It was also found that the alloy sample was no longer a single crystal, and that it separated into many small domains. We could not separate the domain size from the distribution of strain (microstrain) in the sample, and it seems likely that some microstrain is present. This leads to some parts of the surface being significantly more active for ORR than others, and the activity will then be dominated by the most active domains.

The overlayer strain on a Gd/Pt(111) sample with a rotated alloy and overlayer was measured twice, and we found that the two measurements gave similar results. Surprisingly the Gd/Pt(111) sample with an unrotated overlayer proved to have a stronger compression.

The variation of the alloy rotation may tie into the complex structure formed on the Gd/Pt(111) sample. A complicated stacking sequence was found, but as early measurements have shown [83] the structure is similar to the Cu_5Ca prototype structure.

Finally the overlayer showed strain relaxation upon repeated potential cycling. This explains the loss of activity of the Pt_xGd nanoparticles after stability tests. It was suspected that the overlayer would relax, as the average Pt-Pt distance was seen to relax towards bulk Pt. However, the in-situ XRD measurements on the Gd/Pt(111) crystal showed that the overlayer does indeed relax. Beside the slight strain relaxation the overlayer remained stable, which could be a part of the explanation for the high stability of this class of materials.

CHAPTER 9

Precious metal oxides for OER

In this chapter XANES analysis of both RuO_2 and IrO_2 will be presented, and all measurements have been done under OER conditions. This will give access to electronic structure information during OER. Oxide surfaces are more complex and not as well understood as metal surfaces, and more research into these materials is required to get a further understanding of their electrocatalytic properties. Detailed knowledge of the atomic and electronic structure of IrO_2 and RuO_2 under OER conditions may help guide designs of new materials that are active and stable electrocatalysts for OER while minimizing or eliminating the precious metal contents.

9.1 Metallic and oxidized Ru nanoparticles

These nanoparticles were fabricated using a magnetron cluster source with a time-of-flight mass spectrometer to only deposit nanoparticles of a certain size. All the particles produced were metallic nanoparticles, but to convert some samples into oxide nanoparticles they were annealed in 1 bar pure O_2 at 400 °C for 1 minute [92]. The metallic particles from the cluster source were nominally 5 nm in diameter, and from transmission electron microscope (TEM) images a size distribution of 4.9 ± 0.3 nm were found. Selected TEM images and the measured size distribution are seen in figure 9.1 for both the metallic and thermally oxidized nanoparticles. The oxidized particles remain mostly separate, and only a small fraction conglomerate into larger particles. This is also evident in the size distribution that shows a mostly narrow size range of 5.2 ± 0.5 nm, but with a small tail going to larger particle sizes. Fabrication and characterization of Ru nanoparticles were done by Bela Sebok and Ander Bodin.

At the highly oxidative conditions at OER potentials in acid the metallic particles are expected to oxidize, forming an electrochemically derived oxide in contrast to the thermal oxide. To get more insight into the difference between these two oxides we did in-situ XAS, and analyzed the XANES region to get more chemical information regarding the Ru.

The in-situ XAS experiments were done at BL14-3 in fluorescence mode using a 4-element vortex detector. The in-situ cell was a back-illumination type cell with an 8

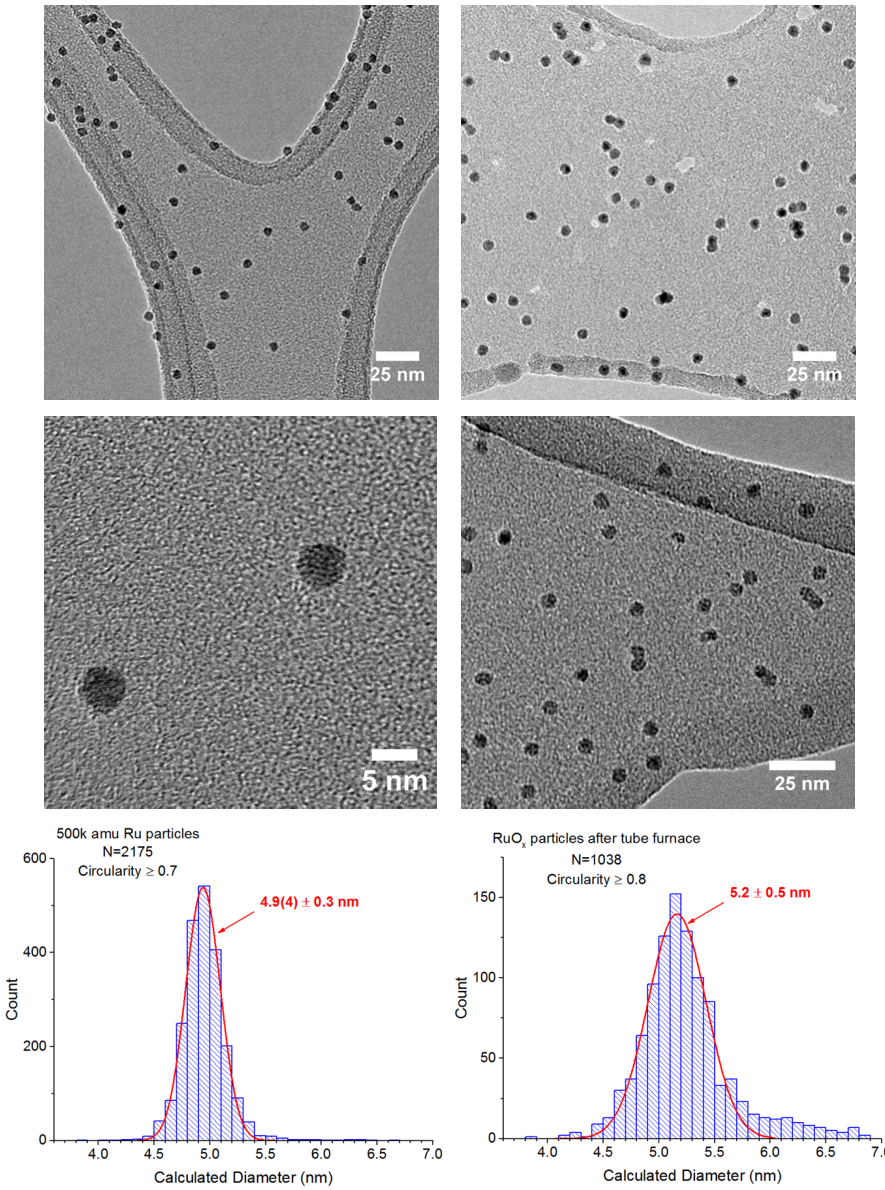

Figure 9.1: The figure shows selected TEM images and size distributions of the size-selected nanoparticles, both the metallic Ru (left) and oxidized RuO_x (right). The thermally oxidized nanoparticles remain mostly separate, and from the TEM images and size distribution it is seen that a small number conglomerate into larger particles. *The TEM images and analysis was carried out by Bela Sebok and Anders Bodin.*

µm thick glassy carbon window, as described in section D.2. For these experiments we also measured a metallic Ru foil in transmission and RuO_2 powder in fluorescence as reference materials. The Ru metal foil was a part of the SSRL reference foil collection, and the RuO_2 powder was obtained from Sigma-Aldrich (238058-1G, 99.9% purity, micrometer sized particles).

9.1.1 Metallic Ru nanoparticles

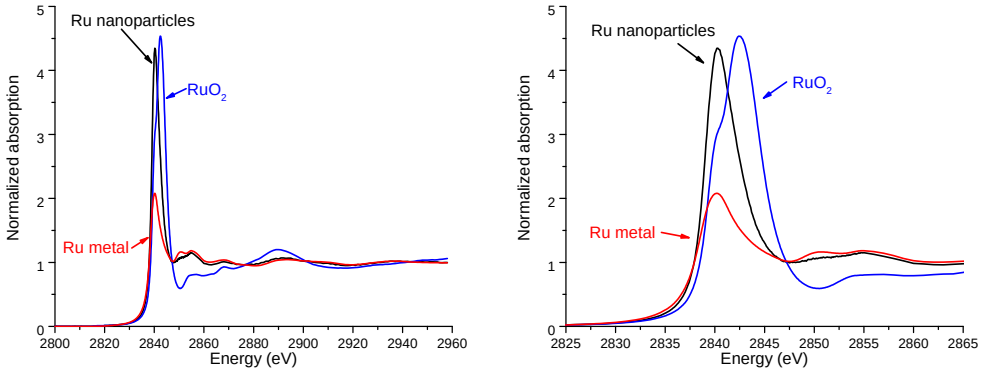

Figure 9.2: The left panel shows the full spectrum of dry metallic Ru nanoparticles compared to Ru metal and RuO_2 reference materials. The right panel shows the same spectra zoomed in around the white line. It is seen that the nanoparticle sample shows very similar features to the metallic Ru reference, indicating that it is indeed mostly metallic. The tall white line could indicate the presence of an oxide at the surface formed by exposure to air.

XANES spectra show that the metallic Ru nanoparticles are indeed metallic, as the white line position and the features above the white line are almost identical to the metallic Ru foil reference. An interesting difference is the rather tall white line of these metallic nanoparticles, which could indicate the presence of an oxide, most likely formed at the surface due to exposure to air. Figure 9.2 shows a comparison of the dry metallic Ru nanoparticle spectrum compared to the references.

The in-situ measurements were done in 0.1 M HNO_3 electrolyte, which was chosen to eliminate fluorescence from Cl (if using $HClO_4$ or HCl) and S (if using H_2SO_4). The measurement protocol was to measure the sample dry, at open circuit potential (OCV) immediately after exposure to electrolyte, at open circuit potential after 16 cycles in the potential range 0.8 to 1.2 V vs. RHE. Following were measurements while fixing the potential at 0.8 to 1.4 V vs. RHE in steps of 0.1 V. Some of these spectra are compared in figure 9.3. Here it is seen that the particles remain unchanged simply from the exposure to electrolyte (Dry and OCV1). The spectrum at OCV after

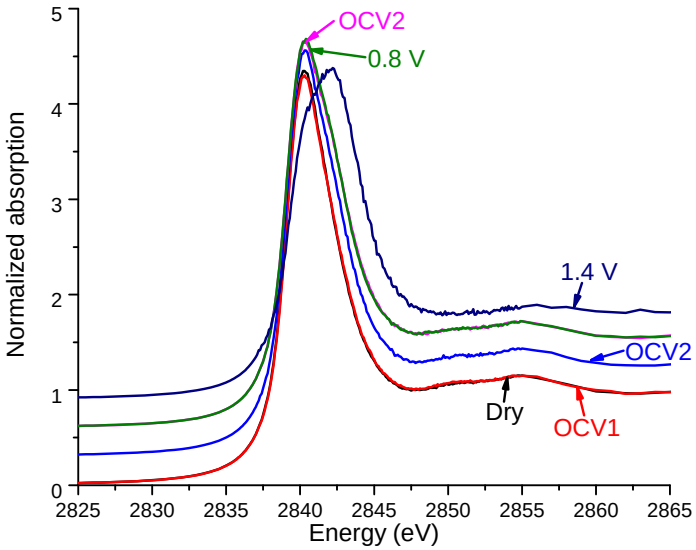

Figure 9.3: The figure shows selected spectra of metallic Ru nanoparticles. First they are compared while dry (Dry) and at open circuit potential before potential cycling (OCV1), which initially shows no changes. The sample was then measured after potential cycling, both before and after being in air for 24 hours, and both of these spectra are identical (OCV2). The OCV2 and 0.8 V spectra are identical, which is expected as the potential is similar to the open circuit potential of RuO_x. Finally at 1.4 V the spectrum has drastically changed, indicating a complete transformation to RuO_x.

the first electrochemical cycling (OCV2) show very few changes, although a slight shoulder at the high energy side of the white line had formed, indicating growth of an oxide. Due to problems with the setup this sample cell was drained and left for about 24 hours in air, after which it was filled with electrolyte again, cycled 6 times in the same potential range and measured again to check for changes. This is the second OCV2 measurement in the figure, and shows almost no change compared to the first OCV2 measurement. This spectrum is compared to the one acquired at 0.8 V vs. RHE, which is identical. This is expected as the open circuit potential of RuO_x is around that potential. Finally the spectrum at 1.4 V vs. RHE is shown, and here a drastic change is visible. The shape of the white line is much more similar to the RuO_2 reference above, and most of the Ru must have been converted to RuO_x. The white line intensity is quite low for this spectrum, which is opposite to the expected trend. However, this is most likely to issues in normalizing the spectra due to a small Cl contamination. The Cl contamination does not seem to adsorb on the RuO_x, otherwise it would immediately be evolved as Cl_2 gas, as the overpotential

for chlorine evolution is lower than for oxygen evolution [96]. Instead it is believed the Cl exists in organic compounds from the epoxy glue, which is in solution and is assumed to have no or very little interaction with the RuO_x nanoparticles.

Figure 9.4 shows the relative amount of Ru and Cl as a function of the scan number. This is estimated from the absolute height of the non-normalized spectra. The jump of Ru in the two OCV2 measurements is due to repositioning of the sample, that impacts how much signal gets into the detector. The Cl K-edge is found at 2822 eV, only 16 eV below the Ru L_3-edge, making the separation of the two difficult. The amount of Cl is also shown on the figure, and is expressing the height of the Cl absorption edge relative to the dry Ru sample. The separation of the spectra were done by fitting a Lorentzian tail to the rising white line of the Ru edge plus a step at the Cl edge. The Cl step height was then subtracted and the Ru spectrum normalized. This procedure is robust when the spectrum is dominated by Ru, but some error in the white line height is expected at 1.35 and 1.4 V. The maximum error is the magnitude of the Cl/(Cl + Ru) step height ratio, although the actual error is more estimated to be 20% of this magnitude.

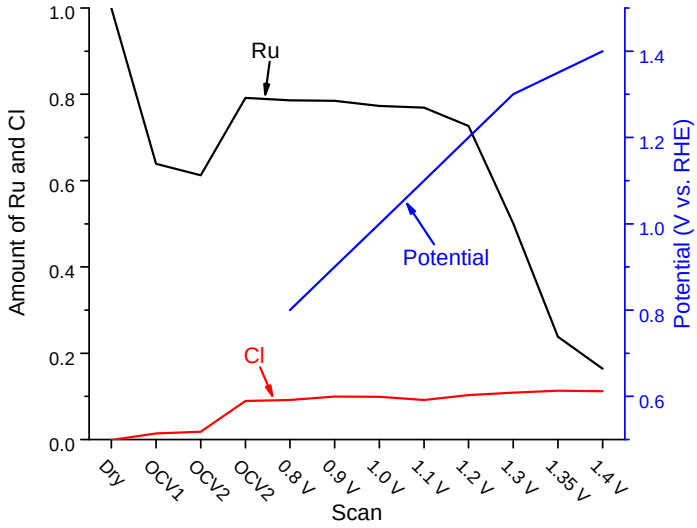

Figure 9.4: The figure shows the relative amount of Ru and Cl on the X-ray window surface as a function of scan number. At 1.2 V the Ru starts dissolving, and at 1.4 V less than 20% is left. The Cl contamination remains mostly constant, but as the amount of Ru decrease the ratio of Ru and Cl becomes almost 1:1, making the normalization of the Ru spectra difficult. The increase in Ru amount between the two OCV2 measurements is due to repositioning of the sample, as this measurement is sensitive to the measured signal rather than the actual Ru content.

The OER current was measured with a standard 3-electrode setup while the XAS

spectra were acquired. Figure 9.5 shows the current and potential as a function of time. Above 1.2 V vs. RHE where the OER starts the current does not seem to increase significantly, but this graph shows the measured current, not current density. During OER conditions the current remain almost constant, despite the large dissolution of Ru from the sample surface. Taking the mass of Ru into account from figure 9.4 it is seen that the current at 1.4 V is 5 times higher per Ru atom than at 1.2 V as only 20% of the Ru atoms are still left at the high potential.

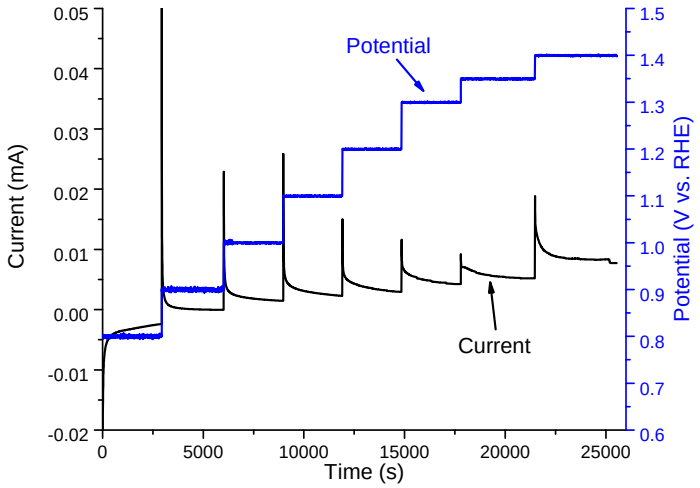

Figure 9.5: The figure shows the potential and current as a function of time while measuring the XAS spectra. The current shown here is the actual measured current, but taking into account that only 20% Ru remains at 1.4 V the current density normalized by mass would give a much higher current density at the high potentials.

Figure 9.6 shows the evolution of the white line shape as a function of potential. The left panel shows the spectra stacked on top of each other, and the right panel shows the white line intensity as a color scale.

To quantify the changes in the white line it was fitted. The step was approximated by an arctan function with a center at the inflection point around 2839.2 eV, and the white line itself was fitted by two Lorentzian components. The width of both Lorentzians were fixed to 2.8 eV (FWHM) in order to get stable fits across the entire data set. This width is consistent with the calculated life-time broadening at the Ru L_3-edge of 2 eV [129] plus broadening from the finite width of the d-band and experimental broadenings. The fit was performed in the energy range 2800 eV to 2844.2 eV, 5 eV above the inflection point.

For the pure RuO_2 the two peak components (see figure 9.2) can be ascribed to t_{2g} and e_g bands that form due to crystal field splitting [151]. In the rutile crystal structure the crystal field is octahedral with a slight distortion, and so a low energy

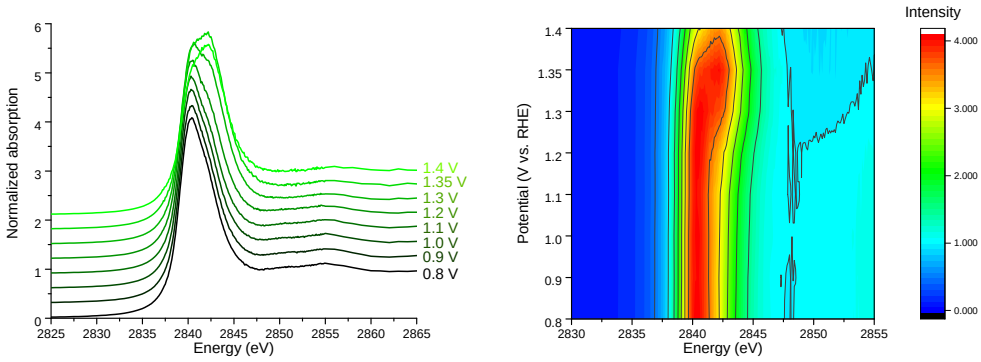

Figure 9.6: The left panel shows the white line of the spectra as it evolves with increasing potential, and the right panel shows the same evolution but with the energy on the x-axis, potential on the y-axis, and the white line intensity represented as a color (and contours). It is seen that the white line starts changing at 1.2 V, as the intensity rises at 2842 eV, at which point the OER and dissolution starts. The peak shifts to higher energy and intensity is transfered into the high-energy shoulder.

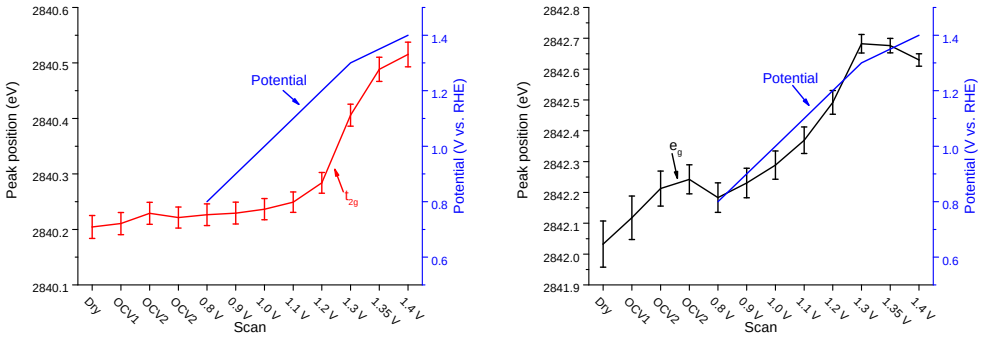

Figure 9.7: The left panel shows the position of the t_{2g} peak as a function of electrochemical treatment, along with the applied potential. The right panel shows the same for the e_g peak. The t_{2g} peak follows the inflection point, and it remains almost constant until 1.2 or 1.3 V where it sharply increases. The e_g peak on the other hand seems to follow the potential linearly, except at the highest potentials.

component t_{2g} and a high energy component e_g are formed. In the case of a mixture of metal and oxide the metallic white line overlaps with the low energy component t_{2g}. Figure 9.7 shows the position of these two components as a function of condition. Here the t_{2g} has been used to name the low energy component, even though it also contains a metallic part. Furthermore, the splitting due to crystal field may not be present in the electrochemically derived oxide as it is likely more disordered. However, the coexistence of a metallic and oxidized Ru component makes it impossible to separate the two, and the t_{2g} and e_g labels are used even though they may be metallic and oxide peaks, respectively. The t_{2g} component follows the inflection point, and the jump we see at 1.2 to 1.3 V vs. RHE can be contributed to a sudden increase in the oxidation state of Ru. The e_g peak moves linearly with the potential, except at very high potentials the peak shifts a bit down again. In bulk RuO_2 the the two peaks are found at 2840.66 ± 0.06 eV and 2842.87 ± 0.03 eV, both values slightly higher than what we see for this sample, so the average oxidation state of these nanoparticles is lower than +4.

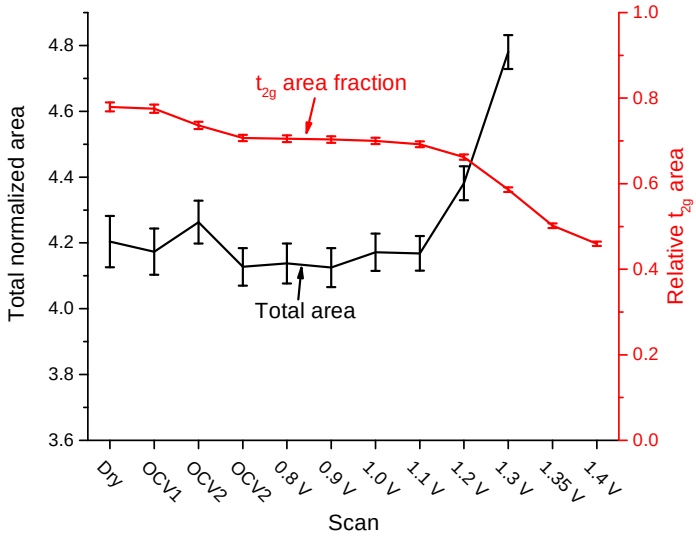

Figure 9.8: The figure shows total white line area and the t_{2g}/total area ratio, as a function of the electrochemical conditions. The overall peak area increases at 1.2 V, consistent with an increase in oxidation state. The last two points of the total area have been removed due to the Cl contamination. The area ratio on the other hand is insensitive to the Cl, and the further decrease in the ratio indicates further oxidation.

Finally the area of the two components of the white line can be compared. Figure 9.8 shows the total area of the white line (or rather the combined heights of the two peaks, since the width is fixed), as well as the t_{2g}/total area (height) ratio. The rise

in the total area at 1.2 V vs. RHE indicate the formation of an oxide as more holes in the Ru 4d band is generated. The ratio between the two peak should not be impacted by the Cl issues, and so the decrease in the t_{2g} peak area is real. This is consistent with the formation of an oxide, as bulk RuO_2 has a t_{2g}/total area ratio of 0.31 ± 0.01. In this case the t_{2g} area only reaches 0.45, indicating that some metallic Ru may still be left (recall that the t_{2g} peak overlaps with the metallic Ru peak).

9.1.2 Thermally oxidized RuO_x nanoparticles

Figure 9.9 shows the XAS spectra of the dry RuO_x nanoparticles compared to the bulk RuO_2 powder and metallic Ru foil. Here it is seen that the nanoparticles are very similar to bulk RuO_2, and only the white line shape is slightly different with a bit more area for the nanoparticle sample. This means that the particles are fully oxidized and no metallic core survived the oxidation treatment. The splitting into the t_{2g} and e_g bands is not as pronounced as the RuO_2 reference, and it is speculated that it can be due to disorder in the crystal structure of the nanoparticles.

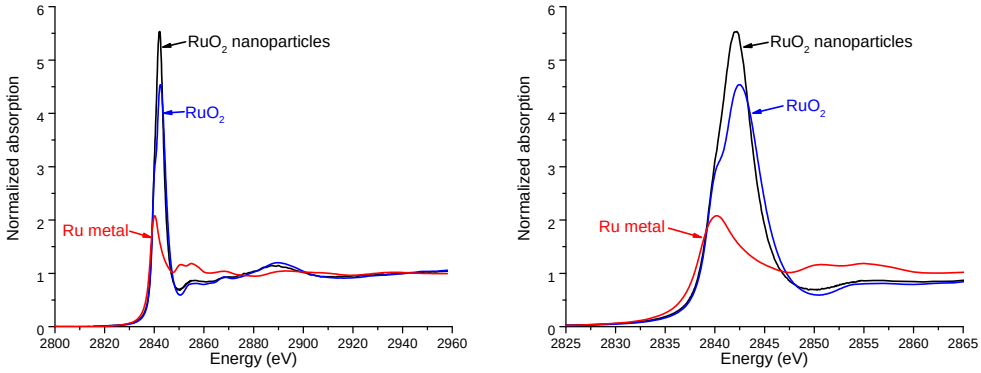

Figure 9.9: The left panel shows the full spectrum of the RuO_x nanoparticles along with the RuO_2 and metallic Ru references. The shape of the nanoparticle spectrum is very much like RuO_2. On the right panel the white line region is seen more clearly, and here it is evident that the nanoparticle white line does not show as distinct separation of the t_{2g} and e_g bands. This is speculated to be due to disorder of the crystal structure.

The measurement scheme of the oxidized particles is similar to that of the metallic particles. We measured the spectrum with dry nanoparticles, at OCV after introducing electrolyte (OCV1), and again at OCV after 5 cycles in the potential range 0.8 to 1.3 V vs. RHE (OCV2). After this procedure we measured the spectrum with a constant potential, gradually stepping from 0.8 V up to 1.3 V, back down to 0.8 V, and finally up to 1.7 V vs. RHE. The potential steps and the measured current can be seen in figure 9.10. From this figure it is also seen that the OER onset is between

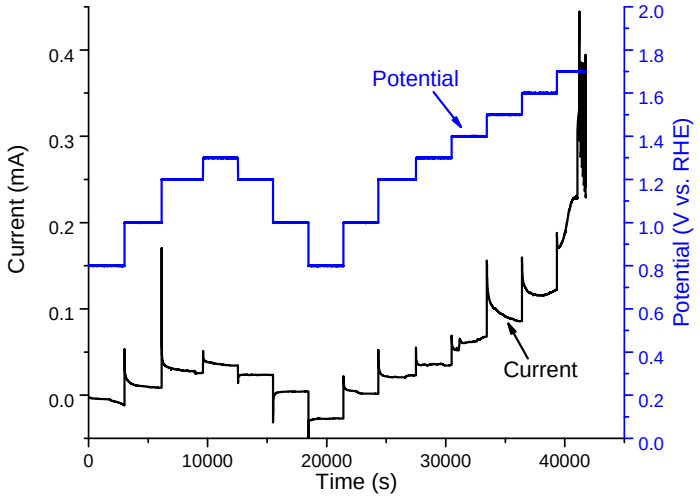

Figure 9.10: The figure shows the potential and current as a function of time while measuring the XAS spectra. The current shown here is the actual measured current, which is seen to rise significantly at and above 1.4 V when OER starts.

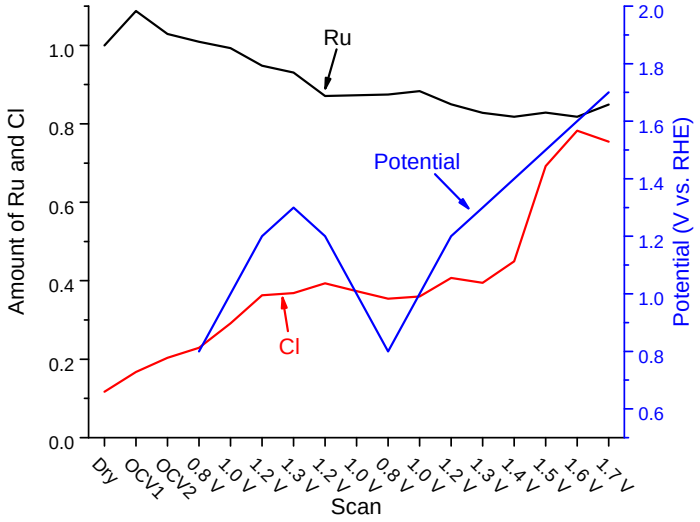

Figure 9.11: The figure shows the relative amount of Ru and Cl as a function of scan number. These thermally oxidized nanoparticles are indeed more stable than their metallic counterpart, as ∼80% of the Ru remains at the end of the experiment. As this experiment went on for longer the Cl contamination became significant towards the end.

1.3 and 1.4 V vs. RHE, and as the potential is increased up to 1.7 V the current increases significantly.

As discussed earlier we expect these nanoparticles to be significantly more stable than their metallic counterpart. Figure 9.11 shows the relative amount of Ru as a function of the scan number, and these particles are indeed more stable as ∼80% of the Ru remains at the end of the experiment. For these thermally oxidized particles the experiment went on for almost twice as long and the highest potential was higher than for the metallic particles. Over the course of this experiment the Cl contamination increased, and even though a large fraction of the Ru remains, the absorption step height of Cl approaches that of Ru at the end of the experiment. This means that the normalized height of the Ru white line at the last 3 data points has a larger error.

Figure 9.12 shows the spectra as the applied potential is varied. In general the spectra are changing very little, in contrast to the metallic Ru nanoparticles that went through electrochemical oxidation. Upon close inspection one may see the e_g peak move to higher energy with higher potential, and it is most easily seen on the contour lines on the plot in the right panel. In the last few potentials the white line intensity drops, which is due to the Cl and Ru separation error.

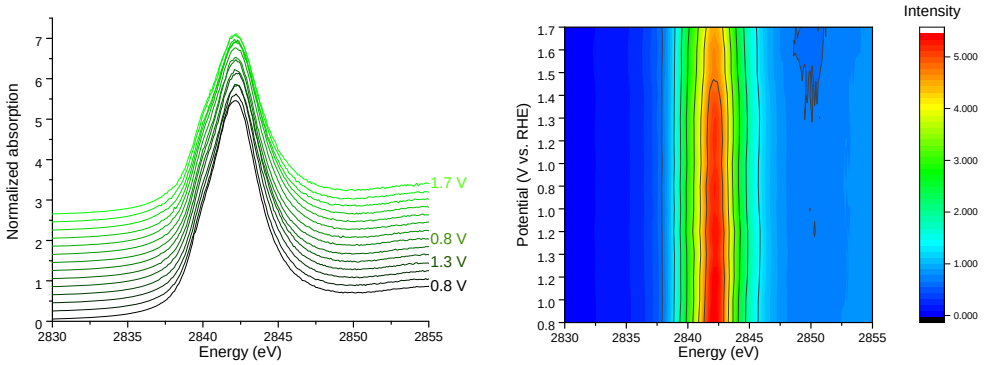

Figure 9.12: The left panel shows the white line of the spectra as it evolves with increasing potential, and the right panel shows the same evolution but with the white line intensity represented as a color scale. It is seen that the spectra only changes subtly, but from the contour lines on the right plot the e_g peak seems to move slightly towards higher energy with increasing potential.

As in the case of the metallic nanoparticles the white line changes were quantified by fitting an arctan function to the absorption step and two Lorentzian peaks to the white line. Again the width of the Lorentzian peaks were fixed to 2.8 eV (FWHM) to get more stable fits. The position of the t_{2g} and e_g peaks are plotted along with the electrochemical potential in figure 9.13. We see here that the peak positions did not change much, only around 0.2 eV over the entire potential range. The t_{2g} peak

drops slightly when the potential is returned to 0.8 V vs. RHE, but drops again when the potential is increased above 1.4 V vs. RHE. The e_g peaks follows the potential, except a down-shift in peak position is also seen above 1.4 V vs. RHE. The changes in the e_g peak are clearer and have less error than the t_{2g} peak, probably because the e_g peak dominates the white line.

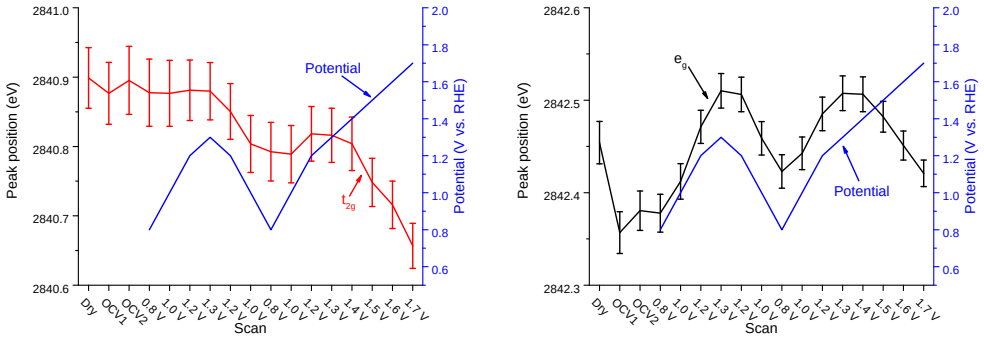

Figure 9.13: The left panel shows the position of the t_{2g} peak as a function of electrochemical treatment, along with the applied potential. The right panel shows the same for the e_g peak. The t_{2g} moves very little at low potentials, whereas the e_g peak follows the potential until 1.3 V. But above 1.4 V vs. RHE both peaks shift to lower energies.

Lastly we turn to the total white line area and the t_{2g}/total area ratio, which is shown in figure 9.14. From this graph we see that the total area remains constant, except at potential above 1.4 V vs. RHE. Again this drop could be an issue with the normalization due to the increasing Cl signal. Furthermore, the t_{2g} area fraction remains constant as well, and has a value close to RuO_2 of 0.31 ± 0.01. This is consistent with complete thermal oxidation into RuO_2. The peak positions for the RuO_x nanoparticles are around 2840.8 eV and 2842.45 eV, whereas bulk RuO_2 has the peak positions at 2840.66 ± 0.06 eV and 2842.87 ± 0.03 eV. Here it is seen that the t_{2g} peak is higher and the e_g peak is lower than bulk RuO_2, which could simply be due to the shape difference of the white lines.

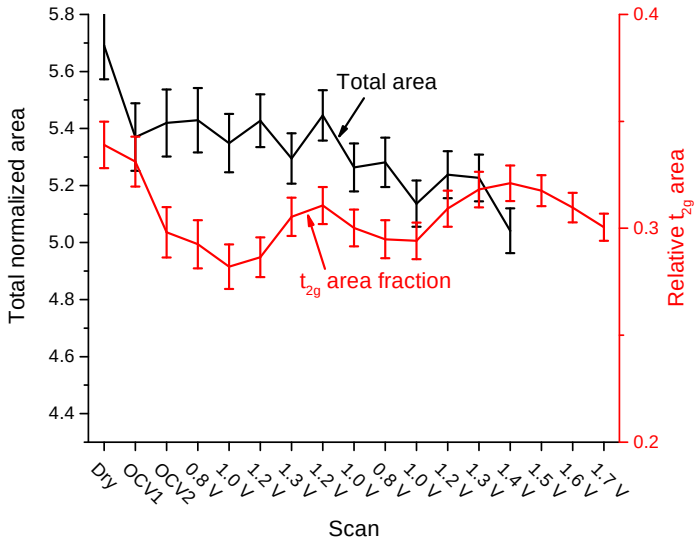

Figure 9.14: The figure shows total white line area and the t_{2g}/total area ratio, as a function of the electrochemical conditions. The total area remains constant, the last 3 points for the total area has been removed due to the increasing Cl signal. The peak ratio is also constant, and is close to a peak ratio of 0.31 ± 0.01 for bulk RuO_2.

9.1.3 Discussion

In total this data shows that the metallic Ru nanoparticles were indeed mostly metallic in the as-prepared state. Even electrochemical cycling in the range 0.8 to 1.2 V vs. RHE did not change the particles significantly. Only when keeping the potential at 1.2 V or higher for extended amounts of time did the particles start to oxidize, further oxidizing as the current density increased at higher potentials. At the starting point of OER the dissolution of Ru also starts. According to the Pourbaix diagram for Ru it should oxidize to RuO_2 above 0.9 V vs. RHE at pH = 1 [86], however these particles remain metallic until higher potentials. That is most likely due to kinetic barriers, since the as-prepared nanoparticles showed signs of a surface oxide that can protect the particle against further oxidation. At 1.2-1.3 V vs. RHE the Pourbaix diagram indicates further oxidation to RuO_4, which dissolves in aqueous electrolyte. This coincides with the onset or OER and dissolution, and the increase in the measured oxidation state could be due to the surface oxide being stripped away and the metallic core oxidizes, giving a larger volume fraction of oxide. Despite the oxidation of the surface Ru the average oxidation state of the particles does not reach the +4 state, as both the t_{2g} and e_g peaks have lower energies than the RuO_2 powder reference.

For both the thermally oxidized and metallic nanoparticles a down-shift in the white line position was observed at the onset of OER. This is in contrast to the

behavior seen at potentials below OER onset where the peak positions follow the applied potential. The interpretation of these observations is that Ru gets more oxidized with increasing potential until OER onset, at which point the oxidation state decrease with higher current densities. A possible explanation for this is RuO_2 being on the strong binding side of the volcano. Below the reaction onset potential the OER cannot proceed, and it gets stuck at the Ru=O (double-bonded O) where Ru has the highest oxidation state. Once the OER overpotential is overcome the reaction can proceed, and the intermediate species covering the Ru surface are now determined from kinetics rather than thermodynamics. That includes the possibility of having a distribution of intermediate species that does not oxidize Ru as much as Ru=O. In the case of metallic particles an alternative hypothesis is: Less oxidized Ru in the core gets exposed as the RuO_x at the surface dissolves, leading to a decrease in average oxidation state.

9.2 IrO_x protection layer

To get more insight into the chemical state of IrO_2 during OER on this hybrid system we brought a sample with 2 Å (half a monolayer) of IrO_2 on top of a 40 nm RuO_2 thin film to the synchrotron. This time we did XAS at the Ir L_3 edge at 11215 eV, so as to get information about the Ir 5d valence states. Furthermore, we were able to get beam time at beam line 6-2 equipped with an emission spectrometer enabling HERFD XAS to be measured, revealing more detailed structure in the white line peak shape. Having seen features in the RuO_2 white line indicating a band splitting into t_{2g} and e_g bands we anticipated similar features for IrO_2 as both oxides have the same rutile structure.

As the beam line is equipped with a high energy resolution spectrometer a particular emission line may be chosen. To get the highest signal we chose the L_{α_1} emission line at 9175 eV ($3d^{5/2}$ to $2p^{3/2}$), and an emission line scan around this emission line is seen in figure 9.15 for the dry sample. For this particular choice of absorption and emission lines the synthetic HERFD lifetime broadening may be estimated from eq. (B.7). The initial state is an L_3 core-hole with a lifetime broadening of 5.25 eV [129], the final state is an M_5 core-hole with a lifetime broadening of 2.3 eV [152], which combined gives an estimated HERFD lifetime broadening of 2.1 eV, much narrower than the intrinsic L_3 broadening. This allows much better resolution of details in the white line, and it gives a similar peak broadening as the conventional XAS measurements of the Ru L_3 edge.

The dry sample spectrum was compared to standards of metallic Ir thin film and IrO_2 thin film, and the spectra are seen in figure 9.16. First of all the sample spectrum is seen to be very similar to the pure IrO_2 thin film as expected, except the sample spectrum white line is significantly higher. Furthermore, the white line of the oxides show no features besides a main peak, in contrast to the band splitting observed in RuO_2.

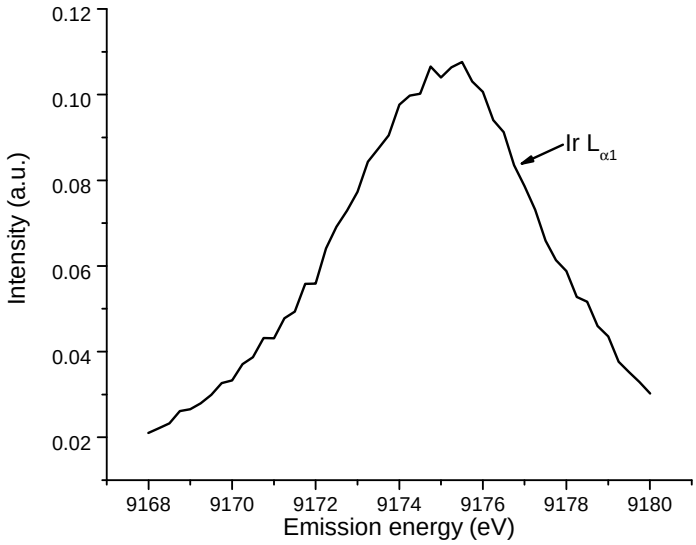

Figure 9.15: The figure shows the Ir L_{α_1} emission line measured with a high energy resolution spectrometer on a dry sample with 2 Å IrO_2 on 40 nm RuO_2. This emission line corresponds to an M_5 ($3d^{5/2}$) to L_3 ($2p^{3/2}$) electron transition and has a maximum at 9175 eV.

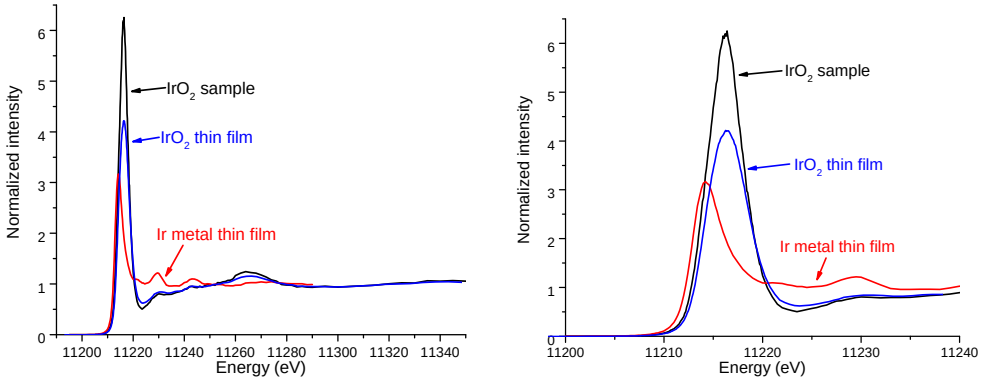

Figure 9.16: The left panel shows the full spectrum of the IrO_2 sample compared to thin film references of IrO_2 and metallic Ir. The right panel shows the same spectra zoomed in on the white line. The sample spectrum is very similar to the IrO_2 reference as expected, only the white line intensity is somewhat higher on the sample. In general few features are visible on the oxide white lines, in contrast to RuO_2.

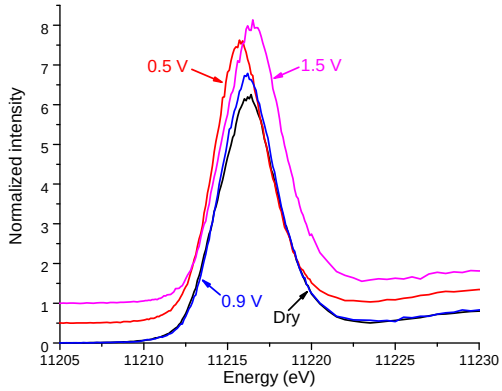

Figure 9.17: The figure shows a comparison of some selected spectra of the hybrid thin film sample at dry, 0.5 V, 0.9 V, and 1.5 V vs. RHE. The dry spectrum is at the same position as the 0.9 V spectrum, indicating identical oxidation stage, whereas the 0.5 V and 1.5 V spectra show more reduced and oxidized spectra, respectively.

Upon exposing the hybrid thin film to electrolyte (0.05 M H_2SO_4) and applying a potential the peak shifts according to the potential when reducing or oxidizing the surface. Figure 9.17 shows the sample spectra dry, at 0.5 V, 0.9 V, and 1.5 V vs. RHE, and the dry spectrum has the same peak position as the 0.9 V spectrum. The 0.5 V and 1.5 V spectra are shifted down and up in energy, respectively, consistent with reduction at lower potentials and oxidation at higher potentials.

The potential was kept constant during XAS measurements, and varied from 0.5 V, up to 1.6 V, and down to 0.6 V. After replacing the electrolyte the potential was increased from 1.0 V to 1.75 V. The potential and current during the last potential increase from 1.0 V to 1.75 V is seen in figure 9.18. A small OER current spike starts at 1.5 V vs. RHE, but significant OER current does not start until 1.6 V. At higher potentials the current decays, indicating thin film dissolution, and as the graph shows the total measured current the, current density may be higher at the highest potentials.

The white line is shown as a function of applied potential in figure 9.19. In this figure the spectra are also showed as contours with the energy on the x-axis, potential on the y-axis, and the intensity represented as color. The shift in the peak position are clearly seen following the potential.

The peak position is quantified by fitting a Lorentzian peak to the white line with an arctan function centered at the inflection point, and the fitting range is from 11195 eV to 5 eV above the inflection point (giving an upper limit of about 11220 eV). The left panel of figure 9.20 shows the white line peak position at each XAS scan. The changes in peak position can be correlated to a change in the oxidation state from measuring different standards, and from [105] the Ir^{+4} peak moves approximately

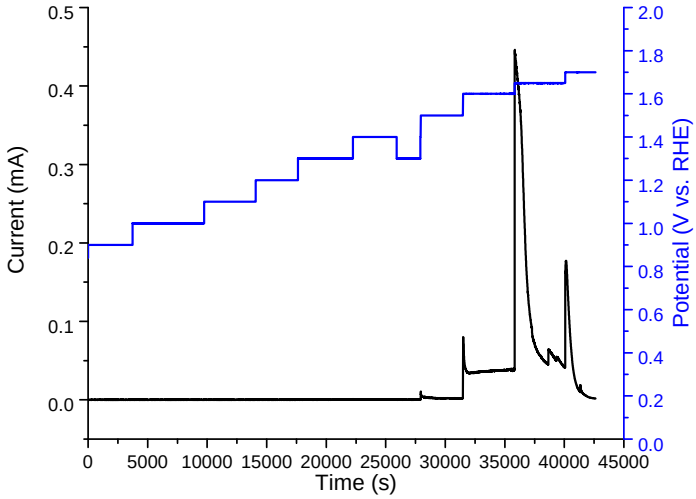

Figure 9.18: The figure shows the potential and current as a function of time while measuring the XAS spectra. The current shown here is the actual measured current, which is seen to rise significantly at and above 1.6 V when OER starts. The decay of the current at the highest potentials indicate catalyst dissolution, so that the current density may be higher at the highest potentials, even though the total current drops.

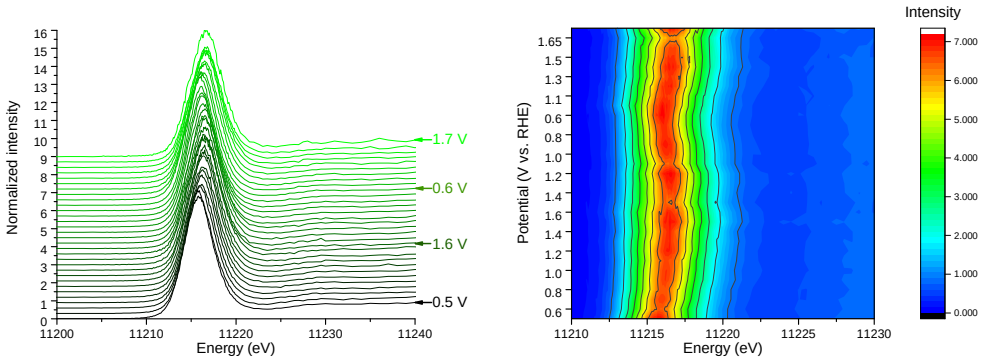

Figure 9.19: The left panel shows the white line of the spectra as it evolves with changing potential, and the right panel shows the same evolution but with the white line intensity represented as a color scale. The change of the white line is clearly seen to follow the potential.

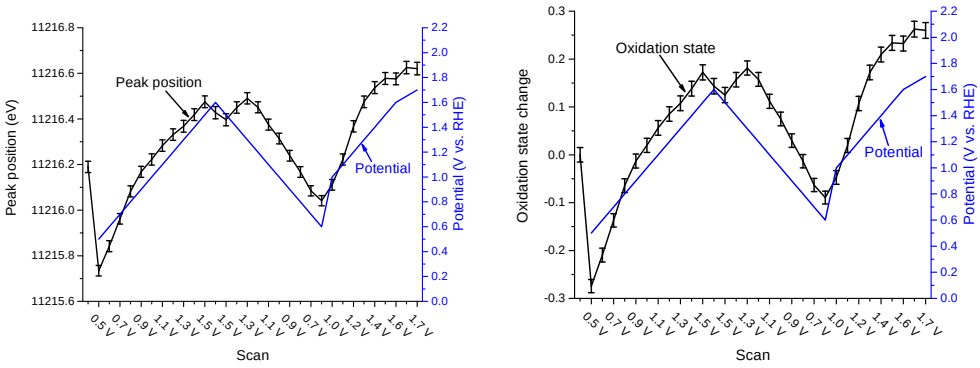

Figure 9.20: The figure shows the peak position of the white line in the left panel, and changes in oxidation state relative to the dry sample in the right panel. The oxidation state changes are calculate using a core level shift of 1.66 eV per oxidation level [105]. When decreasing the potential a hysteresis in the oxidation state is seen, and above 1.6 V vs. RHE the oxidation state saturates around +0.25 relative to dry.

linearly by 1.66 eV per oxidation state. This factor is used to convert the peak position to change in oxidation state relative to the dry sample, as seen in the right panel of figure 9.20. In this graph the oxidation state changes by half a unit going from 0.5 V to 1.75 V vs. RHE. At 1.6 V the first time the hanging meniscus in the cell was broken due to oxygen bubbles, and so the potential control was lost. After restoring the hanging meniscus the potential was reestablished at 1.6 V, and the measurements were continued. This could explain the drop in oxidation state at the first peak in potential, and it seems to take time for the oxidation state to recover. When decreasing the potential again a significant hysteresis is observed. Above 1.6 V vs. RHE the oxidation state seems to be fixed at +0.25 units relative to the dry sample.

Finally the height and width of the peak was analyzed, and the results are seen in figure 9.21. The peak height seems constant across the different applied potentials, although with significant scatter. The peak width (FWHM) follows the applied potential very closely, and does not show any appreciable hysteresis, however the peak width decrease faster than it increased, even though the potential steps are identical.

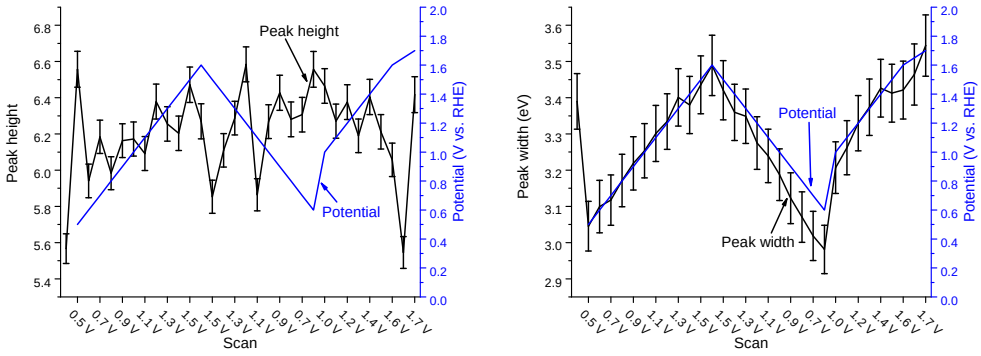

Figure 9.21: The left panel shows the white line height and the right panel shows the width (FWHM), both as a function of condition. The white line height does not show any changes in response to the potential, whereas the peak width follows the potential almost perfectly. As the white line is a direct probe of the unoccupied states of the Ir valence band the changes in peak width reflect a change in the valence band filling.

9.2.1 Discussion

Overall the changes in the oxidation state observed are much smaller than what has been observed for pure IrO_2 catalysts [111], and it is therefore suggested that the Ir does not take part in OER on this hybrid IrO_2/RuO_2 catalyst. However, it is still electrochemically active as it changes oxidation state. Due to the very thin IrO_2 layer all the Ir atoms are indeed at the surface, and so a large inactive bulk amount of Ir cannot explain the small change of the white line position. Furthermore, in [111] a white line splitting into t_{2g} and e_g bands were observed by conventional XAS at certain potentials, and we did not observe any splitting using the higher resolution HERFD XAS technique, this further supports that Ir does not take part in OER on the hybrid film.

The change in oxidation state found from the core level shift is consistent with the changes in the white line width. The white line is a direct probe of the unoccupied states of the valence band (likely an Ir 5d and O 2p hybridized band), and so the change in its width shows the valence band being depleted of electrons at higher potentials and refilled when decreasing the potential. Changes in the peak width directly reflects changes in the conduction band width, and so compared to the dry sample the conduction band becomes 0.1 eV wider at 1.6 V and 0.3 eV narrower at 0.5 V vs. RHE.

The proposed protection mechanism for the underlying RuO_2 is that IrO_x takes up extra oxygen, thus stabilizing RuO_2 from further oxidation and dissolution.

CHAPTER 10

Conclusion

In this project we have seen investigations of oxygen electrocatalysts trying to gain more understanding of the active surface and how that affects catalytic performance.

In the case of the oxygen reduction reaction we found that on model systems of both Pt_xGd and Pt_xY a compressive Pt overlayer is formed immediately upon exposure to acid electrolyte. For the nanopaticle model system the activity of the catalyst correlates with the degree of compression of the Pt-Pt distance, as expected from the d-band model. When the Pt atoms are compressed the d-band widens due to increasing overlap of the d-orbitals of the neighboring atoms, which lowers the d-band center, as the filling of the band has to remain constant. This in turn lowers both the bonding and anti-bonding states between the Pt surface and O adsorbate, which leads to increased occupation of the anti-bonding states thus weakening the oxygen bond.

The single crystal model systems showed that the Pt-Gd alloy system is highly complex, as evidenced in the literature. Finding a proper structure for the Pt-rich phase remains a challenge, however the origin of the Pt compression arises from the kagome layers in the alloy. The detailed structure of the overlayer is sensitive to the detailed alloy structure, and were seen to vary between different samples prepared in the same way. The overlayer thickness varies both between different Gd/Pt(111) samples as well as between Gd/Pt(111) and Y/Pt(111). The thickness varies, and in general a thinner overlayer seems to provide a higher average compression.

The goal for designing a real catalyst material relies on a high degree of control of the overlayer. The overlayer itself is in a meta-stable state, as compressed pure Pt is not stable in itself, thus it is important to stabilized the overlayer as much as possible to make a durable catalyst. At the same time the amount of compression should also be controlled, as this governs the activity of the catalyst. And a more compressed overlayer is likely to be less stable, so in a real catalyst a compromise probably needs to be made between activity and stability.

On the oxygen evolution reaction side the picture is not as clear as for ORR on metals, as the transition metal oxides investigated are more complex materials. In acid electrolyte RuO_2 is a very promising material displaying high catalytic activity, although not stable enough for commercial use. Here we hypothesized that the RuO_2 binds O intermediates a bit too strong like IrO_2, although being closer to the top of the volcano. This is an important input to people working on DFT calculations, as more detailed understanding of real catalysts can guide the design of better materials.

Furthermore we demonstrated that a sub-monolayer coverage of IrO_x on the surface of a RuO_2 thin film can stabilize the Ru against dissolution. XAS measurements showed that the IrO_x most likely does not participate in the OER on this hybrid film, but it absorbs some oxygen, which might be a part of the protection mechanism.

Development of new theories and materials benefit greatly from a close collaboration between experiments, computation, and theory. In this way new insight gained can be used to design new materials with novel properties.

APPENDIX A

Synchrotron Facility

The vast majority of experiments described here have been carried using X-ray techniques at the Stanford Synchrotron Radiation Lightsource (SSRL) facility. In this chapter the synchrotron facility will be briefly introduced.

A.1 Facility overview

The SSRL facility is located at the Stanford Linear Accelerator Center (SLAC) by Stanford University, California, USA. This national laboratory has a long and rich history in both high energy physics and X-ray research. This story starts with a colliding storage ring named SPEAR (Stanford Positron Electron Asymmetric Ring), which was an add-on to the linear accelerator at SLAC thought up during the 1960's. It was finally built in 1972 to collide beams of electrons and positrons from the linear accelerator, and although a smaller facility than originally intended it still made significant contributions. In 1974 the J/Ψ and τ particles were discovered, which were awarded the Nobel Prizes in physics in 1976 and 1995, respectively. Soon after its opening the potential use of the bright X-rays generated in the accelerator was realized, and in 1973 Stanford Synchrotron Radiation Project (SSRP) was put in motion. This was one of the first synchrotron facilities in the world, and it worked by parasitically taking out X-rays from a hole in the shielding wall of the storage ring [153]. The importance of synchrotron X-ray sources was quickly realized, and more experiment time was awarded to X-ray research, and in 1980 the Stanford Synchrotron Radiation Laboratory (SSRL) had 50% of the experiment time [154].

In 1997 the SPEAR storage ring was 100% dedicated as a synchrotron facility, and it had its own booster ring to feed electrons into the storage ring, so that the linear accelerator was no longer needed for operation. In 2004 the storage ring was upgraded by completely replacing all the magnets and accelerator structures, and is now known as SPEAR3, which is a third generation light source. Today the electrons run in the 234 m circumference ring at an energy of 3 GeV and a current of 500 mA, and is run in top-off mode, meaning that the current is injected frequently to maintain constant current (about 5 mA is injected every 5 minutes). Today the synchrotron has more than 30 end stations with a wide range of techniques, covering X-ray diffraction, spectroscopy, imaging, and more, using both soft and hard X-rays.

Most of the end stations have their radiation delivered by bending magnets or

wigglers, and a few beam lines are equipped with undulators. See figure A.1 for a map of the current beam lines at SSRL, as well as their sources.

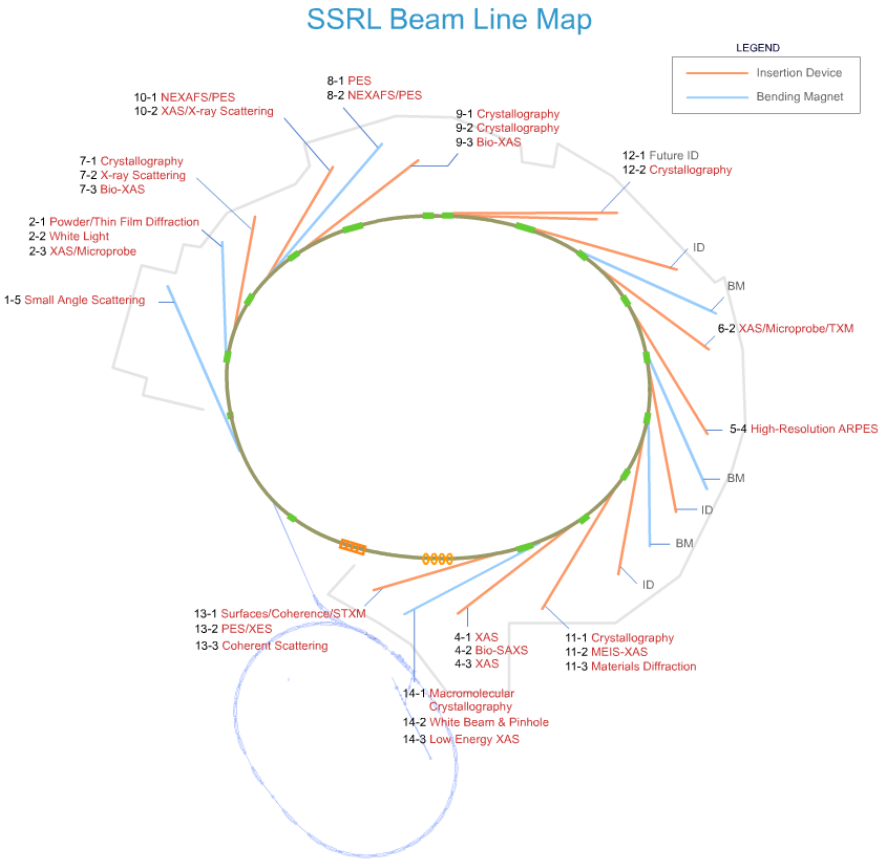

Figure A.1: The figure shows an overview of the beam lines and sources at SSRL. The image is from [155].

APPENDIX B

More XAS

This chapter describes more details of the EXAFS technique, as well as introducing the more advanced HERFD-XAS technique.

B.1 EXAFS equation derivation

A rigorous treatment of the absorption process may start with Fermi's golden rule,

$$\mu(E) \propto |\langle i|H|f\rangle|^2 \,, \tag{B.1}$$

where $\langle i|$ is the initial state consisting of an X-ray photon, no core-hole, and no photo-electron, $|f\rangle$ is the final state consisting of no X-ray photon, a core-hole, and a photo-electron, and H is the interaction Hamiltonian. The initial state is not affected whether there is a neighboring atom or not, since the core electron is so tightly bound, but the photo-electron in the final state may interact with other atoms, and the final state is therefore sensitive to the absorbing atom's surroundings. Assuming that the final state can be written as a sum of two parts with one not changed by the environment, and the other only consists of change from neighbors,

$$|f\rangle = |f_0\rangle + |\Delta f\rangle \,, \tag{B.2}$$

the EXAFS function can be written as [123],

$$\chi(E) \propto \langle i|H|\Delta f\rangle \,. \tag{B.3}$$

Evaluating this interaction leads to $\chi(E)$ being proportional to the amplitude of the backscattered wave function of the photo-electron. Using the phase propagation e^{kR}, where R is the distance to the neighboring atom, the EXAFS function becomes [123],

$$\chi(k) = \frac{f(k)}{kR^2} \sin(2kR + \phi(k)) \,, \tag{B.4}$$

where $f(k)$ and $\phi(k)$ are the k-dependent backscattering amplitude and phase from the neighboring atom, respectively. For the elements Pt to Pb (number 78 to 82) the backscattering amplitude has a sharp minimum at the same k-value as a 180° change in the phase, which was named the generalized Ramsauer-Townsend

effect [156]. This was important to know in the early days of synchrotron radiation when the backscattering properties were calculated from tabulated values either from measurements or calculations, since interpolation and extrapolation could lead to wrong backscattering functions. Today this is no longer the case as backscattering properties are most often calculated when needed from first principles calculations using programs such as FEFF, which yields accurate enough results to use in EXAFS data processing [127, 157, 158]. In general an absorbing atom has N neighboring atoms, and since not just a single atom is absorbing, but rather all the atoms whose absorption edge is being measured, disorder and thermal vibrations must be taken into account as well by multiplying by $e^{-2k^2\sigma^2}$, where σ is the rms (root-mean-square) displacement of the interatomic distance [123]. Furthermore, there may be multiple types of neighboring atoms at different distances, and in order to build the entire EXAFS signal these contributions are summed,

$$\chi(k) = \sum_j \frac{N_j e^{-2k^2\sigma_j^2} f_j(k)}{kR_j^2} \sin(2kR_j + \phi_j(k)) \,. \tag{B.5}$$

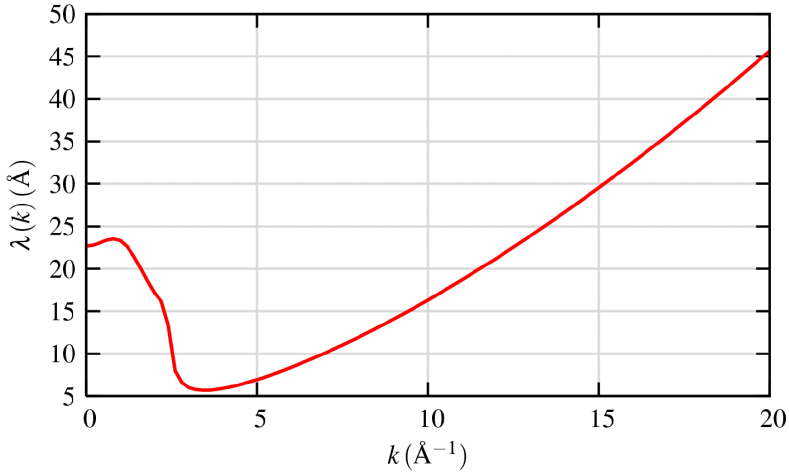

Figure B.1: The figure shows a model of the k-dependent mean free path of the photo-electron. Both the elastic mean free path of the photo-electron and the short lifetime of the core-hole excited absorber is taken into account in this model. The figure is from [123].

Finally the photo-electron only gives rise to EXAFS if it is scattered elastically, and for low energy electrons the mean free path in solids is quite short, as the universal curve shows [159, 160]. Furthermore, the lifetime of the core-hole excited absorber is very short, and the backscattered photo-electron has to return to the absorber before it relaxes. These two effects can be combined in a dampening term of the photo-

electron wave function of $e^{-2R/\lambda(k)}$, where $\lambda(k)$ is the k-dependent mean free path taking both the elastic mean free path of the photo-electron and the finite lifetime of the core-hole into account. The shape of $\lambda(k)$ is quite general, and a model of the parameter is seen in figure B.1.

Including the mean free path term in the model of $\chi(k)$, the final EXAFS equation is given,

$$\chi(k) = \sum_j \frac{S_0^2 N_j e^{-2k^2\sigma_j^2} e^{-2R_j/\lambda(k)} f_j(k)}{kR_j^2} \sin(2kR_j + \phi_j(k)) \,. \tag{B.6}$$

Here the amplitude reduction factor, S_0, has also been included, which includes the effect of other electrons relaxing into the core hole.

B.2 HERFD-XAS

As mentioned in section 4.3 the energy resolution of XAS spectra are typically limited by the lifetime broadening, which in the case of heavy elements can be very severe. This puts a limit to how detailed information about the DOS can be achieved from XANES spectra. The High Energy Resolution Fluorescence Detected X-ray Absorption Spectroscopy is an advanced type of XAS spectroscopy, in which an energy resolution better than the initial core-hole lifetime broadening may be achieved [161].

When using this technique the typical fluorescence detector is replaced by a spectrometer with a high energy resolution, typically with a resolution of around $E/\Delta E \approx 10000$ [162]. This allows the emission energy to be scanned independently of the excitation energy, and the individual emission lines can be resolved. By selecting a single emission line only a single decay channel is monitored, and the observed decay rate will therefore decrease leading to an apparent increase in the lifetime of the core-hole excited state, thus decreasing the broadening of the absorption spectrum.

The more rigorous treatment is based on an analysis of resonant inelastic X-ray scattering (RIXS), in which the scattered intensity is measured as a function of excitation energy and emission energy loss. Such a RIXS spectrum is shown in the left panel of figure B.2, which shows the scattered intensity at different energy losses around the Fe K-edge for an Fe_2O_3 sample. By fixing the emission energy to e.g. the $K_{\beta_{1,3}}$ emission line in the example in the figure, the intensity is recorded along the black diagonal line when scanning the excitation X-ray energy. The effect of scanning in the diagonal direction is that the width of the peaks will be projected onto the x-axis, which decrease the widths. This allows the effective lifetime broadening, Γ_{HERFD}, to be determined from the lifetime broadening of the initial core-hole excited state, Γ_i, and that of the final core-hole excited state, Γ_f [163],

$$\Gamma_{\text{HERFD}} = \frac{1}{\sqrt{\frac{1}{\Gamma_i^2} + \frac{1}{\Gamma_f^2}}} \,. \tag{B.7}$$

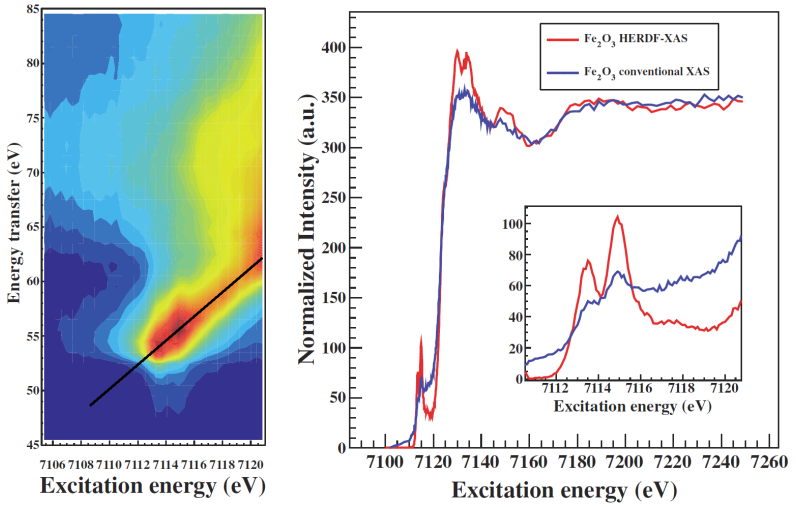

Figure B.2: The left panel shows a resonant inelastic X-ray scattering (RIXS) map of Fe_2O_3 around the Fe K-edge. By monitoring the $K_{\beta_{1,3}}$ emission line, the intensity is traced along the black line of the left panel, and the obtained XAS spectrum is shown in the right panel. It is seen that the energy resolution is much better than conventional XAS. The figure is adapted from [162].

From this relation it is seen that the HERFD measurement can significantly improve the energy resolution, and in the case of a large lifetime broadening for the initial state compared to the final state, the HERFD broadening will be dominated by the final state lifetime broadening. Taking the example of Fe_2O_3 in figure B.2, the lifetime broadening of the K (1s) core-hole generated by the initial absorption is 1.25 eV [129], the lifetime broadening of the M_2 ($3p^{1/2}$) final core-hole excited state when observing the $K_{\beta_{1,3}}$ emission line is 2.50 eV [152], leading to a total HERFD broadening of 1.08 eV. From the XAS spectra in the right panel of figure B.2 it is seen that the HERFD effect is not only improving the peak widths, it is also enhancing the intensity of peaks, making electronic structure changes easier to detect. Another example is the Pt L_3 edge, which is shown with conventional XAS in figure 4.13, where the L_3 ($2p^{3/2}$) core-hole state has a lifetime broadening of 5.31 eV [129]. When observing the L_{α_1} emission line the final state is an M_5 ($3d^{5/2}$) core-hole excited state with a lifetime broadening of 2.5 eV [152], leading to a HERFD broadening 2.3 eV, doubling the energy resolution besides the enhancement of spectral features.

All HERFD-XAS measurements were done at beam line 6-2, as this is the only beam line at SSRL equipped with an emission spectrometer, see appendix E.2 for the detailed setup.

APPENDIX C

More XRD

The chapter contains more details about the structure of crystals. An interesting approach to measuring the reciprocal lattice is also introduced.

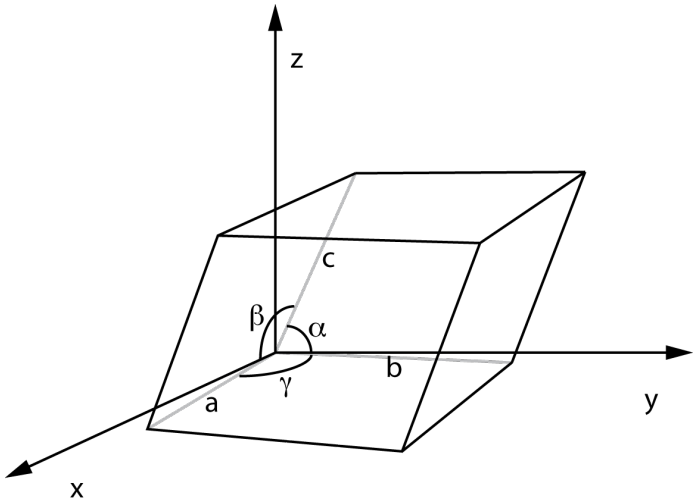

Figure C.1: The figure shows the typical definition of crystal unit cell parameters, the lengths of the lattice vectors are labeled a, b, and c, and the angles in between the lattice vectors are labeled α, β, and γ. The figure is from [164].

C.1 Crystals

In many solid materials the atoms arrange themselves in a particular order with translational symmetry, i.e. forming crystals with long-range ordering. This was discovered early on by the use of X-rays, as diffraction from crystals gives rise to particular patterns with very bright diffraction peaks in certain directions [165].

In a crystal an atom (or set of atoms) repeats itself along certain directions, and a lattice can be formed in 3 dimensions by,

$$\mathbf{R} = n_1\mathbf{a}_1 + n_2\mathbf{a}_2 + n_3\mathbf{a}_3\,, \tag{C.1}$$

where $\mathbf{a}_i$ are lattice vectors giving the directions and periods in which the structure repeats itself and n_i are integers. In describing a crystal the choice of lattice parameters is not unique, and for example doubling the length of a lattice vector gives rise to the same crystal. One way to reduce the amount of options for choosing lattice vectors is to choose the vectors so that the volume is as small as possible, and contains only a single lattice point, which is called the primitive unit cell. However, in terms of intuitively visualizing the crystal structure the primitive unit cell may not always be convenient, and so there is a set of unit cells called conventional unit cells reflecting certain symmetries. The usual definition of unit cell parameters is shown in figure C.1, in which the lengths of the lattice vectors are labeled a, b, and c, and the angles in between the lattice vectors are labeled α, β, and γ.

Name	Lattice restrictions	Body	Face	Side
Triclinic	$a \neq b \neq c$ $\alpha \neq \beta \neq \gamma \neq 90°$	-	-	-
Monoclinic	$a \neq c$ $\alpha = \beta = 90°\,,\ \gamma \neq 90°$	-	-	Yes, on ab-plane
Orthorhombic	$a \neq b \neq c$ $\alpha = \beta = \gamma = 90°$	Yes	Yes	Yes
Tetragonal	$a = b \neq c$ $\alpha = \beta = \gamma = 90°$	-	Yes	-
Rhombohedral	$a = b = c$ $\alpha = \beta = \gamma \neq 90°$	-	-	-
Hexagonal	$a = b$ $\alpha = \beta = 90°\,,\ \gamma = 120°$	-	-	-
Cubic	$a = b = c$ $\alpha = \beta = \gamma = 90°$	Yes	Yes	-

Table C.1: The table shows a list of the 14 Bravais lattices along with the requirements to their unit cell, and whether additional lattice points are required in a body-centered, face-centered, or side-centered position. The lattices are listed from lowest to highest symmetry.

There are 7 conventional unit cells, and for example for cubic symmetry a cubic unit cell is chosen, in which $a = b = c$ and $\alpha = \beta = \gamma = 90°$. However, there are other choices of unit cells that allow cubic symmetry, but by forcing the non-primitive cubic unit cell, other lattice points may be allowed in the unit cell. In case of the cubic unit cell also a body-centered cubic and face-centered cubic cell is required, in which an additional lattice point is placed in the center of the cube and on each face of the cube, respectively [131]. By considering all possible symmetry operations, 14 unique unit cells are found, named the Bravais lattices. These 14 lattices are listed

in table C.1 along with their unit cell requirements, and whether a body-centered, face-centered, or side-centered unit cell exists as well. The side-centered unit cell has a lattice point on the center of two opposing sides of the unit cell.

As alluded to earlier the lattice points in the crystal can be occupied by a single atom, group of atoms, or even entire molecules. The group of atoms on each lattice point is called the basis of the crystal. For example table salt (NaCl) has the so-called rock-salt crystal structure, where the Bravais lattice is face-centered cubic (FCC) and the basis consists of Na at (0,0,0) and Cl at (1/2,1/2,1/2) using coordinates relative to the unit cell. The structure can be seen in figure C.2.

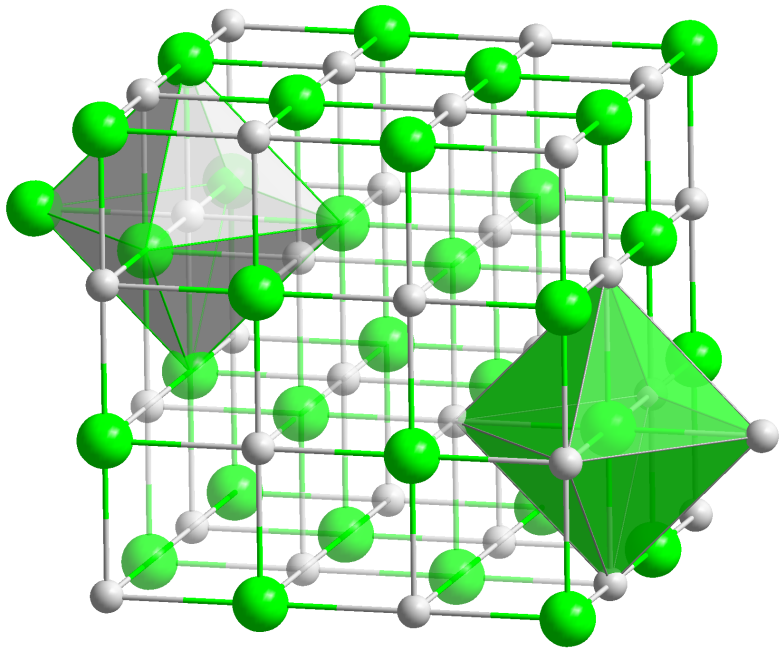

Figure C.2: The figure shows the crystal structure of NaCl, otherwise known as the rock-salt crystal structure. The lattice is face-centered cubic (FCC), and the atomic basis is a Na atom at (0,0,0) and a Cl atom at (1/2,1/2,1/2) in relative coordinates. The creates two interleaved FCC structures of Na and Cl atoms. The figure is from [166].

In the 14 different Bravais lattices different symmetry operations allowed, such rotation axes, mirror planes, and glide planes. All the possible combinations of allowed symmetry operations form the 230 space groups, which have all been tabulated [167]. Another example of a material with an FCC structure is Pt metal, which has just a single Pt atom as basis, and Pt as well as NaCl are in space group 225. This is a very high symmetry space group that has 48 symmetry operations allowed as well

as 3 translations. This means that an atom placed at point (x, y, z) must also occur on all positions generated by all the symmetry and translational operations. In the case of Pt the atom is at (0,0,0), and all the symmetry operations gives the same (0,0,0) position, so only the 3 translations give rise to more atoms in the cubic cell, and so there are 4 Pt atoms in the cubic cell. Similarly Na and Cl are placed at high symmetry positions giving rise to 8 atoms, 4 Na and 4 Cl, in the cubic cell. These special high symmetry sites are called Wyckoff sites, and in the case of NaCl the Na atom is at Wyckoff site a and Cl is a Wyckoff site b for the space group number 225, and they both have a multiplicity of 4 due to the translations. However, if an atom is placed at a general site (x, y, z) (Wyckoff site l), in which the symmetry operations do not lead to replication of any sites, the cubic cell will have 192 atoms due to the combination of the 48 symmetry operations and 3 translations.

C.2 Detecting diffraction patterns

In this section only diffraction patterns obtained with a monochromatic X-ray beam is discussed. Another technique using a 'white' (or more likely 'pink'[1]) X-ray beam can record diffraction data in a different way, which is called Laue-patterns, which will not be discussed further.

When determining which reciprocal lattice points fulfill the diffraction condition, the Ewald sphere construction is very helpful. This construction is in reciprocal space, and consists of a spherical shell placed at the origin with a radius of $k = 2\pi/\lambda$, the wave number of the incoming X-ray photons. The shell represents all the momenta reachable by an elastic scattering event. The reciprocal lattice of the sample crystal is placed at the periphery of the sphere in the direction of the direct beam. In this construction the diffraction spots that are allowed are given by the intersection of the Ewald sphere shell and reciprocal lattice points. The construction is shown in figure C.3, indicating that the intersections of the Ewald sphere and reciprocal lattice points give rise to diffraction spots on a detector.

The typical setup for measuring diffraction patterns, especially single crystal diffraction, is a so-called diffractometer. This device can rotate the sample and detector on a different number of rotation axes, all centered on the sample itself. Diffractometers come with different numbers of rotation circles, and some of the more advanced diffractometers have 6 rotation circles, typically with 2 circles for the detector and 4 circles for the sample (4S + 2D). This allows the detector and sample, and therefore reciprocal lattice, to be rotated so as to fulfill the diffraction condition of desired lattice points. Having 6 circles gives multiple options for reaching the diffraction conditions, and so gives flexibility in moving the sample, allowing complex

[1] An ideal white beam has the same intensity at all frequencies, but the radiation from bending magnets or wigglers produce a spectrum that drops off dramatically at a given critical energy. This spectrum has relatively more low frequency intensity than high frequency, and with a reference to visible light this is called pink light.

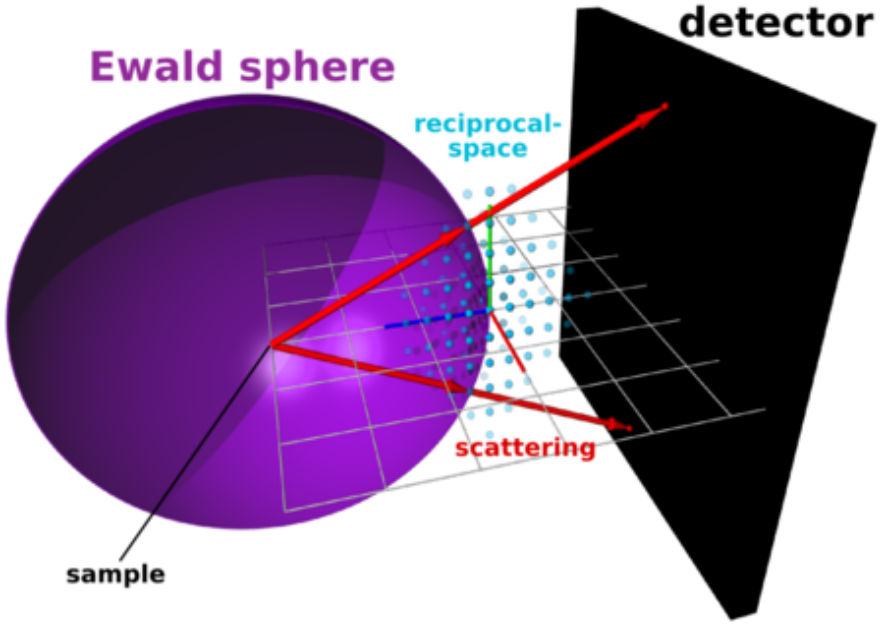

Figure C.3: The figure shows the Ewald sphere construction in reciprocal space. The sphere has a radius of $k = 2\pi/\lambda$, and represents the momentum transfers obtainable from elastic scattering. The reciprocal lattice of the sample crystal is placed at the periphery of the Ewald sphere, and and whenever the sperical shell intersects with a lattice point the diffraction condition is fulfilled. This means that the intensity of the given diffraction spot can be measured with a detector. The figure is from [168].

sample environments to be used. Such a diffractometer is shown in figure C.4 in which all the rotation circles have been set at their 0° position.

Traditionally detectors on diffractometers were point-detectors, which can only record the diffracted intensity right at the angular position of the detector. This can be quite challenging if the crystal structure is complex, since a large number of diffraction spot intensities must be measured. It is even more challenging if the crystal structure is unknown, since surveying a reasonably large area of the reciprocal space is unfeasible. More recently area detectors have become more wide-spread, and in particular the Pilatus series detectors from Dectris are quite popular. They manufacture arrays of 100.000 pixels, and detectors with multiple arrays provide up to 6.000.000 pixels. When using an area detector rather than a point detector a much larger fraction of reciprocal space may be measured simultaneously.

Beam lines specialized for biological sample XRD are often equipped with an area

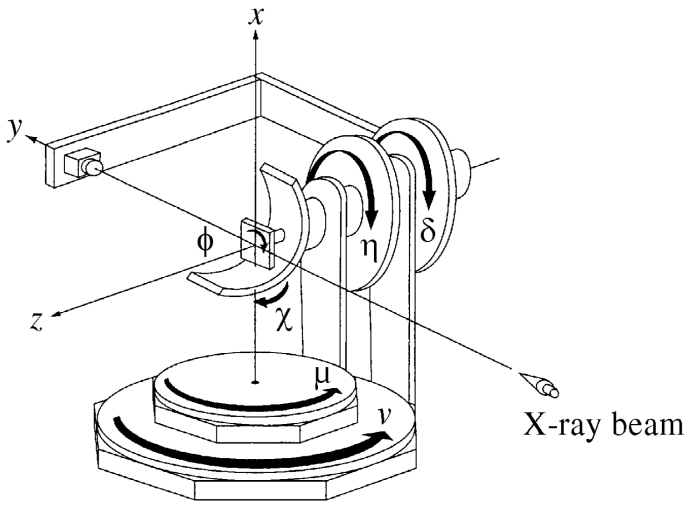

Figure C.4: The figure shows a typical 6-circle diffractometer with 4 sample circles (ϕ, χ, η, and μ) and 2 detector circles (δ and ν). The order of the circles can vary, and different naming conventions exist, and the circle names here are part of the so-called 'PsiC' mode. The combination of the 6 circles provide many options to reach the diffraction condition for a given reciprocal lattice point, which gives flexibility in having a complex sample environment. The figure is from [135].

detector so large that the detector circles of the diffractometer are unnecessary, and are only equipped with sample circles. These biological samples are then rotated, and in a very short time all the visible diffraction peaks have been recorded. Computer programs have been developed to automatically index the diffraction peaks according to the reciprocal lattice (give them an h, k, and l value).

In our case the crystal structures investigated were unknown, and multiple structures were expected in each sample. Therefore for one sample we used a modest sized Pilatus detector with 300.000 pixels mounted on a 6-circle diffractometer to record a large fraction of reciprocal space. On another sample we used a larger and slower MAR345 imaging plate detector, although the principle is the same. In our case the automatic indexing would not work, since the samples had multiple crystal structures, so we developed our own data processing programs to stitch all the diffraction images into a single 3-dimensional dataset showing the intensity as a function of $\mathbf{Q}$, the 3D momentum transfer vector.

Here we will go though the algorithm for constructing the 3D dataset:

1. Calculate the exact coordinate of each pixel of the detector in lab coordinates.

2. Use the detector coordinates to calculate the momentum transfer in circular coordinates, Q and χ_c.

3. (Optional) Remove diffuse background intensity.

4. (Optional) Calculate and apply intensity corrections (see section 6.5).

5. From the diffractometer angles calculate the in-plane, $Q_\parallel$, and out-of-plane, $Q_\perp$, components of the momentum transfer vector, relative to the sample surface, for each pixel.

6. Interpolate the intensity by using the $Q_\parallel$ and $Q_\perp$ as coordinates rather than the pixel numbers. This is done for every position of the crystal, and if more images have been recorded to extend the range in Q-space they will be merged.

7. The direction of the in-plane component $Q_\parallel$ depends on the $Q_\parallel/Q_\perp$ ratio, and this is corrected, so that the dataset is now in cylindrical coordinates, $Q_\parallel$, $Q_\perp$, and ϕ_c.

8. (Optional) Convert coordinates to Cartesian or polar coordinates.

In step 1 a calibration scan is done with a polycrystalline LaB_6 crystal for each position of the detector, and the program WxDiff developed at SSRL [169] can be used to extract the position and orientation of the detector.

From the coordinates of each pixel the magnitude of the scattering vector can be calculated from the scattering angle, θ,

$$2\theta = \arccos\left(\frac{y}{\sqrt{x^2+y^2+z^2}}\right), \tag{C.2}$$

using the coordinate system shown in figure C.4. Similarly the direction of the scattering is calculated by the azimuthal angle, χ_c,

$$\chi_c = \arctan\left(\frac{x}{z}\right). \tag{C.3}$$

The angles χ_c and ϕ_c are computed angles for each pixel position, but rotations around these axes are equivalent to rotations of the diffractometer χ and ϕ circles, respectively.

Decomposing the momentum transfer vector into an in-plane and out-of-plane component comes down to the intersection of a sphere (the Ewald sphere) and a cylinder. The intersection point on the sphere is given by the magnitude Q (radius), the scattering angle 2θ (polar angle), and the angle χ_c (azimuthal angle), and on the cylinder it is described by the radius of the cylinder, $Q_\parallel$, the height, $Q_\perp$, and the azimuthal angle ϕ_c. Figure C.5 shows the definition of these angles in relation to Cartesian coordinates. In this way $Q_\parallel$, $Q_\perp$, and ϕ_c may be calculated from Q and χ_c. The construction of the intersecting Ewald sphere and cylinder is seen in figure

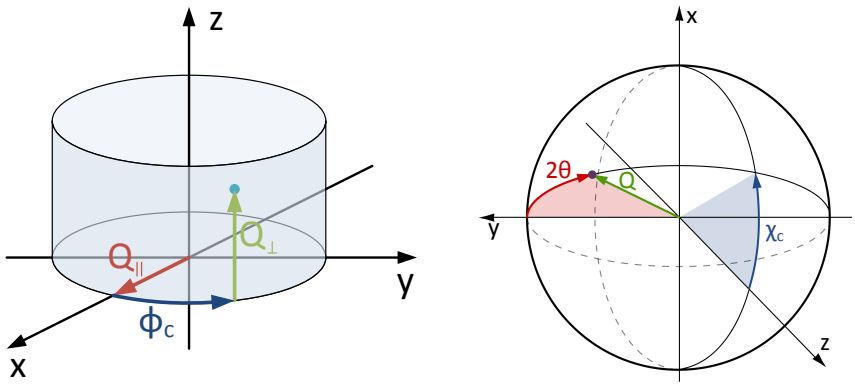

Figure C.5: The figure shows cylindrical coordinates used for the sample (left), which are determined from the scattering angles seen on the Ewald sphere (right). The right figure with the sphere is adapted from [170].

C.6, in which the crystal surface normal is parallel to the diffractometer ϕ rotation axis, $\chi = 90°$, and $\eta = 10°$, similar to measurements presented later.

In the following it is assumed that the crystal surface normal is parallel to the ϕ rotation axis and $\mu = 0$. The sphere is centered on the origin, and the Cartesian coordinates are,

$$\begin{bmatrix} x_s \\ y_s \\ z_s \end{bmatrix} = \begin{bmatrix} k\sin(\chi_c)\sin(2\theta) \\ k\cos(2\theta) \\ k\cos(\chi_c)\sin(2\theta) \end{bmatrix}, \tag{C.4}$$

where again the radius is the incoming X-ray wavenumber, the polar coordinate is the scattering angle, 2θ, and the azimuthal angle is χ_c, which was defined earlier. The cylinder axis is parallel to the ϕ axis this does not affect the Cartesian coordinates,

$$\begin{bmatrix} x_c \\ y_c \\ z_c \end{bmatrix} = \begin{bmatrix} Q_{\parallel}\cos(\phi_c)\cos(\chi)\cos(\eta) + Q_{\perp}\sin(\chi)\cos(\eta) + Q_{\parallel}\sin(\phi_c)\sin(\eta) \\ k + Q_{\parallel}\sin(\phi_c)\cos(\eta) - Q_{\parallel}\cos(\phi_c)\cos(\chi)\sin(\eta) - Q_{\perp}\sin(\chi)\sin(\eta) \\ Q_{\perp}\cos(\chi) - Q_{\parallel}\cos(\phi_c)\sin(\chi) \end{bmatrix}. \tag{C.5}$$

These coordinates comes from a cylinder with radius $Q_{\parallel}$, height $Q_{\perp}$, and azimuthal angle ϕ_c. This cylinder has then been rotated by χ around the y-axis followed by a rotation of $-\eta$ around the z-axis, see the rotation circles and sense in figure C.4. The intersection of the sphere and cylinder is found by equating the Cartesian coordinate components. But before doing so it is possible to simplify the expression by exploiting the definition of χ_c; the point of $\chi_c = 0$ is chosen arbitrarily, and moving the χ circle simply adds a constant to χ_c. So for the derivation we can simply fix $\chi = 90°$, and any change from this angle can be added to χ_c. When doing this we need to replace η by the incidence angle of the incoming X-ray beam,

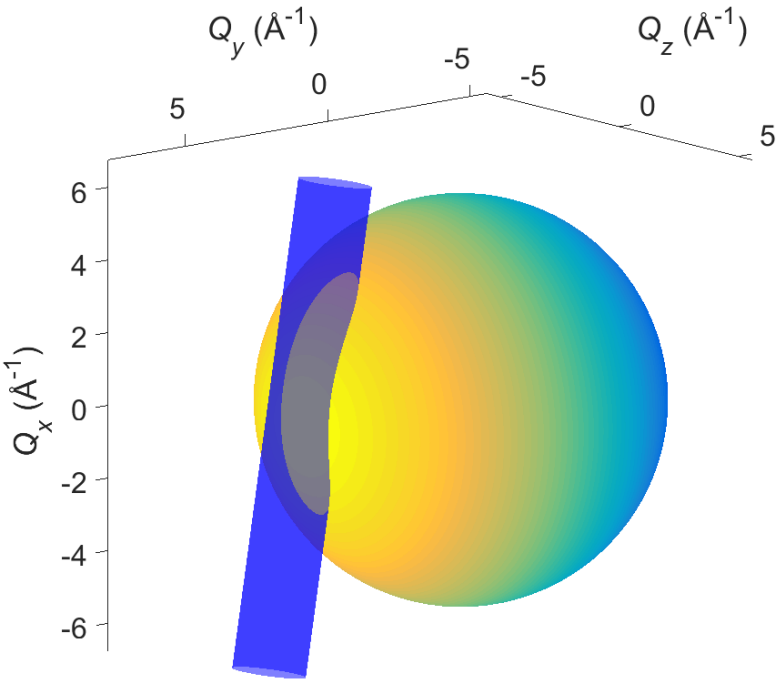

Figure C.6: The figure shows the Ewald sphere being intersected by a cylinder, representing the $Q_{\parallel}$ and $Q_{\perp}$ components. This construction relates Q and χ_c on the sphere to the Q-components and ϕ_c on the cylinder. In this particular example the sample surface normal is parallel to the ϕ rotation axis, $\chi = 90°$, and $\eta = 10°$.

$$\alpha = \arcsin[\sin(\eta)\sin(\chi)]\,. \tag{C.6}$$

Setting $\chi = 90°$ and replacing η by α we get,

$$\begin{bmatrix} x_c \\ y_c \\ z_c \end{bmatrix} = \begin{bmatrix} Q_{\parallel}\sin(\phi_c)\sin(\alpha) + Q_{\perp}\cos(\alpha) \\ k + Q_{\parallel}\sin(\phi_c)\cos(\alpha) - Q_{\perp}\sin(\alpha) \\ -Q_{\parallel}\cos(\phi_c) \end{bmatrix}\,. \tag{C.7}$$

Now we can equate the coordinates for the Ewald sphere and cylinder,

$$k\sin(\chi_c)\sin(2\theta) = Q_{\parallel}\sin(\phi_c)\sin(\alpha) + Q_{\perp}\cos(\alpha)\,, \tag{C.8}$$

$$k\cos(2\theta) = k + Q_{\parallel}\sin(\phi_c)\cos(\alpha) - Q_{\perp}\sin(\alpha)\,, \tag{C.9}$$

$$k\cos(\chi_c)\sin(2\theta) = -Q_{\parallel}\cos(\phi_c)\,. \tag{C.10}$$

Solving these coupled equations yields a simple expression for $Q_\perp$,

$$Q_\perp = k\left[\sin(\alpha) - \cos(2\theta)\sin(\alpha) + \cos(\alpha)\sin(\chi_c)\sin(2\theta)\right] . \tag{C.11}$$

Then utilizing that the components of Q are perpendicular,

$$Q_\parallel = \sqrt{Q^2 - Q_\perp^2} . \tag{C.12}$$

When these components have been calculated the cylinder azimuthal angle may be calculated,

$$\phi_c = \arccos\left(-\frac{k}{Q_\parallel}\cos(\chi_c)\sin(2\theta)\right) . \tag{C.13}$$

Converting the intensity data to be a function of $Q_\perp$, $Q_\parallel$, and ϕ_c is done by two rounds of interpolation, and a complete 3D dataset is obtained. From these cylindrical coordinates one can easily calculate Cartesian or polar coordinates, and use one more round of interpolation to convert the dataset coordinates. Appendix F shows the MatLab code used for processing the data.

The diffraction data presented in this thesis were obtained at beam line 1-5 and 7-2, see appendix E.1 and E.3 for details of these beam lines.

APPENDIX D

In-situ measurement setups

Conventional X-ray experiments are carried out in air (or maybe He) at atmospheric pressure and room temperature (at least for hard and tender[1] X-rays). However, this environment is very far from the working conditions of the materials we study, which are in aqueous or solid electrolyte and under electrical potential. Insight may be gained from ex-situ experiments, however the detailed atomic and electronic structure at the surface may be highly dependent on the environment. This calls for in-situ experiments to study samples under relevant conditions. Some experiments are classified as in-operando, which means that the conditions are very close to the actual operating conditions of the material, whereas in-situ are also used to classify experiments that has an environment closer to operating conditions but are still far from the actual conditions in one or more parameters.

When designing in-situ experiments we are often helped by the fact the X-rays interact relatively weak with matter compared to e.g. electrons. In addition, the higher X-ray energy the less it interacts with matter, often making the design requirements of the setup less stringent. Figure D.1 shows the calculated attenuation length ($1/\mu$) in µm as a function of photon energy over a large energy span for some selected materials. The attenuation length parameter describes the thickness needed to reduce the transmitted intensity by a factor of e. X-rays interact stronger with heavier elements, and so Be ($Z = 4$) is often the choice for X-ray windows in beam lines, for example separating the ultra-high vacuum in the storage ring from the ambient conditions at the experimental station. On the other end of the scale is Pt ($Z = 78$) with a very low attenuation length, even at very high photon energies, and so if the sample contains Pt any kind of transmission may not be feasible. Much closer to Be we find water, the major component of aqueous electrolyte, as well as glassy carbon and Kapton foil. Glassy carbon is often used as a sample support in electrochemical experiments, since it is considered mostly inert in aqueous electrolyte. Kapton foil is an X-ray resistant polymer often used in design of in-situ cells at synchrotrons. At tender X-ray energies (2-5 keV) water has an attenuation length in the order 10-100 µm, and penetration though water should be avoided. At hard X-ray energies (> 5 keV) the attenuation

[1] Sometimes the energy range 2-5 keV in between soft and hard X-rays are called tender X-rays.

length of water is 0.1-10 mm, and designing experiments in which the X-rays pass through the electrolyte becomes possible.

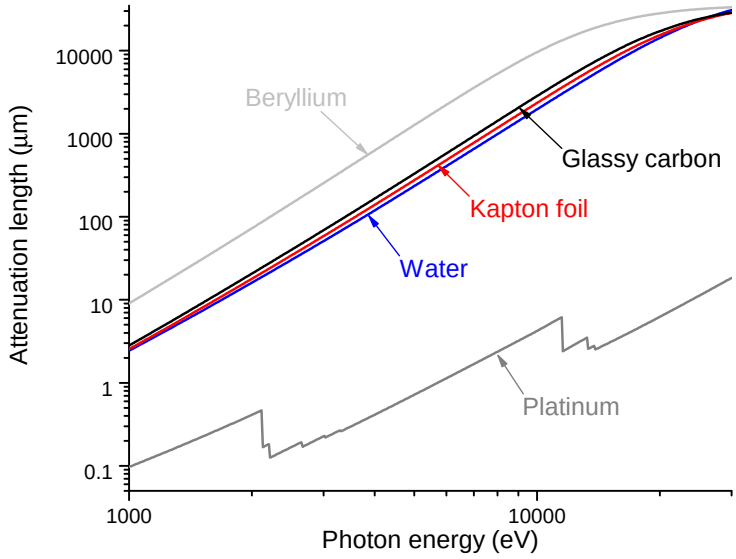

Figure D.1: The figure shows the calculated attenuation lengths ($1/\mu$) in µm as a function of photon energy for selected materials. X-rays are absorbed more strongly by heavier atoms and at lower photon energies, which are both seen clearly from this graph. In the tender X-ray energy range (2-5 keV) the attenuation length of water is on the order 10-100 µm, and it is best to avoid having the X-rays go through water. Whereas at hard X-ray energies ($>$ 5 keV) the attenuation length quickly increases to above 1 mm, making cell designs with electrolyte penetration possible. The calculations were performed on the CXRO website [171].

D.1 Hanging meniscus type cell

The hanging meniscus type cell has a small droplet of electrolyte on the surface of the sample, in order to minimize the X-ray path length through the liquid. A picture of such a cell is seen in figure D.2, which is the particular cell used in several experiments presented here. This cell was designed by Daniel Friebel *et al.* [172]. The sample (working electrode) is mounted on the bottom and an electrical connection is made,

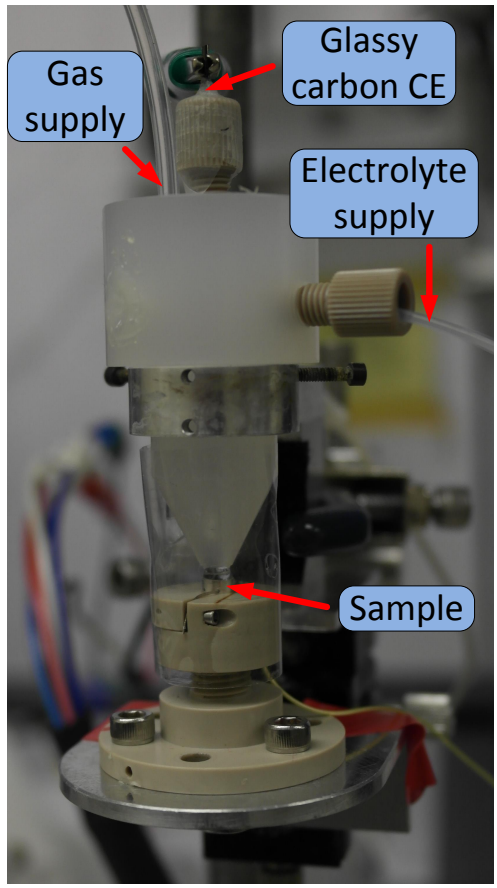

Figure D.2: The figure shows a picture of the hanging meniscus type in-situ cell used for several experiments presented here. The sample (working electrode) is mounted on the bottom and the main electrolyte chamber housing the counter and reference electrodes are suspended above. A motorized syringe is used to control the flow of electrolyte accurately so that the size of the meniscus can be adjusted. The foil around the sample allows for a controlled atmosphere to saturate the electrolyte with a gas and keep a humidified atmosphere to reduce evaporation from the meniscus. The sample is a 5 mm diameter Pt(111) single crystal.

and the main electrolyte chamber housing the counter and reference electrodes are suspended above. A polymer foil may be wrapped around the cell to control the atmosphere and saturate the electrolyte with a particular gas and keep a humidified atmosphere to reduce evaporation from the meniscus. The size of the meniscus is controlled by a motorized syringe that allows fine adjustment of the electrolyte volume. When a circular sample with a 5 mm diameter is used (as shown on the picture) the volume of the meniscus is about 60 µl.

A cross section of the cell is seen in figure D.3, in which the electrode connection ports and the tube for gas flow is seen. The cell has two additional ports identical to the reference electrode port on the side, which can be used to connect the electrolyte supply or an alternative counter electrode.

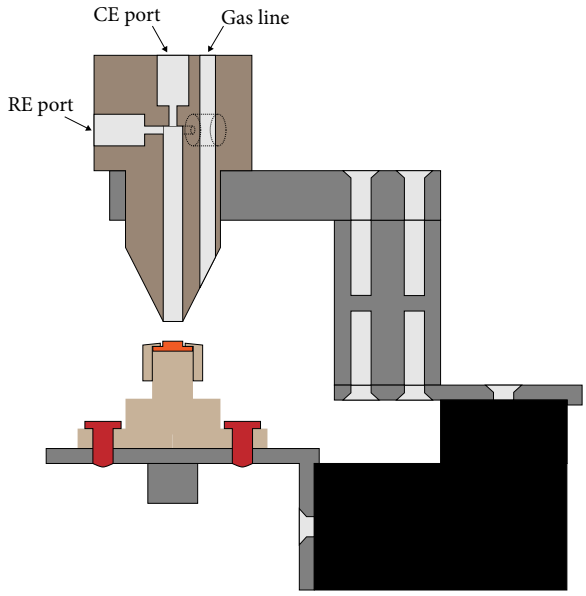

Figure D.3: The figure shows a sketch of the cross section of the hanging meniscus type cell. In this view the top port connector is seen, typically used for the counter electrode, the tube for allowing gas flow to the front of the nozzle, and one of three side connector ports, often used for the reference electrode. The other two side ports (placed at 120° rotation when seen from the top) are used to connect the electrolyte supply and an alternative counter electrode.

This type of cell has great freedom in choosing the sample and technique, since the meniscus can be mounted in any orientation and remains stable even if moved around on a diffractometer. Since the X-rays do not penetrate the substrate, the sample may be a solid Pt single crystal or thin films and nanoparticles on flat substrates. This cell

is also highly suited for grazing incidence measurements, since there are no parts of the setup blocking the sides (except the arm holding the cone, which can be rotated).

The only compromise of this cell is that a significant amount of electrolyte must be penetrated, e.g. for a 5 mm diameter disk the path length through the electrolyte may be 4-6 mm. This limits the X-ray energy to be at least 10 keV to ensure that the attenuation length through water is at least a few millimeters. For example the transmission through 5 mm of water at 11.5 keV photon energy (around Pt L_3 edge) is around 20%.

Another effect to consider is that the water scatters X-rays a lot more than air, and so XRD experiments will have a higher background and in XAS experiments elastically scattered intensity will be much higher. Figure D.4 shows an image from a Pilatus 300K pixel detector at a diffraction experiment where the detector is placed directly in the line of the direct beam (the bottom part of the detector is covered by lead foil so the direct beam does not hit the detector). It is seen that the electrolyte scatters X-rays strongly, and that the top part of the cell shadows some of the scattered X-rays, forming an image of the cell. In the right image the color scale is chosen differently revealing the concave shape of the meniscus at this point during the experiment.

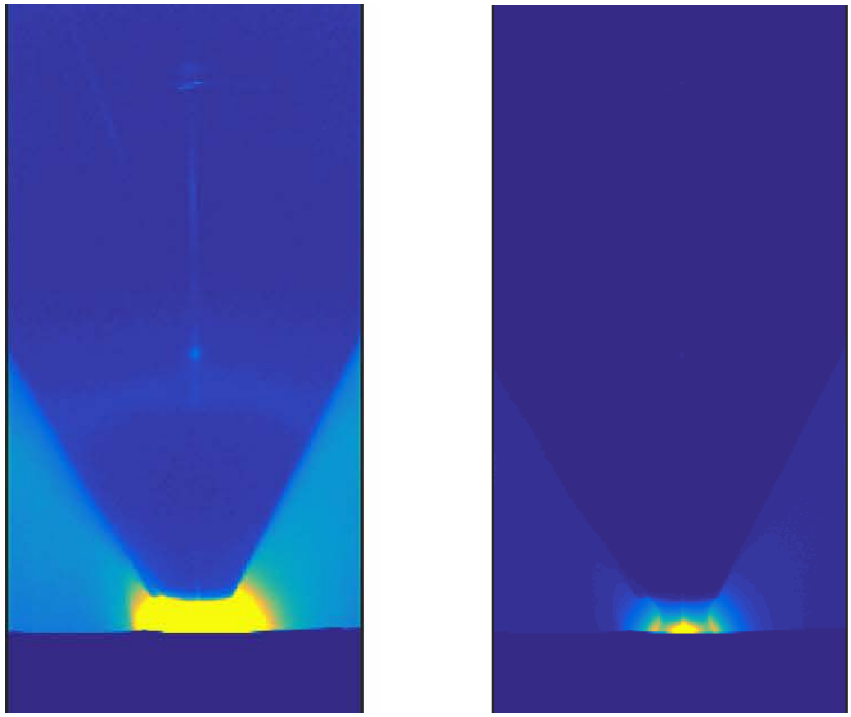

Figure D.4: The figure shows an image from a Pilatus 300K with different color scales. On the left image it is clearly seen how the electrolyte scatters a lot of X-rays, and that the cell covers some of it making a shadow on the detector. On the right panel the color range has been increased to show the details around the electrolyte meniscus, and in this image it is possible to see the concave shaped meniscus at this point during the experiment.

D.2 Back illumination type cell

At lower photon energies it is essential to reduce the X-ray path length through the electrolyte. One option is to avoid the electrolyte entirely, and instead have the X-rays enter and exit the cell through the sample substrate. This works well for sputter deposited thin films and nanoparticles which are either physically deposited or dropcast by ink. Such a cell is seen in figure D.5 which consists of a 50 ml polypropylene bottle with the sample substrate glued onto the side covering a hole in the bottle.

A schematic of the inside of the cell is seen in figure D.6. Since the X-rays do not go through the electrolyte compartment it can be quite large, making it easier to fit electrodes and gases.

Figure D.5: The figure shows pictures of a back illumination cell where the sample material is deposited on the inside on the black glassy carbon window. On the left picture the cell is mounted at an XAS beam line, and the X-rays come from the right at 45° incidence angle on the cell, and exits towards the camera with a 45° exit angle. The right picture shows the entire cell.

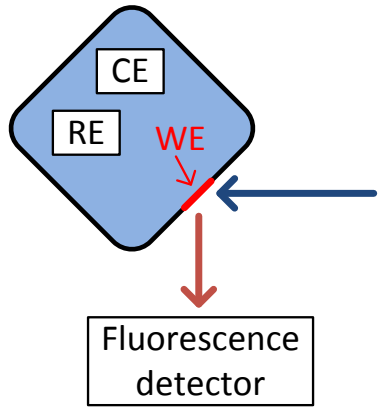

Figure D.6: The figure shows a sketch of the electrochemical setup inside the back illumination cell. The working electrode is on the thin membrane window as discussed, and the reference and counter electrodes are placed in the large electrolyte volume. This setup allows a high degree of freedom on the electrochemical side, e.g. gases could be introduced.

Choosing the window material depends on the application, but membranes made of Si_3N_4 on a Si frame are quite popular and are commercially available down to less than 10 nm thickness. However, when used for electrochemistry the surface of the membrane must be conductive, which can be achieved by coating with a metal, e.g. gold.

We designed a cell for an in-situ XAS experiment measuring the Ru L_3 edge at 2838 eV, which is challenging due to the high absorption of most materials at this photon energy. We chose to make thin glassy carbon windows, which has several benefits over the Si_3N_4; glassy carbon is intrinsically conductive, the lower atomic number means a much thicker membrane will have the same absorption, and Si fluorescence is avoided (as well as Au fluorescence if used as a conductive coating).

Glassy carbon membranes less than 10 µm thick were not available commercially when we designed the experiment, so we made our own. This was done by pyrolizing an 8 µm thick Kapton foil in an inert Ar or N_2 atmosphere at 1000 °C for 40 minutes [173–175]. A picture of the pyrolysis setup is shown in figure D.7, which consists of two graphite plates holding the Kapton foil pieces and two stainless steel bars clamping the whole thing together. This setup goes into a 1 inch diameter quartz tube in a tube furnace.

This back illumination cell works very well for the XAS experiment, and we get a total transmission of both the incoming X-rays (at 2838 eV) and the fluorescence X-rays (at 2558 eV) of about 65%.

The downside of working with this setup is the limited incidence and exit angles, as well as limitations on choice of substrate that allows X-rays to penetrate. The electrolyte inside the cell is still illuminated by the X-rays, and so strong scattering is present as for the hanging meniscus cell.

D.3 Other cell designs

Another cell design found in the literature is a thin electrolyte film setup. In this setup the electrolyte on the sample surface is covered by a polymer film, e.g. Kapton foil, which allows to reduce the thickness of the water layer down to less than 100 µm. This drastically increase the transmission of X-rays at not too grazing incidence angles as compared to the hanging meniscus setup, as well as reduces the scattering since the amount of liquid is reduced. This type of setup has not been used for the experiments presented here, and will not be discussed any further.

In recent years the 3D printing technology has improved dramatically, which allows for cell designs that are otherwise impossible to machine. This could for example be a thin film electrolyte flow cell with exposed edges that allows for grazing incidence measurements. In such a cell electrolyte channels can be integrated into the cell material.

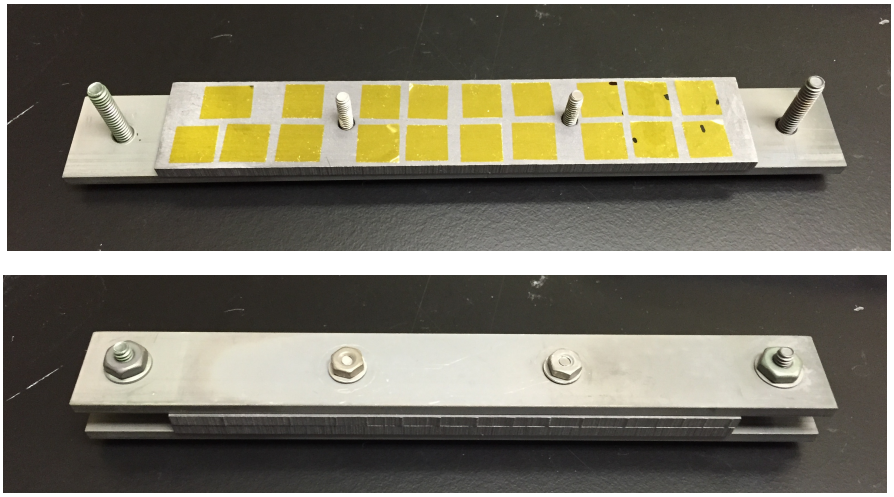

Figure D.7: The figure shows pictures of the setup used to pyrolyze the Kapton foil forming thin glassy carbon sheets. The plates holding the Kapton foil are made of graphite whereas the bars used to clamp the whole setup is stainless steel, and so are the screws and nuts. The pieces of Kapton foil shown here are 10×10 mm^2 and 8 µm thick. The setup is designed to be heated in a 1 inch diameter quartz tube in a tube furnace.

APPENDIX E

Beam lines

This section describes the setup at the different beam lines used for the experiments presented in this thesis.

E.1 Beam line 1-5

Beam line 1-5 is a bending magnet beam line providing hard X-rays in the range 4.6-16 keV, and is built in the same place where the first beam line opened in the 70's. The beam line has now been rebuilt to perform small angle X-ray scattering (SAXS) experiments, but when we did experiments it was set up for wide angle scattering. It was equipped with a Huber Kappa goniometer with the ϕ-axis perpendicular to the θ-axis. This allowed us to rotate the sample around its surface normal (equivalent to the ϕ-rotation on BL7-2) and change the incidence angle (equivalent to the η-rotation on BL7-2). This beam line also has a laser system for aligning the sample surface.

This beam line has a MAR345 imaging plate that allows a large solid angle to be covered. The detector is based on a material that gets excited upon X-ray exposure, and during readout a laser diode relaxes the material, sending out fluorescence light whose intensity is proportional to the X-ray dose on that given spot. The readout process happens by physically spinning the imaging plate at high rotation speeds, and then using a laser diode to read out the intensity radially. This data is transformed to a square image of 3450×3450 pixels, but only has data in the inscribed circle of the square. The whole readout process at this resolution takes about 90 seconds, so even though a large solid angle is covered using this detector a reciprocal space survey experiment is still time consuming.

Figure E.1 shows a picture of the beam line, in which the direct beam comes from the bottom left. The X-rays are scattered and is detected on the large black imaging plate, and the direct beam is blocked by a small diode encased in lead to prevent damage to the detector. The ϕ and ω circles in this particular setting of the Kappa goniometer are equivalent to the ϕ and η circles on the 6-circle diffractometer. By having the large detector it becomes unnecessary to move the detector and stitch multiple exposures.

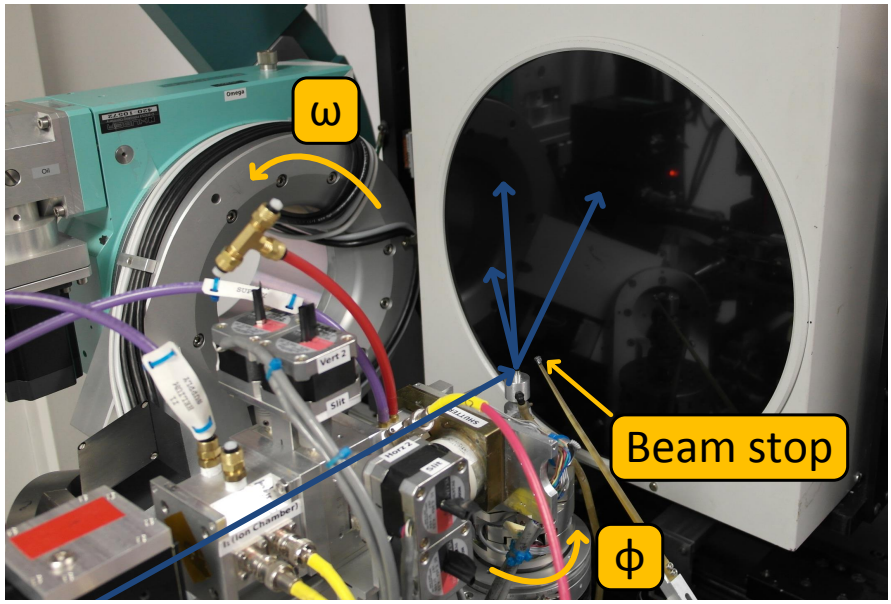

Figure E.1: The figure shows a picture of the setup at BL1-5 before it was rebuilt for small angle X-ray scattering (SAXS) experiments. The beam enters from the bottom left, and the scattered X-rays are detected by the large black MAR345 imaging plate detector. The direct beam is blocked by a diode encased in lead to prevent it from damaging the detector by a direct exposure. In this particular setting of the Kappa goniometer the ϕ axis rotates the sample around its surface normal and the ω axis sets the incidence angle, and so these two rotations are similar to the ϕ and η rotations on the 6-circle diffractometer.

E.2 Beam line 6-2

Beam line 6-2 is the central experimental station at the beam line 6 wiggler, delivering focused hard X-rays in the range 4-18.2 keV. The beam line has two monochromator crystal sets, one that provides a high flux peak flux of 2×10^{13} photons/s at a typical resolving power of $E/\Delta E \approx 10000$, and one that provides a higher energy resolution of $E/\Delta E \approx 33000$ at the cost of a reduced peak flux of 3×10^{12} photons/s.

The experimental station is equipped with a Johann-type spectrometer with a set of 7 bent crystals arranged on separate Rowland circles [162]. In the Rowland circle geometry the analyzer crystal is placed on the periphery on a circle of radius R, and the origin (sample) and detector are positioned on the same periphery symmetrically above and below the analyzer crystal, as shown in figure E.2. In this geometry the Bragg diffraction condition is always fulfilled, and the distance between the sample

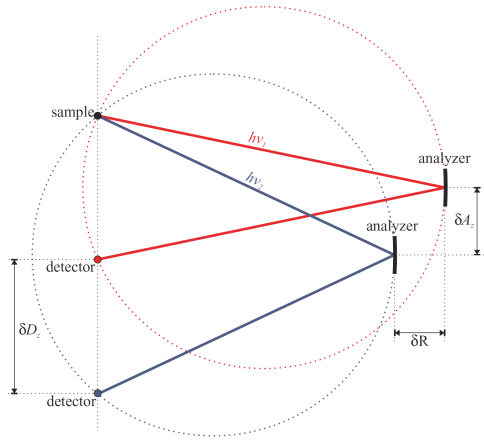

Figure E.2: The figure shows a schematic view of the Rowland circle geometry. By placing the sample and detector symmetrically above and below the analyzer crystal plane the Bragg diffraction condition is always satisfied, and the distance between the sample and detector determines which wavelength it is satisfied for. The figure is from [162].

and detector determines which wavelength it is satisfied for.

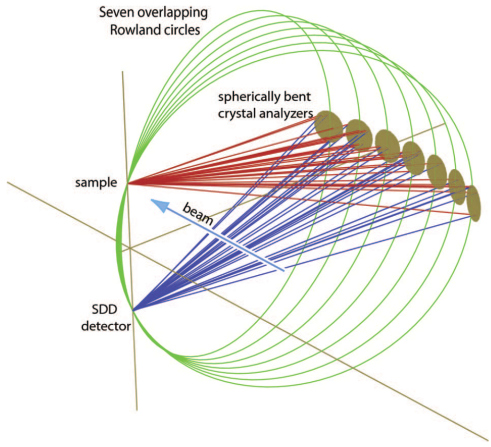

Figure E.3: The figure shows a diagram of the arrangement of the 7 Rowland circles with spherically bent crystals. By using more crystals the total signal detected may be improved, since a larger solid angle is covered. The figure is from [162].

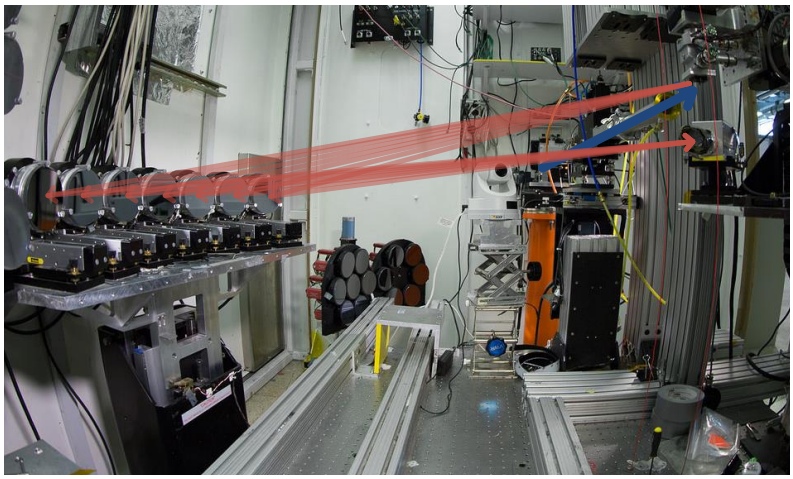

Figure E.4: The figure shows a picture from beam line 6-2, showing the incoming X-rays with the blue arrows, and the scattered fluorescence X-rays with the red arrows. During operation the space between the sample and the analyzer crystals is filled with a bag of He to reduce X-ray absorption in the air. The figure is adapted from [176].

For a flat analyzer crystal the diffraction conditions will only be fulfilled for the part of the crystal on the symmetry line of the Rowland circle. In the Johann spectrometer the analyzer crystal is bent with a radius of $2R$ to fulfill the Bragg condition for X-rays fitting the crystal away from the symmetry plane. By using a spherically bent crystal the X-rays are focused onto a single point where the detector is located. By combining an array of 7 bent crystals the Rowland circles are positioned to overlap, which allows a larger solid angle for detecting the signal. Figure E.3 shows a diagram of the positioning of the 7 Rowland circles relative to the sample and detector. Using this setup an energy resolution of 0.4 eV may be achieved at an emission energy of 6.5 keV [162].

E.3 Beam line 7-2

Beam line 7-2 is a central wiggler beam line providing focused hard X-rays in the range 5-17 keV. The experimental station is equipped with a Huber 6-circle diffractometer (4S + 2D), plus a goniometer head for sample alignment. A laser can be aligned to bounce off the sample surface so that the two goniometer head circles can be used to align the sample surface normal to the ϕ rotation axis. Furthermore, the goniometer head has an x-, y-, and z-stage to center the sample on the diffractometer center.

In terms of detectors this beam line provides a selection between Pilatus 100K (487 $\times$ 195 pixels) and Pilatus 300K (1475 $\times$ 195 pixels) pixel detectors, as well as typical point detectors and Vortex fluorescence detectors. The readout time for a Pilatus detector is a fraction of a second.

Figure E.5 shows a picture of the diffractometer, and the 6 six circles are shown. The beam comes from the right, scatters off the sample, and gets detected by a detector. In this picture a Pilatus 100K has been mounted far away from the sample to provide a high angular resolution over a small solid angle. For the survey type experiments described above the larger Pilatus 300K is preferred, and also placed close to the sample to cover a larger solid angle.

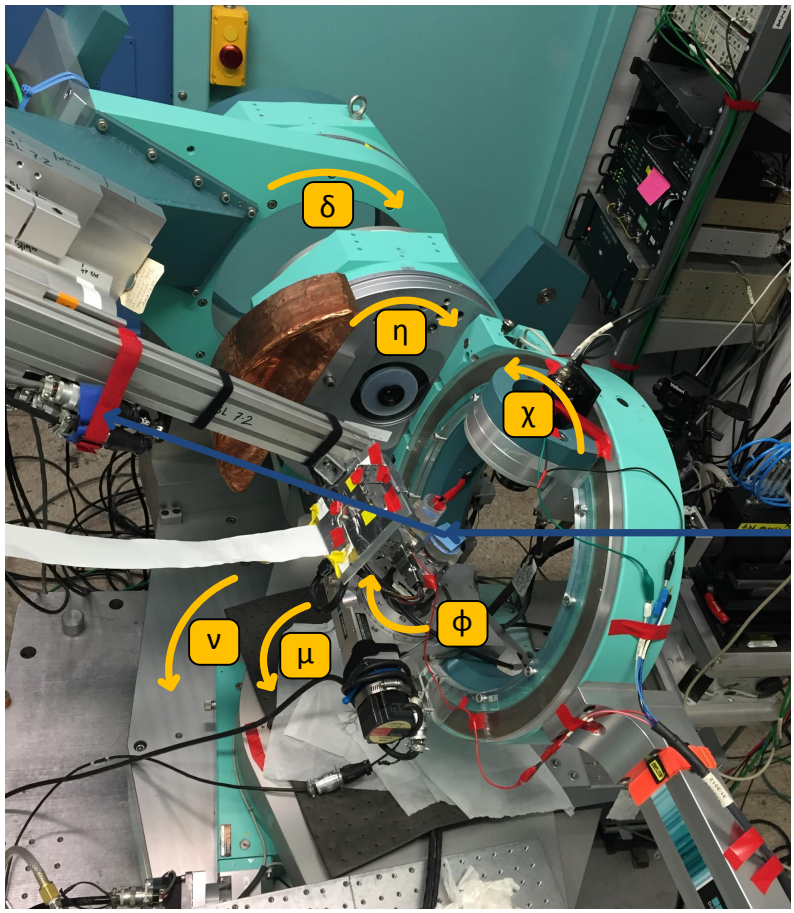

Figure E.5: The figure shows a picture of the 6-circle diffractometer on BL7-2. The names and sense of the 6 circles have been indicated, and the δ and ν circles move the detector whereas the ϕ, χ, η, and μ circles are rotating the sample. In this picture a Pilatus 100K detector has been placed a long distance from the sample to provide high angular resolution over a small solid angle. In a reciprocal space survey experiment the larger Pilatus 300K is preferred, and also placed closer to the sample to cover a larger solid angle.

E.4 Beam line 11-2

Beam line 11-2 at SSRL is the main station at the beam line 11 wiggler, and provides a focused beam in the range 5-20 keV. It is a hard X-ray XAS station, and so has ion chambers for doing XAS in transmission mode and a 100 element Ge semiconductor detector for fluorescence mode. This semiconductor detector is very sensitive and allows the detection of very dilute samples. See figure E.6 for a picture of the XAS setup at the beam line.

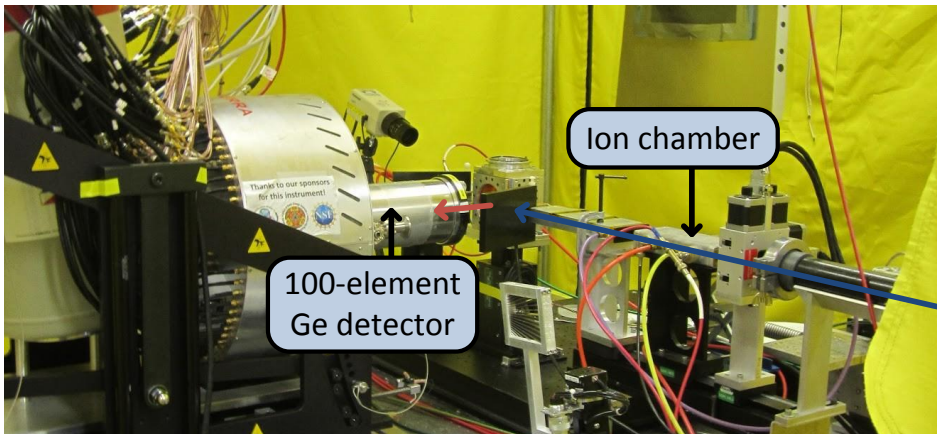

Figure E.6: The figure shows a picture of the beam line 11-2 hutch, in which the X-rays come from the right side (blue arrow) and the scattered fluorescence X-rays enter the 100-element Ge detector (red arrow). The intensity of the beam before hitting the sample is measured by the ion chamber.

Furthermore, the beam line can be set up in a grazing incidence geometry, that allows for a very surface sensitive measurement. For example when measuring a very low coverage of nanoparticles on a flat substrate the grazing incidence geometry becomes beneficial by illuminating a larger substrate area and therefore more nanoparticles, as well as enhancing the X-ray intensity by the surface due to the evanescent wave (see section 5).

This beam line has been used to measure EXAFS on Pt_xGd nanoparticles and thin films using the grazing incidence geometry. Both the Pt L_3 edge (11564 eV) and Gd L_3 edge (7243 eV) have been measured.

E.5 Beam line 14-3

Beam line 14-3 is a bending magnet experimental station that provides unfocused tender X-rays in the range 2100-5000 eV. It is an XAS beam line that is equipped with ion chambers and a 4-element Vortex semiconductor fluorescence detector.

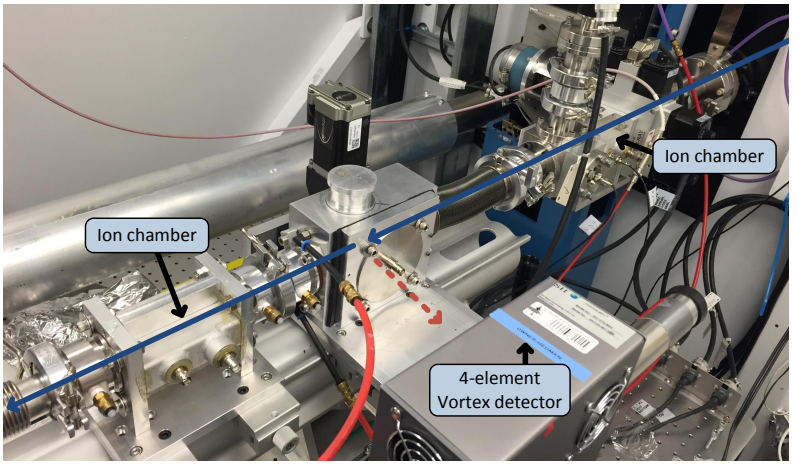

Figure E.7: The figure shows a picture of beam line 14-3 set up for transmission mode XAS. In this mode the X-ray intensity is measured before and after the sample by the two ion chambers. The incoming X-rays are indicated by the blue arrow. The beam line can also be set up for fluorescence mode, in which the scattered fluorescence X-rays will be detected at 90° (red arrow) by the 4-element Vortex detector.

Due to the low energy of the X-rays the entire beam path is in He to avoid absorption by N_2 and O_2 in air.

This beam line has been used to measure in-situ XANES spectra of RuO_x nanoparticles and thin films. See figure E.7 for the beam line set up in transmission XAS mode, and figure E.8 shows the fluorescence setup at the very similar beam line 4-3.

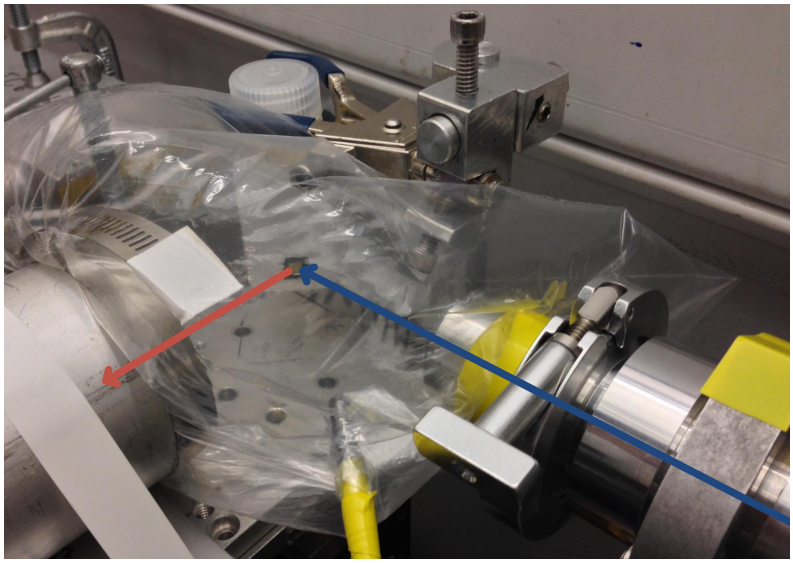

Figure E.8: The figure shows a picture from beam line 4-3, which is very similar to 14-3, set up in fluorescence mode. The incoming X-rays are indicated by the blue arrow, and the intensity has been detected by an ion chamber. The fluorescence X-rays scatter off the sample (red arrow) and is detected by a 4-element Vortex detector (not shown). Note that the sample is mounted inside a plastic bag, which is filled with He to reduce absorption of the X-rays.

APPENDIX F

MatLab program

This appendix contains a sample script with the parameters to process a single dataset and all the functions used to process the data. The code and their function is,

1. A script listing the name of the raw data and provides parameters for various calculation steps. Furthermore logical flags in the `param` struct indicates whether a background should be subtracted and what kind of datasets should be generated. This script has been designed to run on a 20-core server, and the code utilizes parallelization during certain steps to speed up processing.

2. The main function of the processing program. Here certain parameters are set based on the specified detector type. Flags are in the `param` struct is checked, and default values are often used if not specified.

3. From the base name of the data files and number of files a complete list of path- and file-names are generated.

4. The images and initial beam intensity are read if images are from a Pilatus detector.

5. The images and initial beam intensity are read if images are from a MAR345 imaging plate.

6. The pixel coordinates are calculated in lab coordinates from the calibration parameters obtained from the LaB_6 calibration in WxDiff, and Q and χ_c are calculated.

7. Fit and remove a smooth background if desired.

8. Apply intensity corrections in terms of Lorentz and polarization factors if desired.

9. Calculate $Q_{\parallel}$ and $Q_{\perp}$ coordinates from Q and χ_c.

10. Interpolate and combine images at each step in the ϕ rotation.

11. Shift the data along the ϕ direction by the amount ϕ_c, so that each slice in ϕ will have the same ϕ_c value.

12. Save the dataset as an HDF5 file.

13. Convert the dataset from cylindrical $Q_{\parallel}$, $Q_{\perp}$, and ϕ_c coordinates to polar Q, χ_c, and ϕ_c coordinates.

14. Convert the dataset from cylindrical $Q_{\parallel}$, $Q_{\perp}$, and ϕ_c coordinates to reciprocal lattice H, K, and L coordinates.

15. Convert the dataset from cylindrical $Q_{\parallel}$, $Q_{\perp}$, and ϕ_c coordinates to Cartesian Q_x, Q_y, and Q_z coordinates.

16. Save the Cartesian dataset with the DICOM file format, which is a 3D volume data format developed for MRI scanners.

Dataset script

```
% Clear workspace
clear;

% Kill any existing parallel pools
mycluster = parcluster('local');
delete(mycluster.Jobs);

% Start a pool of parallel workers to speed up 2D interpolation
pool = parpool(20,'IdleTimeout',600);
```

As prepared

Parameters for the data processing

```
param.detector = 'Pilatus300K';
param.ngam = 6;
param.det_orientation = 'vertical';
param.h5name = '/SCRATCH/anfils/PtGd_AP_Alloy';
%param.dicom = '/SCRATCH/anfils/PtGd_AP_Overlayer';
param.basename = '/zhome/b1/6/51501/PhD/PtGd_Diff_SSRL/Apr2014/PtGdAP/
b_friebel_PtGd_AP_detail_scan2';
param.numscans = 10806;
param.chid = 90;
param.theta = 0.2;
param.phimin = -180;
param.phimax = 180;
param.scale3D = 0.1;
param.scale2D = 1;
param.normalize = 1;
param.parallel = 1;
param.polarization = 0.95;
param.save_format = 'single';
param.rm_horizon = 1;
param.rm_bkgnd = 1;
param.depth_correction = [0.1 5.32395]; % Use [11 54672.1] for
 overlayer, [0.1 5.32395] for alloy, and [3000 5.46721] for bulk Pt
param.intensity_correction = 1;
param.save_QxyQzPhi = 1;
param.save_QChiPhi = 0;
param.save_HKL = 0;
param.save_QxQyQz = 1;

wxdiff.cen = [67.3338 1579.4336;...
    67.7721 1287.7768;...
    66.4744 1033.7100;...
    65.3203 806.7406;...
    65.9152 595.9482;...
    66.6082 396.2771];
wxdiff.L = [2333.3521 2161.5464 2035.3960 1946.0580 1879.9312
 1836.0097];
wxdiff.alpha = [1.1325 1.0427 0.9263 0.7830 0.6248 0.3959];
wxdiff.delta = [-0.7625 -0.6773 -0.5946 -0.5228 -0.4618 -0.4114];
```

```
wxdiff.lambda = 1.12713;
wxdiff.epsilon = -0.39;

param.wxdiff = wxdiff;

% Process the data!
param = Data_Processing(param);
```

Clean up

```
delete(pool);
clear;
```

Published with MATLAB® R2016a

Main function

```
function param = Data_Processing(param)
% This function automates the dataprocessing, requiring the minimum
 data
% input from the user.

% Calculate the total time
t_total = tic;

% Check if scale has been specified
if ~isfield(param,'scale3D')
    param.scale3D = 1;
end

% Check if the detector field has been specified
if ~isfield(param,'detector')
    error('Detector must be specified (Pilatus300K, Pilatus100K,
 MAR3450, MAR2300)');
end

% Check if the parallel field has been specified
if ~isfield(param,'parallel')
    param.parallel = 0;
end

% Determine if a standard detector is used and set the pixel numbers
switch param.detector
    case 'Pilatus300K'
        param.npx = 195;
        param.npy = 1475;
    case 'Pilatus100K'
        param.npx = 195;
        param.npy = 487;
    case 'MAR3450'
        param.npx = 3450;
        param.npy = 3450;
    case 'MAR2300'
        param.npx = 2300;
        param.npy = 2300;
    otherwise
        if ~isfield(param,'npx') || ~isfield(param,'npy')
            error('A standard detector OR image size must be
 specified');
        end
end

% Generate the list of files for import
[flist,param] = Flist_Gen(param);

% Import the files depending on detector type
disp('Starting to import data files');
t = tic;
switch param.detector
```

```
    case {'Pilatus300K','Pilatus100K'}
        [pic,param] = Pic_Imp(flist,param);
    case {'MAR3450','MAR2300'}
        [pic,param] = Pic_Imp_MAR(flist,param);
    otherwise
        [pic,param] = Pic_Imp(flist,param);
end
t = toc(t);
disp(strcat('Time elapsed: ',num2str(t/60),' minutes'));

% Cut out raw data if the field 'mask' has been specified
if isfield(param,'mask')
    disp('Cutting out the raw data according to the mask');
    t = tic;
    m = param.mask;
    if m(1,2) > param.npy || m(2,2) > param.npx
        error('The mask dimensions must not exceed the detector pixel
 dimensions');
    end
    pic = pic((param.npy - m(1,2) + 1):(param.npy - m(1,1) +
 1),m(2,1):m(2,2),:,:);
    param.npx = m(2,2) - m(2,1) + 1;
    param.npy = m(1,2) - m(1,1) + 1;
    t = toc(t);
    disp(strcat('Time elapsed: ',num2str(t/60),' minutes'));
end

% Calculate Q and chi
disp('Starting to calculate Q and chi');
t = tic;
[Q,Chi,param] = Q_Chi_Calc(param);
t = toc(t);
disp(strcat('Time elapsed: ',num2str(t/60),' minutes'));

% Remove background unless specified not to remove background
if ~isfield(param,'rm_bkgnd')
    param.rm_bkgnd = 1;
end
if param.rm_bkgnd
    disp('Starting to calculate and subtract background');
    t = tic;
    [pic,param] = Backgrnd_Calc(pic,Q,Chi,param);
    t = toc(t);
    disp(strcat('Time elapsed: ',num2str(t/60),' minutes'));
end

% Apply Lorentz, Polarization, and distance corrections
if ~isfield(param,'intensity_correction')
    param.intensity_correction = 1;
end
if param.intensity_correction
    disp('Applying Lorentz, Polarization, and distance corrections');
    t = tic;
    [pic,param] = Intensity_Correction(pic,param);
```

```
    t = toc(t);
    disp(strcat('Time elapsed: ',num2str(t/60),' minutes'));
end

% Calculate Qxy and Qz
disp('Starting to calculate Qxy and Qz');
t = tic;
[Qxy,Qz,param] = Qxy_Qz_Calc(Q,Chi,param);
t = toc(t);
disp(strcat('Time elapsed: ',num2str(t/60),' minutes'));

% Do the interpolation and stitching to generate Qxy,Qz,Phi image
disp('Starting to stitch images');
t = tic;
[QxyQzPhi,QxyQzPhi_lim,param] = Stitch(Qxy,Qz,pic,param);
QxyQzPhi_lim.Phimin = param.phimin;
QxyQzPhi_lim.Phimax = param.phimax;
t = toc(t);
disp(strcat('Time elapsed: ',num2str(t/60),' minutes'));

% Clear pic variable to free up memory
clear 'pic';

% Perform the phi correction
if param.nphi > 1
    disp('Starting phi correction');
    t = tic;
    [QxyQzPhi,QxyQzPhi_lim,param] =
 Phi_Correction(QxyQzPhi,QxyQzPhi_lim,Q,Chi,Qxy,Qz,param);
    t = toc(t);
    disp(strcat('Time elapsed: ',num2str(t/60),' minutes'));
end

% Remove data below the horizon
if ~isfield(param,'rm_horizon');
    param.rm_horizon = 0;
end
if param.rm_horizon
    disp('Starting to remove data below the horizon');
    t = tic;
    qz =
 linspace(QxyQzPhi_lim.Qzmin,QxyQzPhi_lim.Qzmax,size(QxyQzPhi,1));
    QxyQzPhi(qz < 0,:,:) = [];
    qz = qz(qz > 0);
    QxyQzPhi_lim.Qzmin = min(qz);
    t = toc(t);
    disp(strcat('Time elapsed: ',num2str(t/60),' minutes'));
end

% Clear more variables to free memory
clear 'Q';
clear 'chi';
clear 'Qx';
clear 'Qz';
```

```
% Save Qxy,Qz,Phi image
if ~isfield(param,'save_QxyQzPhi')
    param.save_QxyQzPhi = 1;
end
if param.save_QxyQzPhi
    disp('Saving QxyQzPhi image');
    t = tic;
    HDFfile = param.h5name;
    param =
 Save_Image_HDF(HDFfile,'QxyQzPhi',QxyQzPhi,QxyQzPhi_lim,param);
    t = toc(t);
    disp(strcat('Time elapsed: ',num2str(t/60),' minutes'));
end

% Generate and save Q,Chi,Phi image
if ~isfield(param,'save_QChiPhi')
    param.save_QChiPhi = 1;
end
if param.save_QChiPhi
    disp('Converting to QChiPhi image');
    t = tic;
    [QChiPhi,QChiPhi_lim,param] =
 Qxzphi2Qchi(QxyQzPhi,QxyQzPhi_lim,param);
    t = toc(t);
    disp(strcat('Time elapsed: ',num2str(t/60),' minutes'));

    disp('Saving QChiPhi image');
    t = tic;
    HDFfile = param.h5name;
    param =
 Save_Image_HDF(HDFfile,'QChiPhi',QChiPhi,QChiPhi_lim,param);
    t = toc(t);
    disp(strcat('Time elapsed: ',num2str(t/60),' minutes'));
    clear 'QChiPhi';
end

% Generate and save H,K,L image
if ~isfield(param,'save_HKL')
    param.save_HKL = 1;
end
if param.nphi > 1 && param.save_HKL
    disp('Converting to HKL image');
    t = tic;
    [HKL,HKL_lim,param] = Qxzphi2hkl(QxyQzPhi,QxyQzPhi_lim,param);
    t = toc(t);
    disp(strcat('Time elapsed: ',num2str(t/60),' minutes'));

    disp('Saving HKL image');
    t = tic;
    HDFfile = param.h5name;
    param = Save_Image_HDF(HDFfile,'HKL',HKL,HKL_lim,param);
    t = toc(t);
    disp(strcat('Time elapsed: ',num2str(t/60),' minutes'));
```

```
    clear 'HKL';
end

% Generate and save Qx,Qy,Qz image
if ~isfield(param,'save_QxQyQz')
    param.save_QxQyQz = 1;
end
if param.nphi > 1 && param.save_QxQyQz
    disp('Converting to Qxyz image');
    t = tic;
    [QxQyQz,QxQyQz_lim,param] =
 Qxzphi2Qxyz(QxyQzPhi,QxyQzPhi_lim,param);
    t = toc(t);
    disp(strcat('Time elapsed: ',num2str(t/60),' minutes'));

    disp('Saving Qxyz image');
    t = tic;
    HDFfile = param.h5name;
    param = Save_Image_HDF(HDFfile,'QxQyQz',QxQyQz,QxQyQz_lim,param);
    t = toc(t);
    disp(strcat('Time elapsed: ',num2str(t/60),' minutes'));

    if isfield(param,'dicom')
        disp('Saving Qxyz as DICOM');
        t = tic;
        DICOMfile = param.dicom;
        param = Save_DICOM(DICOMfile,QxQyQz,QxQyQz_lim,param);
        t = toc(t);
        disp(strcat('Time elapsed: ',num2str(t/60),' minutes'));

        disp('Saving log10(Qxyz) as DICOM');
        t = tic;
        param = Save_DICOM(strcat(DICOMfile,'_log'),log10(QxQyQz
+1),QxQyQz_lim,param);
        t = toc(t);
        disp(strcat('Time elapsed: ',num2str(t/60),' minutes'));
    end

    clear 'QxQyQz';
end

% Save the parameters in a separate file
save(strcat(HDFfile,'.mat'),'param');

% Display the total time elapsed
t_total = toc(t_total);
disp(strcat('Total time elapsed: ',num2str(t_total/60),' minutes'));
```

Published with MATLAB® R2016a

File name generator

```
function [flist,param] = Flist_Gen(param)
% Function generates a file list for importing Pilatus 300K data using
 the
% PicImp function. It takes the base name, excluding any numbers, and
% number of scans as input.

% Extract the required parameters
basename = param.basename;
p = param.numscans;

% Pre-allocate the file list
flist = cell(p,1);

% Generate the file list depending on the detector used
switch param.detector
    case {'Pilatus300K','Pilatus100K'}
        for i = 1:p
            x = sprintf('%04d',i-1);
            if mod(i-1,1000) == 0 && i ~= 1 && i < 10000
                x = x(1:end-3);
            elseif mod(i-1,100) == 0 && i ~= 1 && i < 10000
                x = x(1:end-2);
            elseif mod(i-1,10) == 0 && i ~= 1 && i < 10000
                x = x(1:end-1);
            end
            flist{i} = strcat(basename,'_',x,'.raw');
        end
    case 'MAR3450'
        for i = 1:p
            x = sprintf('%02d',i);
            flist{i} =
 strcat(strrep(basename,'_01_01_',strcat('_01_',x,'_')),'.mar3450');
        end
    case 'MAR2300'
        for i = 1:p
            x = sprintf('%02d',i);
            flist{i} =
 strcat(strrep(basename,'_01_01_',strcat('_01_',x,'_')),'.mar2300');
        end
end
```

Published with MATLAB® R2016a

Import Pilatus images

```
function [pic,param] = Pic_Imp(flist,param)
% This function imports the files whose name is in the flist variable,
 in
% the same order. It uses the default size of the Pilatus 300K
 detector.
% If the norm flag is on, the .csv file belonging to the scan is
 opened,
% and each scan is normalized by monitor.

% Check if the norm flag has been specified, if not set it to 0
if ~isfield(param,'normalize')
    norm = 0;
else
    norm = param.normalize;
end

% Check if the parallel flag has been specified
if ~isfield(param,'parallel')
    param.parallel = 1;
end

% Set up import parameters
p = length(flist); % Number of pictures to import
npx = param.npx; % Number of pixels in the horizontal direction
npy = param.npy; % Number of pixels in the vertical direction
pic = zeros(npy,npx,p);

% Open .csv file containing monitor values if norm is on
if norm == 1
    monf = flist{1};
    monf = strcat(monf(1:end-9),'.csv'); % Make to correct filename of
 the .CSV file containing monitor values
    k = strfind(monf,'b_friebel_'); % Find where in the string the
 letters 'b_friebel_' appears
    monf(k:k+9) = []; % Remove the letters 'b_friebel_' from the
 filename, since the .csv file does not have it.
    if p == 6
        mon = csvread(monf,1,0); % Read the corresponding .csv file.
        mon = mon(:,6); % Using i1 column for normalization.
 Alternative use column 5, which is Monitor
    else
        mon = csvread(monf,2,0); % Read the corresponding .csv file.
        mon = mon(:,7); % Using i1 column for normalization.
 Alternative use column 5, which is Monitor
    end
    mon = mon/max(mon); % Normalize monitor values, so that picture
 values do not deviate too much when normalization is not used
else
    mon = ones(p,1);
end

% Read in each image, reshape and normalize it
```

```
if param.parallel
    parfor i = 1:p
        f = fopen(flist{i});
        A = fread(f,'int32'); % Read pixel values in a list
        fclose(f);
        pic(:,:,i) = reshape(A,npy,npx)/mon(i); % Reshape and save the
 pixel data in array form and apply normalization
    end
else
    for i = 1:p
        f = fopen(flist{i});
        A = fread(f,'int32'); % Read pixel values in a list
        fclose(f);
        pic(:,:,i) = reshape(A,npy,npx)/mon(i); % Reshape and save the
 pixel data in array form and apply normalization
    end
end

% Restructure the output taking into account that there are ngam gamma
 files,
% and also sort them

% Calculate number of phi steps
ngam = param.ngam;
nphi = p/ngam;
param.nphi = nphi;

% Separate the gamma and phi steps (assuming that the scan is done by
% completing all the phi steps for each gamma step)
pic = reshape(pic,npy,npx,nphi,ngam);

% Switch the dimensions so that the gamma step is the 3rd index
pic = permute(pic,[1 2 4 3]);

% Inverse order of the gamma steps, so that they have the correct
 order
% when stitched
pic = flip(pic,3);
```

Published with MATLAB® R2016a

Import MAR345 images

```
function [pic,param] = Pic_Imp_MAR(flist,param)
% This function imports the files whose name is in the flist variable,
 in
% the same order. It uses the default size of the Pilatus 300K
 detector.
% If the norm flag is on, the .csv file belonging to the scan is
 opened,
% and each scan is normalized by monitor.

% Check if the norm flag has been specified, if not set it to 0
if ~isfield(param,'normalize')
    norm = 0;
else
    norm = param.normalize;
end

% Set up import parameters
nphi = length(flist); % Number of pictures to import
param.nphi = nphi;
f = fopen(flist{1});
h1 = fread(f,16,'*uint32');
fclose(f);
npx = h1(2); % Number of pixels in the horizontal direction (relative
 to the hutch)
npy = h1(2); % Number of pixels in the vertical direction (relative to
 the hutch)
pic = zeros(npy,npx,nphi);

% Open .csv file containing monitor values if norm is on
if norm == 1
    monf = flist{1};
    monf = strrep(monf,'_01_01_','_'); % Remove the scan number
    monf = strrep(monf,'.mar3450','.csv'); % Make to correct filename
 of the .CSV file containing monitor values
    mon = csvread(monf,1,0);
    mon = mon(:,5); % Using mon column for normalization.
    mon = mon/max(mon); % Normalize monitor values, so that picture
 values do not deviate too much when normalization is not used
else
    mon = ones(nphi,1);
end

% Read in each image, reshape and normalize it
parfor i = 1:nphi
    % Read the file header and compressed data
    f = fopen(flist{i});        % Open the file
    h1 = fread(f,16,'*uint32'); % Header parameters
    h2 = fread(f,4032,'*char'); % Header comments
    lh = h1(3);                 % Number of high pixels
    lha = 2*8*ceil(lh/8);       % Number of high pixel numbers
    dh = fread(f,lha,'*uint32');% High value pixels
    d = fread(f,'*uint16');     % Compressed data
```

```
    fclose(f);                  % Close the file

    % Decompress and rotate the image
    s = h1(2);                  % Side length of uncompressed image
    img = unpack345(d,s);       % Uncompress the image
    img = double(rot90(img,1)); % Rotate the image

    % Put in the high value pixels
    for j = 1:2:lh
        img(dh(j)) = dh(j+1);
    end

    % Final array of data
    pic(:,:,i) = img/mon(i); % Reshape and save the pixel data in
 array form and apply normalization
end

% Reshape the data to be 4D
pic = permute(pic,[1 2 4 3]);
```

Published with MATLAB® R2016a

Calculate Q and χ_c

```
function [Q,chi,param] = Q_Chi_Calc(param)
% Calculate Q and chi for Pilatus 300K detector using calibration
% parameters from wxdiff, using the exact output from the wxdiff
% calibration:
%
% cen is the center pixel in units of pixels (with x and y components
 as
% defined by wxdiff)
% L is the detector distance in units of pixels
% alpha is first detector tilt in units of radians
% delta is second detector tilt in units of radians
% lambda is the wavelength of the incoming x-rays in units of Å
% epsilon is a rotation of the detector around the beam in degrees
% detector is a string saying what type of detector is used
% (pilatus,mar3450,mar2300)

% Extract the wxdiff parameters
wxdiff = param.wxdiff;
cen = wxdiff.cen;
L = wxdiff.L;
alpha = wxdiff.alpha;
delta = wxdiff.delta;
lambda = wxdiff.lambda;
epsilon = wxdiff.epsilon;

% Get the image size parameters
npx = param.npx;
npy = param.npy;
ngam = param.ngam;

% Set up the correction parameters based on the detector and
 orientation
switch param.detector
    case {'Pilatus300K','Pilatus100K'}
        bx = cen(:,1);
        by = cen(:,2);
        s = -1;
    case {'MAR3450','MAR2300'}
        bx = npx - cen(:,2);
        by = cen(:,1);
        s = 1;
end

% Correct the beam center if a mask has been specified
if isfield(param,'mask')
    m = param.mask;
    bx = bx + m(1,1) - 1;
    by = by - m(2,1) + 1;
end

% Change sign of delta
delta = -delta;
```

```
% Perform the stepwise calculation of Q and chi
Q = zeros(npy,npx,ngam);
chi = Q;
for i = 1:ngam
    % Calculate 2theta and gamma angles
    tth = atan(tan(delta(i))*cos(alpha(i)));
    gam = asin(sin(delta(i))*sin(alpha(i)));

    % Calculate the angle of the delta rotation axis
    x = acos((cos(tth) - cos(gam)*cos(delta(i)))/
(sin(gam)*sin(delta(i))));

    % Calculate rotation axis (for delta rotation)
    u = [sin(x) cos(x) 0];
    ux = u(1);
    uy = u(2);
    uz = u(3);

    % Perform delta rotation
    a1 = delta(i);
    n(1) = ux*uz*(1 - cos(a1)) + uy*sin(a1);
    n(2) = uy*uz*(1 - cos(a1)) - ux*sin(a1);
    n(3) = cos(a1) + uz^2*(1 - cos(a1));

    % In-plane direction vectors
    v1 = [n(3)/n(1) 0 -1];
    v1 = v1/sqrt(dot(v1,v1));
    v2 = cross(n,v1);

    % Set up parameters for parametrization
    [dx,dy] = meshgrid(0:npx-1,npy-1:-1:0);
    dx = dx - by(i) + 0.5;
    dy = dy - bx(i) + 0.5;

    % Calculate x, y, and z
    x = v1(1)*dx + v2(1)*dy;
    y = v1(2)*dx + v2(2)*dy;
    z = v1(3)*dx + v2(3)*dy - L(i);

    % Rotate the detector around the z-axis to account for detector
 tilt
    x1 = cosd(epsilon)*x - sind(epsilon)*y;
    y1 = sind(epsilon)*x + cosd(epsilon)*y;
    x = x1;
    y = y1;

    % Calculate Q and chi
    sig = acosd(-z./sqrt(x.^2 + y.^2 + z.^2));
    Q(:,:,i) = (4*pi/lambda)*sind(sig/2);
    chi(:,:,i) = atan2d(s*y,s*x);
end

% Add 180 degrees to chi
```

```
chi = chi + 180;

% Invert Q and chi in the y-direction to make it fit the data
Q = flip(Q,1);
chi = flip(chi,1);
```

Published with MATLAB® R2016a

Remove smooth background

```
function [pic,param] = Backgrnd_Calc(pic,Q,Chi,param)
% Fit a planar background for log10(pic) vs Q.

% Get the image dimensions
s1 = size(pic,1);
s2 = size(pic,2);
s3 = size(pic,3);
s4 = size(pic,4);

% Find the phi slice with least scattering peaks
if s4 > 1
    m = squeeze(sum(sum(sum(pic,3),2),1));
    [~,i4] = min(m);
    picf = pic(:,:,:,i4);
else
    picf = pic;
end

% Define the background function
g = @(a1,a2,b1,b2,c,d,x,y) a1.*b1.^(-x) + a2.*b2.^(-x) + c + d.*y;

% Fit the background function with all the data
p1 = fit([Q(:) Chi(:)],picf(:),g,...
    'StartPoint',[5e3 5e3 1 10 1e3 -10],...
    'Lower',[0 0 0 0 0 -Inf],...
    'Upper',[Inf Inf Inf Inf Inf Inf]);

% Perform the fit again, but excluding points that are more than 10%
 above
% the previous fit
p2 = fit([Q(:) Chi(:)],picf(:),g,...
    'StartPoint',[5e3 5e3 1 10 1e3 -10],...
    'Lower',[0 0 0 0 0 -Inf],...
    'Upper',[Inf Inf Inf Inf Inf Inf],...
    'Exclude',picf(:) > 1.1*p1([Q(:) Chi(:)]));

% Calculate and reshape the background function
bkgnd = p2([Q(:) Chi(:)]);

% Reshape the background into the original shape
bkgnd = reshape(bkgnd,s1,s2,s3);

% Repeat the background function so that it has the same dimension as
 pic
bkgnd = repmat(bkgnd,[1,1,1,s4]);

% Subtract the background from the picture
pic = pic - bkgnd;

% Make sure there are no negative values in the picture
pic(pic < 0) = 0;
```

Published with MATLAB® R2016a

Apply Lorentz and polarization corrections

```
function [pic,param] = Intensity_Correction(pic,param)
% This function will apply an intensity correction to take the
 incoming
% angle, outgoing angle, and polarization into account.

% Check if the horizontal polarization has been specified
if ~isfield(param,'polarization')
    param.polarization = 0.05;
end

% Check if escape depth intensity is specified
if ~isfield(param,'depth_correction');
    param.depth_correction = [0 1];
end

% Extract the wxdiff parameters
wxdiff = param.wxdiff;
cen = wxdiff.cen;
L = wxdiff.L;
alpha = wxdiff.alpha;
delta = wxdiff.delta;
lambda = wxdiff.lambda;
epsilon = wxdiff.epsilon;

% Get the image size parameters
npx = param.npx;
npy = param.npy;
ngam = param.ngam;
nphi = param.nphi;

% Set up the correction parameters based on the detector and
 orientation
switch param.detector
    case {'Pilatus300K','Pilatus100K'}
        bx = cen(:,1);
        by = cen(:,2);
        s = -1;
    case {'MAR3450','MAR2300'}
        bx = npx - cen(:,2);
        by = cen(:,1);
        s = 1;
    otherwise
        bx = cen(:,1);
        by = cen(:,2);
        s = 1;
end

% Change sign of delta
delta = -delta;

% Perform the stepwise calculation of the x, y, z coordinates of the
 pixels
```

```
x = zeros(npy,npx,ngam);
y = x;
z = x;
for i = 1:ngam
    % Calculate 2theta and gamma angles
    tth0 = atan(tan(delta(i))*cos(alpha(i)));
    gam0 = asin(sin(delta(i))*sin(alpha(i)));

    % Calculate the angle of the delta rotation axis
    x0 = acos((cos(tth0) - cos(gam0)*cos(delta(i)))/
(sin(gam0)*sin(delta(i))));

    % Calculate rotation axis (for delta rotation)
    u = [sin(x0) cos(x0) 0];
    ux = u(1);
    uy = u(2);
    uz = u(3);

    % Perform delta rotation
    a1 = delta(i);
    n(1) = ux*uz*(1 - cos(a1)) + uy*sin(a1);
    n(2) = uy*uz*(1 - cos(a1)) - ux*sin(a1);
    n(3) = cos(a1) + uz^2*(1 - cos(a1));

    % In-plane direction vectors
    v1 = [n(3)/n(1) 0 -1];
    v1 = v1/sqrt(dot(v1,v1));
    v2 = cross(n,v1);

    % Set up parameters for parametrization
    [dx,dy] = meshgrid(0:npx-1,npy-1:-1:0);
    dx = dx - by(i) + 0.5;
    dy = dy - bx(i) + 0.5;

    % Calculate x, y, and z
    x(:,:,i) = v1(1)*dx + v2(1)*dy;
    y(:,:,i) = v1(2)*dx + v2(2)*dy;
    z(:,:,i) = v1(3)*dx + v2(3)*dy - L(i);

    % Rotate the detector around the z-axis to account for detector
 tilt
    x1 = cosd(epsilon)*x - sind(epsilon)*y;
    y1 = sind(epsilon)*x + cosd(epsilon)*y;
    x = x1;
    y = y1;
end

% Calculate the air attenuation correction
D = sqrt(x.^2 + y.^2 + z.^2);
E = 12398.42/lambda;
u = 3.627e-5*E^2.681 - 2.043e5;
T = exp(D/u);
T = T/min(T(:));
T = flip(T,1);
```

```
% Calculate the 2theta and gamma angles
gam = atan2d(-z,-x) - 90;
d = sqrt(x.^2 + z.^2);
tth = atand(y./d);

% Manipulate tth and gam to make them compatible with the data
gam = s*flip(gam,1);
tth = flip(tth,1);

% Calculate the Lorentz correction
beta_in = asind(sind(param.theta)*sind(param.chid));
L = abs(1./(sind(tth).*cosd(beta_in).*cosd(gam)));

% Calculate the polarization correction
ph = param.polarization;
Phor = 1 - sind(gam).^2;
Pver = 1 - (sind(tth).^2).*(cosd(gam).^2);
P = ph*Phor + (1 - ph)*Pver;

% Calculate the exit angle correction
beta_out = asind(cosd(tth).*cosd(param.chid).*sind(gam)
 + cosd(param.theta).*sind(tth).*sind(param.chid) -
 cosd(gam).*cosd(tth).*sind(param.chid).*sind(param.theta));
t = param.depth_correction(1);
mu = param.depth_correction(2);
mus = mu./(cscd(beta_in) + abs(cscd(beta_out)));
A = abs((1 - exp(-t./mus))./mus);
A = A/A(beta_out == max(beta_out(:)));

% Bundle all the corrections
if param.depth_correction
    C = A.*T./P./L;
else
    C = T./P./L;
end

% Apply the corrections
C = repmat(C,1,1,1,nphi);
pic = C.*pic;
```

Published with MATLAB® R2016a

Calculate $Q_{||}$ and $Q_{\perp}$

```
function [Qx,Qz,param] = Qxy_Qz_Calc(Q,chi,param)
% Convert (Q,chi) data points into Qxy, Qz. Input is the calculated
% magnitude of Q, angle of diffraction chi, wavelength of the x-ray
 beam,
% lambda, chi angle of the diffractometer, and the theta angle of the
% diffractometer.

% Get parameters from the input param
lambda = param.wxdiff.lambda;
chid = param.chid;
theta = param.theta;

% Offset the detector chi angle by 90 degrees
chid = chid - 90;

% Calculate the radius of the Ewald sphere
k0 = 2*pi/lambda;

% A change in the diffractometer chi is equivalent of subtracting the
 angle
% from the diffraction angle chi
chi = chi - chid;

% The in-plane Qx is calculated for phi = 0
Qx = Q.*sqrt(4*k0^2 + Q.^2 + (4*k0^2 - Q.^2).*cosd(2*chi))/
(sqrt(8)*k0);

% Correct the in-plane component Qx if theta is non-zero
if theta ~= 0
    m = @(Qxy) (-k0 + Qxy.*cosd(theta).*sqrt(1 + (1 -
 Q.^2./Qxy.^2).*cosd(theta).^2.*cotd(chi).^2) + sqrt(k0^2
 - (Q.^2 - Qxy.^2).*cosd(theta).^2.*cscd(chi).^2)
 + sqrt(Q.^2 - Qxy.^2).*sind(theta))./
((Q.^2.*cosd(theta).^3.*cotd(chi).^2)./(Qxy.^2.*sqrt(1 + (1 -
 Q.^2./Qxy.^2).*cosd(theta).^2.*cotd(chi).^2)) + cosd(theta).*sqrt(1
 + (1 - Q.^2./Qxy.^2).*cosd(theta).^2.*cotd(chi).^2) +
 (Qxy.*cosd(theta).^2.*cscd(chi).^2)./sqrt(k0^2 - (Q.^2 -
 Qxy.^2).*cosd(theta).^2.*cscd(chi).^2) - (Qxy.*sind(theta))./
sqrt(Q.^2 - Qxy.^2));
    for n = 1:10
        Qx = Qx - m(Qx);
    end
end

% Give the correct sign to the in-plane Qx
Qx = sign(cosd(chi)).*real(Qx);

% The out-of-plane Qz is calculated from the in-plane component
Qz = sign(sind(chi)).*abs(sqrt(Q.^2 - Qx.^2));
```

Published with MATLAB® R2016a

Interpolate images to Q-coordinates

```
function [pic,Qlim,param] = Stitch(Qx,Qz,pic,param)
% Combine the 6 gamma steps into a single square image, and
 interpolate it
% so that it may be plotted on a square grid. It also removes the dead
% bands from the detector.

% Check if the parallel flag has been specified
if ~isfield(param,'parallel')
    param.parallel = 1;
end

% Get the size of the arrays
npy = param.npy;
npx = param.npx;
ngam = param.ngam;
nphi = param.nphi;

% Remove dead detector bands and a 2 pixel frame from Pilatus 300K
 data
if strcmp(param.detector,'Pilatus300K')
    rmz = [1:2 486:496 980:990 (npy-1):npy];
    rmx = [1:2 (npx-1):npx];
    if isfield(param,'mask')
        m = param.mask;
        rmz(rmz < m(1,1)) = [];
        rmz(rmz > m(1,2)) = [];
        rmx(rmx < m(2,1)) = [];
        rmx(rmx > m(2,2)) = [];
        rmz = rmz - m(1,1) + 1;
        rmx = rmx - m(2,1) + 1;
    end
    pic(rmz,:,:,:) = [];
    Qx(rmz,:,:,:) = [];
    Qz(rmz,:,:,:) = [];
    pic(:,rmx,:,:) = [];
    Qx(:,rmx,:,:) = [];
    Qz(:,rmx,:,:) = [];
end

% Get the new size of the image
s1 = size(pic,1);
s2 = size(pic,2);
s3 = size(pic,3);
s4 = size(pic,4);

% Reshape the input arrays
pic = reshape(pic,s1,s2*s3,s4);
Qx = reshape(Qx,s1,s2*s3,1);
Qz = reshape(Qz,s1,s2*s3,1);

% Get the minimum and maximum Q-values in the data
Qxmin = min(Qx(:));
```

```
Qxmax = max(Qx(:));
Qzmin = min(Qz(:));
Qzmax = max(Qz(:));

% Calculate a set of query points on a square grid for use in each phi
 step
[Qx2,Qz2] =
 meshgrid(linspace(Qxmin,Qxmax,size(Qx,2)),linspace(Qzmin,Qzmax,size(Q

% Do the interpolation for each phi step
if param.parallel
    parfor i = 1:size(pic,3)
        pic(:,:,i) = griddata(Qx,Qz,pic(:,:,i),Qx2,Qz2,'natural');
    end
else
    for i = 1:size(pic,3)
        pic(:,:,i) = griddata(Qx,Qz,pic(:,:,i),Qx2,Qz2,'natural');
    end
end

% Save the limits of the in-plane and out-of-plane Q-values
Qlim.Qxymin = Qxmin;
Qlim.Qxymax = Qxmax;
Qlim.Qzmin = Qzmin;
Qlim.Qzmax = Qzmax;

% Remove any negative function values, in case they are made during
 the
% interpolation, by setting them to 0
pic(pic<0) = 0;
```

Published with MATLAB® R2016a

Correct for different ϕ_c across detector images

```
function [pic2,Qlim2,param] =
 Phi_Correction(pic,Qlim,Q,chi,Qxy,Qz,param)
% This function will correct the image for the Q-dependence of of phi,
 so
% that truncation rods will become straight. The Q, chi, and Qxy
 arrays
% must be in 3D format.

% Get the incidence angle
theta = param.theta;

% Calculate the change in phi
dphi = sign(-chi + 180).*asind(sqrt((Q./Qxy).^2 - 1).*cosd(theta)./
tand(chi));

% All the values must be positive in order to use the stitch function
dphi = dphi - min(dphi(:));

% Get the phi corrections in the correct format
nphi = param.nphi;
param.nphi = 1;
[dphi,~] = Stitch(Qxy,Qz,dphi,param);
param.nphi = nphi;

% Offset the correction to minimize the angle (the absolute value is
 not
% important, only the relative angle change)
av = sum(dphi(~isnan(dphi)))/numel(dphi(~isnan(dphi)));
dphi = dphi - av;
dphi(isnan(dphi)) = 0;

% Generate the phi values to be used to generate the query points
phi = linspace(Qlim.Phimin,Qlim.Phimax,size(pic,3));
phimin = min(phi);
phimax = max(phi);
if phimax - phimin == 360
    phi2 = phi;
    phi2min = phimin;
    phi2max = phimax;
else
    da = phi(2) - phi(1);
    dphimin = min(dphi(:));
    dphimax = max(dphi(:));
    phi2min = ceil((phimin + dphimin)/da)*da;
    phi2max = floor((phimax + dphimax)/da)*da;
    phi2 = phi2min:da:phi2max;
end

% Interpolate the picture to apply the phi angle correction
s1 = size(pic,1);
s2 = size(pic,2);
phi = squeeze(phi);
```

```
phi2 = squeeze(phi2);
pic2 = zeros(length(phi2),s1,s2);
pic = permute(pic,[3 1 2]);

s3a = size(pic,1);
s3b = size(pic2,1);

pic = reshape(pic,s3a,s1*s2,1);
pic2 = reshape(pic2,s3b,s1*s2,1);
dphi = reshape(dphi,s1*s2,1);

% Do the interpolation in parallel if not using the MAR3450 detector
if strcmp(param.detector,'MAR3450') || param.parallel == 0
    for i = 1:s1*s2
        %phiq = phi2 - dphi(i);
        phiq = phi2 + dphi(i); % Change the sign for the MAR345
 detector
        phiq(phiq < -180) = phiq(phiq < -180) + 360;
        phiq(phiq > 180) = phiq(phiq > 180) - 360;
        pic2(:,i) = interp1(phi,pic(:,i),phiq,'linear',0);
    end
else
    parfor i = 1:s1*s2
        phiq = phi2 - dphi(i);
        phiq(phiq < -180) = phiq(phiq < -180) + 360;
        phiq(phiq > 180) = phiq(phiq > 180) - 360;
        pic2(:,i) = interp1(phi,pic(:,i),phiq,'linear',0);
    end
end

pic2 = reshape(pic2,s3b,s1,s2);

% Pause to allow time for I/O operations to finish
if numel(pic2) > 1e6
    pause(30);
end

pic2 = permute(pic2,[2 3 1]);

% Update the Q limits
Qlim2 = Qlim;
Qlim2.Phimin = phi2min;
Qlim2.Phimax = phi2max;
```

Published with MATLAB® R2016a

Save the 3D dataset in HDF5 format

```
function param = Save_Image_HDF(filename,dataset,pic,Qlim,param)
% This function saves the data 'pic' as compressed uint16 as with the
 name
% 'dataset' in the file 'filename'. The contents of 'Qlim' will be
 saved as
% attributes for the dataset. The data is scaled down so it can be
 saved as
% uint16, and the scale value is also saved as an attribute.

% Check if the data saving type has been specified
if ~isfield(param,'save_format')
    param.save_format = 'uint16';
end

% Calculate the scale factor and convert the image data to the correct
 type
switch param.save_format
    case 'int8'
        scale = max(abs(pic(:)))/127;
        pic2 = int8(round(pic/scale));
        pic = pic2;
        clear 'pic2';
    case 'int16'
        scale = max(abs(pic(:)))/32767;
        pic2 = int16(round(pic/scale));
        pic = pic2;
        clear 'pic2';
    case 'int32'
        scale = max(abs(pic(:)))/2147483647;
        pic2 = int32(round(pic/scale));
        pic = pic2;
        clear 'pic2';
    case 'int64'
        scale = max(abs(pic(:)))/9223372036854775807;
        pic2 = int64(round(pic/scale));
        pic = pic2;
        clear 'pic2';
    case 'uint8'
        scale = max(abs(pic(:)))/255;
        pic2 = uint8(round(pic/scale));
        pic = pic2;
        clear 'pic2';
    case 'uint16'
        scale = max(abs(pic(:)))/65535;
        pic2 = uint16(round(pic/scale));
        pic = pic2;
        clear 'pic2';
    case 'uint32'
        scale = max(abs(pic(:)))/4294967295;
        pic2 = uint32(round(pic/scale));
        pic = pic2;
        clear 'pic2';
```

```
    case 'uint64'
        scale = max(abs(pic(:)))/18446744073709551615;
        pic2 = uint64(round(pic/scale));
        pic = pic2;
        clear 'pic2';
    case 'single'
        scale = 1;
        pic2 = single(pic);
        pic = pic2;
        clear 'pic2';
    case 'double'
        scale = 1;
        pic2 = double(pic);
        pic = pic2;
        clear 'pic2';
    otherwise
        error('Data type must be one of the standard MatLab data
 types');
end

% Add the correct file ending to the file name
filename = strcat(filename,'.h5');

% Generate a valid dataset name (include the slash as the first
 character),
% and initialize the HDF file
if strcmp(dataset(1),'/') == 0
    dataset = strcat('/',dataset);
end

% Initialize the file
if size(pic,3) == 1

 h5create(filename,dataset,size(pic),'Datatype',param.save_format,...
        'ChunkSize',[size(pic,1) 1],'Deflate',9);
else

 h5create(filename,dataset,size(pic),'Datatype',param.save_format,...
        'ChunkSize',[size(pic,1) 1 1],'Deflate',9);
end

% Save the data in the HDF file
h5write(filename,dataset,pic);

% Save the scale as an attribute
dataset = strcat(dataset,'/');
h5writeatt(filename,dataset,'Scale',scale);

% Save the data limits as attributes
Qname = fieldnames(Qlim);
for i = 1:length(Qname)
    h5writeatt(filename,dataset,Qname{i},Qlim.(Qname{i}));
end
```

Published with MATLAB® R2016a

Convert dataset from cylindrical to polar coordinates

```
function [pic2,Qlim2,param] = Qxzphi2Qchi(pic,Qlim,param)
% Convert a Qxy,Qz,Phi image into a Q,Chi,Phi image

% Determine if the scaling has been set, otherwise set it to 1
if ~isfield(param,'scale2D')
    scale = 1;
else
    scale = param.scale2D;
end

% Get the square root of scale, so that the scaling parameter changes
 the
% overall number of pixels
scale = scale^(1/2);

% Get the size of the arrays
s1 = size(pic,1);
s2 = size(pic,2);
s3 = size(pic,3);

% Get the minimum and maximum Q-values in the data
Qxmin = Qlim.Qxymin;
Qxmax = Qlim.Qxymax;
Qzmin = Qlim.Qzmin;
Qzmax = Qlim.Qzmax;
Phimin = Qlim.Phimin;
Phimax = Qlim.Phimax;

% Calculate the number of points to use
nx = round(scale*s2);
nz = round(scale*s1);

% Calculate the Q-range
Qx = max([abs(Qxmin) abs(Qxmax)]);
Qz = max([abs(Qzmin) abs(Qzmax)]);
Q = linspace(0,sqrt(Qx^2 + Qz^2),nx);

% Calculate an approximate chi array from Qxy and Qz
qx = linspace(Qxmin,Qxmax,s2);
qz = linspace(Qzmin,Qzmax,s1);
[Qxf,Qzf] = meshgrid(qx,qz);
Qf = sqrt(Qxf.^2 + Qzf.^2);
k0 = 2*pi/param.wxdiff.lambda;
c2c = (8*k0^2*Qxf.^2./Qf.^2 - 4*k0^2 - Qf.^2)./(4*k0^2 - Qf.^2);
Chi = real(acosd(c2c)/2);

% Make sure that the chi range is correct
Chi(Qxf < 0) = 180 - Chi(Qxf < 0);
Chi(Qzf < 0) = 360 - Chi(Qzf < 0);

% Calculate the new chi range
chimin = min(Chi(:)) - 5;
```

```
chimax = max(Chi(:)) + 5;
if chimin < 0
    chimin = 0;
elseif chimax > 360
    chimax = 360;
end
chi = linspace(chimin,chimax,nz);

% Calculate the Q and chi arrays for the interpolation
[Q,chi] = meshgrid(Q,chi);

% Generate the output array with the in-plane and out-of-plane Q-
values
Qlim2.Qmin = min(Q(:));
Qlim2.Qmax = max(Q(:));
Qlim2.Chimin = min(chi(:));
Qlim2.Chimax = max(chi(:));
Qlim2.Phimin = Phimin;
Qlim2.Phimax = Phimax;

% Convert coordinates to speed up interpolation
Qx2 = cosd(chi).*Q;
Qz2 = sind(chi).*Q;

% Generate a Qx,Qz array of correct size
Qx = linspace(Qxmin,Qxmax,s2);
Qz = linspace(Qzmin,Qzmax,s1);
[Qx,Qz] = meshgrid(Qx,Qz);

% Perform a series of 2D interpolation using the new coordinates
pic2 = zeros(nz,nx,s3);
for i = 1:s3
    pic2(:,:,i) = interp2(Qx,Qz,pic(1:s1,1:s2,i),Qx2,Qz2,'linear');
end

% Remove any negative function values, in case they are made during
 the
% interpolation, by setting them to 0
pic2 = real(pic2);
pic2(pic2<0) = 0;
```

Published with MATLAB® R2016a

Convert dataset from cylindrical to reciprocal lattice coordinates

```
function [pic2,Qlim2,param] = Qxzphi2hkl(pic,Qlim,param)
% Convert a Qxy,Qz,Phi image into an HKL image

% Determine if the scaling has been set, otherwise set it to 1
if ~isfield(param,'scale3D')
    scale = 1;
else
    scale = param.scale3D;
end

% Get the cubic root of scale, so that the scaling parameter changes
 the
% overall number of pixels
scale = scale^(1/3);

% Define the Q-conversion factor to convert from Q to HKL
Qconvx = 2.6144;
Qconvz = 0.9244;

% Get the size of the arrays
s1 = size(pic,1);
s2 = size(pic,2);
s3 = size(pic,3);

% Get the minimum and maximum Q-values in the data
Qxmin = Qlim.Qxymin;
Qxmax = Qlim.Qxymax;
Qzmin = Qlim.Qzmin;
Qzmax = Qlim.Qzmax;
Phimin = Qlim.Phimin;
Phimax = Qlim.Phimax;

% Calculate the number of pixels in each dimension assuming cubic
 voxels
s = s1*s2*s3;
Qx = max([abs(Qxmin) abs(Qxmax)]);
nx = (s*(2*Qx)/(Qzmax - Qzmin))^(1/3);
nz = s/(nx^2);

% Calculate the number of points in-plane and out-of-plane and a list
 of
% indices of the z-planes to use
nx = round(scale*nx);
d = round(s1/(scale*nz));
if d == 0
    d = 1;
end
zi = 1:d:s1;
nz = length(zi);

% Calculate the new z-axis
Qz = linspace(Qzmin,Qzmax,s1);
```

```
dQz = Qz(1 + d) - Qz(1);
Qz2min = (Qz(1 + d) + Qz(1))/2;
Qz2max = Qz2min + (nz - 1)*dQz;
Qz2 = linspace(Qz2min,Qz2max,nz);
L = Qz2/Qconvz;

% Generate a 2D mesh in-plane interpolation
H = linspace(-Qx,Qx,nx)/Qconvx*2/sqrt(3);
[H,K] = meshgrid(H,H);

% Generate the output array with the in-plane and out-of-plane Q-
values
Qlim2.Hmin = min(H(:));
Qlim2.Hmax = max(H(:));
Qlim2.Kmin = min(K(:));
Qlim2.Kmax = max(K(:));
Qlim2.Lmin = min(L(:));
Qlim2.Lmax = max(L(:));

% Convert HKL coordinates to Q coordinates to speed up interpolation
Qx2 = Qconvx*sqrt(H.^2 + K.^2 + H.*K);
phi2 = real(asind((sqrt(3)*Qconvx/2)*(K./Qx2)));

% Generate a Qx,Qz,phi array of correct size
phi = linspace(Phimin,Phimax,s3);
Qx = linspace(Qxmin,Qxmax,s2);
[phi,Qx] = meshgrid(phi,Qx);

% Modify the query points if the MAR detector is used
if Qxmax > 0 && Qxmin < 0
    Qx2(phi2 < 0) = -Qx2(phi2 < 0);
    phi2(phi2 < 0) = phi2(phi2 < 0) + 180;
end

% Average the layers of the original image array
if d > 1
    pici = zeros(nz,s2,s3);
    for i = 1:nz - 1
        pici(i,:,:) = sum(pic(zi(i):zi(i+1)-1,:,:),1)/d;
    end
    pici(end,:,:) = sum(pic(zi(end):end,:,:),1)/length(zi(end):s1);
    pic = pici;
    clear 'pici';
end

% Perform the 2D interpolation using the polar coordinates
pic = permute(pic,[2 3 1]);
pic2 = zeros(nx,nx,nz);
if Qxmax <= 0
    for i = 1:nz
        pic2(:,:,i) = interp2(phi,-
Qx,pic(1:s2,1:s3,i),phi2,Qx2,'linear',0);
    end
else
```

```
    for i = 1:nz
        pic2(:,:,i) =
 interp2(phi,Qx,pic(1:s2,1:s3,i),phi2,Qx2,'linear',0);
    end
end
pic2 = permute(pic2,[3 1 2]);

% Remove any negative function values, in case they are made during
 the
% interpolation, by setting them to 0
pic2 = real(pic2);
pic2(pic2<0) = 0;
```

Published with MATLAB® R2016a

Convert dataset from cylindrical to Cartesian coordinates

```
function [pic2,Qlim2,param] = Qxzphi2Qxyz(pic,Qlim,param)
% Convert a Qxy,Qz,Phi image into a Qx,Qy,Qz image

% Determine if the scaling has been set, otherwise set it to 1
if ~isfield(param,'scale3D')
    scale = 1;
else
    scale = param.scale3D;
end

% Get the cubic root of scale, so that the scaling parameter changes
 the
% overall number of pixels
scale = scale^(1/3);

% Get the size of the image array
s1 = size(pic,1);
s2 = size(pic,2);
s3 = size(pic,3);

% Get the minimum and maximum Q-values in the data
Qxmin = Qlim.Qxymin;
Qxmax = Qlim.Qxymax;
Qzmin = Qlim.Qzmin;
Qzmax = Qlim.Qzmax;
Phimin = Qlim.Phimin;
Phimax = Qlim.Phimax;

% Calculate the number of pixels in each dimension assuming cubic
 voxels
s = s1*s2*s3;
Qx = max([abs(Qxmin) abs(Qxmax)]);
nx = (s*(2*Qx)/(Qzmax - Qzmin))^(1/3);
nz = s/(nx^2);

% Calculate the number of points in-plane and out-of-plane and a list
 of
% indices of the z-planes to use
nx = round(scale*nx);
d = round(s1/(scale*nz));
if d == 0
    d = 1;
end
zi = 1:d:s1;
nz = length(zi);

% Calculate the new z-axis
Qz = linspace(Qzmin,Qzmax,s1);
dQz = Qz(1 + d) - Qz(1);
Qz2min = (Qz(1 + d) + Qz(1))/2;
Qz2max = Qz2min + (nz - 1)*dQz;
Qz2 = linspace(Qz2min,Qz2max,nz);
```

```
% Generate a 2D mesh in-plane interpolation
Qin = linspace(-Qx,Qx,nx);
[Qx,Qy] = meshgrid(Qin,Qin);

% Generate the output array with the in-plane and out-of-plane Q-
values
Qlim2.Qxmin = min(Qx(:));
Qlim2.Qxmax = max(Qx(:));
Qlim2.Qymin = min(Qy(:));
Qlim2.Qymax = max(Qy(:));
Qlim2.Qzmin = min(Qz2);
Qlim2.Qzmax = max(Qz2);

% Convert cartesian coordinates to polar coordinates to speed up
% interpolation
[theta,rho] = cart2pol(Qx,Qy);
theta = theta*180/pi;

% Generate a Qx,Qz,phi array of correct size
phi = linspace(Phimin,Phimax,s3);
Qx = linspace(Qxmin,Qxmax,s2);
[phi,Qx] = meshgrid(phi,Qx);

% Flip the THETA array to take the 0-point of phi into account
theta = -flip(theta,2);

% Modify the query points if the MAR detector is used
if Qxmax > 0 && Qxmin < 0
    rho(theta < 0) = -rho(theta < 0);
    theta(theta < 0) = theta(theta < 0) + 180;
end

% Average the layers of the original image array
if d > 1
    pici = zeros(nz,s2,s3);
    for i = 1:nz - 1
        pici(i,:,:) = sum(pic(zi(i):zi(i+1)-1,:,:),1)/d;
    end
    pici(end,:,:) = sum(pic(zi(end):end,:,:),1)/length(zi(end):s1);
    pic = pici;
    clear 'pici';
end

% Perform the 2D interpolation using the polar coordinates
pic = permute(pic,[2 3 1]);
pic2 = zeros(nx,nx,nz);
if Qxmax <= 0
    for i = 1:nz
        pic2(:,:,i) = interp2(phi,-
Qx,pic(1:s2,1:s3,i),theta,rho,'linear',0);
    end
else
    for i = 1:nz
```

```
        pic2(:,:,i) =
 interp2(phi,Qx,pic(1:s2,1:s3,i),theta,rho,'linear',0);
    end
end
pic2 = permute(pic2,[3 1 2]);

% Remove any negative function values, in case they are made during
 the
% interpolation, by setting them to 0
pic2 = real(pic2);
pic2(pic2<0) = 0;
```

Published with MATLAB® R2016a

Save Cartesian dataset as a DICOM file

```
function param = Save_DICOM(savefile,pic,Qlim,param)
% Function to save the picture data as a DICOM file (that may be
 opened by
% 3DSlicer for 3D view), using lossless JPEG2000 compression. Axis and
% pixel amplitude data are saved in the file.

% Check if the data saving type has been specified
if ~isfield(param,'save_format')
    param.save_format = 'uint16';
end

% Calculate the scale factor and convert the image data to the correct
 type
switch param.save_format
    case 'int8'
        scale = max(abs(pic(:)))/127;
        pic = int8(round(pic/scale));
        b = 1;
    case 'int16'
        scale = max(abs(pic(:)))/32767;
        pic = int16(round(pic/scale));
        b = 2;
    case 'uint8'
        scale = max(abs(pic(:)))/255;
        pic = uint8(round(pic/scale));
        b = 1;
    case 'uint16'
        scale = max(abs(pic(:)))/65535;
        pic = uint16(round(pic/scale));
        b = 2;
    case {'single','double','uint32','uint64'}
        scale = max(abs(pic(:)))/65535;
        pic = uint16(round(pic/scale));
        b = 2;
        warning('DICOM only supports int8, uint8, int16, and uint16.
 Using uint16 format instead.');
    case {'int32','int64'}
        scale = max(abs(pic(:)))/32767;
        pic = int16(round(pic/scale));
        b = 2;
        warning('DICOM only supports int8, uint8, int16, and uint16.
 Using int16 format instead.');
    otherwise
        error('Data type must be a standard MatLab data format');
end

% Check if there are too many elements
N = numel(pic)*b;
if N >= 2^32
    warning('DICOM image not saved, number of elements exceed 2^32');
    return
end
```

```
% Add the correct file extension to the file name
savefile = strcat(savefile,'.dcm');

% Get the dimensions and axis information
nin = size(pic,2);
nout = size(pic,1);
Qinmin = Qlim.Qxmin;
Qinmax = Qlim.Qxmax;
Qoutmin = Qlim.Qzmin;
Qoutmax = Qlim.Qzmax;

% Calculate the pixel spacing in all 3 spatial dimensions
psOut = (Qoutmax - Qoutmin)/nout;
psIn = (Qinmax - Qinmin)/nin;
PixelSpacing = [psOut psIn]; % Pixel Spacing parameter in DICOM
 (0028,0030)
SliceThickness = psIn; % Slice Thickness parameter in DICOM
 (0018,0050)

% Calculate the origin in the scan (upper left corner of image
ImgPos = [Qoutmin Qinmin Qinmin]; % Image Position parameter in DICOM
 (0020,0030)

% Reshape the image to have the MRI slices in the 4th dimension (3rd
% dimension is reserved for RGB data), and save the image initially to
% autogenerate DICOM metadata
pic = reshape(pic,nout,nin,1,nin);
dicomwrite(pic,savefile,'CompressionMode','JPEG2000 lossless');

% Load the automatically generated metadata and add more fields
s = 1;
info = dicominfo(savefile);
info.SliceThickness = s*SliceThickness;
info.SpacingBetweenSlices = s*SliceThickness;
info.ImagePositionPatient = s*ImgPos;
info.ImageOrientationPatient = [1 0 0 0 0 1];
info.ImagerPixelSpacing = s*PixelSpacing;
info.ImageComments = num2str(scale,10);

% Save the data as a DICOM file using the modified metadata
dicomwrite(pic,savefile,'CompressionMode','JPEG2000
 lossless',info,'CreateMode','Copy');
```

Published with MATLAB® R2016a

Bibliography

[1] *Human Development Index (HDI) | Human Development Reports*. URL: http://hdr.undp.org/en/content/human-development-index-hdi.

[2] *International Energy Statistics - EIA*. URL: https://www.eia.gov/cfapps/ipdbproject/IEDIndex3.cfm?tid=44&pid=44&aid=2.

[3] *Population, total | Data*. URL: http://data.worldbank.org/indicator/SP.POP.TOTL.

[4] IEA. *Key world energy statistics 2015*. Edited by IEA. International Energy Agency, November 2015.

[5] NASA Global Climate Change. *Carbon dioxide concentration | NASA Global Climate Change*. URL: http://climate.nasa.gov/vital-signs/carbon-dioxide.

[6] NASA Global Climate Change. *Global surface temperature | NASA Global Climate Change*. URL: http://climate.nasa.gov/vital-signs/global-temperature.

[7] Nathan S. Lewis and Daniel G. Nocera. "Powering the planet: Chemical challenges in solar energy utilization". In: *Proceedings of the National Academy of Sciences* 103.43 (October 2006), pages 15729–15735. DOI: 10.1073/pnas.0603395103.

[8] Frederick T. Wagner, Balasubramanian Lakshmanan, and Mark F. Mathias. "Electrochemistry and the Future of the Automobile". In: *The Journal of Physical Chemistry Letters* 1.14 (July 2010), pages 2204–2219. DOI: 10.1021/jz100553m.

[9] *PEMFC (Proton Exchange Membrane Fuel Cell)*. URL: http://mechanical-engg.com/blogs/entry/873-pemfc-proton-exchange-membrane-fuel-cell/.

[10] DP Wilkinson et al. *Handbook of fuel cells–fundamentals, technology and applications*. Volume 3. Wiley, 2003.

[11] Hubert A. Gasteiger et al. “Activity benchmarks and requirements for Pt, Pt-alloy, and non-Pt oxygen reduction catalysts for PEMFCs”. In: *Applied Catalysis B: Environmental*. Fuel processing and PEM Fuel Cells: advanced cata;ysts, adsorbents and electrocatalysts 56.1–2 (March 2005), pages 9–35. DOI: 10.1016/j.apcatb.2004.06.021.

[12] Weiting Yu, Marc D. Porosoff, and Jingguang G. Chen. “Review of Pt-Based Bimetallic Catalysis: From Model Surfaces to Supported Catalysts”. In: *Chemical Reviews* 112.11 (November 2012), pages 5780–5817. DOI: 10.1021/cr300096b.

[13] A. Hamnett. “Mechanism and electrocatalysis in the direct methanol fuel cell”. In: *Catalysis Today*. Fuel Cells and Catalysis 38.4 (November 1997), pages 445–457. DOI: 10.1016/S0920-5861(97)00054-0.

[14] Vinod Kumar Puthiyapura et al. “Biobutanol as Fuel for Direct Alcohol Fuel Cells—Investigation of Sn-Modified Pt Catalyst for Butanol Electro-oxidation”. In: *ACS Applied Materials & Interfaces* 8.20 (May 2016), pages 12859–12870. DOI: 10.1021/acsami.6b02863.

[15] Krzysztof A. Lewinski, Dennis van der Vliet, and Sean M. Luopa. “NSTF Advances for PEM Electrolysis - the Effect of Alloying on Activity of NSTF Electrolyzer Catalysts and Performance of NSTF Based PEM Electrolyzers”. In: *ECS Transactions* 69.17 (September 2015), pages 893–917. DOI: 10.1149/06917.0893ecst.

[16] Daniel Friebel et al. “Structure, Redox Chemistry, and Interfacial Alloy Formation in Monolayer and Multilayer Cu/Au(111) Model Catalysts for CO2 Electroreduction”. In: *The Journal of Physical Chemistry C* 118.15 (2014), pages 7954–7961. DOI: 10.1021/jp412000j.

[17] Uwe Rodemerck et al. “Catalyst Development for CO2 Hydrogenation to Fuels”. In: *ChemCatChem* 5.7 (July 2013), pages 1948–1955. DOI: 10.1002/cctc.201200879.

[18] *Platinum Price | Platinum Price Chart History | Price of Platinum Today*. URL: http://www.apmex.com/spotprices/platinum-price.

[19] *Iridium Prices and Iridium Price Charts - InvestmentMine*. URL: http://www.infomine.com/investment/metal-prices/iridium/.

[20] No machine-readable author provided Smokefoot assumed. *Catalysis Scheme*. July 2008. URL: https://commons.wikimedia.org/wiki/File:CatalysisScheme.png.

[21] Brian D. James, Jennie M. Moton, and Whitney G Colella. *Mass Production Cost Estimation of Direct H2 PEM Fuel Cell Systems for Transportation Applications: 2013 Update*. URL: http://energy.gov/sites/prod/files/2014/11/f19/fcto_sa_2013_pemfc_transportation_cost_analysis.pdf.

[22] Peter C. K. Vesborg and Thomas F. Jaramillo. “Addressing the terawatt challenge: scalability in the supply of chemical elements for renewable energy”. In: *RSC Advances* 2.21 (August 2012), pages 7933–7947. DOI: 10.1039/C2RA20839C.

[23] *Number of cars produced worldwide 2015*. URL: https://www.statista.com/statistics/262747/worldwide-automobile-production-since-2000/.

[24] Verónica Celorrio et al. “Oxygen reduction reaction at LaxCa1−xMnO3 nanostructures: interplay between A-site segregation and B-site valency”. In: *Catalysis Science & Technology* (July 2016). DOI: 10.1039/C6CY01105E.

[25] Turgut Sönmez et al. “Voltammetric Studies of the Mechanism of the Oxygen Reduction in Alkaline Media at the Spinels Co3O4 and NiCo2O4”. In: *Journal of The Electrochemical Society* 163.10 (January 2016), H884–H890. DOI: 10.1149/2.0111610jes.

[26] Kevin J. May et al. “Influence of Oxygen Evolution during Water Oxidation on the Surface of Perovskite Oxide Catalysts”. In: *The Journal of Physical Chemistry Letters* 3.22 (November 2012), pages 3264–3270. DOI: 10.1021/jz301414z.

[27] Gang Wu et al. “High-Performance Electrocatalysts for Oxygen Reduction Derived from Polyaniline, Iron, and Cobalt”. In: *Science* 332.6028 (April 2011), pages 443–447. DOI: 10.1126/science.1200832.

[28] Marcel Risch et al. “La0.8Sr0.2MnO3− Decorated with Ba0.5Sr0.5Co0.8Fe0.2O3− : A Bifunctional Surface for Oxygen Electrocatalysis with Enhanced Stability and Activity”. In: *Journal of the American Chemical Society* 136.14 (April 2014), pages 5229–5232. DOI: 10.1021/ja5009954.

[29] J. K. Nørskov et al. “Origin of the Overpotential for Oxygen Reduction at a Fuel-Cell Cathode”. In: *The Journal of Physical Chemistry B* 108.46 (November 2004), pages 17886–17892. DOI: 10.1021/jp047349j.

[30] Vojislav Stamenkovic et al. “Changing the Activity of Electrocatalysts for Oxygen Reduction by Tuning the Surface Electronic Structure”. In: *Angewandte Chemie* 118.18 (April 2006), pages 2963–2967. DOI: 10.1002/ange.200504386.

[31] Vladimir Tripković et al. “The oxygen reduction reaction mechanism on Pt(1 1 1) from density functional theory calculations”. In: *Electrochimica Acta*. EMERGING TRENDS AND CHALLENGES IN ELECTROCHEMISTRYSelection of papers from the 60th Annual Meeting of the International Society of Electrochemistry 16–21 August 2009, Beijing, China 55.27 (November 2010), pages 7975–7981. DOI: 10.1016/j.electacta.2010.02.056.

[32] Michael Busch et al. “Beyond the top of the volcano? – A unified approach to electrocatalytic oxygen reduction and oxygen evolution”. In: *Nano Energy* (). DOI: 10.1016/j.nanoen.2016.04.011.

[33] Ifan E. L. Stephens et al. “Understanding the electrocatalysis of oxygen reduction on platinum and its alloys”. In: *Energy & Environmental Science* 5.5 (April 2012), pages 6744–6762. DOI: 10.1039/C2EE03590A.

[34] S. Yamamoto et al. “In situ x-ray photoelectron spectroscopy studies of water on metals and oxides at ambient conditions”. In: *Journal of Physics: Condensed Matter* 20.18 (May 2008), page 184025. DOI: 10.1088/0953-8984/20/18/184025.

[35] Cheng Hao Wu, Robert S. Weatherup, and Miquel B. Salmeron. “Probing electrode/electrolyte interfaces in situ by X-ray spectroscopies: old methods, new tricks”. In: *Physical Chemistry Chemical Physics* 17.45 (November 2015), pages 30229–30239. DOI: 10.1039/C5CP04058B.

[36] Venkatasubramanian Viswanathan et al. “Unifying the 2e– and 4e– Reduction of Oxygen on Metal Surfaces”. In: *The Journal of Physical Chemistry Letters* 3.20 (October 2012), pages 2948–2951. DOI: 10.1021/jz301476w.

[37] Heine A. Hansen, Venkatasubramanian Viswanathan, and Jens K. Nørskov. “Unifying Kinetic and Thermodynamic Analysis of 2 e– and 4 e– Reduction of Oxygen on Metal Surfaces”. In: *The Journal of Physical Chemistry C* 118.13 (April 2014), pages 6706–6718. DOI: 10.1021/jp4100608.

[38] J. L. Zhang et al. “Controlling the catalytic activity of platinum-monolayer electrocatalysts for oxygen reduction with different substrates”. In: *Angewandte Chemie International Edition* 44.14 (2005), 2132–2135.

[39] Wei-Ping Zhou et al. “Improving Electrocatalysts for O2 Reduction by Fine-Tuning the Pt-Support Interaction: Pt Monolayer on the Surfaces of a Pd3Fe(111) Single-Crystal Alloy”. In: 131.35 (September 9, 2009), pages 12755–12762. DOI: 10.1021/ja9039746.

[40] Anand Udaykumar Nilekar and Manos Mavrikakis. “Improved oxygen reduction reactivity of platinum monolayers on transition metal surfaces”. In: 602.14 (July 15, 2008), pages L89–L94. DOI: 10.1016/j.susc.2008.05.036.

[41] V. Stamenkovic et al. “Changing the activity of electrocatalysts for oxygen reduction by tuning the surface electronic structure”. In: *Angewandte Chemie International Edition* 45.18 (2006), 2897–2901.

[42] J Rossmeisl, A Logadottir, and J. K. Nørskov. “Electrolysis of water on (oxidized) metal surfaces”. In: *Chemical Physics* 319.1-3, SI (Dec 7 2005), 178–184.

[43] F. Abild-Pedersen et al. “Scaling Properties of Adsorption Energies for Hydrogen-Containing Molecules on Transition-Metal Surfaces”. In: *Physical Review Letters* 99.1 (July 2007), page 016105. DOI: 10.1103/PhysRevLett.99.016105.

[44] V. R. Stamenkovic et al. “Improved oxygen reduction activity on $Pt_3Ni(111)$ via increased surface site availability”. In: *Science* 315.5811 (Jan 26 2007), 493–497.

[45] J. Greeley et al. “Alloys of platinum and early transition metals as oxygen reduction electrocatalysts”. In: *Nature Chemistry* 1.7 (Oct 2009), 552–556.

[46] Strasser P. et al. “Lattice-strain control of the activity in dealloyed core–shell fuel cell catalysts”. In: *Nature Chemistry* 2.6 (June 2010). 10.1038/nchem.623, pages 454–460. DOI: 10.1038/nchem.623.

[47] H. A. Hansen. “Density Functional Theory Studies of Electrochemical Processes”. PhD thesis. DTU Physics, Center for Individual Nanoparticle Functionality, Center for Atomic-scale Materials Design, 2009.

[48] Ifan E. L. Stephens et al. “Tuning the Activity of Pt(111) for Oxygen Electroreduction by Subsurface Alloying”. In: *Journal of the American Chemical Society* 133.14 (April 2011), pages 5485–5491. DOI: 10.1021/ja111690g.

[49] J. Rossmeisl et al. “Steady state oxygen reduction and cyclic voltammetry”. In: *Faraday Discussions* 140 (2008), 337–346.

[50] J. R. Kitchin et al. “Modification of the surface electronic and chemical properties of Pt(111) by subsurface 3d transition metals”. In: *Journal of Chemical Physics* 120.21 (2004), pages 10240–10246. DOI: 10.1063/1.1737365.

[51] J. R. Kitchin et al. “Role of Strain and Ligand Effects in the Modification of the Electronic and Chemical Properties of Bimetallic Surfaces”. In: *Physical Review Letters* 93.15 (October 2004), page 156801. DOI: 10.1103/PhysRevLett.93.156801.

[52] T. Bligaard and J. K. Nørskov. “Ligand effects in heterogeneous catalysis and electrochemistry”. In: *Electrochimica Acta*. Surface Imaging/Spectroscopy at Solid/Liquid Interface (ISSIS)Selection of papers from the International Symposium on Surface Imaging/Spectroscopy at Solid/Liquid Interface (ISSIS) , May 28 to June 1, 2006, Krakow, Poland 52.18 (May 2007), pages 5512–5516. DOI: 10.1016/j.electacta.2007.02.041.

[53] Jianbo Wu et al. “Icosahedral Platinum Alloy Nanocrystals with Enhanced Electrocatalytic Activities”. In: *Journal of the American Chemical Society* 134.29 (July 2012), pages 11880–11883. DOI: 10.1021/ja303950v.

[54] V Stamenkovic et al. “Surface composition effects in electrocatalysis: Kinetics of oxygen reduction on well-defined Pt3Ni and Pt3Co alloy surfaces”. In: *Journal of Physical Chemistry B* 106.46 (Nov 21 2002), 11970–11979.

[55] M. T. Paffett et al. “Electrochemical and surface science investigations of PtCr alloy electrodes”. In: *Journal of Electroanalytical Chemistry and Interfacial Electrochemistry* 220.2 (April 1987), pages 269–285. DOI: 10.1016/0022-0728(87)85114-8.

[56] Ugo Bardi, B. C. Beard, and P. N. Ross. “Surface oxidation of a Pt–20% CO alloy: An x-ray photoelectron spectroscopy and low-energy electron diffraction study on the [100] and [111] oriented single-crystal surfaces”. In: *Journal of Vacuum Science & Technology A* 6.3 (May 1988), pages 665–670. DOI: 10.1116/1.575149.

[57] Mark T. Paffett, Jerome G. Beery, and Shimshon Gottesfeld. "Oxygen Reduction at Pt0.65Cr0.35, Pt0.2Cr0.8 and Roughened Platinum". In: *Journal of The Electrochemical Society* 135.6 (June 1988), pages 1431–1436. DOI: 10.1149/1.2096016.

[58] B. Hammer and J. K. Nørskov. "Electronic factors determining the reactivity of metal surfaces". In: *Surface Science* 343.3 (1995), pages 211–220. DOI: 10.1016/0039-6028(96)80007-0.

[59] B. Hammer and J. K. Nørskov. "Theoretical surface science and catalysis - Calculations and concepts". In: *Advances in Catalysis, VOL 45: Impact of Surface Science on Catalysis*. Edited by Gates, B. C. and Knozinger, H. Volume 45. Advances in Catalysis. 2000, 71–129. ISBN: 0-12-007845-7.

[60] A. Nilsson et al. "The electronic structure effect in heterogeneous catalysis". In: *Catalysis Letters* 100.3-4 (), pages 111–114. DOI: 10.1007/s10562-004-3434-9.

[61] Sarp Kaya et al. "Electronic structure effects in catalysis probed by X-ray and electron spectroscopy". In: *Journal of Electron Spectroscopy and Related Phenomena*. Spectroscopy of Energy Materials 190, Part A (October 2013), pages 113–124. DOI: 10.1016/j.elspec.2013.04.015.

[62] Vojislav R. Stamenkovic et al. "Trends in electrocatalysis on extended and nanoscale Pt-bimetallic alloy surfaces". In: *Nature Materials* 6.3 (March 2007), pages 241–247. DOI: 10.1038/nmat1840.

[63] S. Chen et al. "Platinum-Alloy Cathode Catalyst Degradation in Proton Exchange Membrane Fuel Cells: Nanometer-Scale Compositional and Morphological Changes". In: *Journal of the Electrochemical Society* 157.1 (2010), A82–A97. DOI: 10.1149/1.3258275.

[64] F. Maillard et al. "Durability of Pt3Co/C nanoparticles in a proton-exchange membrane fuel cell: Direct evidence of bulk Co segregation to the surface". In: *Electrochemistry Communications* 12.9 (September 2010), pages 1161–1164. DOI: 10.1016/j.elecom.2010.06.007.

[65] L. Dubau et al. "Nanoscale compositional changes and modification of the surface reactivity of Pt3Co/C nanoparticles during proton-exchange membrane fuel cell operation". In: *Electrochimica Acta* 56.2 (December 2010), pages 776–783. DOI: 10.1016/j.electacta.2010.09.038.

[66] Laetitia Dubau et al. "Probing the structure, the composition and the ORR activity of Pt3Co/C nanocrystallites during a 3422 h PEMFC ageing test". In: *Applied Catalysis B: Environmental* 142–143 (October 2013), pages 801–808. DOI: 10.1016/j.apcatb.2013.06.011.

[67] Mehtap Oezaslan, Marc Heggen, and Peter Strasser. "Size-Dependent Morphology of Dealloyed Bimetallic Catalysts: Linking the Nano to the Macro Scale". In: *Journal of the American Chemical Society* 134.1 (January 2012), pages 514–524. DOI: 10.1021/ja2088162.

[68] Chen Chen et al. “Highly Crystalline Multimetallic Nanoframes with Three-Dimensional Electrocatalytic Surfaces”. In: *Science* 343.6177 (Mar 21 2014), 1339–1343. DOI: 10.1126/science.1249061.

[69] U. Vej-Hansen et al. “Correlation between diffusion barriers and alloying energy in binary alloys”. In: *Physical Chemistry Chemical Physics* Accepted (2015). DOI: 10.1039/xxxxxxxxxx.

[70] I. E. L. Stephens et al. “Oxygen Electroreduction Activity and X-Ray Photoelectron Spectroscopy of Platinum and Early Transition Metal Alloys”. In: *ChemCatChem* 4.3 (2012), pages 341–349. DOI: 10.1002/cctc.201100343.

[71] P. Malacrida et al. “Enhanced activity and stability of Pt-La and Pt-Ce alloys for oxygen electroreduction: the elucidation of the active surface phase”. In: *J. Mater. Chem. A* 2 (12 2014), pages 4234–4243.

[72] M. Escudero-Escribano et al. “Pt_5Gd as a Highly Active and Stable Catalyst for Oxygen Electroreduction”. In: *Journal of the American Chemical Society* 134.40 (Oct 10 2012), 16476–16479. DOI: 10.1021/ja306348d.

[73] T. P. Johansson et al. “Towards the elucidation of the high oxygen electroreduction activity of PtxY: surface science and electrochemical studies of Y/Pt(111).” In: *Physical Chemistry Chemical Physics* 16.27 (2014), pages 13718–13725. DOI: 10.1039/c4cp00319e.

[74] Elisabeth T. Ulrikkeholm et al. “PtxGd alloy formation on Pt(111): Preparation and structural characterization”. In: *Surface Science*. Insights into Surface Phenomena: In Honor of John T. Yates Jr 652 (October 2016), pages 114–122. DOI: 10.1016/j.susc.2016.02.009.

[75] T. P. Johansson. “New materials for oxygen reduction electrodes”. PhD thesis. Center for Individual Nanoparticle Functionality, Department of Physics, Technical University of Denmark, 2012.

[76] Elisabeth Therese Ulrikkeholm. “Single crystal studies of platinum alloys for oxygen reduction electrodes”. PhD thesis. Center for Individual Nanoparticle Functionality, Department of Physics, Technical University of Denmark, 2014.

[77] Anders F. Pedersen et al. “Probing the nanoscale structure of the catalytically active overlayer on Pt alloys with rare earths”. In: *Nano Energy* (). DOI: 10.1016/j.nanoen.2016.05.026.

[78] María Escudero-Escribano et al. “Tuning the activity of Pt alloy electrocatalysts by means of the lanthanide contraction”. en. In: *Science* 352.6281 (April 2016), pages 73–76. DOI: 10.1126/science.aad8892.

[79] Patricia Hernandez-Fernandez et al. “Mass-selected nanoparticles of Pt_xY as model catalysts for oxygen electroreduction”. In: *Nature Chemistry* 6.8 (2014), pages 732–738. DOI: 10.1038/nchem.2001.

[80] W. M. Haynes, editor. *Standard thermodynamic properties of chemical substances*. 94th edition. CRC Handbook of Chemistry and Physics. CRC Press, 2013, pages 5–17.

[81] Brian Peter Knudsen. "Synthesis of platinum rare earth alloy catalysts for fuel cells". PhD thesis. Center for Individual Nanoparticle functionality, Department of Physics, Technical University of Denmark, 2016.

[82] Amado Velázquez-Palenzuela et al. "The enhanced activity of mass-selected PtxGd nanoparticles for oxygen electroreduction". In: *Journal of Catalysis*. Special Issue: The Impact of Haldor Topsøe on Catalysis 328 (August 2015), pages 297–307. DOI: 10.1016/j.jcat.2014.12.012.

[83] W. Bronger. "Preparation and X-Ray investigation af platinum alloys with rare-earth metals (Pt5Ln and Pt3Ln phases)". In: *Journal of the less-common metals* 12.1 (1967), 63–68.

[84] N. Baenziger and J. L. Moriarty. "Gadolinium and Dysprosium Intermetallic Phases .1. Crystal Structures of DyGa and GdPt and their realted compounds". In: *Acta Crystallographica* 14.9 (1961), 946–&. DOI: 10.1107/S0365110X61002758.

[85] S. Curtarolo, D. Morgan, and G. Ceder. "Accuracy of ab initio methods in predicting the crystal structures of metals: A review of 80 binary alloys". In: *CALPHAD-Computer coupling of phase diagrams and thermochemistry* 29.3 (2005), pages 163–211.

[86] M. Pourbaix. *Atlas of electrochemical equilibria in aqueous solutions*. National Association of Corrosion Engineers, 1974. URL: http://books.google.dk/books?id=QjxRAAAAMAAJ.

[87] Charles C. L. McCrory et al. "Benchmarking Heterogeneous Electrocatalysts for the Oxygen Evolution Reaction". In: *Journal of the American Chemical Society* 135.45 (November 2013), pages 16977–16987. DOI: 10.1021/ja407115p.

[88] Laurence D. Burke et al. "The oxygen electrode. Part 8.—Oxygen evolution at ruthenium dioxide anodes". In: *Journal of the Chemical Society, Faraday Transactions 1: Physical Chemistry in Condensed Phases* 73 (January 1977), pages 1659–1671. DOI: 10.1039/F19777301659.

[89] Jean Horkans and M. W. Shafer. "An Investigation of the Electrochemistry of a Series of Metal Dioxides with Rutile-Type Structure: MoO2, WO 2, ReO2, RuO2, OsO2, and IrO2". In: *Journal of The Electrochemical Society* 124.8 (August 1977), pages 1202–1207. DOI: 10.1149/1.2133528.

[90] Sergio Trasatti. "Electrocatalysis by oxides — Attempt at a unifying approach". In: *Journal of Electroanalytical Chemistry and Interfacial Electrochemistry* 111.1 (July 1980), pages 125–131. DOI: 10.1016/S0022-0728(80)80084-2.

[91] Kelsey A. Stoerzinger et al. "Orientation-Dependent Oxygen Evolution Activities of Rutile IrO2 and RuO2". In: *The Journal of Physical Chemistry Letters* 5.10 (May 2014), pages 1636–1641. DOI: 10.1021/jz500610u.

[92] Elisa A. Paoli et al. "Oxygen evolution on well-characterized mass-selected Ru and RuO2 nanoparticles". In: *Chemical Science* (October 2014). DOI: 10.1039/C4SC02685C.

[93] Youngmin Lee et al. “Synthesis and Activities of Rutile IrO2 and RuO2 Nanoparticles for Oxygen Evolution in Acid and Alkaline Solutions”. In: *The Journal of Physical Chemistry Letters* 3.3 (February 2012), pages 399–404. DOI: 10.1021/jz2016507.

[94] Rasmus Frydendal et al. “Benchmarking the Stability of Oxygen Evolution Reaction Catalysts: The Importance of Monitoring Mass Losses”. In: *ChemElectroChem* (October 2014), pages 2075–2081. DOI: 10.1002/celc.201402262.

[95] A. T. Kuhn and C. J. Mortimer. “The Kinetics of Chlorine Evolution and Reduction on Titanium-Supported Metal Oxides Especially RuO2 and IrO2”. In: *Journal of The Electrochemical Society* 120.2 (February 1973), pages 231–236. DOI: 10.1149/1.2403425.

[96] Heine A. Hansen et al. “Electrochemical chlorine evolution at rutile oxide (110) surfaces”. In: *Physical Chemistry Chemical Physics* 12.1 (December 2009), pages 283–290. DOI: 10.1039/B917459A.

[97] Henri Bernard Beer. “The Invention and Industrial Development of Metal Anodes”. In: *Journal of The Electrochemical Society* 127.8 (August 1980), pages 303C–307C. DOI: 10.1149/1.2130021.

[98] Ch Comninellis and G. P. Vercesi. “Characterization of DSA®-type oxygen evolving electrodes: Choice of a coating”. In: *Journal of Applied Electrochemistry* 21.4 (), pages 335–345. DOI: 10.1007/BF01020219.

[99] S Trasatti. “Electrocatalysis: understanding the success of DSA®”. In: *Electrochimica Acta* 45.15–16 (May 2000), pages 2377–2385. DOI: 10.1016/S0013-4686(00)00338-8.

[100] Lars-Åke Näslund et al. “The Role of TiO2 Doping on RuO2-Coated Electrodes for the Water Oxidation Reaction”. In: *The Journal of Physical Chemistry C* 117.12 (March 2013), pages 6126–6135. DOI: 10.1021/jp308941g.

[101] R. Kötz and S. Stucki. “Oxygen Evolution and Corrosion on Ruthenium-Iridium Alloys”. In: *Journal of The Electrochemical Society* 132.1 (January 1985), pages 103–107. DOI: 10.1149/1.2113735.

[102] R. Kötz and S. Stucki. “Stabilization of RuO2 by IrO2 for anodic oxygen evolution in acid media”. In: *Electrochimica Acta* 31.10 (October 1986), pages 1311–1316. DOI: 10.1016/0013-4686(86)80153-0.

[103] Hong Nhan Nong et al. “IrOx core-shell nanocatalysts for cost- and energy-efficient electrochemical water splitting”. In: *Chemical Science* 5.8 (June 2014), pages 2955–2963. DOI: 10.1039/C4SC01065E.

[104] M. K. Debe et al. “Initial Performance and Durability of Ultra-Low Loaded NSTF Electrodes for PEM Electrolyzers”. In: *Journal of The Electrochemical Society* 159.6 (January 2012), K165–K176. DOI: 10.1149/2.065206jes.

[105] Kripasindhu Sardar et al. “Water-Splitting Electrocatalysis in Acid Conditions Using Ruthenate-Iridate Pyrochlores”. In: *Angewandte Chemie International Edition* 53.41 (October 2014), pages 10960–10964. DOI: 10.1002/anie.201406668.

[106] Nemanja Danilovic et al. “Using Surface Segregation To Design Stable Ru-Ir Oxides for the Oxygen Evolution Reaction in Acidic Environments”. In: *Angewandte Chemie* (October 8, 2014), n/a–n/a. DOI: 10.1002/ange.201406455.

[107] Nemanja Danilovic et al. “Activity–Stability Trends for the Oxygen Evolution Reaction on Monometallic Oxides in Acidic Environments”. In: *The Journal of Physical Chemistry Letters* 5.14 (July 17, 2014), pages 2474–2478. DOI: 10.1021/jz501061n.

[108] Tobias Binninger et al. “Thermodynamic explanation of the universal correlation between oxygen evolution activity and corrosion of oxide catalysts”. In: *Scientific Reports* 5 (July 2015), page 12167. DOI: 10.1038/srep12167.

[109] Serhiy Cherevko et al. “Stability of nanostructured iridium oxide electrocatalysts during oxygen evolution reaction in acidic environment”. In: *Electrochemistry Communications* 48 (November 2014), pages 81–85. DOI: 10.1016/j.elecom.2014.08.027.

[110] Isabela Costinela Man. “Theoretical study of electro-catalysts for oxygen evolution”. PhD thesis. Technical University of Denmark, 2011.

[111] Alessandro Minguzzi et al. “Observing the oxidation state turnover in heterogeneous iridium-based water oxidation catalysts”. In: *Chemical Science* 5.9 (May 2014), page 3591. DOI: 10.1039/C4SC00975D.

[112] M. B. Vukmirovic, R. L. Sabatini, and R. R. Adzic. “Growth of RuO2 by electrochemical and gas-phase oxidation of an Ru(0 0 0 1) surface”. In: *Surface Science* 572.2–3 (November 2004), pages 269–276. DOI: 10.1016/j.susc.2004.09.001.

[113] Tong-Chang Liu and B. E. Conway. “Evaluation of electroactive intermediate states in anodic O2 evolution at chemically formed nickel oxide: Comparison with behaviour at nickel metal anodes”. In: *Journal of Applied Electrochemistry* 17.5 (), pages 983–996. DOI: 10.1007/BF01024365.

[114] M. Vuković. “Oxygen evolution on an electrodeposited ruthenium electrode in acid solution —the effect of thermal treatment”. In: *Electrochimica Acta* 34.2 (February 1989), pages 287–291. DOI: 10.1016/0013-4686(89)87099-9.

[115] Isabela C. Man et al. “Universality in Oxygen Evolution Electrocatalysis on Oxide Surfaces”. In: *ChemCatChem* 3.7 (July 2011), pages 1159–1165. DOI: 10.1002/cctc.201000397.

[116] Niels Bendtsen Halck. “Efficient oxygen electrocatalysis on special active sites”. PhD thesis. Tehcnical University of Denmark, Department of Physics, 2014.

[117] *Conversation with Jan Rossmeisl*. September 2016.

[118] Jin Suntivich et al. "A Perovskite Oxide Optimized for Oxygen Evolution Catalysis from Molecular Orbital Principles". In: *Science* 334.6061 (December 2011), pages 1383–1385. DOI: 10.1126/science.1212858.

[119] J. Als-Nielsen and D. McMorrow. *Elements of Modern X-Ray physics*. Edited by Wiley. Wiley, 2006.

[120] S. Marks et al. "The Advanced Light Source elliptically polarizing undulator". In: *Particle Accelerator Conference, 1997. Proceedings of the 1997*. Volume 3. May 1997, 3221–3223 vol.3. DOI: 10.1109/PAC.1997.753161.

[121] A. Thopmson et al. *X-ray Data Booklet*. Third. Lawrence Berkeley Laboratory, October 2009.

[122] A. N. Mansour, J. W. Cook, and D. E. Sayers. "Quantitative technique for the determination of the number of unoccupied d-electron states in a platinum catalyst using the L2,3 x-ray absorption edge spectra". In: *The Journal of Physical Chemistry* 88.11 (May 1984), pages 2330–2334. DOI: 10.1021/j150655a029.

[123] *Tutorials.pdf*. URL: http://xafs.org/Tutorials?action=AttachFile&do=get&target=Newville_xas_fundamentals.pdf.

[124] J. H. Hubbell et al. "A Review, Bibliography, and Tabulation of K, L, and Higher Atomic Shell X-Ray Fluorescence Yields". In: *Journal of Physical and Chemical Reference Data* 23.2 (March 1994), pages 339–364. DOI: 10.1063/1.555955.

[125] M. O. Krause. "Atomic radiative and radiationless yields for K and L shells". In: *Journal of Physical and Chemical Reference Data* 8.2 (April 1979), pages 307–327. DOI: 10.1063/1.555594. (Visited on July 31, 2016).

[126] *Vortex®-60EX X-ray Detector : Hitachi High-Technologies GLOBAL*. URL: http://www.hitachi-hightech.com/global/product_detail/?pn=ana-vortex-60ex.

[127] John J. Rehr et al. "Parameter-free calculations of X-ray spectra with FEFF9". In: *Physical Chemistry Chemical Physics* 12.21 (May 2010), pages 5503–5513. DOI: 10.1039/B926434E.

[128] M. Brown, R. E. Peierls, and E. A. Stern. "White lines in x-ray absorption". In: *Physical Review B* 15.2 (January 1977), pages 738–744. DOI: 10.1103/PhysRevB.15.738.

[129] M. O. Krause and J. H. Oliver. "Natural widths of atomic K and L levels, K X-ray lines and several KLL Auger lines". In: *Journal of Physical and Chemical Reference Data* 8.2 (April 1979), pages 329–338. DOI: 10.1063/1.555595.

[130] J. D. Watson and F. H. C. Crick. "Molecular Structure of Nucleic Acids: A Structure for Deoxyribose Nucleic Acid". In: *Nature* 171.4356 (April 1953), pages 737–738. DOI: 10.1038/171737a0.

[131] B. E. Warren. *X-Ray Diffraction*. Courier Corporation, May 2012. ISBN: 978-0-486-14161-9.

[132] J. I. Langford and A. Wilson. "Scherrer after sixty years: A survey and some new results in the determination of crystallite size". In: *Journal of applied crystallography* 11 (1978), pages 102–113.

[133] Detlef-M. Smilgies. "Scherrer grain-size analysis adapted to grazing-incidence scattering with area detectors". In: *Journal of Applied Crystallography* 42.6 (December 2009), pages 1030–1034. DOI: 10.1107/S0021889809040126.

[134] E. Vlieg. "Integrated Intensities Using a Six-Circle Surface X-ray Diffractometer". In: *Journal of Applied Crystallography* 30.5-1 (October 1997), pages 532–543. DOI: 10.1107/S0021889897002537.

[135] H. You. "Angle calculations for a '4S+2D' six-circle diffractometer". In: *Journal of Applied Crystallography* 32.4 (August 1999), pages 614–623. DOI: 10.1107/S0021889899001223.

[136] A. L. Patterson. "A Direct Method for the Determination of the Components of Interatomic Distances in Crystals". In: *Zeitschrift für Kristallographie - Crystalline Materials* 90.1 (1935), pages 517–542.

[137] J. R. Fienup. "Reconstruction of an object from the modulus of its Fourier transform". In: *Optics Letters* 3.1 (July 1978), pages 27–29. DOI: 10.1364/OL.3.000027.

[138] J. R. Fienup and C. C. Wackerman. "Phase-retrieval stagnation problems and solutions". In: *Journal of the Optical Society of America A* 3.11 (November 1986), pages 1897–1907. DOI: 10.1364/JOSAA.3.001897.

[139] Eliyahu Osherovich. "Numerical methods for phase retrieval". arXiv: 1203.4756. PhD thesis. March 2012.

[140] George M. Sheldrick. "A short history of *SHELX*". In: *Acta Crystallographica Section A Foundations of Crystallography* 64.1 (January 2008), pages 112–122. DOI: 10.1107/S0108767307043930.

[141] S. M. Webb. "SIXPack a Graphical User Interface for XAS Analysis Using IFEFFIT". In: *Physica Scripta* (2005), page 1011. DOI: 10.1238/Physica.Topical.115a01011.

[142] B. Ravel and M. Newville. "*ATHENA* , *ARTEMIS* , *HEPHAESTUS* : data analysis for X-ray absorption spectroscopy using *IFEFFIT*". In: *Journal of Synchrotron Radiation* 12.4 (July 2005), pages 537–541. DOI: 10.1107/S0909049505012719.

[143] M. Abes et al. "Direct measurements of field-induced strain at magnetoelectric interfaces by grazing incidence x-ray diffraction". In: *Applied Physics Letters* 102.1 (January 2013), page 011601. DOI: 10.1063/1.4773358.

[144] Martin Hangaard Hansen. "DFT-Simulations of low temperature fuel cells catalysis". PhD thesis. Technical University of Denmark, 2016.

[145] Jan Rossmeisl et al. "Steady state oxygen reduction and cyclic voltammetry". In: *Faraday Discussions* 140 (October 2008), pages 337–346. DOI: 10.1039/B802129E.

[146] Vojislav R. Stamenkovic et al. “Improved Oxygen Reduction Activity on Pt3Ni(111) via Increased Surface Site Availability”. In: *Science* 315.5811 (January 2007), pages 493–497. DOI: 10.1126/science.1135941.

[147] A. H. Ayyad, J. Stettner, and O. M. Magnussen. “Electrocompression of the Au(111) Surface Layer during Au Electrodeposition”. In: *Physical Review Letters* 94.6 (February 2005), page 066106. DOI: 10.1103/PhysRevLett.94.066106.

[148] Masaru Itakura et al. “Crystal Structures of H-Pd5Ce and Pd5La and Their Electrical Resistivities at Low Temperatures”. In: *Japanese Journal of Applied Physics* 27.4R (April 1988), page 684. DOI: 10.1143/JJAP.27.684.

[149] C. W. Allen, P. Delavignette, and S. Amelinckx. “Electron microscopic studies of the laves phases TiCr2 and TiCo2”. In: *physica status solidi (a)* 9.1 (1972), pages 237–246. DOI: 10.1002/pssa.2210090127.

[150] J. Aufrecht et al. “Layer-stacking irregularities in C36-type Nb–Cr and Ti–Cr Laves phases and their relation with polytypic phase transformations”. In: *Philosophical Magazine* 90.23 (August 2010), pages 3149–3175. DOI: 10.1080/14786435.2010.482068.

[151] Z. Hu et al. “Multiplet effects in the Ru ${L}_{2,3}$ x-ray-absorption spectra of Ru(IV) and Ru(V) compounds”. In: *Physical Review B* 61.8 (February 2000), pages 5262–5266. DOI: 10.1103/PhysRevB.61.5262.

[152] Eugene J. McGuire. “Atomic M-Shell Coster-Kronig, Auger, and Radiative Rates, and Fluorescence Yields for Ca-Th”. In: *Physical Review A* 5.3 (March 1972), pages 1043–1047. DOI: 10.1103/PhysRevA.5.1043.

[153] Herman Winick. “The Stanford Synchrotron Radiation Project (SSRP)”. In: *Vacuum Ultraviolet Radiation Physics IV*. Volume 1. Citeseer. 1974, page 776.

[154] *The ring on the parking lot - CERN Courier*. URL: http://cerncourier.com/cws/article/cern/28865.

[155] *SSRL Beam Lines Map | Stanford Synchrotron Radiation Lightsource*. URL: http://ssrl.slac.stanford.edu/content/beam-lines/map.

[156] A. G. McKale et al. “Generalized Ramsauer-Townsend effect in extended x-ray-absorption fine structure”. In: *Physical Review B* 38.15 (November 1988), pages 10919–10921. DOI: 10.1103/PhysRevB.38.10919.

[157] S. I. Zabinsky et al. “Multiple-scattering calculations of x-ray-absorption spectra”. In: *Physical Review B* 52.4 (July 1995), pages 2995–3009. DOI: 10.1103/PhysRevB.52.2995.

[158] A. L. Ankudinov et al. “Real-space multiple-scattering calculation and interpretation of x-ray-absorption near-edge structure”. In: *Physical Review B* 58.12 (September 1998), pages 7565–7576. DOI: 10.1103/PhysRevB.58.7565.

[159] I. Chorkendorff and H. Niemantsverdriet. *Concepts in modern catalysis and kinetics*. Wiley-VCH, 2003. ISBN: 3-527-31672-4.

[160] I. Chorkendorff. *Surface Physics/Chemistry*. 2010.

[161] K. Hämäläinen et al. "Elimination of the inner-shell lifetime broadening in x-ray-absorption spectroscopy". In: *Physical Review Letters* 67.20 (November 1991), pages 2850–2853. DOI: 10.1103/PhysRevLett.67.2850.

[162] D. Sokaras et al. "A seven-crystal Johann-type hard x-ray spectrometer at the Stanford Synchrotron Radiation Lightsource". In: *Review of Scientific Instruments* 84.5 (May 2013), page 053102. DOI: 10.1063/1.4803669.

[163] F. M. F. de Groot, M. H. Krisch, and J. Vogel. "Spectral sharpening of the Pt L edges by high-resolution x-ray emission". In: *Physical Review B* 66.19 (November 2002), page 195112. DOI: 10.1103/PhysRevB.66.195112.

[164] Mcpazzo. *English: Image of a crystal unit cell definition. a, b, and c are unit cell lengths. alpha is the angle between b anc c, beta is the angle between a and c, and gamma is the angle between a and b.* URL: https://commons.wikimedia.org/wiki/File:UnitCell.png.

[165] W. Friedrich. "Die Geschichte der Auffindung der Röntgenstrahlinterferenzen". In: *Naturwissenschaften* 10.16 (), pages 363–366. DOI: 10.1007/BF01565289.

[166] *File:NaCl polyhedra.png*. en. URL: https://en.wikipedia.org/wiki/File:NaCl_polyhedra.png.

[167] Th. Hahn et al., editors. *International Tables for Crystallography: Space-group symmetry*. 1st edition. Volume A. International Tables for Crystallography. Chester, England: International Union of Crystallography, October 2006. ISBN: 978-0-7923-6590-7 978-1-4020-5406-8.

[168] *450px-3D_ewald_example.png (450×323)*. URL: http://gisaxs.com/images/thumb/6/6b/3D_ewald_example.png/450px-3D_ewald_example.png.

[169] SCB Mannsfeld. *WxDiff*. 2009.

[170] Inductiveload. *A diagram of spherical coordinates, defining a point by colatitude, , longitude, , and radius, .* August 2008. URL: https://commons.wikimedia.org/wiki/File:Spherical_Coordinates_(Colatitude,_Longitude).svg.

[171] *CXRO - The Center for X-ray Optics*. URL: http://www.cxro.lbl.gov/.

[172] Daniel Friebel et al. "In situ X-ray probing reveals fingerprints of surface platinum oxide". In: *Physical Chemistry Chemical Physics* 13.1 (December 2010), pages 262–266. DOI: 10.1039/C0CP01434F.

[173] Stephen F Dinetz et al. "A comparative study of the gaseous products generated by thermal and ultra-violet laser pyrolyses of the polyimide PMDA-ODA". In: *Journal of Analytical and Applied Pyrolysis* 63.2 (June 2002), pages 241–249. DOI: 10.1016/S0165-2370(01)00157-7.

[174] H. B. Brom et al. "On a new conducting polymer-pyrolyzed Kapton". In: *Solid State Communications* 35.2 (July 1980), pages 135–139. DOI: 10.1016/0038-1098(80)90230-6.

[175] C. Z. Hu and J. D. Andrade. "Pyrolyzed, conducting kapton polyimide: An electrically conducting material". In: *Journal of Applied Polymer Science* 30.11 (November 1985), pages 4409–4415. DOI: 10.1002/app.1985.070301116.

[176] *SSRL Beam Line 6-2*. URL: https://www.flickr.com/photos/slaclab/19082230809/.

Journal of Catalysis 328 (2015) 297–307

Contents lists available at ScienceDirect

Journal of Catalysis

journal homepage: www.elsevier.com/locate/jcat

The enhanced activity of mass-selected Pt_xGd nanoparticles for oxygen electroreduction

Amado Velázquez-Palenzuela [a], Federico Masini [a], Anders F. Pedersen [a], María Escudero-Escribano [a], Davide Deiana [b], Paolo Malacrida [a], Thomas W. Hansen [b], Daniel Friebel [c], Anders Nilsson [c], Ifan E.L. Stephens [a], Ib Chorkendorff [a,*]

[a] Center for Individual Nanoparticle Functionality (CINF), Department of Physics, Technical University of Denmark, Kongens Lyngby DK-2800, Denmark
[b] Center for Electron Nanoscopy (CEN), Technical University of Denmark, Kongens Lyngby DK-2800, Denmark
[c] SLAC National Accelerator Laboratory, 2575 Sand Hill Road, MS31, Menlo Park, CA 94025, USA

ARTICLE INFO

Article history:
Received 24 September 2014
Revised 31 October 2014
Accepted 9 December 2014

This research article is dedicated to the memory of Haldor Topsøe (1913–2013), who was always a strong proponent of fundamental research toward improved catalysis.

Keywords:
Electrocatalysis
Fuel cells
Oxygen reduction reaction
Nanoparticles
Platinum–gadolinium alloy
Core/shell
Strain effect

ABSTRACT

Mass-selected platinum–gadolinium alloy nanoparticles (Pt_xGd NPs) are synthesized for the first time as oxygen reduction reaction (ORR) electrocatalysts using the gas aggregation technique, under ultrahigh vacuum (UHV) conditions. The morphology of the Pt_xGd catalysts is characterized, and their catalytic performance toward the ORR is assessed in acidic media using a half-cell configuration. The Pt_xGd 8-nm catalyst shows a high activity (3.6 A $(mg\ Pt)^{-1}$), surpassing the highest activity reached so far with Pt_xY NP catalysts. In addition, the optimum Pt_xGd catalyst also presents high stability, as suggested by the accelerated stability tests under ORR potential cycling. Extended X-ray absorption fine structure (EXAFS) spectroscopy measurements confirm that as-prepared Pt_xGd NPs are compressively strained, relative to pure Pt, and that a Pt_xGd core/Pt-rich shell structure is adopted after partial Gd leaching. The activity correlates strongly with the compressive strain. On that basis, we propose that the ORR enhancement is due to the compressive strain within the Pt shell induced by the alloy core. The results herein confirm the suitability of Pt_xGd NPs as cathode nanocatalysts for proton exchange membrane fuel cells (PEMFCs).

1. Introduction

Both electrocatalysis and traditional heterogeneous catalysis focus on surface reactions that involve multistep reaction pathways, with sequential breaking and/or creation of chemical bonds. The catalyst consists of supported nanoparticles whose atomic and electronic structures are analyzed by means of common characterization techniques, such as X-ray photoelectron spectroscopy (XPS), transmission electron microscopy (TEM), or X-ray absorption spectroscopy (XAS) [1]. The main difference between the fields is that in electrocatalysis, the structure of the electrified metal/solution interface needs to be taken into account, which contains solvent molecules and other charged species. Despite these inherent challenges, it turns out that the factors that control the reactivity of surfaces toward gas/solid catalytic reactions are largely the same as for electrocatalytic reactions, that is the binding to the reaction intermediates [2]. Sabatier's principle states that the optimum catalyst should bind neither too weakly nor too strongly to the reaction intermediates [3]. According to the density functional theory (DFT) calculations of Nørskov, Rossmeisl and coworkers, the binding energies of the reaction intermediates in multielectron reactions tend to scale linearly together [4,5]. Consequently, the binding energy of just one reaction intermediate can be used as descriptor to predict the trends in activity for electrocatalytic reactions; plotting the activity as a function of such a descriptor then results in a Sabatier volcano. This model has been able to describe trends for a number of electrocatalytic reactions [6–15], in particular the oxygen reduction reaction (ORR) [4,13,16–22]. It turns out that proton exchange membrane fuel cells (PEMFCs) are limited by the ORR. Consequently, large loadings of Pt nanoparticle catalysts are required at the cathode to limit potential losses, as Pt is the most active pure metal catalyst for the reaction [23]. Typically, the Pt loading at the PEMFC cathode, where the ORR takes place,

* Corresponding author.

http://dx.doi.org/10.1016/j.jcat.2014.12.012
0021-9517/

is around one order of magnitude higher than the Pt loading at the anode (0.4 mg Pt cm^{-2} versus 0.05 mg Pt cm^{-2}) where the hydrogen oxidation reaction (HOR), which is far more facile, occurs [23–27]. As a result, the high cost and short supply of Pt hinder the large-scale uptake of PEMFCs, despite their promise as efficient, potentially zero-emission source of power for automotive vehicles and portable devices [28].

A suitable strategy in order to improve the ORR activity, and hence, reduce the Pt loading at the cathode, is to use Pt alloys instead of pure Pt [16,23,28–30]. The effect of alloying is to weaken the binding of the surface to the hydroxyl intermediates. In accordance with the volcano model [4], the overpotential on pure Pt catalysts is due to the reduction of *OH (where *OH is an adsorbed hydroxyl intermediate) [4,16,31–34]. The optimum catalyst for the ORR should have an *OH binding energy 0.1 eV weaker than Pt(1 1 1), or an O* binding 0.2 eV weaker; excessive weakening of HO* will cause the reaction to be limited by the formation of the superhydroxyl intermediate, HOO* [35]. Typically, the surface atoms of a Pt alloy will consist of pure Pt, as most other metals will be unstable at the oxidizing, acidic, conditions of a PEMFC cathode. Thereby, the introduction of a second metal in the Pt structure induces a change in the electronic structure of the Pt surface atoms; this can either be induced because of direct interactions with the second metal, that is the *ligand effect* [19,36,37] and/or the existence of lattice compression (*strain effect*), as a result of a decrease of the Pt–Pt interatomic distances [38–40].

In recent years, efforts have been focused on Pt alloys with late transition metals (LTM), such as Fe, Ni, Cu, and Co; they have shown considerably greater activity compared to pure Pt [41–51]. The active phase in these alloys is a Pt overlayer whose thickness strongly depends on the catalyst pre-treatment [46]. Thus, the Pt overlayer is typically one monolayer thick when the Pt–LTM alloy is subjected to annealing in ultrahigh vacuum (UHV) conditions prior to the electrochemical characterization ("Pt-skin" surface) [46]. In contrast, a considerably thicker, ~1-nm Pt overlayer, equivalent to 3–4 monoatomic Pt layers, is achieved when the alloy is exposed to the acidic electrolyte, because of leaching of the less noble metal from the outermost atomic layers of the surface (denoted by Markovic, Stamenkovic and coworkers as a "Pt-skeleton" surface) [46,52]. On such a thick Pt overlayer, ligand effects can be excluded, and hence, the ORR enhancement should be due to surface strain effects.

Although these Pt alloy catalysts show significant initial enhancements in activity, relative to pure Pt, over time their performance tends to degrade: the second element will segregate to the surface and dissolve into the electrolyte, via a process known as dealloying [43,48,53–58].

As a result of the instability of alloys of Pt and late transition metals, we, in collaboration with theory group of Nørskov and Rossmeisl, screened for a more stable class of Pt alloy ORR catalysts, using computational DFT-based screening methods [18]. We searched for alloys that were not only predicted to be active, on the basis of the O* binding, but also stable, as predicted by the alloying energy; the output of the screening was that both Pt_3Y and Pt_3Sc should be active and stable. Subsequent experiments on sputter-cleaned polycrystalline Pt_3Y showed that it exhibited exceptionally high activity for the ORR, only surpassed by single crystal Pt_3Ni(1 1 1) with an annealed "Pt-skin" structure [50]. The considerable negative alloying energy (or heats of formation) of Pt_3Y and Pt_3Sc ($\Delta H_{f(alloy)} \approx -4$ eV/formula unit) is also shared by other Pt alloys with early transition metals and lanthanides, such as Pt_5La, Pt_5Ce, and Pt_5Gd; this contrasts with the negligible heat of formation of the Pt–LTM intermetallic compounds (LTM = Fe, Co, Cu, Ni; $\Delta H_{f(alloy)} > -1$ eV) [59,60] (we note that despite their denomination as "rare earths," the lanthanide metals are much more abundant and more inexpensive than Pt [61]). We are aware that despite the significant heat of formation of the Pt–lanthanides alloys, there is still an immense driving force for the dealloying of the solute metal under the corrosive environment of a PEMFC cathode. Nevertheless, we expect that the dealloying mechanism ultimately involves an energy barrier for diffusion determined at least partially driven by the heat of formation of the bulk alloy, hence its use as a descriptor of the kinetic stability [18]. This notion is consistent with surface science experiments performed at our laboratory: a Cu monolayer on Pt(1 1 1) will diffuse subsurface at ~500 K [62]; under the same conditions, an Y monolayer on Pt(1 1 1) will diffuse subsurface at ~800 K [63]. This is likely due to the stronger interaction between Pt and Y than between Pt and Cu, ($\Delta H_{f(Pt3Y)} \approx -4.04$ eV/formula unit than $\Delta H_{f(Pt3Cu)} \approx -0.56$ eV/formula unit) [18]. On the other hand, adsorbed O* or subsurface oxide may induce the segregation of the solute element [64], but only when the oxygen atom is in close vicinity to the solute metal.

Our subsequent electrochemical experiments also revealed that other Pt–lanthanide alloys show superior activity for the ORR in the bulk polycrystalline form, in particular Pt_5Gd, which shows a similar activity to Pt_3Y [30,59,60,65]. We must emphasize that sputter-cleaned polycrystalline Pt_5Gd and Pt_3Y alloys have displayed the highest ORR activities ever reported in the literature, to the best of our knowledge the highest for samples prepared in this manner (fivefold increase at 0.9 V, compared to polycrystalline Pt) [60,65]. Furthermore, these intermetallic compounds exhibit a high stability under ORR conditions. For example, Pt_5Gd only exhibits 15% activity loss after 10,000 cycles between 0.6 and 1.0 V in O_2-saturated electrolyte [59,60]. In comparison, Todoroki and coworkers demonstrated that Pt-enriched Ni/Pt(1 1 1) lost 75% of its initial activity under similar experimental conditions [48]. Moreover, the great stability of Pt–early transition metal alloys has been also confirmed by Lim and co-workers through analysis of sputtered thin-film electrodes [66].

It turns out that the origin of activity of Pt_3Y was somewhat more complicated than we originally anticipated [63,65]. Angle-resolved X-ray photoelectron spectroscopy (AR-XPS) analysis of the sputter-cleaned alloyed electrodes showed that a Pt-skeleton structure is developed after the electrochemical experiment, the Pt overlayer being around 1 nm thick. A similar structure was also found for Pt_5Gd alloy after the electrochemical measurement [60], and, consequently, the ORR enhancement in both cases was attributed to compressive strain imposed onto the Pt overlayer by the alloy bulk. Such behavior seems counterintuitive, given that Y and Gd have a larger covalent radius than Pt [67]; one could expect that the resulting alloy would induce surface tensile strain, leading to a stronger adsorption of *OH and a higher overpotential for the ORR. Nevertheless, we explain the superior ORR activity of Pt_xY and Pt_5Gd compared to pure Pt by considering the inherent structural characteristics of such alloys. In order to accommodate the different Pt and second metal atomic radii, most of the Pt atoms are arranged in *kagomé* nets with a very short Pt–Pt nearest-neighbor distance (<2.7 Å) and with larger voids in which the solute atoms reside with bond lengths greater than 3 Å to their neighbor atoms (see Fig. S1 in the Supplementary information for an illustrative example of such arrangement). On the basis of the described structure, we proposed that Pt_xY and Pt_5Gd alloys impose compressive strain onto the Pt overlayer [60,65], resulting in weaker *OH adsorption and enhanced oxygen reduction activity.

In light of our results with extended surfaces of Pt_xY and Pt_xGd, we aimed to synthesize the catalysts in the more technologically relevant nanoparticulate form. Nevertheless, this task is not trivial, because of the difficulties of synthesizing the non-noble metal in the metallic state, due to the particularly negative standard reduction potential of Gd or Y ($U^0(Gd^{3+}/Gd) = -2.28$ V and $U^0(Y^{3+}/Y) = -2.37$ V); in comparison, late transition metals, such as Ni, have

a much more positive dissolution potential ($U^0(Ni^{2+}/Ni) = -0.25$ V) [68]. This drawback makes it highly challenging to synthesize Pt_xGd and Pt_xY alloy nanoparticles by means of traditional wet chemical methods, which would involve the exposure of the non-noble metal to oxygen or water [69]. Consequently, in order to prove that nanoparticles of this class of catalysts could be worthy of further investigation, and eventual chemical synthesis, we resorted to a physical method for producing Pt_xY nanoparticles [70]. Our chosen route was the gas aggregation method, combined with time-of-flight separation after sputtering of a primary alloy target [70–75]. Apart from providing a proof-of-concept, this method also produces catalysts with a well-defined size, shape, morphology, and composition, providing significant scientific insight. The corresponding ORR activities displayed in the electrochemical experiments avoid typical secondary factors, such as possible interactions of the nanoparticles with a high surface area carbon substrate or the influence of the metal precursors/solvents employed in the synthesis [76–80]. Our work showed that the ORR activity of Pt_xY nanoparticles supported on a planar glassy carbon support showed a marked size dependence; the 9-nm catalyst showing an exceptionally high mass activity of 3.05 A $(mg\ Pt)^{-1}$ only surpassed by the performance of annealed Pt_3Ni nanoframes [41]. In addition, the Pt_xY catalyst retained 63% of the activity after accomplishing the long-term stability test under ORR conditions. These results confirmed that the high ORR activity of the sputter-cleaned Pt_3Y alloy [18] could be extended to the nanoparticulate form and that they show moderate stability.

Herein, we extend this approach to perform structural and electrochemical characterization of Pt_xGd alloy nanoparticles synthesized by the gas aggregation method, following the same procedure used for the production of Pt_xY nanoparticles. The activity of the Pt_xGd nanoparticles toward the ORR was evaluated in half-cell configuration by using the rotating ring-disk electrode (RRDE) technique. In addition, the composition and morphology changes of the catalysts before and after the electrochemical test were characterized by means of XPS, transmission electron microscopy (TEM), and extended X-ray absorption fine structure (EXAFS) spectroscopy measurements.

2. Materials and methods

2.1. Synthesis of mass-selected Pt_xGd nanoparticles

The nanoparticles were prepared using a magnetron sputter gas aggregation source (Birmingham Instruments Inc.), combined with time-of-flight mass filtering, and deposited onto glassy carbon electrodes mounted in an multichamber ultrahigh vacuum (UHV) system (Omicron, Multiscan Lab) with a base pressure in the 10^{-11} mbar region. The gas aggregation technique involves Ar^+ sputtering of an alloy target (in this study a Pt 9:1 Gd alloy target from Kurt J. Lesker Inc.), to produce an atomic vapor that is condensed into nanoparticles through collisions with cooled Ar and He gas. It must be noted that the composition of the target determines the atomic ratio of the mass-selected nanoparticles, as demonstrated with Pt_xY nanoparticles in our preceding publications [70,81]. It turns out the use of a target with the same composition than the corresponding extended, polycrystalline alloy of interest leads to nanoparticles with high solute content that would corrode in excess [65,70,81]. Consequently, in the present study, we used the same 9:1 ratio for the synthesis of Pt-rich Pt_xGd nanocatalysts.

The gas aggregation method is particularly useful in the context of metallic formation of nanoparticles from metals such as gadolinium that has high affinities for oxygen, as it is an ultrahigh vacuum compatible method: oxygen is present in extremely low levels and therefore it can entirely be avoided in the as-deposited Pt–Gd alloy particles. The second major advantage arises from the fact that many of the nanoparticles produced via aggregation of Ar^+ sputtering atoms are ionized [82]; thus, the particles can be filtered based on their mass-to-charge ratio, which in turn allows the deposition of particles with narrow size distributions. In our experiments, the Pt–Gd nanoparticles are filtered using a time-of-flight mass filter [83].

Following the particle production and filtering stages, the ionized nanoparticles were directed using Einzel lenses onto glassy carbon electrode supports mounted in the vacuum chamber. The Einzel lenses can be used to control the breadth and position of the particle beam, which gives control of the total number of particles that are deposited onto the electrode surface, as well as the density of the nanoparticles. The combination of particle counting and mass selection allows us to accurately estimate the amount of catalyst deposited onto the glassy carbon substrate. The mass that was used for the calculation of the mass activity was the mass calculated from the deposition current.

Assuming spherical and singly charged particles, the total deposited mass was calculated from the formula $M_{dep} = m_p I_{dep} t$, where m_p is the single particle mass, set using the mass filter, I_{dep} the deposition current and t the deposition time. This mass, from the deposition current, combined with the Pt:Gd ratio estimated from the XPS measurements of the as-prepared catalysts, was used to determine the mass activity for the ORR.

Elemental characterization of the as-prepared glassy carbon-supported Pt–Gd nanoparticles was performed in-situ for each nanoparticles size, that is without breaking the vacuum, using X-ray photoelectron spectroscopy (XPS). The X-ray source was an XR-50 from Specs GmbH., with aluminum and magnesium anodes. XPS and ISS measurements after air exposure and after electrochemical testing were conducted in a different UHV system.

2.2. X-ray photoelectron spectroscopy (XPS)

X-ray photoelectron spectroscopy (XPS) measurements were acquired in two different UHV chambers. A preliminary analysis of the as-prepared nanoparticles was performed in-situ, soon after deposition. In this first experimental setup, the X-ray source (XR-50 manufactured by SPECS GmbH) consisted of Mg anode (Mg Kα emission line at 1253.6 eV). The XPS spectra were measured with an Omicron hemispherical analyzer with a pass energy of 25 eV. Ex-situ measurements of the samples after air exposure, after ORR activity tests, and after stability tests were instead performed in a Theta-Probe instrument (Thermo Scientific). This instrument is equipped with a monochromatized Al Kα source (emission line at 1486.7 eV), and XPS spectra were obtained at an analyzer pass energy of 100 eV. In all cases, the atomic concentrations were quantified by integration of the Pt 4f, Gd 4d, O 1s, C 1s peaks after removal of a Shirley-type background. The resulting XPS intensities were corrected for the transmission function of the analyzers, Wagner sensitivity factors [84], and electron mean free path estimated from the TPP-2M formula [85].

2.3. Transmission electron microscopy (TEM) analysis

Bright-field transmission electron microscopy (TEM) and high-angle annular dark-field scanning transmission electron microscopy (HAADF-STEM) were performed in a FEI Titan Analytical 80-300 equipped with a CEOS C_s probe aberration corrector on the condenser lens. Identical location (IL) studies were carried out in bright-field TEM at 300 kV accelerating voltage. The particle size distributions (PSDs) were extracted from HAADF-STEM micrographs acquired at 300 kV accelerating voltage. Within each specimen, the HAADF-STEM images were analyzed with the same microscope condition, constant acquisition dwell time as well as

the HAADF detector settings. For the TEM measurements, the nanoparticles were deposited directly onto lacey carbon-coated Au TEM grids. The setup for the electrochemical stability test under ORR conditions was adapted from the procedure developed from an earlier study at our laboratory [86].

2.4. Electrochemical measurements

The electrochemical testing of the Pt_xGd nanoparticles was carried out in a custom-made three-electrode glass cell provided with an external jacket attached to a water bath with temperature control. The counter electrode was a Pt wire, and the reference was a $Hg|Hg_2SO_4$ electrode, both separated from the working electrode compartment using ceramic frits. The electrolyte, 0.1 M $HClO_4$, was prepared using high-purity 70% $HClO_4$ (Merck, Suprapur) and ultrapure water (Millipore Milli-Q, resistivity >18.2 MΩ cm^{-1}), whereas all the gases used in the electrochemical tests were grade 5N5 (AGA). All the measurements were accomplished at 23 ± 1 °C.

The electrochemical experiments were performed with a VMP2 multi-channel potentiostat (Bio-Logic Instruments) computer controlled using EC-Lab software. The rotating ring-disk electrode (RRDE) assemblies and the glassy carbon (GC) substrates (5 mm diameter) were acquired from Pine Instruments Corporations and HTW, respectively. All the potentials indicated in the text are referred to the reversible hydrogen electrode (RHE) measured in the same electrolyte and corrected for Ohmic losses.

In each experiment, the GC disk containing the as-prepared Pt_x-Gd nanoparticles was inserted into a RRDE Teflon holder and used as working electrode for the electrochemical test. Subsequently, the electrode was immersed into the electrochemical cell under potential control at 0.10 V in N_2-saturated 0.1 M $HClO_4$ electrolyte and subjected to potential cycling between 0.05 V and 1.00 V at 50 mV s^{-1} until a stable cyclic voltammogram was achieved. Following this, the ORR performance of the Pt_xGd nanoparticles was evaluated by means of hydrodynamic voltammetry in O_2-saturated solution. After the ORR experiment, CO-stripping analysis was carried out for determining the electrochemical surface area (ECSA) of the Pt_xGd nanoparticles. For this purpose, CO gas was first bubbled into the electrolyte for 2 min, while the working electrode potential was kept at 0.05 V; then, the remaining CO dissolved in solution was removed by sparging Ar for 15 min whereas keeping the potential control. Afterward, the potential was scanned up to 1.00 V in CO-free Ar-purged solution at 50 mV s^{-1}. The corresponding electrochemical active surface area (ECSA) of the Pt_xGd catalysts was estimated assuming a ratio of 420 μC cm^{-2} [87].

The long-term stability of the Pt_xGd nanoparticles was subjected to analysis by cycling between 0.60 and 1.00 V at 100 mV s^{-1} in quiescent O_2-saturated 0.1 M $HClO_4$ solution for a total of 10,000 potential cycles. The ORR activity was evaluated after 1000 and 10,000 potential cycles. A second CO-stripping experiment was performed in order to probe the possible change of the electrochemical area after the stability test.

2.5. Extended X-ray absorption fine structure (EXAFS) analysis

Grazing incidence X-ray absorption spectroscopy (GI-XAS) measurements were carried out at beam line 11-2 at the Stanford Synchrotron Radiation Lightsource (SSRL). An absorption spectrum around the Pt L_3 edge (11,564 eV) was acquired for each sample, and the energy range was 11,334–12,273 eV, which corresponds to an EXAFS range up to a photoelectron wave number of 13.6 $Å^{-1}$. The samples were aligned in grazing incidence geometry near the critical angle of total external reflection in order to maximize the fluorescence yield. The fluorescence photons from the Pt atoms in the nanoparticles were captured using a 100-element Ge solid-state detector. Several spectra were recorded for each sample and subsequently averaged to increase the signal-to-noise ratio. The data analysis was done using the program SixPACK, which is based on the IFEFFIT program. EXAFS fitting was done in *R*-space using a *k*-weighting of k^2, a *k*-range of 3–11 $Å^{-1}$, and an *R*-range of around 1.5–3.2 Å. A detailed description of the data treatment and the fitting procedure can be found in the Supplementary information.

3. Results

3.1. Synthesis of mass-selected Pt_xGd nanoparticles

The mass-selected Pt_xGd particles were prepared through combination of gas aggregation of a Pt_9Gd target and time-of-flight separation as shown in Fig. 1. The charged nanoparticles were subsequently deposited directly onto a planar glassy carbon substrate under ultrahigh vacuum conditions. In order to define the overall particle composition, XPS measurements were acquired in-situ after deposition. Fig. S2 shows that the Pt:Gd ratios were rather similar in all cases, irrespective of the particle size, with an average value of 3.6 ± 0.8.

3.2. X-ray photoelectron spectroscopy (XPS)

Further XPS characterization was carried out ex-situ after exposure of the samples to air and after electrochemical ORR activity testing. Fig. 2 reports the XPS spectra of the Gd 4d core-level region for a 9-nm sample in different conditions: very similar spectra

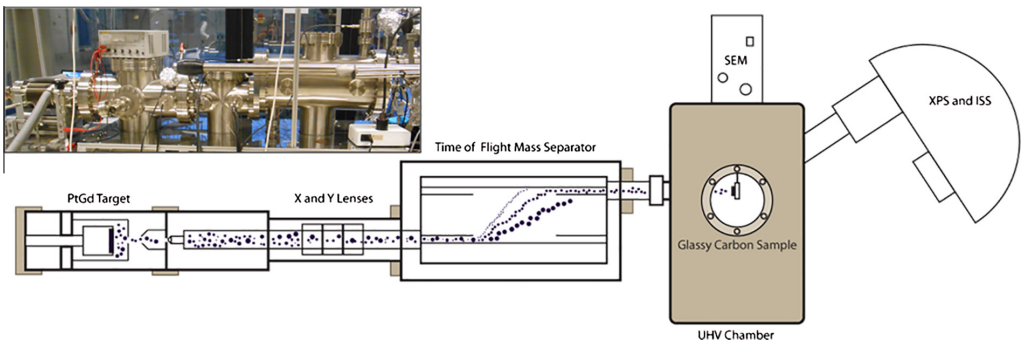

Fig. 1. Schematic representation of the nanoparticle source used for the synthesis and characterization of the Pt_xGd nanoparticles in UHV conditions. The inset shows a photograph of the actual apparatus.

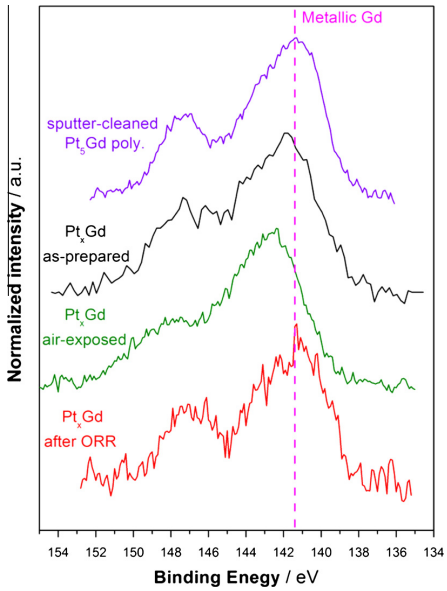

Fig. 2. Detailed XPS survey of Gd 4d core-level region spectra for sputter-cleaned polycrystalline Pt_5Gd and for the Pt_xGd nanoparticles (9 nm) as-prepared (under UHV conditions), after air exposure and after the ORR measurement.

were also taken for different particle sizes indicating that the following considerations can be extended to all Pt_xGd nanoparticles. As typical for the lanthanide metals, the XPS features of Gd are in general quite complex due to presence of localized electrons in the 4f shell. The localized f electrons couple through Russell–Saunders and spin–orbit coupling and result in a complex broad multiplet structure, see Fig. 2 [88]. In principle, this could be fitted using the multiplet structure, but we have here chosen to perform a careful analysis of the peak position and a comparison with the reference spectrum of a sputter-cleaned Pt_5Gd polycrystalline alloy where Gd atoms are in a completely metallic state allows us to monitor the chemical state of Gd. In the case of the as-deposited 9-nm Pt_xGd nanoparticles, the position of the Gd 4d spectrum is very similar to the polycrystalline sample, demonstrating that the synthesis of alloyed nanoparticles was successful and that no Gd oxidation occurred. However, as soon as the nanoparticles are taken out of the deposition chamber and exposed to air, a clear shift of the Gd 4d features and a change of shape can be observed and the new peak position agrees with the formation of Gd oxide on the surface [88]. Notably, these oxidized components are completely removed after electrochemical measurements, suggesting that the oxide is not stable in acid and dissolves in the electrolyte, in agreement with the Pourbaix diagram for Gd [68]. The remaining Gd signal resembles closely the as-prepared nanoparticles and that of clean polycrystalline Pt_5Gd; this indicates that a Pt overlayer is formed during the acid leaching of surface Gd and this Pt shell protects the alloyed Gd in the core from further oxidation or dissolution [60]. The formation of such core–shell structure is also supported by the measured Pt:Gd ratios in Fig. S2: for all particle sizes

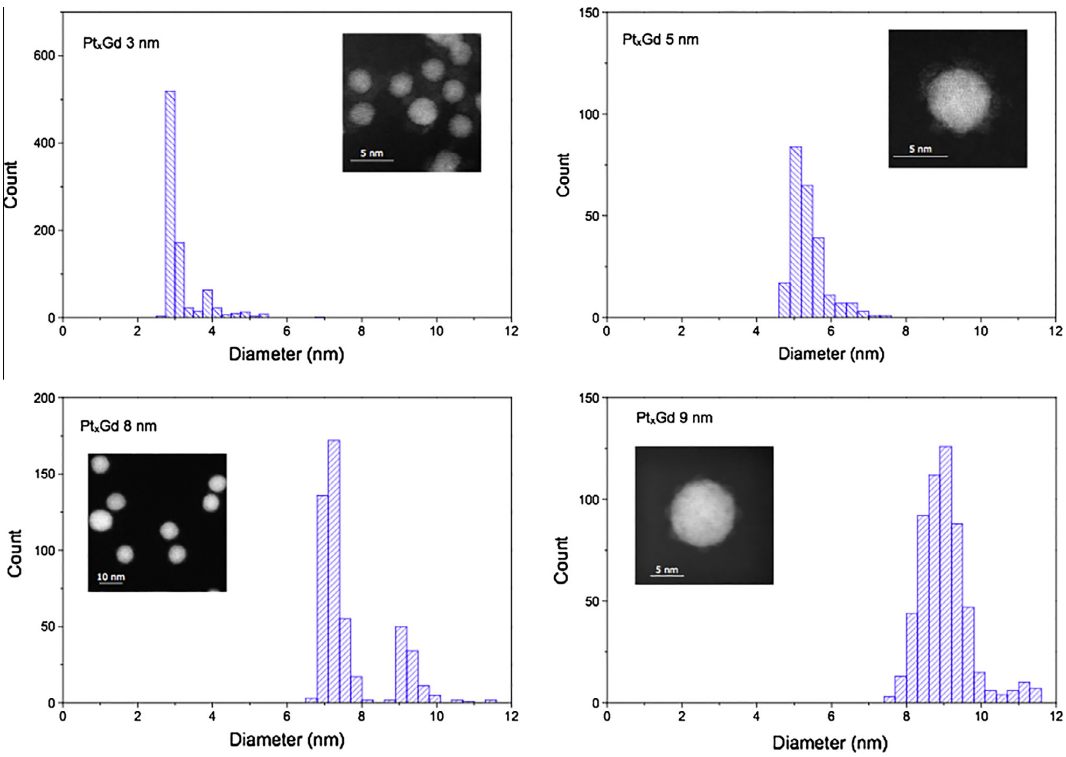

Fig. 3. Particle size distributions and representative HAADF-STEM micrographs of the different Pt_xGd nanoparticle catalysts.

and in particular for the small nanoparticles, the relative amount of Pt after electrochemistry is considerably higher than for the as-prepared or air-exposed nanoparticles. It should be noticed that analogous XPS evidences were found for Pt_xY nanoparticles in our previous study, supporting the notion that a similar core–shell structure is formed [70].

3.3. Transmission electron microscopy (TEM) analysis

Fig. 3 shows the particle size distribution (PSD) histograms of the different particles determined by HAAD-STEM. As seen, nanoparticulate catalysts with mean particle sizes ranging between ~3 and ~9 nm were synthesized. For simplicity, the particle sizes are rounded up to the closest integer to denominate the different catalysts; however, when plotting electrochemical or morphological parameters as a function of the size, the actual measured value and the corresponding standard deviation are employed, as indicated in Table S1 in the Supplementary information. The PSDs present narrow peaks at the selected sizes indicating the successful mass selection. The satellite peaks at higher diameters correspond to double-charge nanoparticles, with a mass twice the intended one. This undesired effect is minimized by optimizing the synthesis conditions, namely by stabilization of the deposition current during the nanoparticles deposition [81]. IL Bright-field TEM of the 8-nm sample is shown in Fig. 4. The images of the as-prepared Pt_xGd catalyst and the following stability test under ORR conditions indicate the high stability of the nanoparticles on the carbon film support. A closer inspection of the exact same nanoparticles at high magnification reveals an amorphous shell covering the particles on the untreated sample that disappears after ORR catalytic test. In light of the XPS results, the amorphous shell can be ascribed to an oxide formed during air exposure. Presumably, the oxide would be dissolved in the electrolyte in the early stages of the electrochemical experiments.

3.4. ORR measurements of Pt_xGd catalysts

Following the sample preparation and the preliminary morphological characterization, the alloyed nanoparticles supported on glassy carbon were electrochemically tested in 0.1 M $HClO_4$ using a rotating ring-disk assembly. As a first step, the catalysts were electrochemically activated by means of potential cycling between 0.05 V and 1.00 V in N_2-saturated electrolyte until a stable voltammogram was achieved, as indicated in Fig. S3 of the Supplementary information, and subsequently the ORR experiment was carried out in O_2-saturated electrolyte under hydrodynamic conditions. The activity of the Pt alloy catalysts at 0.9 V, expressed in terms of specific activity and mass activity (normalized by Pt loading), is presented in Fig. 5 as a function of the nanoparticle size. For comparison purposes, our previous results obtained with mass-selected Pt_xY and Pt nanoparticles are also included [70,71]. The activities of sputter-cleaned, polycrystalline Pt_5Gd and Pt_3Y extended surfaces, as well as sputter-cleaned, polycrystalline Pt are also presented in Fig. 5. The obtained size dependence of the specific activity for the Pt_xGd nanoparticles is in agreement with the trend found for both mass-selected Pt_xY and Pt nanoparticulate catalysts, namely the ORR-specific activity increases with the nanoparticle size, with the activity of the larger nanoparticles approaching the result reported for the corresponding extended, polycrystalline surface. From Fig. 5, it is manifest the superior activity of the Pt_xGd nanoparticles compared to pure Pt catalysts, with the only exception of the analyzed smallest size (3 nm),

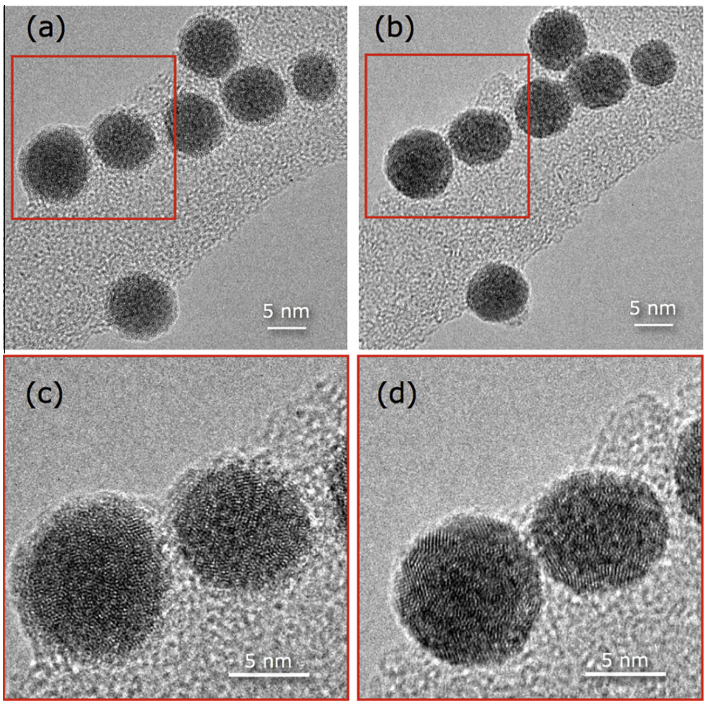

Fig. 4. Bright-field IL-TEM micrographs of 8-nm Pt_xGd nanoparticles before (a) and after (b) stability test. The (c and d) images are a magnification of the red squares drawn in (a and b), respectively. (For interpretation of the references to color in this figure legend, the reader is referred to the web version of this article.)

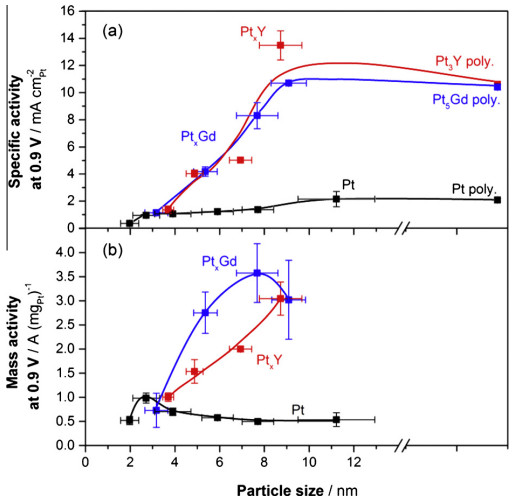

Fig. 5. (a) Specific activity and (b) mass activity of Pt_xGd nanoparticles (blue). Data taken at 0.9 V from cyclic voltammetry recorded at 50 mV s^{-1}, 1600 rpm, and 23 ± 1 °C in O_2-saturated 0.1 M $HClO_4$. For comparison, the previously published mass and specific activities of mass-selected Pt_xY (red) and pure Pt nanoparticles (black) are also plotted [70,71]. Additionally, the specific activities obtained under the same conditions of sputter-cleaned polycrystalline Pt_5Gd and Pt_3Y extended surface electrodes, as well as sputter-cleaned polycrystalline Pt, are presented [60]. Each data point corresponds to the mean value from at least two independent electrochemical tests. The horizontal error bars show the standard deviation in the particle size distribution (PSD) whereas the vertical error bars show the standard deviation in electrochemical measurements. The lines serve as a guide for the eye. The Supplementary information contains details of the quantification of mass and surface area carried out for the activity evaluation. (For interpretation of the references to color in this figure legend, the reader is referred to the web version of this article.)

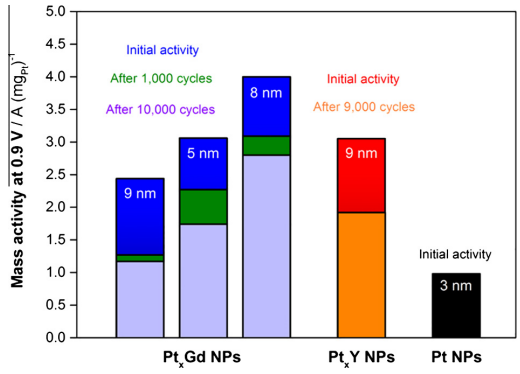

Fig. 6. The initial mass activity of Pt_xGd nanoparticles (blue), and after 1000 cycles (green) and 10,000 cycles (violet) of stability test under ORR conditions. The initial performance of the most active Pt_xY catalyst (red) and after 9000 cycles of stability test (orange) is also displayed [70]. For a suitable comparison, the maximum activity reported for mass-selected Pt NPs is also plotted (black) [71]. Data taken at 0.9 V from cyclic voltammetry recorded at 50 mV s^{-1}, 1600 rpm, and 23 ± 1 °C in O_2-saturated 0.1 M $HClO_4$. Stability test carried out by potential cycling between 0.6 and 1.0 V at 100 mV s^{-1}, 0 rpm, and 23 ± 1 °C in O_2-saturated 0.1 M $HClO_4$ solution. A detailed description of the stability test procedure is found in the Supporting information. (For interpretation of the references to color in this figure legend, the reader is referred to the web version of this article.)

similar to the performance achieved with the Pt_xY nanoparticles of a comparable particle size (4 nm) [70]. Additionally, the enhanced activity factor of the Pt_xGd catalysts is similar to that observed for Pt_xY nanoparticles, indicating that the equivalent promotional effect for the ORR found with Pt_3Y and Pt_5Gd bulk alloys is also attained in the nanoparticulate form. This is a subject of special interest regarding the potential application of Pt_xY and Pt_xGd electrocatalysts in PEMFC cathodes. Moreover, the specific activity of the 9-nm samples of each alloy (13.5 mA cm^{-2} and 10.7 mA cm^{-2} for Pt_xY and Pt_xGd, respectively) is comparable, or marginally higher, than that reported for carbon-supported annealed Pt_3Ni nanoframes (~20 nm), synthesized by Stamenkovic and co-workers (8.5 mA cm^{-2}) [41].

On the other hand, the mass activity evaluated as a function of the size reveals not only the greater mass activity of the Pt_xGd catalysts compared to pure Pt nanoparticles, but also the higher performance versus the Pt_xY catalysts. In the case of the Pt_xGd nanoparticles, the size dependence of the mass activity originates a volcano plot with the highest mass activity achieved with the 8 nm size and being equal to 3.6 A $(mg\ Pt)^{-1}$, which is significantly higher than the optimum mass activity reported for the Pt_xY nanoparticles in our previous work (3.0 A $(mg\ Pt)^{-1}$, with 9 nm as set particle size). Moreover, the maximum mass activity is ~3.6 times higher than the optimum result found with the pure Pt nanoparticles synthesized using the same size-selection experimental procedure [71] and roughly 6.5 times higher than the most active carbon-supported pure Pt electrocatalyst (0.55 A $(mg\ Pt)^{-1}$) [89]. The remarkable mass activity peak of the Pt_xGd nanoparticles also represents *the highest ORR activity reported in the literature for solid nanoparticles* (opposed to hollow or porous nanocatalysts) *based on an acid-leached structure*; it is only overtaken overall by the performance of Pt_3Ni nanoframes (5.7 A $(mg\ Pt)^{-1}$) [41].

In order to investigate the stability of the Pt_xGd nanoparticles, long-term potential cycling experiments under ORR conditions were carried out. For this purpose, the alloyed electrodes were cycled between 0.6 V and 1.0 V for 10,000 cycles in O_2-saturated 0.1 M $HClO_4$ [53,55]. Fig. 6 displays the results of the stability test in terms of the evolution of the mass activity with the extended cycling treatment for mass-selected Pt_xGd nanoparticles with average particle size of 5 nm, 8 nm, and 9 nm. For comparison purpose, the stability test results obtained with the most active Pt_xY catalyst (9 nm), as well as the initial activity of Pt 3-nm nanoparticles, are included in Fig. 6. It can be seen that for the three analyzed sizes the magnitude of the ORR activity losses is similar to that found with the Pt_xY nanoparticles, that is 30–55% [70], and that most of the activity loss occurs in the early stages of the stability test (first 1000 cycles). According to the CO-stripping analysis data, the electrochemical active surface area remains invariable after the stability test, indicating that a possible decrease of the available surface area (e.g. nanoparticles sintering, agglomeration, or detachment) cannot be accounted for the ORR activity losses. A similar conclusion could be extracted from the results of the IL-TEM analysis, shown in Fig. 4 for the case of the Pt_xGd 8-nm catalyst. As seen, no significant changes were detected in the catalyst general morphology after the stability test, with the exception of the dissolution of the oxide layer covering the as-prepared nanoparticles. The most active Pt_xGd nanoparticles (8 nm) retain 70% of the initial activity after 10,000 cycles, indicating that their stability is comparable (or slightly better) than that of Pt_xY nanoparticles of the optimum size (9 nm) [70]. Consequently, even after the extended potential cycling treatment, the Pt_xGd nanoparticles of 8 nm are still ~5 times more active than pure Pt nanoparticles with a comparable size and ~2.8 times more active than the maximum mass activity achieved with the mass-selected Pt nanoparticles (3 nm).

3.5. EXAFS analysis of Pt_xGd catalysts

Motivated by our previous investigation on polycrystalline Pt_5Gd, which revealed that the compressive strain was the main

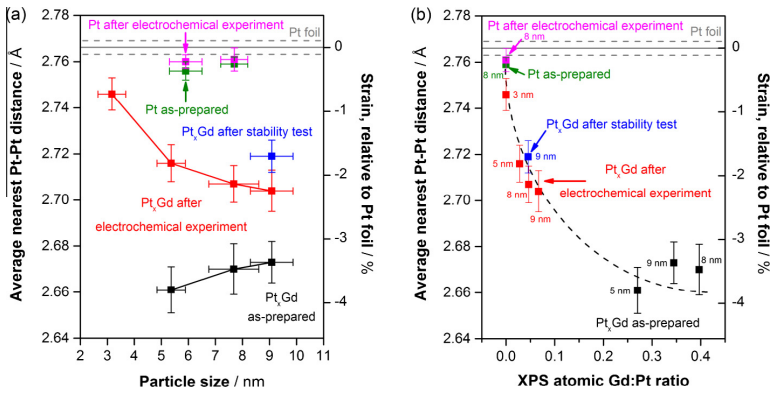

Fig. 7. (a) Average nearest-neighbor Pt–Pt distance measured by EXAFS as a function of the particle size for Pt$_x$Gd nanoparticles as-prepared (black), after electrochemical experiment (red) and after stability test (blue). For comparison purpose, the EXAFS results obtained for as-prepared (green) and electrochemically tested (pink) mass-selected Pt nanoparticles, reported in our preceding publication [70], are also shown; (b) average nearest-neighbor Pt–Pt distance measured by EXAFS as a function of the atomic Gd:Pt ratio estimated from XPS measurements for Pt$_x$Gd nanoparticles as-prepared (black), after electrochemical experiment (red) and after stability test (blue). The Pt–Pt interatomic distances determined by EXAFS in our previous work for as-prepared (green) and electrochemically tested (pink) mass-selected Pt nanoparticles, with zero Gd content, are shown for comparison [70]. The corresponding average particle size is specified. Measurements were performed in situ on a Pt foil (continuous gray horizontal line in a and b; the dashed gray horizontal lines show the error from the fitting software, see details in the Supporting information) as a reference. The left *y*-axis in (a and b) represents the nearest-neighbor Pt–Pt distance, whereas the right *y*-axis shows the strain percentage relative to the Pt–Pt distance measured for the Pt foil. The horizontal error bars in (a) account for the standard deviation in the particle size distribution (PSD) and the vertical error bars in (a and b) represent the standard deviation from the fitting software, respectively. The dashed black line in (b) serves as a guide for the eye. (For interpretation of the references to color in this figure legend, the reader is referred to the web version of this article.)

cause of the superior of performance of the alloy compared to pure Pt [60], we carried out grazing-incident extended X-ray absorption fine structure measurements (GI-EXAFS) for the quantification of the strain in the Pt$_x$Gd nanoparticles. For that purpose, samples as-prepared, after the standard electrochemical experiment and after the long-term stability test, were considered. The average nearest-neighbor distances between the Pt atoms were calculated through fitting of the EXAFS spectra. Details of the fitting procedure are described in detail in the Supplementary information. The result of the analysis is summarized in Fig. 7(a), where the Pt–Pt interatomic distance and the consequent compressive strain are plotted versus the average nanoparticle size for the three different experimental conditions. The EXAFS results obtained for as-prepared and electrochemically tested mass-selected Pt nanoparticles, reported in our preceding publication [70], are also presented. The average Pt–Pt distance for bulk Pt (Pt foil) is included in the plot for comparison and used for the estimation of the relative strain. In general, the as-prepared Pt$_x$Gd nanoparticles exhibit a smaller Pt–Pt distance than bulk Pt, indicating the existence of a compressive strain before the electrochemical analysis. The magnitude of such strain slightly decreases with the nanoparticle size, changing from −3.8% to −3.4% (compared to bulk Pt) for the 5-nm and the 9-nm nanoparticles, respectively. In the case of the catalysts after ORR test, they show significant larger Pt–Pt distances compared to the as-prepared samples but still lower compared to bulk Pt. The Pt–Pt distances after the standard electrochemical test are remarkably size dependent, varying smoothly from −0.7% to −2.2% for the 3 nm and the 9 nm size catalysts, respectively. In addition, the 9-nm Pt$_x$Gd sample subjected to the stability test exhibits less compressive strain than the counterpart after the conventional electrochemical measurement (−1.7% versus −2.2%, respectively), demonstrating that the accelerated stability test produces some relaxation in the Pt$_x$Gd nanoparticles. On the other hand, the average Pt–Pt distance/strain estimated by EXAFS measurements can be also associated with the XPS atomic Gd:Pt ratio of the Pt$_x$Gd nanoparticles under different conditions, being the corresponding relationship displayed in Fig. 7(b) (the data for mass-selected Pt nanoparticles and Pt foil presented for comparative purpose). The obtained trend reveals that the compressive strain in the Pt$_x$Gd nanoparticles is strongly related to the Gd content in the catalyst, increasing with the fraction of solute atoms.

4. Discussion

The interpretation of the XPS spectra shown in Fig. 2 combined with the angle-resolved XPS results of polycrystalline Pt$_5$Gd from our previous research (see Section 1) [60] strongly supports the formation of a core/shell structure after acid leaching of Gd atoms from the outermost layers of the nanoparticles. Therefore, such model can be also used for explaining the trends derived from the EXAFS analysis, shown in Fig. 7. We could rationalize the obtained findings considering that the as-prepared Pt$_x$Gd nanoparticles are under compressive strain as a result of the alloying; this is to be expected, given that the closest nearest-neighbor Pt–Pt distance in Pt$_5$Gd hexagonal structure is 2.65 Å, or ∼5% compressive strain relative to pure Pt (2.77 Å) [60,90] (see Fig. S1 in the Supplementary information). Once the Pt$_x$Gd nanoparticles are exposed to the electrolyte and subjected to the electrochemical characterization, the Gd atoms are leached out from the outermost atomic layers of the nanoparticles, leading to the formation of a pure Pt overlayer; this overlayer would be under compressive strain, induced by the underlying Pt$_x$Gd alloy core, resembling the structure of polycrystalline Pt$_5$Gd after electrochemical characterization [60]. Similarly, the scanning transmission electron microscopy energy-dispersive X-ray spectroscopy (STEM-EDS) mapping of mass-selected Pt$_x$Y nanoparticles revealed that a core/shell structure was developed after the ORR test, the Pt-rich being shell ∼1 nm thick, in agreement with the thickness of ∼3 monoatomic layers estimated for polycrystalline Pt–lanthanides alloys [70]. Logically, some strain relief could occur in the pure Pt shell of the Pt$_x$Gd nanoparticles in the absence of the Gd atoms. However, previous investigations with single crystal surfaces have revealed that some degree of compression would still be retained in the

outermost surface of the layer Pt shell [39]. Additionally, the size dependence for the strain after the ORR presented in Fig. 7(a) is due to the smaller pure alloy core for smaller nanoparticles, as also evidenced by the size dependence of Gd:Pt ratio in Fig. 7(b).

It is interesting to note that the strain in the 9-nm nanoparticles relaxes further, following the stability test. To some degree, this is only to be accepted; once the Gd is removed from the overlayer, there will be a driving force for it to relax toward pure Pt. It is curious, however, to note that in the case of the 9-nm particle, this relaxation is accompanied by a slight increase in the Pt:Gd XPS ratio, as shown in Fig. 7(b); this is analogous to the behavior of extended surfaces of polycrystalline Pt_5La and Pt_5Ce alloys following extended cycling [59]. Since Gd diffusion is likely to be very slow at room temperature through the Pt overlayer (see Section 1), we speculate that the dealloying occurs via an alternative mechanism, perhaps involving subsurface oxide formation [91]. Nonetheless, the majority of the activity losses occur during the first 1000 cycles, as shown in Fig. 6. This suggests that the rate of degradation slows significantly after 1000 cycles, at which point the catalyst has reached some kind of metastable state.

In order to gain some insight into the role of the strain in the ORR activity of the Pt_xGd nanoparticles, the specific activity is plotted as a function of the corresponding strain relative to Pt foil after ORR and after stability test in Fig. 8. In addition, the previous results of activity versus strain after ORR for Pt_xY NPs and for Pt NPs are included for comparison. *As a result, it is manifest that the ORR activity of Pt, Pt_xY, and Pt_xGd all follows the same trend, that is the activity enhancement is largely controlled by the strain in the nanoparticles*. This is also consistent with Strasser and co-workers' investigations of dealloyed Pt_xCu nanoparticles [39]. It should be noted that the strain dependence of the ORR activity reported in Ref. [39] was found significantly less intense than that presented in this work, most likely due to excessive relaxation of the compressive strain in the Pt overlayer of the dealloyed Pt_xCu nanoparticles [39]. Moreover, the trend displayed in Fig. 8 also resembles the relationship established in our previous work focused on polycrystalline Pt–lanthanides alloys [59], where the specific activity of polycrystalline Pt_5Gd, Pt_5Ce, and Pt_5La was correlated with the interatomic Pt distance in the bulk, based on X-ray diffraction (XRD) measurements. Consequently, we conjecture that the compressive strain causes the weakening of the oxygenated intermediates adsorption, leading to the consequent enhancement of the ORR activity. According to DFT calculations, the necessary strain for optimizing the ORR performance is −2% (relative to an unstrained Pt(1 1 1) surface) [39]. This value is reached by the bulk compressive strain of the most active Pt_xGd nanoparticles (−2.2%), without reaching a maximum in activity. We expect that the local strain within the outermost layer of the Pt shell, which is responsible for the ORR activity, would be somewhat reduced compared to the overall strain plotted in Fig. 8, because of strain relaxation. This would result in an unknown shift of the plot to the right and, subsequently, we propose that the trend exhibited in Fig. 8 represents *the strong *OH binding side of a volcano plot. Accordingly, should a slightly greater degree of strain be imposed onto the surface*, by refining the atomic ratio of the second metal or increasing the nanoparticle size, *it might be possible to reach the peak of the volcano*.

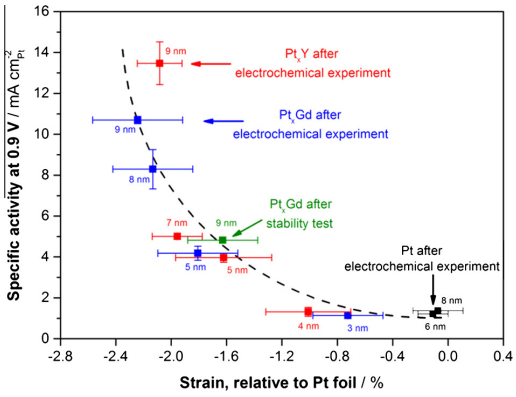

Fig. 8. Specific activity results for the ORR on Pt_xGd nanoparticles as a function of the strain, relative to bulk Pt, determined through EXAFS after electrochemical experiment (blue) and after the stability test (green). Data collected from Fig. 5, Fig. 6, and Fig. 7. The previous data reported for mass-selected Pt_xY (red) and Pt nanoparticles (black) after electrochemical experiment are included for comparison purposes [70]. The dashed black line acts as a guide for the eye. The horizontal and vertical error bars show the standard deviation in the strain estimation and in the electrochemical measurements, respectively. (For interpretation of the references to color in this figure legend, the reader is referred to the web version of this article.)

5. Conclusions

We have shown in the present work that the excellent catalytic properties of polycrystalline Pt_5Gd (enhanced ORR activity compared to pure Pt and stability upon cycling) also extend to nanoparticles. The maximum mass activity reached with the Pt_xGd nanoparticles (8 nm, 3.6 A (mg Pt)$^{-1}$ at 0.9 V) represents a notable improvement compared to our preceding results obtained with Pt_xY nanoparticles; in the literature, it is only surpassed by Pt_3Ni nanoframes [41]. Additionally, the optimum Pt_xGd catalyst exhibits similar, albeit very slightly improved, stability versus the most active Pt_xY nanoparticles previously reported (70% retention of the initial activity versus 63% for Pt_xY).

In addition, we have also confirmed that the mechanism for the ORR enhancement accounts for the compressive strain within the Pt shell induced by the Pt_xGd core. As a result, a direct relationship between the ORR activity of the Pt_xGd nanoparticles and their compressive strain can be established. We have also shown that the activity of pure Pt nanoparticles, Pt_xY, and Pt_xGd can all be correlated to the lattice strain.

Our work confirms that Pt_xGd alloy nanoparticles are of great interest for applications in PEMFC cathodes. Nevertheless, we are aware that the ultrahigh vacuum procedure used in this research is not valid for catalyst mass production; eventually low-priced chemical methods should be employed for such purpose. Therefore, our efforts are currently directed to the development of suitable chemical procedures to obtain Pt_xGd alloy in nanoparticulate form; using such methods we may have control over both particle size and Gd content, and ultimately the strain, which controls the oxygen reduction activity.

Acknowledgments

We thankfully acknowledge the EU PF7's initiative Fuel Cell and Hydrogen Joint Undertaking's project CathCat (GA 303492), the Danish National Research Foundation's Center for Individual Nanoparticle Functionality (DNRF54), and the Danish Ministry of Science's UNIK initiative Catalysis for Sustainable Energy (CASE) for providing the funding for this research. We also thank the Danish Council for Strategic Research's project NACORR. The A.P. Møller and Chastine Mc-Kinney Møller Foundation is gratefully acknowledged for its contribution toward the establishment of the Centre for Electron Nanoscopy in the Technical University of Denmark. This research was partly carried out at the Stanford Synchrotron Radiation Lightsource, a National User Facility operated by

Stanford University on behalf of the U.S. Department of Energy, Office of Basic Energy Sciences. We thank John R. Bargar, Apurva Mehta, Ryan C. Davis, Matthew Latimer, and Erik J. Nelson for their support with the GI-EXAFS setup and helpful discussions.

Appendix A. Supplementary material

Supplementary data associated with this article can be found, in the online version, at http://dx.doi.org/10.1016/j.jcat.2014.12.012.

References

[1] A. Wieckowski, M. Neurock, Adv. Phys. Chem. 2011 (2011) 1.
[2] J.K. Nørskov, T. Bligaard, J. Rossmeisl, C.H. Christensen, Nat. Chem. 1 (2009) 37.
[3] P. Sabatier, Ber. Dtsch. Chem. Ges. 44 (1911) 1984.
[4] J.K. Nørskov, J. Rossmeisl, A. Logadottir, L. Lindqvist, J.R. Kitchin, T. Bligaard, H. Jónsson, J. Phys. Chem. B 108 (2004) 17886.
[5] J. Rossmeisl, A. Logadottir, J.K. Nørskov, Chem. Phys. 319 (2005) 178.
[6] J. Greeley, T.F. Jaramillo, J. Bonde, I.B. Chorkendorff, J.K. Nørskov, Nat. Mater. 5 (2006) 909.
[7] J.K. Nørskov, T. Bligaard, A. Logadottir, J.R. Kitchin, J.G. Chen, S. Pandelov, U. Stimming, J. Electrochem. Soc. 152 (2005) J23.
[8] A.A. Peterson, J.K. Nørskov, J. Phys. Chem. Lett. 3 (2012) 251.
[9] H.A. Hansen, I.C. Man, F. Studt, F. Abild-Pedersen, T. Bligaard, J. Rossmeisl, Phys. Chem. Chem. Phys. 12 (2010) 283.
[10] I.C. Man, H.Y. Su, F. Calle-Vallejo, H.A. Hansen, J.I. Martínez, N.G. Inoglu, J. Kitchin, T.F. Jaramillo, J.K. Nørskov, J. Rossmeisl, Chem. Cat. Chem. 3 (2011) 1159.
[11] H. Dau, C. Limberg, T. Reier, M. Risch, S. Roggan, P. Strasser, Chem. Cat. Chem. 2 (2010) 724.
[12] M.T.M. Koper, J. Electroanal. Chem. 660 (2011) 254.
[13] S. Siahrostami, A. Verdaguer-Casadevall, M. Karamad, D. Deiana, P. Malacrida, B. Wickman, M. Escudero-Escribano, E.A. Paoli, R. Frydendal, T.W. Hansen, I. Chorkendorff, I.E.L. Stephens, J. Rossmeisl, Nat. Mater. 12 (2013) 1137.
[14] T.F. Jaramillo, K.P. Jørgensen, J. Bonde, J.H. Nielsen, S. Horch, I. Chorkendorff, Science 317 (2007) 100.
[15] A.A. Peterson, F. Abild-Pedersen, F. Studt, J. Rossmeisl, J.K. Nørskov, Energy Environ. Sci. 3 (2010) 1311.
[16] V. Stamenkovic, B.S. Mun, K.J.J. Mayrhofer, P.N. Ross, N.M. Markovic, J. Rossmeisl, J. Greeley, J.K. Nørskov, Angew. Chem. Int. Ed. 45 (2006) 2897.
[17] A.U. Nilekar, M. Mavrikakis, Surf. Sci. 602 (2008) L89.
[18] J. Greeley, I.E.L. Stephens, A.S. Bondarenko, T.P. Johansson, H.A. Hansen, T.F. Jaramillo, J. Rossmeisl, I. Chorkendorff, J.K. Nørskov, Nat. Chem. 1 (2009) 552.
[19] I.E.L. Stephens, A.S. Bondarenko, F.J. Perez-Alonso, F. Calle-Vallejo, L. Bech, T.P. Johansson, A.K. Jepsen, R. Frydendal, B.P. Knudsen, J. Rossmeisl, I. Chorkendorff, J. Am. Chem. Soc. 133 (2011) 5485.
[20] V. Viswanathan, H.A. Hansen, J. Rossmeisl, J.K. Nørskov, J. Phys. Chem. Lett. 3 (2012) 2948.
[21] A. Verdaguer-Casadevall, D. Deiana, M. Karamad, S. Siahrostami, P. Malacrida, T.W. Hansen, J. Rossmeisl, I. Chorkendorff, I.E.L. Stephens, Nano Lett. 14 (2014) 1603.
[22] A.S. Bandarenka, H.A. Hansen, J. Rossmeisl, I.E.L. Stephens, Phys. Chem. Chem. Phys. 16 (2014) 13625.
[23] H.A. Gasteiger, S.S. Kocha, B. Sompalli, F.T. Wagner, Appl. Catal. B: Environ. 56 (2005) 9.
[24] K.C. Neyerlin, W. Gu, J. Jorne, H.A. Gasteiger, J. Electrochem. Soc. 154 (2007) B631.
[25] K.E. Swider-Lyons, S.A. Campbell, J. Phys. Chem. Lett. 4 (2013) 393.
[26] C.M. Zalitis, D. Kramer, A.R. Kucernak, Phys. Chem. Chem. Phys. 15 (2013) 4329.
[27] M. Wesselmark, B. Wickman, C. Lagergren, G. Lindbergh, Electrochem. Commun. 12 (2010) 1585.
[28] F.T. Wagner, B. Lakshmanan, M.F. Mathias, J. Phys. Chem. Lett. 1 (2010) 2204.
[29] A. Rabis, P. Rodriguez, T.J. Schmidt, ACS Catal. 2 (2012) 864.
[30] I.E.L. Stephens, A.S. Bondarenko, U. Grønbjerg, J. Rossmeisl, I. Chorkendorff, Energy Environ. Sci. 5 (2012) 6744.
[31] A.S. Bondarenko, I.E.L. Stephens, H.A. Hansen, F.J. Pérez-Alonso, V. Tripkovic, T.P. Johansson, J. Rossmeisl, J.K. Nørskov, I. Chorkendorff, Langmuir 27 (2011) 2058.
[32] D. Friebel, V. Viswanathan, D.J. Miller, T. Anniyev, H. Ogasawara, A.H. Larsen, C.P. O'Grady, J.K. Nørskov, A. Nilsson, J. Am. Chem. Soc. 134 (2012) 9664.
[33] V. Viswanathan, H.A. Hansen, J. Rossmeisl, J.K. Nørskov, ACS Catal. 2 (2012) 1654.
[34] H.S. Casalongue, S. Kaya, V. Viswanathan, D.J. Miller, D. Friebel, H.A. Hansen, J.K. Nørskov, A. Nilsson, H. Ogasawara, Nat. Commun. 4 (2013) 2817.
[35] J. Rosmeisl, G.S. Karlberg, T. Jaramillo, J.K. Nørskov, Faraday Discuss. 140 (2008) 337.
[36] J.R. Kitchin, J.K. Nørskov, M.A. Barteau, J.G. Chen, J. Chem. Phys. 120 (2004) 10240.
[37] F. Calle-Vallejo, J.I. Martínez, J.M. García-Lastra, J. Rossmeisl, M.T.M. Koper, Phys. Rev. Lett. 108 (2012) 116103.
[38] M. Mavrikakis, B. Hammer, J. Nørskov, Phys. Rev. Lett. 81 (1998) 2819.
[39] P. Strasser, S. Koh, T. Anniyev, J. Greeley, K. More, C. Yu, Z. Liu, S. Kaya, D. Nordlund, H. Ogasawara, M.F. Toney, A. Nilsson, Nat. Chem. 2 (2010) 454.
[40] S. Mukerjee, S. Srinivasan, M.P. Soriaga, J. McBreen, J. Electrochem. Soc. 142 (1995) 1409.
[41] C. Chen, Y. Kang, Z. Huo, Z. Zhu, W. Huang, H.L. Xin, J.D. Snyder, D. Li, J.A. Herron, M. Mavrikakis, M. Chi, K.L. More, Y. Li, N.M. Markovic, G.A. Somorjai, P. Yang, V.R. Stamenkovic, Science 343 (2014) 1339.
[42] S. Chen, P.J. Ferreira, W. Sheng, N. Yabuuchi, L.F. Allard, Y. Shao-Horn, J. Am. Chem. Soc. 130 (2008) 13818.
[43] S.I. Choi, S. Xie, M. Shao, J.H. Odell, N. Lu, H.C. Peng, L. Protsailo, S. Guerrero, J. Park, X. Xia, J. Wang, M.J. Kim, Y. Xia, Nano Lett. 13 (2013) 3420.
[44] L. Gan, M. Heggen, S. Rudi, P. Strasser, Nano Lett. 12 (2012) 5423.
[45] I. Spanos, J.J.K. Kirkensgaard, K. Mortensen, M. Arenz, J. Power Sources 245 (2014) 908.
[46] V.R. Stamenkovic, B.S. Mun, K.J.J. Mayrhofer, P.N. Ross, N.M. Markovic, J. Am. Chem. Soc. 128 (2006) 8813.
[47] T. Wadayama, N. Todoroki, Y. Yamada, T. Sugawara, K. Miyamoto, Y. Iijama, Electrochem. Commun. 12 (2010) 1112.
[48] N. Todoroki, Y. Iijima, R. Takahashi, Y. Asakimori, T. Wadayama, J. Electrochem. Soc. 160 (2013) F591.
[49] C. Wang, M. Chi, D. Li, D. Strmcnik, D. van der Vliet, G. Wang, V. Komanicky, K.C. Chang, A.P. Paulikas, D. Tripkovic, J. Pearson, K.L. More, N.M. Markovic, V.R. Stamenkovic, J. Am. Chem. Soc. 133 (2011) 14396.
[50] V.R. Stamenkovic, B. Fowler, B.S. Mun, G. Wang, P.N. Ross, C.A. Lucas, N.M. Markovic, Science 315 (2007) 493.
[51] T. Toda, H. Igarashi, H. Uchida, M. Watanabe, J. Electrochem. Soc. 146 (1999) 3750.
[52] M. Watanabe, K. Tsurumi, T. Mizukami, T. Nakamura, P. Stonehart, J. Electrochem. Soc. 141 (1994) 2659.
[53] A. Ohma, K. Shinohara, A. Iiyama, T. Yoshida, A. Daimaru, ECS Trans. 41 (2011) 775.
[54] H.L. Xin, J.A. Mundy, Z. Liu, R. Cabezas, R. Hovden, L.F. Kourkoutis, J. Zhang, N.P. Subramanian, R. Makharia, F.T. Wagner, D.A. Muller, Nano Lett. 12 (2012) 490.
[55] The US Department of Energy (DOE), Energy Efficiency and Renewable Energy, http://www.eere.energy.gov/hydrogenandfuelcells/mypp/pdfs/fuel_cells.pdf; and the US DRIVE Fuel Cell Technical Team Technology Roadmap, http://www.uscar.org/guest/teams/17/Fuel-Cell-Tech-Team, 2013.
[56] S. Chen, H.A. Gasteiger, K. Hayakawa, T. Tada, Y. Shao-Horn, J. Electrochem. Soc. 157 (2010) A82.
[57] K.C. Neyerlin, R. Srivastava, C. Yu, P. Strasser, J. Power Sources 186 (2009) 261.
[58] L. Dubau, M. López-Haro, L. Castanheira, J. Durst, M. Chatenet, P. Bayle-Guillemaud, L. Guétaz, N. Caqué, E. Rossinot, F. Maillard, Appl. Catal. B: Environ. 142–143 (2013) 801.
[59] P. Malacrida, M. Escudero-Escribano, A. Verdaguer-Casadevall, I.E.L. Stephens, I. Chorkendorff, J. Mater. Chem. A 2 (2014) 4234.
[60] M. Escudero-Escribano, A. Verdaguer-Casadevall, P. Malacrida, U. Grønbjerg, B.P. Knudsen, A.K. Jepsen, J. Rossmeisl, I.E.L. Stephens, I. Chorkendorff, J. Am. Chem. Soc. 134 (2012) 16476.
[61] P.C.K. Vesborg, T.F. Jaramillo, RSC Adv. 2 (2012) 7933.
[62] N. Schumacher, K. Andersson, L.C. Grabow, M. Mavrikakis, J. Nerlov, I. Chorkendorff, Surf. Sci. 602 (2008) 702.
[63] T.P. Johansson, E.T. Ulrikkeholm, P. Hernández-Fernández, M. Escudero-Escribano, P. Malacrida, I.E.L. Stephens, I. Chorkendorff, Phys. Chem. Chem. Phys. 16 (2014) 13718.
[64] C.A. Menning, J.G. Chen, Top. Catal. 53 (2010) 338.
[65] I.E.L. Stephens, A.S. Bondarenko, L. Bech, I. Chorkendorff, Chem. Cat. Chem. 4 (2012) 341.
[66] S.J. Yoo, S.K. Kim, T.Y. Jeon, S.J. Hwang, J.G. Lee, S.C. Lee, K.S. Lee, Y.H. Cho, Y.E. Sung, T.H. Lim, Chem. Commun. 47 (2011) 11414.
[67] B. Cordero, V. Gómez, A.E. Platero-Prats, M. Revés, J. Echeverría, E. Cremades, F. Barragán, S. Alvarez, Dalton Trans. (2008) 2832.
[68] M. Pourbaix, Atlas of Electrochemical Equilibria in Aqueous Solutions, Pergamon Press, Bristol, 1966. p. 330.
[69] Y. Luo, A. Habrioux, L. Calvillo, G. Granozzi, N. Alonso-Vante, Chem. Phys. Chem. 15 (2014) 2136.
[70] P. Hernández-Fernández, F. Masini, D.N. McCarthy, C.E. Strebel, D. Friebel, D. Deiana, P. Malacrida, A. Nierhoff, A. Bodin, A.M. Wise, J.H. Nielsen, T.W. Hansen, A. Nilsson, I.E.L. Stephens, I. Chorkendorff, Nat. Chem. 6 (2014) 732.
[71] F.J. Pérez-Alonso, D.N. McCarthy, A. Nierhoff, P. Hernández-Fernández, C. Strebel, I.E.L. Stephens, J.H. Nielsen, I. Chorkendorff, Angew. Chem. Int. Ed. 51 (2012) 4641.
[72] D.N. McCarthy, C.E. Strebel, T.P. Johansson, A. den Dunnen, J.H. Nielsen, I. Chorkendorff, J. Phys. Chem. C 116 (2012) 15353.
[73] M. Nesselberger, M. Roefzaad, R.F. Hamou, P.U. Biedermann, F.F. Schweinberger, S. Kunz, K. Schloegl, G.K.H. Wiberg, S. Ashton, U. Heiz, K.J.J. Mayrhofer, M. Arenz, Nat. Mater. 12 (2013) 919.
[74] F. Yin, Z.W. Wang, R.E. Palmer, J. Am. Chem. Soc. 133 (2011) 10325.
[75] F. Masini, C.E. Strebel, D.N. McCarthy, A.U.F. Nierhoff, J. Kehres, E.M. Fiordaliso, J.H. Nielsen, I. Chorkendorff, J. Catal. 308 (2013) 282.
[76] C. Galeano, J.C. Meier, V. Peinecke, H. Bongard, I. Katsounaros, A.A. Topalov, A. Lu, K.J.J. Mayrhofer, F. Schüth, J. Am. Chem. Soc. 134 (2012) 20457.
[77] Z.Y. Li, J.P. Wilcoxon, F. Yin, Y. Chen, R.E. Palmer, R.L. Johnston, Faraday Discuss. 138 (2008) 363.

[78] J. Speder, L. Altmann, M. Bäumer, J.J.K. Kirkensgaard, K. Mortensen, M. Arenz, RSC Adv. 4 (2014) 14971.
[79] A. Zana, J. Speder, N.E.A. Reeler, T. Vosch, M. Arenz, Electrochim. Acta 114 (2013) 455.
[80] R.A. Martínez-Rodríguez, F.J. Vidal-Iglesias, J. Solla-Gullón, C.R. Cabrera, J.M. Feliu, J. Am. Chem. Soc. 136 (2014) 1280.
[81] F. Masini, P. Hernández-Fernández, D. Deiana, C.E. Strebel, D.N. McCarthy, A. Bodin, P. Malacrida, I. Stephens, I. Chorkendorf, Phys. Chem. Chem. Phys. (2014), http://dx.doi.org/10.1039/C4CP02144D.
[82] H. Haberland, M. Karrais, M. Mall, Y. Thurner, J. Vac. Sci. Technol. A 10 (1992) 3266.
[83] B. von Issendorff, R.E. Palmer, Rev. Sci. Instrum. 70 (1999) 4497.
[84] C.D. Wagner, L.E. Davis, M.V. Zeller, J.A. Taylor, R.H. Raymond, L.H. Gale, Surf. Interface Anal. 3 (1981) 211.
[85] S. Tanuma, C.J. Powell, D.R. Penn, Surf. Interface Anal. 17 (1991) 911.
[86] F.J. Perez-Alonso, C.F. Elkjær, S.S. Shim, B.L. Abrams, I.E.L. Stephens, I. Chorkendorff, J. Power Sources 196 (2011) 6085.
[87] F. Maillard, E.R. Savinova, U. Stimming, J. Electroanal. Chem. 599 (2007) 221.
[88] D. Raiser, J.P. Deville, J. Electron Spectrosc. Relat. Phenomena. 57 (1991) 91.
[89] M. Nesselberger, S. Ashton, J.C. Meier, I. Katsounaros, K.J.J. Mayrhofer, M. Arenz, J. Am. Chem. Soc. 133 (2011) 17428.
[90] W. Bronger, J. Less Common Metals 12 (1967) 63.
[91] D. Friebel, D.J. Miller, C.P. O'Grady, T. Anniyev, J. Bargar, U. Bergmann, H. Ogasawara, K.T. Wikfeldt, L.G.M. Pettersson, A. Nilsson, Phys. Chem. Chem. Phys. 13 (2011) 262.

Nano Energy ∎ (∎∎∎∎) ∎∎∎–∎∎∎

Contents lists available at ScienceDirect

Nano Energy

journal homepage: www.elsevier.com/locate/nanoen

Probing the nanoscale structure of the catalytically active overlayer on Pt alloys with rare earths

Anders F. Pedersen [a,1], Elisabeth T. Ulrikkeholm [a,1], María Escudero-Escribano [a,b], Tobias P. Johansson [a], Paolo Malacrida [a], Christoffer M. Pedersen [a], Martin H. Hansen [c], Kim D. Jensen [a], Jan Rossmeisl [c], Daniel Friebel [d], Anders Nilsson [d], Ib Chorkendorff [a], Ifan E.L. Stephens [a,e,*]

[a] Department of Physics, Center for Individual Nanoparticle Functionality, Technical University of Denmark, Building 312, 2800 Lyngby, Denmark
[b] Department of Chemical Engineering, Shriram Center, Stanford University, 443 Via Ortega, Stanford, CA 94305, USA
[c] Department of Chemistry, University of Copenhagen, Universitetsparken 5, 2100 Copenhagen, Denmark
[d] SLAC National Accelerator Laboratory, 2575 Sand Hill Road, MS31, Menlo Park, CA 94025, USA
[e] Massachusetts Institute of Technology, Department of Mechanical Engineering, 77 Massachusetts Avenue, Cambridge, MA 02139, USA

ARTICLE INFO

Article history:
Received 30 December 2015
Received in revised form
20 April 2016
Accepted 17 May 2016

Keywords:
Electrocatalysis
Pt-alloys
Pt(111)
Oxygen reduction
Diffraction

ABSTRACT

Pt_xY and Pt_xGd exhibit exceptionally high activity for oxygen reduction, both in the polycrystalline form and the nanoparticulate form. In order to understand the origin of the enhanced activity of these alloys, we have investigated thin films of these alloys on bulk Pt(111) crystals, *i.e.* Y/Pt(111) and Gd/Pt(111). These surfaces exhibit a 4-fold improvement over Pt(111). We observe the formation of a thick Pt overlayer after the electrochemical measurements, both on Y/Pt(111) and Gd/Pt(111). Using surface sensitive X-ray diffraction we revealed that crystalline closely packed Pt overlayers were formed. The diffraction experiments showed that the strain and crystallinity of the overlayers are strongly dependent on the electrochemical treatment, and in general show lateral compression.

1. Motivation

Polymer electrolyte membrane fuel cells (PEMFCs) are highly promising as a low emission source of power for portable applications, in particular automotive vehicles [1]. However, as a consequence of the slow kinetics of the oxygen reduction reaction (ORR) PEMFCs require a copious amount of Pt to catalyse the reaction. In order for PEMFCs to be scaled up beyond the niche market they occupy today, the amount of Pt needs to be decreased by up to an order of magnitude [2–4]. Arguably the most viable route to achieve this goal is to alloy Pt with other, less noble metals, thus improving the catalytic activity. Most investigations pertaining to Pt ORR alloys over the past two decades have focused on alloying Pt with late transition metals such as Fe, Co and Ni [5–9]. These catalysts exhibit significant initial improvements in activity over pure Pt, but tend to degrade over time [10,11]. The cause of the degradation is the leaching out of the less noble solute component into the acidic electrolyte, a process known as dealloying [12,13]. Recent advances show that the stability of bimetallic Pt catalysts can be enhanced significantly, at least during short term tests [7,8,14,15]. Nonetheless, it still remains to be seen whether these catalysts can survive long term tests in fuel cells [16].

Earlier studies on Pt and Pt alloys suggest that the active site is located on the closely packed (111) surface [17–20]. According to a model based on density functional theory (DFT) calculations, the catalytic activity for oxygen reduction shows a *Sabatier*-volcano dependence on the binding to the key reaction intermediate, HO^* (where HO^* denotes a hydroxyl group adsorbed on an active site) [21]. The optimal catalyst should exhibit moderate binding to HO^*, neither too strong nor too weak, with a binding to HO^* around ~0.1 eV weaker than Pt(111). Alloys such as Pt_3Ni or Pt_3Co exhibit improved activity because they exhibit closer to optimal binding of HO^* [22]. The first surface layer of these alloys is composed of pure Pt, as the solute metal will be unstable against dissolution to the electrolyte [6,23]. Scanning tunnelling microscopy experiments

* Corresponding author at: Department of Physics, Center for Individual Nanoparticle Functionality, Technical University of Denmark, Building 312, 2800 Lyngby, Denmark.
E-mail address: ifan@fysik.dtu.dk (I.E.L. Stephens).
[1] These authors contributed equally to this work.

http://dx.doi.org/10.1016/j.nanoen.2016.05.026
2211-2855/

indicated that pure Pt overlayers on acid-leached Pt alloys have smooth (111)-like surfaces [24]. The overlayer exhibits weakened binding to HO^* through ligand or strain effects. Ligand effects are due to the direct interaction of the Pt surface atoms with the underlying atoms of the non-noble metal in the second atomic layer [25,26]. Similarly, a compressive lateral strain to the surface can also bring about a weakening of the binding of HO^*, by raising the position of the d-band center relative to the *Fermi* level [27].

Alloys of Pt and late transition metal have negligible alloy formation energies [22]. This, in turn causes low bulk diffusion barriers [28], which could explain their apparent susceptibility to degradation by dealloying [12,13,16]. Given these limitations, we embarked on a series of investigations to search for active and stable Pt alloys for the ORR. A DFT-based screening study identified Pt_3Sc and Pt_3Y to be particularly promising candidates [22]. We anticipated that they would have enhanced kinetic stability against dealloying as a result of their highly negative alloying energy, *i.e.* a strong bond between Pt and Sc or Y.

Based on the predictions from DFT, we tested bulk sputter-cleaned polycrystalline electrodes of Pt_3Sc and Pt_3Y in rotating disk electrode (RDE) measurements in 0.1 M $HClO_4$. Relative to Pt, Pt_3Y exhibited >6 times improvement in ORR activity over polycrystalline Pt, constituting the most active catalyst ever prepared in this manner [22]. We tested a number of smooth polycrystalline electrodes of Pt rare earth alloys, exhibiting equivalent values of the alloying energy to Pt_3Y, mostly of the Pt_5M composition (where M=Y, Ce, La, Gd) [29,30]. The most active amongst these was Pt_5Gd, which exhibited activity just as high as Pt_3Y [31]. Moreover, we also found that model, mass-selected nanoparticles of Pt_xY and Pt_xGd exhibited an exceptionally high mass activity of up to 3.6 A/mg Pt at 0.9 V with respect to a reversible hydrogen electrode (RHE) [32,33]. During the course of 10,000 cycles between 0.6 and 1.0 V the nanoparticulate catalysts lose around 30% of their activity. However, most of the activity losses occur between 0 and 1000 cycles [33]. This suggests that during the first 1000 cycles, the catalyst reaches a metastable, partially dealloyed state (the thermodynamically stabilised state would be a pure Pt particle with all the rare earth component dissolved into solution).

We initially predicted the high activity of Pt_3Y would be contingent on the formation of a specific structure with a single atom-thick Pt overlayer and at least 25% Y in the second atomic layer [22]. On the basis that Y is larger than Pt, we expected the overlayer would be under tensile strain. Hence, a thick pure Pt overlayer would bind reaction intermediates stronger than a pure Pt surface, putatively the opposite effect required for an enhancement in ORR activity. Thus, according to our understanding at the time, a ligand effect from subsurface Y was essential to outweigh the effect of the tensile strain imposed onto the surface Pt atoms. Consequently, it came to our surprise to find that X-ray photoelectron spectroscopy (XPS) measurements of the electrodes, performed post-ORR, suggested that the Pt overlayer was at least 3–4 atoms thick on Pt_3Y [29] and other Pt_5M alloys [30]. We later corroborated our XPS observations with elemental analysis based on transmission electron microscopy on nanoparticulate Pt_xY [32]. The key to understanding our observations came by analysing the bulk structure of the polycrystalline Pt_5M alloys, as deduced from X-ray diffraction (XRD). They form an unusual $CaCu_5$ structure that accommodates alloy components with different atomic radii in a way that is distinct from FCC and HCP alloys, which have uniform bond lengths [30,34]. Despite the larger size of M, relative to Pt, the closest Pt-Pt nearest neighbour distance in the core is smaller than that of pure Pt [31]. According to our DFT calculations, the 3–4 atom thick Pt overlayer concealing Pt_5M would be equivalent to a compressed closely packed pure Pt overlayer [31]. This notion is also consistent with our extended X-ray absorption fine structure (EXAFS) measurements, which showed that even after exposure to ORR conditions, the nanoparticles of Pt_xY and Pt_xGd remained under compressive strain. Moreover, the surface specific ORR activity showed an exponential dependence on the degree of compressive strain [32,33]: this is exactly the trend we would expect, should we consider the strain to be imposed from the core on the catalytically active surface atoms.

Despite having established that the catalyst activity was strongly correlated to the bulk lattice strain, the structure of the overlayer remained elusive. To this end, following the precedent set by earlier combined surface science- and electrochemistry studies of Pt-based ORR catalysts [18,26,35–37], we prepared single crystalline surfaces of Pt and rare earths. We were unable to source bulk single crystals of these specific alloys. Instead we formed alloy thin films by vacuum depositing $\sim$200 Å Y or Gd on Pt(111) single crystal substrates. UHV and XRD measurements show that these structures exhibit an in-plane compression of 5–6% [38,39]. The Gd/Pt(111) structures exhibit similar structural motifs to those of the $CaCu_5$ structure we observed in the polycrystalline alloys [31,38]. The alloy film followed the orientation of the Pt(111) substrate half the time; otherwise it was rotated by 30°. Upon testing the Y/Pt(111) electrode for the ORR, we measured an activity of 7.9 mA cm^{-2}, representing a 4-fold improvement over Pt(111) at 60 °C [39]. Significant leaching resulted in the formation of a $\sim$1 nm thick Pt overlayer, similar to what we observed on the polycrystalline and nanoparticulate samples. Thus we consider the structures formed in vacuum to be precursors to the active phase.

In this paper, we report the electrochemical activity of Gd/Pt(111) for the ORR. Moreover, we use surface X-ray diffraction [40] to elucidate the strain in the electrochemically formed Pt overlayer on both Y/Pt(111) and Gd/Pt(111). We rationalise our trends with DFT calculations. By doing so we provide a fundamental link between the previously observed bulk strain and the nanoscale surface strain that controls the catalysis of oxygen reduction.

2. Experimental setup

2.1. Sample preparation and characterisation in ultra high vacuum

We have provided a full description of the UHV preparation of Y/Pt(111) and Gd/Pt(111) elsewhere [38,39]. In brief, the sample preparation and initial characterisation were performed in a UHV chamber with a base pressure of 10^{-10} Torr. The chamber is equipped with standard UHV surface science techniques such as XPS, ion scattering spectroscopy (ISS), low-energy electron diffraction (LEED), and a quadrupole mass spectrometer for temperature programed desorption (TPD). ISS is performed using He^+ ions accelerated over an acceleration voltage of 1.2 kV. For the XPS experiments the K radiation of a Mg anode was used (1253.4 eV).

Non-destructive depth profiles of the surface were made using Angle Resolved XPS (AR-XPS). These experiments were carried out in another UHV chamber; hence the sample was exposed to air prior to these experiments. The electron analyser of this system allows to collect separate XPS signals for different emission angles, and in particular 16 angle intervals between 20° and 80° from the surface normal. After subtraction of a *Shirley* type background and integration of the Pt 4f and Y 3d (or Gd 4d) peak areas, the XPS signals were processed using the simulation tool, ARProcess (Thermo Avantage software), which uses a maximum entropy method combined with a genetic algorithm to define the depth profiles: emission angles over 65° were omitted to minimise the effects of elastic scattering.

The samples were based on Pt(111) single crystals (MaTecK GmbH, Germany, 5 mm diameter and 3 mm thick). They were mounted with a hairpin shaped tungsten wire onto the feed-

Please cite this article as: A.F. Pedersen, et al., Probing the nanoscale structure of the catalytically active overlayer on Pt alloys with rare earths, Nano Energy (2016), http://dx.doi.org/10.1016/j.nanoen.2016.05.026

through on the manipulator end. The temperature was measured using a type K thermocouple. The samples could be resistively heated and cooled using liquid nitrogen. The main chamber is equipped with four metal evaporators and a quartz crystal microbalance (QCM), which makes it possible to evaporate metals on the surface of the sample at a well-known evaporation rate. The evaporators were made by cutting flakes of a Gd (Alfa Aesar, 99.9%, 0.127 mm thick) or Y (Goodfellow, 99.9%, 0.15 mm thick) foil and attaching them to a coil shaped 0.25 mm 99.95% tungsten wire. Separate crystals were used for the rotating ring disk electrode measurements and the synchrotron based XRD measurements. However, they were prepared under identical conditions.

2.2. Electrochemical methods

The electrochemical rotating ring disk electrode (RRDE) measurements on Gd/Pt(111), Y/Pt(111) and Pt(111) single crystalline electrodes were performed using RRDE assemblies provided by Pine Instruments Corporation. We used a VMP2 potentiostat (Bio-Logic Instruments), controlled by a computer with EC-Lab software. A standard two-compartment glass cell was used, which was equipped with a water jacket attached to a hot water bath to control the temperature. All glassware were cleaned for 24 h in a "piranha" solution consisting of a 3:1 mixture of 96% H_2SO_4 and 30% H_2O_2, followed by multiple runs of heating (to 85–90 °C) and rinsing with ultrapure water (Millipore Milli-Q, 18.2 MΩ cm, TOC <5 ppb). All electrochemical experiments were carried out in 0.1 M $HClO_4$. The counterelectrode (CE) was a Pt wire (Chempur 99.9%, 0.5 mm diameter) and, the reference electrode (RE), a Hg/Hg_2SO_4, K_2SO_4 (0.6 M) (Schott instruments), was separated from the working electrode (WE) compartment by a ceramic frit. All the potentials in the text are referenced to the reversible hydrogen electrode (RHE), and are corrected for Ohmic losses, measured by fitting the high frequency impedance spectra taken typically from 500 kHz to 100 Hz. 0 V *vs.* RHE was established by performing the hydrogen oxidation and evolution reactions (HOR and HER, respectively) on a Pt electrode by means of cyclic voltammetry (CV) in H_2-saturated 0.1 M $HClO_4$ at 50 mV s^{-1} and 1600 rpm. The value for conversion to the RHE was taken as the average intersection with the potential axis of the anodic and cathodic curves. The RRDE was immersed into the electrochemical cell under potential control of ~0.1 V *vs.* RHE into an N_2-saturated (N5, Air Products) electrolyte. The ORR activity measurements were conducted in an electrolyte saturated with O_2 (N5, Air Products) at 1600 rpm and 50 mV s^{-1}.

Prior to the electrochemical measurements, the Pt(111) single crystal was flame-annealed according to the *Clavilier's* method [41]. Pt(111) was annealed for a few minutes (2–10 min) in the flame of Liquefied Petroleum Gas (LPG) for 5 min and cooled in a reducing 1:1H_2/Ar atmosphere until room temperature (typically 5 min). The electrode surface was then protected by a droplet of ultrapure water, mounted in RRDE assembly and transferred to the electrochemical cell.

2.3. Synchrotron X-ray diffraction

X-ray diffraction measurements were performed on Gd/Pt(111) and Y/Pt(111) both in the as-prepared state, and after electrochemical conditioning. The X-ray diffraction experiments on the Y/Pt(111) and Gd/Pt(111) single crystalline alloys were carried out at the Stanford Synchrotron Radiation Lightsource (SSRL) at beam lines 1–5 and 7–2. The Y/Pt(111) crystal was measured at BL1-5, which is equipped with a Huber Kappa goniometer (ϕ-axis perpendicular to θ-axis) and a Rayonix MAR345 image plate detector. The Gd/Pt(111) crystal was brought to BL7-2, which has a Huber six-circle (4+2) diffractometer and a Dectris Pilatus 300 K pixel detector. Both diffractometer stages were equipped with goniometer heads that allowed the crystal surface normal to be aligned to the ϕ-rotation axis using a laser. All the data were acquired at a fixed incidence angle of 0.2° to maximise surface sensitivity, and the photon energy was set to 11 keV to avoid fluorescence background from Pt. A sketch of the geometry of the scattering experiment is shown in Fig. 1. The acquired diffraction data was combined to form a 3 dimensional image of parts of the *Q*-space, and the intensity was corrected for the *Lorentz* factor, polarisation, and geometrical effects using our own MatLab scripts.

The electrochemical conditioning of the Gd/Pt(111) and the Y/Pt(111) samples was conducted at SSRL. For Gd/Pt(111), we performed 1461 cycles from −0.1 V to 0.8 V and 125 cycles from 0.0 V to 1.00 V, followed by 106 cycles from 0.0 V to 1.1 V and 98 cycles from 0.0 V to 1.20 V *vs.* RHE. The Y/Pt(111) was measured as-prepared, and after 175 cycles from −0.1 V to 0.8 V and 189 cycles from 0.05 V to 1.05 V, followed by 261 cycles from 0.05 to 1.20 V and 202 cycles from 0.05 V to 1.30 V *vs.* RHE. All the diffraction data was acquired *ex-situ*. The electrochemical potential cycling at the synchrotron facility was performed using a standard

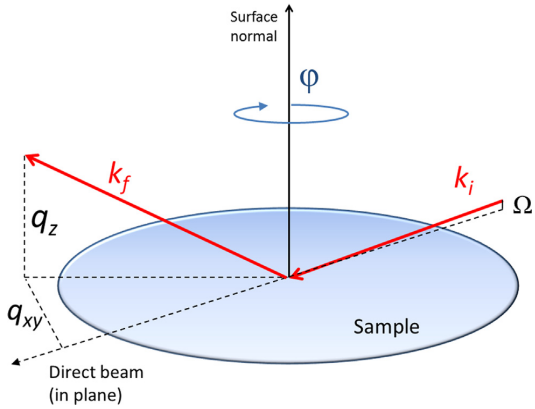

Fig. 1. A sketch of the experimental setup used to acquire the X-ray diffraction data using an area detector. During all the experiments the incidence angle was kept at Ω=0.2° to maximise surface sensitivity. The sample was rotated in steps of 0.2° around the surface normal, and at each step an image was acquired. All the images were combined to form a 3-dimensional representation of the *Q*-space.

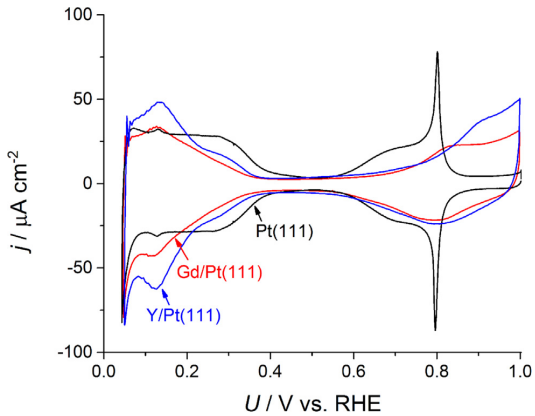

Fig. 2. Stable (R)RDE based cyclic voltammograms in N_2-saturated 0.1 M $HClO_4$ at 50 mV s^{-1} and 23 °C of Gd/Pt(111), Y/Pt(111) and Pt(111) electrodes. The sharpness of the butterfly peak at ~0.8 V in comparison to the literature [45] indicates that the crystal is highly ordered [46], validating our preparation procedure.

Please cite this article as: A.F. Pedersen, et al., Probing the nanoscale structure of the catalytically active overlayer on Pt alloys with rare earths, Nano Energy (2016), http://dx.doi.org/10.1016/j.nanoen.2016.05.026

Table 1
Potential shifts (in absolute values) required to adsorb the charge Q, corresponding to coverages of OH and H adsorption of 1/8, 1/6, 1/4 and 1/3 ML. They have been obtained from the CVs in Fig. 2 and shown for Gd/Pt(111) and Y/Pt(111) relative to Pt(111).

Q/μC cm^{-2}	$\lvert\Delta U_{HO^*\ Gd/Pt\ (111)}\rvert$/V	$\lvert\Delta U_{H^*\ Gd/Pt\ (111)}\rvert$/V	$\lvert\Delta U_{HO^*\ Y/Pt\ (111)}\rvert$/V	$\lvert\Delta U_{H^*\ Y/Pt\ (111)}\rvert$/V
30	0.107	0.074	0.099	0.054
40	0.104	0.075	0.099	0.057
60	0.110	0.073	0.095	0.050
80	0.136	0.062	0.107	0.036

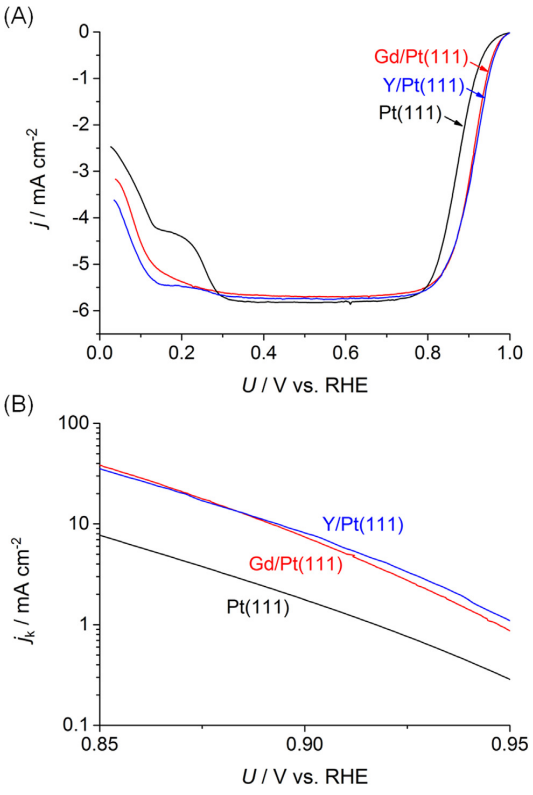

Fig. 3. (A) Rotating ring disk electrode polarisation curves for the ORR on Gd/Pt (111), Y/Pt(111) and Pt(111). (B) Tafel plots showing the kinetic current density of Gd/Pt(111), Y/Pt(111) and Pt(111) as a function of the potential. The measurements were performed in O_2-saturated 0.1 M $HClO_4$ at 50 mV s^{-1}, 1600 rpm and 23 °C.

3-electrode setup with a Ag/AgCl reference electrode (Innovative Instruments, Inc. LF-1.6, 3.4 M AgCl) and a glassy carbon counter-electrode. The two samples were measured at different beam times; two different reference electrodes were used. Due to safety reasons it was not possible to calibrate the RHE scale at the beam time, as we were unable to saturate our electrolytes with H_2. Following the beam time, during our analysis of the data, we used the onset of hydrogen evolution to estimate the RHE scale. We came to realise that there was a ~0.05 V offset between the onset of hydrogen evolution between the two reference electrodes. Consequently, the potential window for the Y/Pt(111) measurements is offset positively by 0.05 V, relative to Gd/Pt(111) measurements. The cell is a hanging meniscus type, also described elsewhere [42]. The electrolyte was N_2 saturated 0.1 M $HClO_4$ surrounded by a humidified N_2 atmosphere.

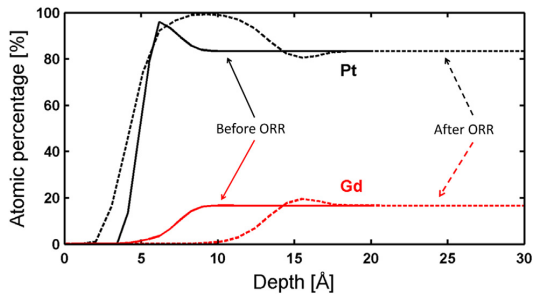

Fig. 4. AR-XPS depth profiles of the Gd/Pt(111) sample before (solid lines) and after (dashed lines) the electrochemical treatment. These measurements have been performed in another UHV setup, and hence during the transfer the sample has been exposed to atmospheric air prior to these measurements. O and C signals were seen as a result from exposure to air, but have been omitted here for clarity. The depth profile including the surface contamination of O and C may be seen in S. M. Fig. 3.

3. Results

3.1. Electrochemical experiments and X-ray photoelectron spectroscopy characterisation

The Gd/Pt(111) and Y/Pt(111) samples were transferred directly from the UHV setup to the electrochemical cell. The samples were exposed to the laboratory air for up to 45 min, whilst it was unmounted from the UHV chamber. The RRDE was immersed into the electrochemical cell under potential control of 0.1 V *vs.* RHE into N_2-saturated 0.1 M $HClO_4$. CVs between 0.05 and 1.00 V *vs.* RHE at 50 mV s^{-1} were recorded in N_2-saturated electrolyte. The cycling removes adventitious contamination accumulated on the surface during the transfer from the UHV chamber to the electrochemical cell. Fig. 2 shows a negative potential shift for both Gd/Pt(111) and Y/Pt(111) in the H adsorption region (between 0.45 and 0.05 V *vs.* RHE), as well as a positive shift in the OH adsorption region (between 0.55 V and 0.85 V *vs.* RHE), relative to Pt(111). The potential shifts (in absolute values) for both the OH and H adsorption regions, $|\Delta U_{HO^*M/Pt(111)}| = |U_{HO^*Pt(111)} - U_{OH^*M/Pt(111)}|$ and $|\Delta U_{H^*\ M/Pt(111)}| = |U_{H^*Pt(111)} - U_{H^*M/Pt(111)}|$, where M is Gd or Y, are shown in Table 1. These values indicate the shift in the potential required to adsorb 1/8, 1/6, 1/4 and 1/3 monolayers (MLs) of OH (HO^*) and H (H^*), that is 30, 40, 60 and 80 μC cm^{-2} [43]. These shifts are in agreement with a Pt overlayer under compressive strain [44].

The oxygen reduction reaction activity of Gd/Pt(111), Y/Pt(111) and Pt(111) electrodes was measured in O_2-saturated 0.1 M $HClO_4$ once stable CVs in N_2-saturated electrolyte were obtained (see Supplementary Material (S.M.) Figs. 1 and 2 for initial and stable CVs). The oxygen reduction values for Pt(111) are marginally higher than other data elsewhere in the literature [18,45]; we can

Please cite this article as: A.F. Pedersen, et al., Probing the nanoscale structure of the catalytically active overlayer on Pt alloys with rare earths, Nano Energy (2016), http://dx.doi.org/10.1016/j.nanoen.2016.05.026

account for this marginal difference on the basis that we correct our data for Ohmic losses. The kinetic current density, *i.e.* the current density in the absence of any mass-transfer effects, was calculated by the *Koutecky-Levich* equation, $j_k=(j_l \cdot j)/(j_l-j)$, where j_l is the diffusion limited current density and j the measured current density. The *Tafel* plots (as a function of the potential, U) are shown in Fig. 3 for both electrodes. The kinetic current density of Gd/Pt(111) at 0.9 V *vs.* RHE is $j_{k,\ Gd/Pt(111)}=7.3 \pm 1.4$ mA cm^{-2}, exhibiting a 4-fold ORR activity enhancement over Pt(111) ($j_{k,\ Pt(111)}$ 1.73 ± 0.07 mA cm^{-2} at 23 °C). This enhancement is similar to that measured on Y/Pt(111) [39] ($j_{k,Y/Pt(111)}=7.9$ mA cm^{-2} at 60 °C), presenting a near 4-fold improvement over Pt(111) as $j_{k,\ Pt(111)}$ 1.93 mA cm^{-2} at 60 °C. Moreover, it approaches the improvement of polycrystalline Pt_5Gd and Pt_3Y over polycrystalline Pt [22,31].

We performed AR-XPS, before and after the electrochemical testing; from these measurements we produced the depth profiles shown in Fig. 4. Consistent with the other alloys tested at our laboratory, including polycrystalline Pt_5Gd [31], Pt_xY nanoparticles [32] and Y/Pt(111) [39], the thickness of the Pt overlayer has increased significantly to ~10 Å after the electrochemical treatment, suggesting that the Gd has leached out from the surface layer. See S.M. Fig. 4 for a depth profile on the Y/Pt(111) crystal after XRD measurements.

3.2. X-ray diffraction experiments

Fig. 5 shows the X-ray diffraction pattern for the Pt_5M alloy phase, as prepared, *i.e.* before electrochemical conditioning. The structure shows an in-plane compression compared to Pt(111), and it has a complicated stacking sequence. One of the most important structural features is the formation of so-called kagomé layers, in which a pure Pt layer is compressed, and forms a (2×2) network

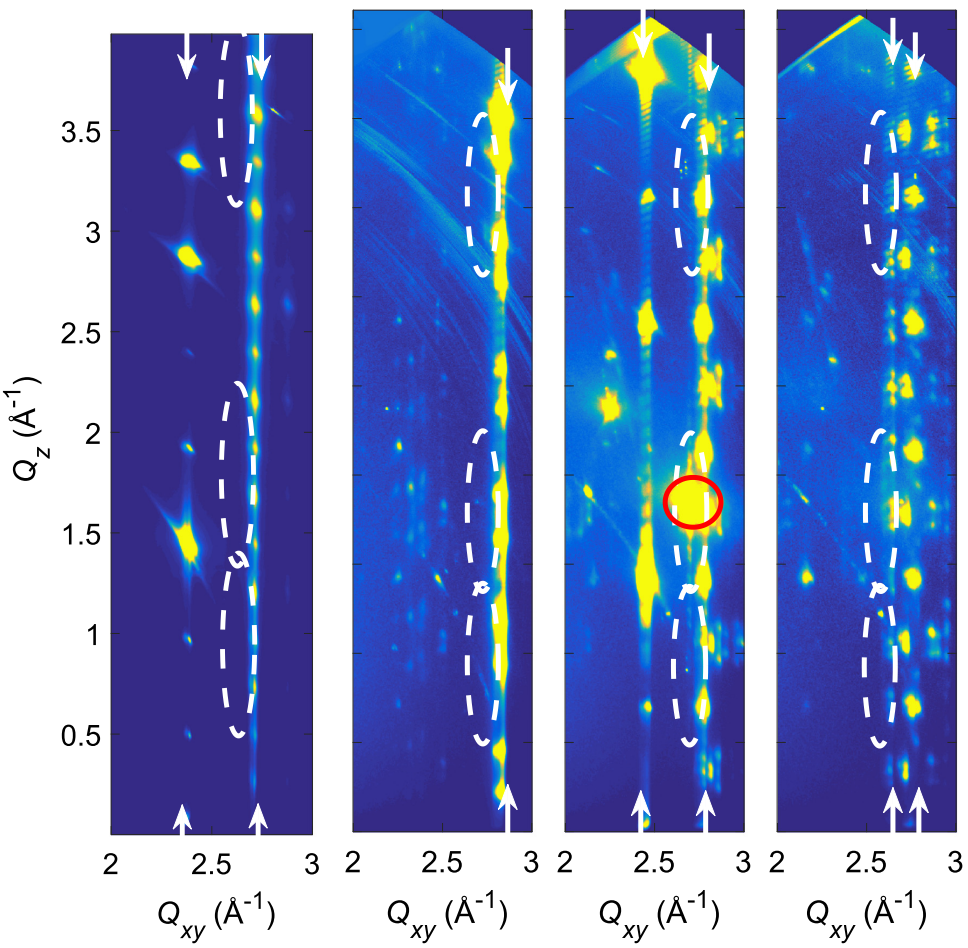

Fig. 5. Diffraction images of Gd/Pt(111) and Y/Pt(111) taken before electrochemical potential cycling. (a) Gd/Pt(111), $\phi=28°-32°$. (b)-(d) Y/Pt(111), (b) $\phi=28°-32°$, (c) $\phi=-2°-2°$, (d) $\phi=3°-7°$. Locations for the overlayer diffraction spots in Fig. 7 from the overlayers on the Gd/Pt(111) and Y/Pt(111) before electrochemical potential cycling are indicated by the dashed ellipses (spots not seen here since the thick overlayer has not been formed yet). With the exception of the (0,1,2) peak from the Pt substrate (red circle in (c)), all of the diffraction peaks are from the Pt_5M alloy phase, columns of *Bragg* peaks indicated by the arrows.

Please cite this article as: A.F. Pedersen, et al., Probing the nanoscale structure of the catalytically active overlayer on Pt alloys with rare earths, Nano Energy (2016), http://dx.doi.org/10.1016/j.nanoen.2016.05.026

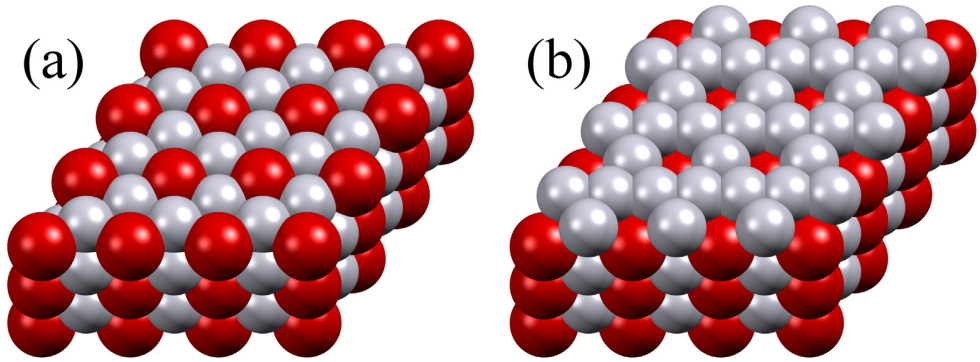

Fig. 6. Schematic of the $CaCu_5$ structure, with Gd atoms shown in red and Pt atoms in grey. (a) shows the bulk structure terminated with the hexagonal layer with a Pt_2Gd stoichiometry, and (b) shows the bulk structure terminated with the pure Pt kagomé layer. The Pt-Pt distances in the kagomé layer is shorter than in bulk Pt, opening up room to accommodate the larger Gd atoms in the layers above and below.

of vacancies in order to accommodate a larger Gd atom in the layer above or below. Fig. 6 shows a schematic of such a kagomé layer in the $CaCu_5$ structure; we consider this kagomé layer to be essential for the compression of the Pt-Pt distance relative to Pt(111) [38]. We deduced that the red circled spot corresponds to the Pt(111) substrate. For a more convenient description in the context of the Pt(111) surface, the FCC structure of bulk Pt can be represented with a hexagonal unit cell with the unit cell vectors of the lengths $a=b=2.775$ Å parallel to the surface and $c=6.797$ Å for the unit cell vector along the surface normal, $\alpha = \beta = 90^o$, and $\gamma = 120^o$. Using this unit cell, the measured range of Q-space shows diffraction peaks from the Pt(111) substrate with a 3-fold in-plane symmetry at (h,k,l) positions (1,0,1), (1,0,4), and (0,1,2) and 120° rotations thereof; the (0,1,2) reflection appears in Figs. 5c, 7c, and 8c. All other peaks originate from the alloy.

Fig. 7 shows the typical diffraction peaks that form on Y/Pt(111) and Gd/Pt(111) post- electrochemical potential cycling. All the features demarcated by the white dashed ellipsoids only appear after electrochemical measurements, suggesting that they are associated with the Pt overlayer; these features resemble those of the host Pt(111) substrate, although they are rotated by 30°; this rotation is identical to the orientation of the close-packed rows of Pt atoms within the kagomé layers of the Pt_5M alloy, as observed with LEED [38,39]. For each in-plane vector of the overlayer, diffraction spots are seen at L=1, L=2, and L=4, where the absence of the L=3 peaks indicate FCC structure like the Pt(111) substrate, but with two types of domains in the overlayer that are rotated 60° from each other. The image shows the intensity as a function of the in-plane (Q_{xy}) and out-of-plane (Q_z) components of scattering vector Q for the Gd/Pt(111) crystal after initial electrochemical potential cycling. In the figure the overlayer peaks at $Q_{xy} \approx 2.64$ Å^{-1} and $Q_z \approx$ [0.9; 1.8; 3.6] Å^{-1} are weak and quite broad, especially in the z-direction, indicating that the overlayer is very thin [47]. The other diffraction peaks in the image originate from the Pt_5Gd alloy phase (see Fig. 5). Fig. 7b and c show the overlayer peaks from the Y/Pt(111) crystal; there are two different sets of overlayer peaks, one set that is rotated 30° from the Pt(111) substrate, and one set that is unrotated from the substrate.

In the second set of electrochemical experiments we cycled Gd/Pt (111) up to 1.20 V *vs.* RHE and Y/Pt(111) up to 1.30 V *vs.* RHE, following which we repeated the diffraction experiments. As shown in Fig. 8a, for the Gd/Pt(111) crystal there were no significant changes as only one overlayer was still observed at 30° rotation. In case of the Y/Pt(111) crystal, the overlayer rotated 30° disappeared completely, see Fig. 8b, but the unrotated overlayer was still visible, as seen in Fig. 8c. Furthermore, a new overlayer seems to appear at ±5° rotation from the Pt(111), although very weak; this overlayer feature is shown in Fig. 8d. This slightly rotated layer was not visible after the first electrochemical cycling between 0.05 V and 1.0 V, as seen in Fig. 7d.

The diffraction pattern of the overlayer suggests that the Pt overlayer has an FCC structure, similar to bulk Pt, albeit with different lattice parameters. By comparing the positions of the overlayer peaks and the Pt(111) substrate peaks, we can determine the strain in both the in-plane and out-of-plane directions. Furthermore, we can estimate the thickness and lateral domain size using *Scherrer's* formula with a shape factor of 0.886 [48]. The positions and widths of the overlayer diffraction peaks were determined by fitting a sum of a 2D Gaussian and Lorentzian, and the resulting structural parameters are shown in Fig. 9 and in Table 2. Only the 30° rotated and unrotated layers on the two crystals were fitted. The ±5° rotated overlayer was too weak in its diffracted intensity to fit; moreover, upon visual inspection of the diffraction image its structure also appears to be different from the FCC structure that we found on the other overlayers.

To further investigate the structure of the overlayer, we made a number of simulations of the overlayer peaks, considering an FCC and an HCP structure, which differ from each other only in terms of layer stacking. The simulation results in S.M. Figs. 5 and 6 show the diffraction patterns from a varying number of atomic layers from 1 to 9. A visual comparison to Fig. 7 suggests that the overlayer on Gd/Pt(111) crystal has about 5 atomic layers and the overlayer on the Y/Pt(111) crystal only has 3 layers. This is consistent with the thickness inferred from the peak widths, as well as the AR-XPS results on the polycrystalline samples of same composition. We can also conclude that the structure of the overlayer does not have HCP stacking.

By estimating the domain size using the Scherrer equation, we implicitly neglect any peak broadening due to microstrain, *i.e.* inhomogeneous interatomic Pt-Pt distance in the overlayer. However, we do anticipate that the localised strain might vary significantly, which could also lead to peak broadening. Even so, we cannot distinguish the two possibilities on the basis of the XRD. Nonetheless, we can calculate a minimum and maximum value of strain. For the Gd/Pt(111) crystal the in-plane strain ranges from −1.39% to +0.79% after the first electrochemical cycling between 0.05 V and 1.05 V and −1.06% to +0.94% after the second electrochemical cycling between 0.05 V and 1.30 V. For the 30° rotated overlayer on the Y/Pt(111) crystal the in-plane strain ranges from −3.78% to +1.02% after the first electrochemical cycling between 0.05 V and 1.05 V; the in-plane strain in the unrotated layer ranges from −2.17% to +1.20% after the same treatment. After the second electrochemical cycling between 0.05 V and 1.30 V it ranges from

Please cite this article as: A.F. Pedersen, et al., Probing the nanoscale structure of the catalytically active overlayer on Pt alloys with rare earths, Nano Energy (2016), http://dx.doi.org/10.1016/j.nanoen.2016.05.026

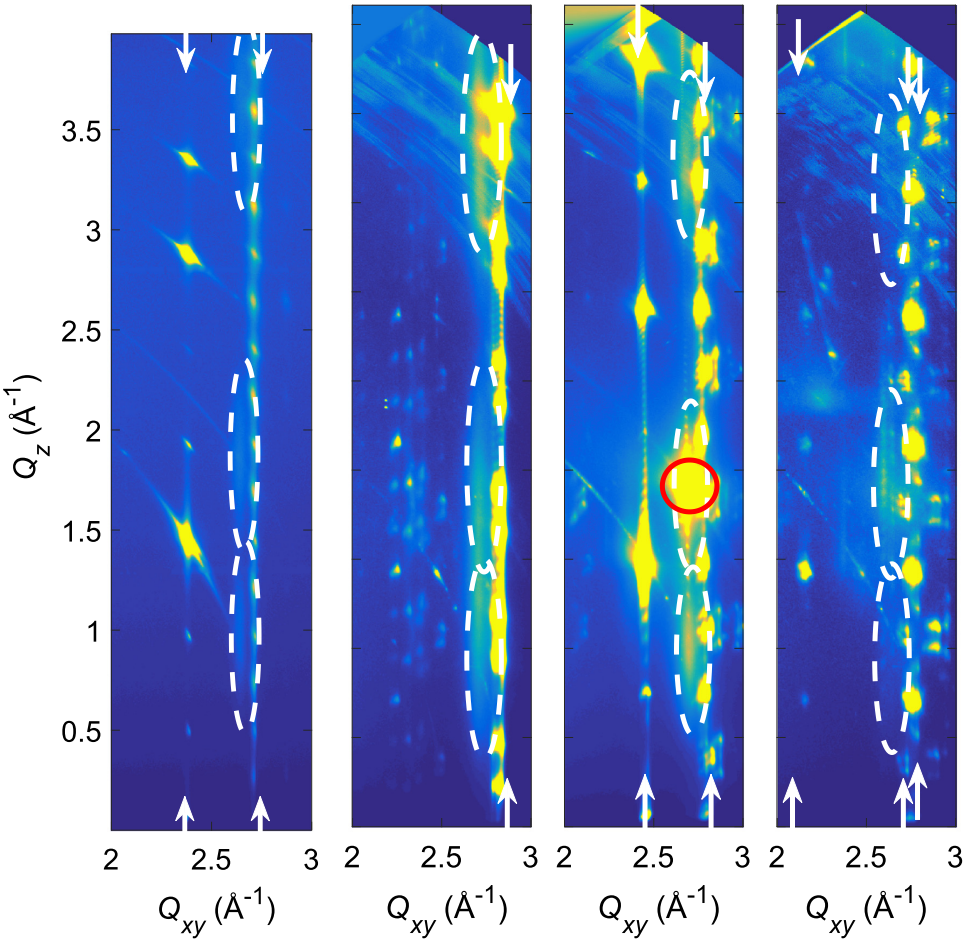

Fig. 7. Diffraction measurements of Gd/Pt(111) and Y/Pt(111) after cycling between 0.05 and 1.0 V. The same regions in reciprocal space are shown as in Fig. 5. Three weak diffraction spots at $Q_{xy} \approx 2.64$ Å^{-1} and $Q_z \approx$ [0.9; 1.8; 3.6] Å^{-1} originate from the overlayer, as indicated by the dashed ellipses. The peak indicated by the red circle is from the Pt(111) substrate. All other peaks are from the Pt_5M bulk alloy.

−1.19% to +1.61%. These values of strain have been calculated by adding or subtracting half of the peak width at half height (HWHM) to the peak center position.

4. Theoretical calculations

On a completely homogeneous surface, the difference in OH binding energies on Pt(111) and Gd/Pt(111) can be obtained from the electrochemical experiments, according to Eq. (1) [26].

$$\Delta E_{Gd/Pt(111)*OH} - \Delta E_{Pt*OH} = e(\Delta U_{*OH}) \quad (1)$$

where e is the elemental charge, $\Delta E_{Gd/Pt(111)*OH}$ and ΔE_{Pt*OH} are the OH binding energies on Gd/Pt(111) and Pt(111), respectively. ΔU_{*OH} is the difference in potential of Gd/Pt(111) relative to Pt(111) for adsorbing a fixed amount of charge corresponding to a given coverage of OH. By integrating charge in the cyclic voltammogram shown in Fig. 2, we estimate a shift of around 0.1 V in U_{*OH} for Gd/Pt(111), relative to Pt(111) (see Table 1). We can also estimate the change in binding energy for H using a similar relationship

$$\Delta E_{H*Gd/Pt(111)} - \Delta E_{H*Pt} = -e(\Delta U_{*H}) \quad (2)$$

where $\Delta E_{H*Gd/Pt(111)}$ and ΔE_{Pt*H} are the binding energies of H on Gd/Pt(111) and Pt(111), respectively, and ΔU_{*H} is the shift in potential at a given coverage of H. The potential shift for hydrogen adsorption is around 0.07 V at 1/4 ML. Based on earlier DFT calculations [49], the shift in OH binding would correspond to a strain of −3.5%, whereas the shift in H binding would correspond to a strain of −3.0%. Both values are significantly greater than the strain we measured in the overlayer. See S.M. Section 4 for more details regarding these calculations.

Please cite this article as: A.F. Pedersen, et al., Probing the nanoscale structure of the catalytically active overlayer on Pt alloys with rare earths, Nano Energy (2016), http://dx.doi.org/10.1016/j.nanoen.2016.05.026

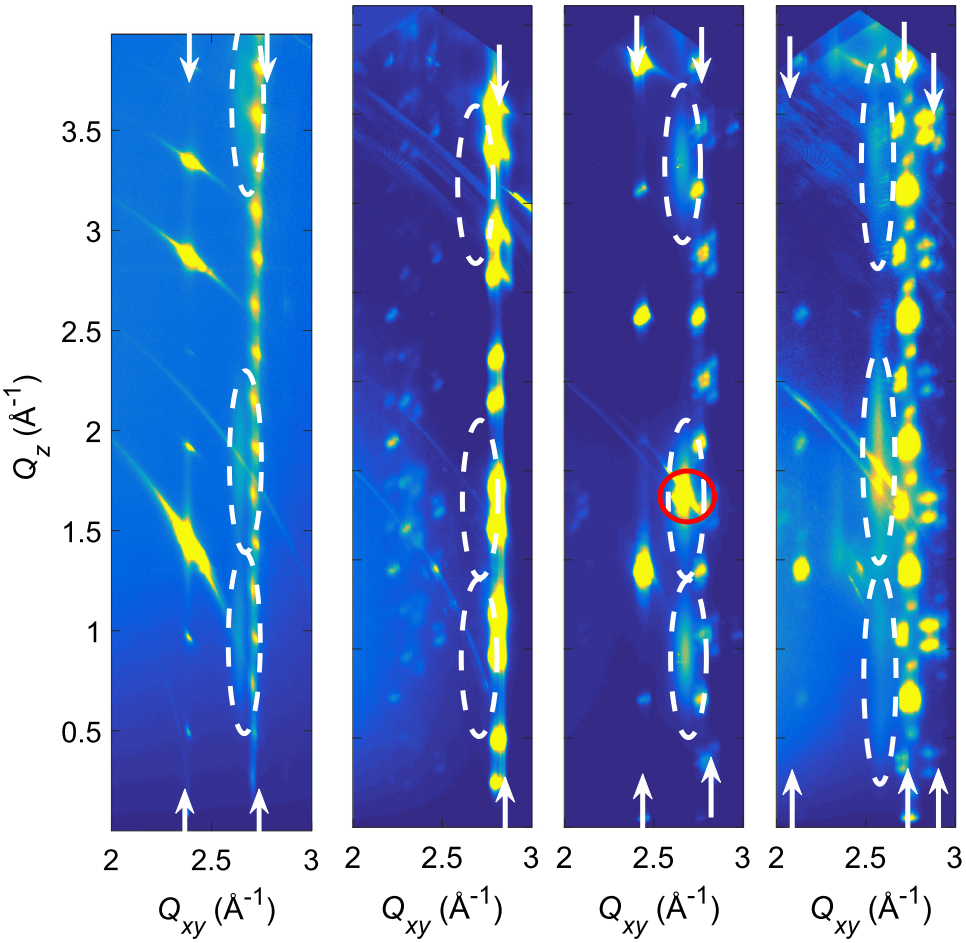

Fig. 8. Diffraction measurements of Gd/Pt(111) and Y/Pt(111) after the second electrochemical potential cycling between 0.05 V and 1.2 V. The same regions in reciprocal space are shown as in Figs. 5 and 7. The 3 weak spots seen at $Q_{xy} \approx 2.64$ Å^{-1} and $Q_z \approx$ [0.9; 1.8; 3.6] Å^{-1} are from the overlayer, marked by the dashed ellipses. The remaining peaks are from the Pt_5Gd alloy phase, columns of Bragg peaks indicated by the arrows, except one Pt(111) substrate peak on unrotated overlayer from the Y/Pt(111) crystal, shown by the red circle.

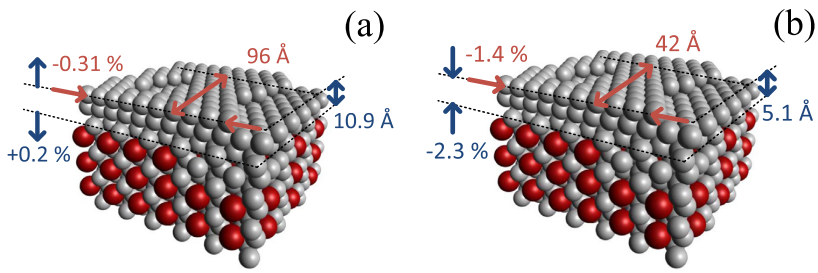

Fig. 9. Schematic illustration of a pure Pt overlayers on Pt_5X alloy substrates. (a) A 30° rotated Pt overlayer on Gd/Pt(111). (b) A 30° rotated Pt overlayer on Y/Pt(111). Fitting results for the strain and domain sizes along in-plane (red) and out-of-plane directions (blue) are indicated for the two samples.

Please cite this article as: A.F. Pedersen, et al., Probing the nanoscale structure of the catalytically active overlayer on Pt alloys with rare earths, Nano Energy (2016), http://dx.doi.org/10.1016/j.nanoen.2016.05.026

Table 2
Fitting results showing the strain and domain sizes of the overlayers on the Gd/Pt (111) and Y/Pt(111) crystal after two different electrochemical treatments.

Gd/Pt (111) 30°	U_{max} = 1.00 V *vs.* RHE	U_{max} = 1.20 V *vs.* RHE
Strain *xy* (%)	-0.31 ± 0.05	-0.07 ± 0.07
Strain *z* (%)	0.2 ± 0.4	1.1 ± 0.7
d *xy* (Å)	96 ± 5	105 ± 3
d *z* (Å)	10.9 ± 0.3	10.8 ± 0.3
Y/Pt(111) 30°	U_{max} = 1.05 V *vs.* RHE	U_{max} = 1.30 V *vs.* RHE
Strain *xy* (%)	-1.4 ± 0.2	–
Strain *z* (%)	-2.3 ± 0.9	–
d *xy* (Å)	42 ± 3	–
d *z* (Å)	5.1 ± 0.1	–
Y/Pt(111) 0°	U_{max} = 1.05 V *vs.* RHE	U_{max} = 1.30 V *vs.* RHE
Strain *xy* (%)	-0.5 ± 0.2	0.2 ± 0.5
Strain *z* (%)	-3 ± 4	-1.4 ± 2.6
d *xy* (Å)	61 ± 1	75 ± 5
d *z* (Å)	9.7 ± 0.1	16 ± 0.6

5. Discussion

Evidently, for Gd/Pt(111) and Y/Pt(111) a vacuum annealed Pt overlayer structure is not stable when exposed to the electrolyte. This clearly contrasts with the smooth, monolayer-thick annealed Pt overlayers formed on $Pt_3Ni(111)$ [18] and Cu/Pt(111) near-surface alloys [26], which were stable under ORR conditions. This could partially be due to the increased interactions between adsorbed HO^* and O^*, and the solute metal in the second surface layer on the rare earth alloys, Y and Gd. Moreover, the greater degree of compressive strain in the bulk of Pt_5Gd and Pt_5Y, relative to those other alloys, could facilitate leaching from the subsurface layer [39].

Our observation that the Pt overlayer on the dealloyed single crystal surfaces is under compressive strain is consistent with our EXAFS experiments on Pt_xGd and Pt_xY nanoparticles, post-electrochemistry [32,33]. The mean value of the strain on the overlayer of Gd/Pt(111), at −0.31%, is very low in comparison to the compression of the nearest-neighbour distance in the bulk of the alloy layer, and at 2.665 Å this is equivalent to 3.9% compression. Likewise, on the overlayer of the unrotated Y/Pt(111), it is −0.5%. Based on Table 2, it also seems that the strain is correlated with the thickness of the overlayer. Thus, we can conjecture that the strain relaxes further as the thickness increases. This interpretation is consistent with observations on single crystals based on Cu and Pt [37,51]. On the other hand, on the Y/Pt(111) overlayer rotated by 30°, the compression is −1.4%. As we suggested in Section 4, above, the measured strain is lower than we would expect if we were to assume that the shift in the voltammogram is purely due to compressive strain.

Fig. 10 shows a volcano plot, where the oxygen reduction activity, relative to Pt(111) is plotted as function of both OH binding energy (upper *x*-axis), and lateral strain (lower *x*-axis), by virtue of the linear relationship between OH binding and strain [49]. The open circles represent the activity of the Cu/Pt(111) near-surface alloy [26] and the open square represents that of $Pt_3Ni(111)$ [18], both plotted as a function of the voltammetric shift in OH peak as an estimate of the OH binding energy, Eq. (1). We have also plotted the thermodynamic Sabatier-volcano [50] (note that the lower magnitude of the experimental enhancement over Pt(111), relative to that predicted by the theoretical thermodynamic Sabatier-volcano, is likely due to kinetic effects [50,52]). We have located the position of the Gd/Pt(111) points and Y/Pt(111) data points on the *x*-axis according to (a) the voltammetric shift in OH adsorption, ΔU_{*OH}, shown as up-triangles with a blue outline, and (b) the measured strain, shown as down-triangles with a black outline. On

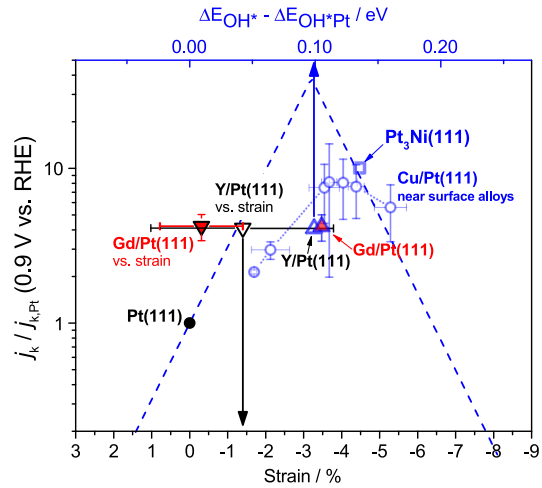

Fig. 10. Oxygen reduction volcano as a function of lateral strain (lower *x*-axis) and OH binding energy (upper *x*-axis), relative to Pt(111). The relation between the strain and shift in OH binding energy is based on DFT calculations [49]. The blue dashed line is the thermodynamic Sabatier analysis, representing the upper limit to activity, neglecting additional kinetic barriers [50]. The activity of Y/Pt(111) and Gd/Pt(111) are plotted *vs.* their measured strain on the bottom axis (down-triangles with black edge), and *vs.* the voltammetric shift on the top axis (up-triangles with blue edge). The error bar in the strain corresponds to the microstrain. For comparison, the blue circles represent the activity of the Cu/Pt(111) near surface alloys [26] and the square vacuum annealed $Pt_3Ni(111)$ [18], both plotted as a function of voltammetric shift for OH adsorption, which we assume to be equal to the shift in OH binding. The Gd/Pt(111) activity enhancement is based on several activity measurements of both Gd/Pt(111) and Pt(111) at 23 °C, whereas the Y/Pt(111) activity enhancement is based on a single measurement of Y/Pt(111) and Pt(111) at 60 °C.

the basis of the voltammetric shift, and comparing our data to the earlier experimental data on other alloys, the activity of Y/Pt(111) and Gd/Pt(111) is lower than we would expect [18,26]. On the other hand, comparing the activity with the measured strain in the overlayer, it is evident that the activity of Y/Pt(111) and Gd/Pt(111) is higher than we would expect.

We can account for this offset between our expectations and the actual enhancement on several accounts. The relationship between OH binding energy and voltammetric shift from Eq. (1) only holds for homogenous surfaces, such as Cu/Pt(111) near-surface alloys [26] and $Pt_3Ni(111)$ [18], as shown on the plot. Although the acid-leached overlayers are crystalline, they are likely to be somewhat heterogeneous. Such heterogeneity is consistent with the large microstrain we estimate in the overlayer on Y/Pt(111) and Gd/Pt(111), represented as error bar in the *x*-axis in Fig. 10. We note that the oxygen reduction activity will be dominated by the sites with the closest to optimum OH binding, whereas the voltammetric shift and the strain in the overlayer are more representative of the entire surface. We also acknowledge that in terms of catalysis, it is the actual surface layer which controls the activity, whereas we are probing the overall strain in the overlayer. Ideally, we would probe the surface layer, post-electrochemistry using UHV based techniques such as LEED [38,39] or scanning tunnelling microscopy [53–55]. However, our current setup precludes this possibility: the transfer from the electrochemical cell to the UHV chamber through the laboratory air builds up a layer of adventitious contamination. To this end, we are currently in the process of building an electrochemical cell which is directly attached to an UHV chamber. It would be of particular interest to probe whether the oxygen reduction activity might be related to defects such as surface steps [56–58] or surface cavities [59], in

Please cite this article as: A.F. Pedersen, et al., Probing the nanoscale structure of the catalytically active overlayer on Pt alloys with rare earths, Nano Energy (2016), http://dx.doi.org/10.1016/j.nanoen.2016.05.026

addition to compressive strain.

Finally, it is worth perusing upon the complete relaxation of the strain and loss of order in the overlayer exposed to more positive potentials. This observation explains our data on polycrystalline Pt_5Gd, where upon cycling to 1.2 V, the catalytic activity degraded rapidly [31]. Presumably the cause of this is due to subsurface oxide formation and its subsequent reduction [60,61].

6. Conclusion

In summary, we have fabricated Y/Pt(111) and Gd/Pt(111) by vacuum deposition. Subsequent ORR activity measurements show an enhancement over Pt(111) by a factor of 4. The single crystals show overlayers of 3–5 atomic layers upon exposure to electrolyte. We confirm that the overlayers are compressed. Upon electrochemical potential cycling between 0.1 V *vs.* RHE and >1.2 V *vs.* RHE, the strain in the overlayer is strongly reduced, which should result in a significant decrease in ORR activity. Peak broadening suggests that some of the domains may have a distribution of strain; we expect that the most strained regions will dominate the oxygen reduction activity. Future studies in this direction will aim to elucidate the actual structure of the first surface layer.

Acknowledgments

We gratefully acknowledge EU PF7's initiative Fuel Cell and Hydrogen Joint Undertaking's project CathCat (GA 303492), as well as the Strategic Research's project NACORR (12-133817) for funding this work. MEE acknowledges the Danish Council for Independent Research for the Sapere Aude: DFF Research Talent Grant. The use of the Stanford Synchrotron Radiation Lightsource, SLAC National Accelerator Laboratory, is supported by the U.S. Department of Energy, Office of Science, Office of Basic Energy Sciences under Contract no. DE-AC02-76SF00515. We also thank Apurva Mehta and Chad Miller for invaluable assistance with both synchrotron data acquisition and processing. AFP also acknowledges the Danish Ministry of Higher Education and Science for an EliteForsk travel grant making an extended stay at SLAC possible. Ifan Stephens is the recipient of the Peabody Visiting Associate Professorship from the Department of Mechanical Engineering at Masscachusetts Institute of Technology.

Appendix A. Supporting information

Supplementary data associated with this article can be found in the online version at http://dx.doi.org/10.1016/j.nanoen.2016.05.026.

References

[1] O. Groger, H.A. Gasteiger, J.P. Suchsland, J. Electrochem. Soc. 162 (2015) A2605–A2622.
[2] M.K. Debe, Nature 486 (2012) 43–51.
[3] H.A. Gasteiger, N.M. Markovic, Science 324 (2009) 48–49.
[4] F.T. Wagner, B. Lakshmanan, M.F. Mathias, J. Phys. Chem. Lett. 1 (2010) 2204–2219.
[5] S. Mukerjee, S. Srinivasan, M.P. Soriaga, J. McBreen, J. Electrochem. Soc. 142 (1995) 1409–1422.
[6] T. Toda, H. Igarashi, H. Uchida, M. Watanabe, J. Electrochem. Soc. 146 (1999) 3750–3756.
[7] C. Chen, Y.J. Kang, Z.Y. Huo, Z.W. Zhu, W.Y. Huang, H.L.L. Xin, J.D. Snyder, D. G. Li, J.A. Herron, M. Mavrikakis, M.F. Chi, K.L. More, Y.D. Li, N.M. Markovic, G. A. Somorjai, P.D. Yang, V.R. Stamenkovic, Science 343 (2014) 1339–1343.
[8] B.H. Han, C.E. Carlton, A. Kongkanand, R.S. Kukreja, B.R. Theobald, L. Gan, R. O'Malley, P. Strasser, F.T. Wagner, Y. Shao-Horn, Energy Environ. Sci. 8 (2015) 258–266.
[9] N. Todoroki, T. Kato, T. Hayashi, S. Takahashi, T. Wadayama, ACS Catal. 5 (2015) 2209–2212.
[10] F. Maillard, L. Dubau, J. Durst, M. Chatenet, J. Andre, E. Rossinot, Electrochem. Commun. 12 (2010) 1161–1164.
[11] F. Hasche, M. Oezaslan, P. Strasser, J. Electrochem. Soc. 159 (2012) B25–B34.
[12] S. Chen, H.A. Gasteiger, K. Hayakawa, T. Tada, Y. Shao-Horn, J. Electrochem. Soc. 157 (2010) A82–A97.
[13] K.J.J. Mayrhofer, V. Juhart, K. Hartl, M. Hanzlik, M. Arenz, Angew. Chem. Int. Ed. 48 (2009) 3529–3531.
[14] K. Sasaki, H. Naohara, Y.M. Choi, Y. Cai, W.F. Chen, P. Liu, R.R. Adzic, Nat. Commun. 3 (2012).
[15] X.Q. Huang, Z.P. Zhao, L. Cao, Y. Chen, E.B. Zhu, Z.Y. Lin, M.F. Li, A.M. Yan, A. Zettl, Y.M. Wang, X.F. Duan, T. Mueller, Y. Huang, Science 348 (2015) 1230–1234.
[16] L. Dubau, M. Lopez-Haro, L. Castanheira, J. Durst, M. Chatenet, P. Bayle-Guillemaud, L. Guetaz, N. Caque, E. Rossinot, F. Maillard, Appl. Catal. B Environ. 142 (2013) 801–808.
[17] G.A. Tritsaris, J. Greeley, J. Rossmeisl, J.K. Nørskov, Catal. Lett. 141 (2011) 909–913.
[18] V.R. Stamenkovic, B. Fowler, B.S. Mun, G.F. Wang, P.N. Ross, C.A. Lucas, N. M. Markovic, Science 315 (2007) 493–497.
[19] D.G. Li, C. Wang, D.S. Strmcnik, D.V. Tripkovic, X.L. Sun, Y.J. Kang, M.F. Chi, J. D. Snyder, D. van der Vliet, Y.F. Tsai, V.R. Stamenkovic, S.H. Sun, N.M. Markovic, Energy Environ. Sci. 7 (2014) 4061–4069.
[20] H. Lv, D. Li, D. Strmcnik, A.P. Paulikas, N.M. Markovic, V.R. Stamenkovic, Nano Energy.
[21] J.K. Nørskov, J. Rossmeisl, A. Logadottir, L. Lindqvist, J.R. Kitchin, T. Bligaard, H. Jonsson, J. Phys. Chem. B 108 (2004) 17886–17892.
[22] J. Greeley, I.E.L. Stephens, A.S. Bondarenko, T.P. Johansson, H.A. Hansen, T. F. Jaramillo, J. Rossmeisl, I. Chorkendorff, J.K. Nørskov, Nat. Chem. 1 (2009) 552–556.
[23] V.R. Stamenkovic, B.S. Mun, K.J.J. Mayrhofer, P.N. Ross, N.M. Markovic, J. Am. Chem. Soc. 128 (2006) 8813–8819.
[24] L.J. Wan, T. Moriyama, M. Ito, H. Uchida, M. Watanabe, Chem. Commun. (2002) 58–59.
[25] J.R. Kitchin, J.K. Nørskov, M.A. Barteau, J.G. Chen, J. Chem. Phys. 120 (2004) 10240–10246.
[26] I.E.L. Stephens, A.S. Bondarenko, F.J. Perez-Alonso, F. Calle-Vallejo, L. Bech, T. P. Johansson, A.K. Jepsen, R. Frydendal, B.P. Knudsen, J. Rossmeisl, I. Chorkendorff, J. Am. Chem. Soc. 133 (2011) 5485–5491.
[27] M. Mavrikakis, B. Hammer, J.K. Nørskov, Phys. Rev. Lett. 81 (1998) 2819–2822.
[28] U. Grønbjerg Vej-Hansen, J. Rossmeisl, I.E.L. Stephens, J. Schiøtz, Phys. Chem. Chem. Phys. 18 (2016) 3302–3307.
[29] I.E.L. Stephens, A.S. Bondarenko, L. Bech, I. Chorkendorff, Chemcatchem 4 (2012) 341–349.
[30] P. Malacrida, M. Escudero-Escribano, A. Verdaguer-Casadevall, I.E.L. Stephens, I. Chorkendorff, J. Mater. Chem. A 2 (2014) 4234–4243.
[31] M. Escudero-Escribano, A. Verdaguer-Casadevall, P. Malacrida, U. Grønbjerg, B. P. Knudsen, A.K. Jepsen, J. Rossmeisl, I.E.L. Stephens, I. Chorkendorff, J. Am. Chem. Soc. 134 (2012) 16476–16479.
[32] P. Hernandez-Fernandez, F. Masini, D.N. McCarthy, C.E. Strebel, D. Friebel, D. Deiana, P. Malacrida, A. Nierhoff, A. Bodin, A.M. Wise, J.H. Nielsen, T.W. Hansen, A. Nilsson, I.E.L. Stephens, I. Chorkendorff, Nat. Chemistry 6 (2014) 732–738.
[33] A. Velázquez-Palenzuela, F. Masini, A.F. Pedersen, M. Escudero-Escribano, D. Deian, P. Malacrida, T.W. Hansen, D. Friebel, A. Nilsson, I.E.L. Stephens, I. Chorkendorff, J. Catal. 328 (2015) 297–307, http://dx.doi.org/10.1016/j.jcat.2014.12.012.
[34] W. Bronger, J. Less-Common Met. 12 (1967) 63.
[35] W.P. Zhou, X.F. Yang, M.B. Vukmirovic, B.E. Koel, J. Jiao, G.W. Peng, M. Mavrikakis, R.R. Adzic, J. Am. Chem. Soc. 131 (2009) 12755–12762.
[36] T. Wadayama, N. Todoroki, Y. Yamada, T. Sugawara, K. Miyamoto, Y. Iijama, Electrochem. Commun. 12 (2010) 1112–1115.
[37] R. Yang, J. Leisch, P. Strasser, M.F. Toney, Chem. Mater. 22 (2010) 4712–4720.
[38] E.T. Ulrikkeholm, A.F. Pedersen, U.G. Vej-Hansen, M. Escudero Escribano, I.E.L. Stephens, A. Mehta, J. Schiøtz, R.K. Feidenhans'l, A. Nilsson, I. Chorkendorff, Surf. Sci., http://dx.doi.org/10.1016/j.susc.2016.02.009, in press.
[39] T.P. Johansson, E.T. Ulrikkeholm, P. Hernandez-Fernandez, M. Escudero-Escribano, P. Malacrida, I.E.L. Stephens, I. Chorkendorff, Phys. Chem. Chem. Phys. 16 (2014) 13718–13725.
[40] Y. Gründer, C.A. Lucas, Nano Energy, (in press), 2016.
[41] J. Clavilier, R. Faure, G. Guinet, R. Durand, J. Electroanal. Chem. 107 (1980) 205–209.
[42] D. Friebel, D.J. Miller, C.P. O'Grady, T. Anniyev, J. Bargar, U. Bergmann, H. Ogasawara, K.T. Wikfeldt, L.G.M. Pettersson, A. Nilsson, Phys. Chem. Chem. Phys. 13 (2011) 262–266.
[43] N.M. Marković, P.N. Ross, Surf. Sci. Rep. 45 (2002) 117.
[44] H.E. Hoster, O.B. Alves, M.T.M. Koper, ChemPhysChem 11 (2010) 1518–1524.
[45] A.M. Gomez-Marin, J.M. Feliu, Catal. Today 244 (2015) 172–176.
[46] J. Clavilier, A. Rodes, K. Elachi, M.A. Zamakhchari, J. Chim. Phys. Phys. Chim. Biol. 88 (1991) 1291–1337.
[47] D.-M. Smilgies, J. Appl. Crystallogr. 46 (2013) 286 286.
[48] D.M. Smilgies, J. Appl. Crystallogr. 42 (2009) 1030–1034.
[49] M. Escudero Escribano, P. Malacrida, M.H. Hansen, U.G. Vej-Hansen, A. Velazquez-Palenzuela, V. Tripkovic, J. Schiøtz, J. Rossmeisl, I.E.L. Stephens, I. Chorkendorff, Science 352 (2016) 73–76.
[50] J. Rossmeisl, G.S. Karlberg, T. Jaramillo, J.K. Nørskov, Faraday Discuss. 140 (2008) 337–346.
[51] P. Strasser, S. Koh, T. Anniyev, J. Greeley, K. More, C.F. Yu, Z.C. Liu, S. Kaya, D. Nordlund, H. Ogasawara, M.F. Toney, A. Nilsson, Nat. Chem. 2 (2010) 454–460.
[52] H.A. Hansen, V. Viswanathan, J.K. Nørskov, J. Phys. Chem. C. 118 (2014) 6706–6718.
[53] A.K. Engstfeld, S. Brimaud, R.J. Behm, Angew. Chem. Int. Ed. 53 (2014) 12936–12940.

[54] N. Todoroki, Y. Asakimori, T. Wadayama, Phys. Chem. Chem. Phys. 15 (2013) 17771–17774.
[55] M. Mercer, H. Hoster, Nano Energy, accepted (2016).
[56] A. Kuzume, E. Herrero, J.M. Feliu, J. Electroanal. Chem. 599 (2007) 333–343.
[57] A. Hitotsuyanagi, M. Nakamura, N. Hoshi, Electrochim. Acta 82 (2012) 512–516.
[58] K. Kodama, R. Jinnouchi, N. Takahashi, H. Murata, Y. Morimoto, J. Am. Chem. Soc. 138 (2016) 4194–4200.
[59] F. Calle-Vallejo, J. Tymoczko, V. Colic, Q.H. Vu, M.D. Pohl, K. Morgenstern, D. Loffreda, P. Sautet, W. Schuhmann, A.S. Bandarenka, Science 350 (2015) 185–189.
[60] H. You, D.J. Zurawski, Z. Nagy, R.M. Yonco, J. Chem. Phys. 100 (1994) 4699–4702.
[61] M. Wakisaka, S. Asizawa, H. Uchida, M. Watanabe, Phys. Chem. Chem. Phys. 12 (2010) 4184–4190.

Anders Filsøe Pedersen is a PhD student in the group of Professor Ib Chorkendorff and Associate Professor Ifan Stephens at the Department of Physics at the Technical University of Denmark (DTU). His co-supervisor is Professor Andes Nilsson, and he spends most time at the Stanford Linear Accelerator Center National Laboratory at Stanford University in California. His research interest lies in synchrotron research on Pt alloys, as well as oxides for the oxygen evolution reaction. In 2015 he received an EliteForsk travel grant from the Ministry of Higher Education and Science.

Elisabeth Therese Ulrikkeholm is a Post Doc at the Center for individual Nanoparticle Functionality (CINF). The focus of her research is mainly on the behavior of single crystal alloys.

She obtained her Masters degree in physics from the Niels Bohr Institute (University of Copenhagen) in 2010. In 2014 she obtained her PhD from the Department of Physics, at the Technical University of Denmark, under the supervision of Professor Ib Chorkendorff.

María Escudero Escribano received her PhD in Chemistry from the Autonomous University of Madrid (2011). In 2012, she joined the Electrocatalysis Group at the Department of Physics at the Technical University of Denmark (DTU), as a postdoctoral researcher. She received several prizes for her work, including the *Suschem Young Chemistry Researcher* Award 2011 and the *Sapere Aude: Research Talent* Grant 2014 (Danish Council for Independent Research). She currently carries out her research at Stanford University and DTU. Her research combines electrochemical techniques with *in situ* X-ray based measurements, spectroscopies and microscopies, in order to investigate problems pertaining to electrochemical energy conversion.

Tobias Johansson researched his PhD at the Center for Individual Nanoparticle Functionality in the Department of Physics at the Technical University of Denmark (DTU) in 2012. The main focus of his PhD thesis was the study of alloy materials as catalysts for the oxygen reduction reaction. He continued his research in catalysis as a postdoctoral researcher at DTU. He combined electrocatalysis, ultra-high vacuum experiments and insight from DFT to elucidate the oxygen reduction reaction, ammonia synthesis and CO electroreduction.

Paolo Malacrida obtained his PhD in Physics at the Technical University of Denmark (DTU) in 2014, under the supervision of Professor Ib Chorkendorff. Both his PhD and his following experience as a postdoctoral researcher in the same group were focused on the study of novel cathode materials for PEMFC. He gained particular experience with the application and development of spectroscopic techniques such as X ray photoelectron spectroscopy, ultraviolet photoelectron spectroscopy and ion scattering spectroscopy applied to electrocatalysts, in particular Pt-based alloys. He is currently employed at Novo Nordisk A/S.

Christoffer Mølleskov Pedersen is an industrial PhD student in the group of Professor Ib Chorkendorff and Associate Professor Ifan Stephens at the Department of Physics at the Technical University of Denmark (DTU), as part of the Industrial PhD Programme of the Danish Council for Technology and Innovation (DCTI). His co-supervisor is Leif H. Christensen from the Danish Technological Institute (DTI). He is developing catalysts for direct methanol fuel cells, specifically for the methanol oxidation and oxygen reduction reaction.

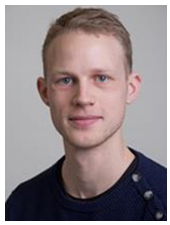

Martin Hangaard Hansen is a PhD student with the Center for Atomic-scale Materials design at the Department of Physics, the Technical University of Denmark (DTU). He obtained his Master's degree in Physics and Nanotechnology from DTU in 2013 under the supervision of Prof. Jan Rossmeisl, with whom he continued as a PhD student. His research is focused on electrocatalysis and new methods for modeling the electrolyte-electrode interface with density functional theory.

Kim Degn Jensen obtained his B.Sc. and M.Sc. in Physics at the Technical University of Denmark (DTU) 2006–2012. He worked at Grundfos Direct Sensors™ from 2012 to 2015. He is currently pursuing his PhD at DTU Physics, at CINF, under guidance and supervision of Prof. Ib Chorkendorff, Associate Prof. Ifan Stephens and Dr. María Escudero Escribano. His PhD thesis aims to study the oxygen reduction reaction (ORR) electrocatalysis for proton exchange membrane fuel cells. He is currently investigating the ORR activity of model Pt (111) surface and subsurface alloys, as well as the poisoning effect by spectator species such as phosphate anions.

Jan Rossmeisl is Professor of theoretical chemistry at Department of Chemistry and the Nano-Science center at Copenhagen University. Before joining University of Copenhagen in April 2015, Jan was an Associate Professor and group leader for the theoretical catalysis group at Department of Physics at the Technical University of Denmark. Jan holds Masters (2000) and PhD (2004) degrees in physics from the Technical University of Denmark. Since 2007 he has supervised more than 20 PhD students and post doctoral researchers. He is coauthor on more than 110 publications in peer reviewed journals, co-inventor of 4 patents and co-founder of two startup companies. Research interests include: electrocatalysis, energy conversion, atomic scale simulations, rational interface design for catalysis.

Please cite this article as: A.F. Pedersen, et al., Probing the nanoscale structure of the catalytically active overlayer on Pt alloys with rare earths, Nano Energy (2016), http://dx.doi.org/10.1016/j.nanoen.2016.05.026

Daniel Friebel obtained his PhD in Chemistry at Bonn University in Germany where he used scanning tunnelling microscopy to image solid/liquid interfaces with atomic resolution. In 2007, a postdoctoral research fellowship from Alexander von Humboldt Foundation brought him to Anders Nilsson's Surface Science and X-ray Spectroscopy Group at SLAC National Accelerator Laboratory, and he became Associate Staff Scientist in 2012. His research at SLAC focuses on the development of *in situ* and operando X-ray spectroscopy and scattering techniques to study catalytic reactions for sustainable energy conversion.

Anders Nilsson received a PhD in physics at Uppsala University, Sweden (1989) in the laboratory created by Kai Siegbahn. He is currently professor in Chemical Physics at Stockholm University and in Photon Science at the SLAC National Accelerator Laboratory and Stanford University. He received the Lindbomska Award at the Swedish Royal Academy of Science, the Royal Oscar Award at Uppsala University in 1994, the Shirley Award in Berkeley 1998, the Humboldt Award for senior scientist in 2010 and was awarded honorable doctor at Denmarks Technical University in 2015. His research interests include synchrotron radiation and X-ray laser spectroscopy and scattering, chemical bonding and reactions on surfaces, ultrafast science heterogeneous catalysis, electrocatalysis in fuel cells, photocatalysis for converting sunlight to fuels, structure of water and aqueous solutions.

Professor Ib Chorkendorff got his PhD in 1985 in experimental surface science from Odense University, Denmark. After working as a post-doc with Prof. John T. Yates Jr. at University of Pittsburgh, USA, he was employed in 1987 at DTU to establish an experimental activity, investigating fundamental aspects of heterogeneous catalysis. In 2005 he established the Center for Individual Nanoparticle Functionality (CINF), and broadened these activities to include technologies for producing solar fuels utilising electro- and photo-catalysis, for finding new and effective materials for improving sustainable energy conversion and environmental protection. Ib Chorkendorff is currently consulting Professsor at SUNCAT at Stanford University.

Ifan Stephens leads the Electrocatalysis Group at the Department of Physics at the Technical University of Denmark (DTU). He obtained his PhD in Materials Science at the University of Cambridge. He first joined DTU in 2008 as a postdoctoral researcher and became a member of faculty in 2011. He currently holds the position of Associate Professor. In 2015, he was awarded the Peabody Visiting Associate Professorship by the Department of Mechanical Engineering at the Massachusetts Institute of Technology. He conducts frontier research into the elucidation and testing of electrocatalytic surfaces. The aim of his investigations is to enable and accelerate the development of electrochemical devices for energy conversion and chemical synthesis.

Please cite this article as: A.F. Pedersen, et al., Probing the nanoscale structure of the catalytically active overlayer on Pt alloys with rare earths, Nano Energy (2016), http://dx.doi.org/10.1016/j.nanoen.2016.05.026

Surface Science 652 (2016) 114–122

Contents lists available at ScienceDirect

Surface Science

journal homepage: www.elsevier.com/locate/susc

Pt_xGd alloy formation on Pt(111): Preparation and structural characterization

Elisabeth T. Ulrikkeholm[a,1], Anders F. Pedersen[a,1], Ulrik G. Vej-Hansen[b], Maria Escudero-Escribano[a], Ifan E.L. Stephens[a], Daniel Friebel[c], Apurva Mehta[d], Jakob Schiøtz[b], Robert K. Feidenhansl'[e], Anders Nilsson[c], Ib Chorkendorff[a,*]

[a] Department of Physics, Center for Individual Nanoparticle Functionality, Building 312, Technical University of Denmark, 2800 Lyngby, Denmark
[b] Department of Physics, Center for Atomic-scale Materials Design, Building 307, Technical University of Denmark, 2800 Lyngby, Denmark
[c] Department of Chemical Engineering, SUNCAT Center for Interface Science and Catalysis, Stanford University, Stanford, CA, USA
[d] Stanford Synchrotron Light Source, SLAC National Laboratory, 2575 Sand Hill Road, 94025 Menlo Park, CA, USA
[e] Niels Bohr Institute, University of Copenhagen, DK-2100 Copenhagen, Denmark

ARTICLE INFO

Available online 19 February 2016

Keywords:
Platinum alloys
Single crystals
X-ray diffraction
Alloy formation

ABSTRACT

Pt_xGd single crystals have been prepared in ultra high vacuum (UHV). This alloy shows promising catalytic properties for the oxygen reduction reaction. The samples were prepared by using vacuum deposition of a thick layer of Gd on a sputter cleaned Pt(111) single crystal, resulting in a ~63 nm thick alloy layer. Subsequently the surfaces were characterized using X-ray photoelectron spectroscopy (XPS), low energy electron diffraction (LEED), ion scattering spectroscopy (ISS) and temperature programmed desorption (TPD) of CO. A Pt terminated alloy was observed upon annealing the sample to 600 °C. The LEED and synchrotron XRD experiments have shown that a slightly compressed (2 × 2) alloy appear. The alloy film followed the orientation of the Pt(111) substrate half the time, otherwise it was rotated by 30°. The TPD spectra show a well-defined peak shifted down 200 °C in temperature. The crystal structure of the alloy was investigated using ex-situ X-ray diffraction experiments, which revealed an in-plane compression and a complicated stacking sequence. The crystallites in the crystal are very small, and a high degree of twinning by merohedry was observed.

1. Introduction

One of the most promising technologies for utilizing the energy stored in hydrogen is the low temperature polymer electrolyte membrane fuel cell (PEMFC). However, as a consequence of a large potential loss on the cathode these devices require a large amount of Pt to catalyze the Oxygen Reduction Reaction (ORR). To lower the Pt loading and improve the activity, Pt based alloys can be used instead of pure Pt [1,2,3,4,5,6]. However, bimetallic alloys tend to dealloy in the acidic environment in a fuel cell, causing the catalyst to degrade [7,8,9]. More recently we have investigated platinum and rare earth element bimetallic alloys because of their large negative heat of formation, which may provide a catalyst that is less prone to electrochemical dealloying [10,11,12]. These alloys show a high activity for the ORR, and Pt_xGd in particular exhibit an exceptionally high activity for oxygen reduction, both in the polycrystalline form and the nanoparticulate form [12,13,14].

Gd modified Pt(111) single crystals have been investigated in order to understand the origin of the enhanced activity of this alloy. This article contains a thorough description of the alloy prepared in UHV combined with investigations of the crystal structure. Characterizing the alloy and its structural motifs is imperative for understanding the highly active Pt overlayer surface that forms during ORR [12,10,14,15,16].

The ideal catalyst for ORR will have a slightly weaker reactivity than Pt(111), and bind oxygen 0.2 eV weaker [17,18]. To probe the reactivity of the surface, CO temperature programmed desorption experiments have been performed. Yates was amongst the pioneers of this techniques, which his group used on single crystals to study the dynamics of molecules, the effect of steps on the reactivity of Pt(112) [19], and reaction pathways on Ni(111) [20]. X-ray diffraction experiments made on polycrystalline Pt_5Gd have shown that this alloy has a large unit cell with a complicated stacking [21,22]. Furthermore, these studies never found the crystal structure for Pt_5Gd using powder samples. In this article, we demonstrate how we can

* Corresponding author.
E-mail address: ibchork@fysik.dtu.dk (I. Chorkendorff).
[1] These authors contributed equally to this work.

http://dx.doi.org/10.1016/j.susc.2016.02.009
0039-6028/

determine the space group, unit cell, and structural motifs behind a Pt–Pt compression using a 3-dimensional diffraction pattern. Due to the complicated stacking expected for this alloy, single crystal diffraction is essential, since it provides much more structural information than powder diffraction. We publish this work in memory of John T. Yates and his great contribution to the field of surface science.

2. Experimental setup

The sample preparation and the UHV characterization were performed in a vacuum chamber with a base pressure of $1.0 \cdot 10^{-10}$ Torr. The chamber is equipped with standard UHV surface science techniques; X-ray photoelectron spectroscopy (XPS), ion scattering spectroscopy (ISS), low energy electron diffraction (LEED), and a quadrupole mass spectrometer for temperature programmed desorption (TPD). ISS is performed using He^+ ions accelerated over a voltage of 1.25 kV. The XPS experiments were performed using K_α radiation from a Mg anode (1253.4 eV). The sample, a Pt(111) single crystal, 5 mm in diameter and 3 mm thick, was supplied by MaTecK, GmbH, Germany. The sample was mounted in a hairpin shaped tungsten wire which was then mounted onto the feed-through on the manipulator end [23]. The temperature is measured using a type K thermocouple. The sample can be resistively heated at a linear ramp regulated by a PID controller, and cooled to $T = -190$ °C using liquid nitrogen. The main chamber is equipped with a water cooled metal Gd evaporator and a quartz crystal microbalance (QCM), which makes it possible to evaporate Gd on the surface of the sample at a well known evaporation rate. The evaporator was made by cutting flakes of a Gd foil and attaching them to a coil shaped 0.25 mm 99.95% tungsten wire. The Gd flakes were cut from a 0.127 mm 99.9% Gd foil supplied by Alfa Aesar.

After the Gd/Pt(111) single crystal was made with a thick alloy in the UHV chamber at DTU, it was transported to the Stanford Synchrotron Radiation Lightsource (SSRL). The sample was transported and measured in air, and no surface cleaning was necessary since the alloy phase was quite thick (estimated to be ~63 nm) and protected from oxidation by the Pt overlayer. The diffraction experiments were carried out at beam line 7 – 2, which was equipped with a Huber six-circle (4 + 2) diffractometer and a Dectris Pilatus 300 K imaging detector. The diffractometer stage was equipped with a goniometer head that allowed the crystal surface normal to be aligned to the phi rotation axis using a laser. All the data was acquired at a fixed incidence angle of 0.2° to maximize surface sensitivity, and the photon energy was set to 11.0 keV to avoid fluorescence background from the Pt. A sketch of the setup is seen in Fig. 1 [24]. At each detector position a circular diffraction pattern from a polycrystalline LaB_6 sample was recorded, so that the position of the detector could be calculated. Data was acquired by rotating the crystal in steps of 0.2°, and a rocking scan was performed in each spot. This was repeated using 6 different positions of the detector. The acquired diffraction data was stitched together to form a 3-dimensional image of parts of the Q-space, and the intensity has been corrected for the Lorentz factor, polarization, and geometrical effects using MatLab scripts developed by the authors.

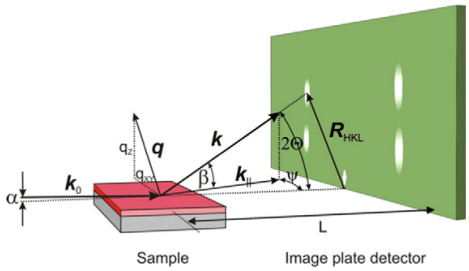

Fig. 1. A sketch of the experimental setup used for the X-ray diffraction measurements. The incidence angle was fixed at $\alpha = 0.2°$ for all measurements. The whole reciprocal space is reconstructed by rotating the sample around its surface normal and stitching each slice of data. The image is from [24].

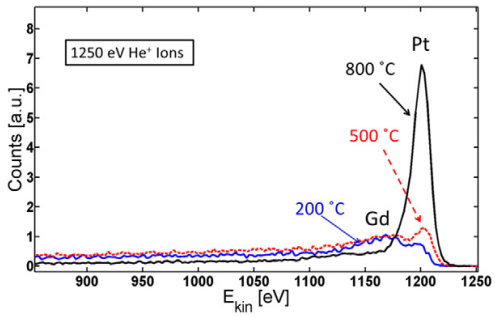

Fig. 2. ISS spectra measured at different temperatures. At $T = 200$ °C the sample is dominated by Gd and only a small amount of Pt can by seen, at $T = 500$ °C the platinum signal becomes more pronounced, and at $T = 800$ °C the Pt signal becomes dominant indicating the formation of a Pt overlayer.

3. Results

3.1. Alloy formation

Earlier experiments have shown that it is possible to prepare a well-organized crystalline structure by vacuum deposition of monolayers of lanthanide metals on a sputter cleaned Pt single crystal [25,26,27,28]. Our experiments with deposition of thick layers of Y on Pt(111) have shown that it is possible to simulate a crystal that behaves like a single crystal [15]. On the basis of these promising results, we initiated experiments on Gd modified Pt(111) single crystals.

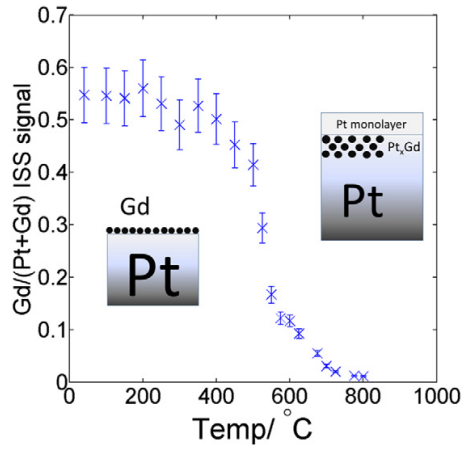

Fig. 3. The 'Gd' to the 'Gd + Pt' ratio probed with ISS as a function of temperature. The intensities have been found by comparing the peak intensities. No sensitivity factors have been used and hence the ratio can only be considered qualitatively. At $T = 450$ °C the amount of Gd decreases significantly indicating alloy formation terminated by a Pt overlayer.

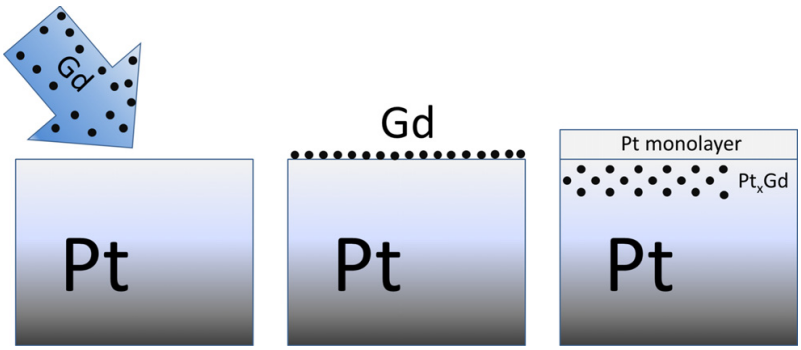

Fig. 4. The deposition process. Gd is deposited on the surface of Pt(111) at room temperature. At this temperature the Gd is not mobile. After heating up the crystal Gd becomes mobile and migrate to the subsurface region and a Pt surface monolayer is formed.

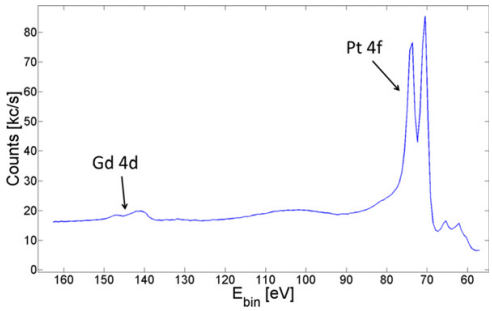

Fig. 5. XPS performed after Gd deposition and annealing to 800 °C.

3.1.1. Creating a near surface alloy

To probe whether Gd and Pt would form an alloy, a thin layer of 2 nm Gd was deposited on a sputter cleaned, annealed Pt(111) surface. XPS measurements performed after the deposition showed that the Gd was partially oxidized, see S.I. Section 1. During the evaporation an increase in the pressure to approximately $1.0 \cdot 10^{-9}$ mbar due to degasing of the evaporator could not be avoided. Gadolinium has a high affinity to oxygen ($\Delta H = -1819.6$ kJ/mol, corresponding to an energy gain of 9.4 eV per Gd atom for $2Gd + 1.5O_2 \rightarrow Gd_2O_3$), and can oxidize even under UHV conditions [29]. To remove the traces of gadolinium oxide, the sample was gently sputtered using Ar ions for 10 min. The composition of the atoms in the surface of the sample was probed using ISS immediately after. The sample was then heated in steps of 25 °C and the composition of the surface was evaluated after each heating step. ISS spectra for representative temperatures can be seen in Fig. 2. At $T = 200$ °C the spectrum is dominated by Gd, at $T = 500$ °C the Pt signal becomes visible, and at $T = 800$ °C the surface is completely dominated by Pt, indicating a formation of a Pt_xGd alloy terminated by a Pt overlayer.

In Fig. 3 the relative intensity of the Gd signal can be seen as a function of temperature. It can be seen that the amount of Gd in the surface drops rapidly at $T = 450$ °C, and at temperatures above $T = 500$ °C, the spectra are dominated by Pt, indicating inter-diffusion of Gd and the formation of a Pt overlayer.

The alloying process is sketched in Fig. 4.

XPS was performed to verify that the Gd has merged to the subsurface layer, and that the decrease in the Gd intensity is not a consequence of He^+ sputtering of the gadolinium atoms in the surface during the ISS experiment, see Fig. 5. Furthermore, an overview spectrum can be seen in S.I. Section 1. From the XPS measurement, it can be seen that the gadolinium is still present, indicating that it has merged to the subsurface region and has created a near surface alloy (NSA). It is possible to calculate the stoichiometry of the alloy under the assumption that the surface is terminated by a single layer of platinum [30]. The quantification of the XPS spectrum can be seen in Table 1.

To probe the reactivity of the thin Pt_xGd alloy terminated by Pt, CO TPD was performed on a CO saturated surface. $2.0 \cdot 10^{-7}$ Torr CO was dosed for 30 min while the sample was cooled from 400 °C to −190 °C, corresponding to a dosage of 360 L. The sample was heated at a constant rate of 2 °C/s during the TPD experiments. The CO TPD can be seen in Fig. 6 where it is compared to a CO TPD made on a CO saturated Pt(111) surface. The experiment was performed several times, and has shown a high degree of reproducibility. This indicates that there were no dissociation of CO. In the CO TPD made on the Gd/Pt(111) sample a sharp peak appears at $T = -10$ °C. This peak has a shoulder to higher temperatures at $T = 0$ °C, and a less pronounced shoulder to lower temperatures at $T = -60$ °C. The integrated intensity of the desorption peaks were calculated to

Table 1
Concentrations of the different elements in the Gd/Pt(111) quantified with XPS after the gadolinium deposition and annealing to 800 °C.

Pt [%]	Gd [%]	x for Pt/Pt_xGd
89.7	10.3	6.9

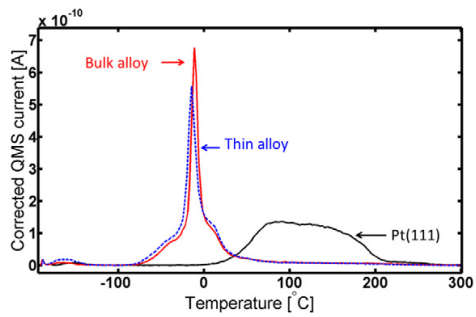

Fig. 6. TPDs on CO saturated surfaces. Blue curve: TPD made on the thin, near surface alloy of Gd/Pt(111), red curve TPD made on the bulk alloy, black curve TPD made on a sputter cleaned, annealed Pt(111) surface. The TPDs are made at a constant heating rate of 2 °C/s.

Table 2
Concentrations of the different elements in the Gd/Pt(111) quantified with XPS after the gadolinium deposition.

	Pt [%]	Gd [%]	O [%]	x for Pt/Pt_xGd
Before	74.0	17.4	8.5	3.2
After	87.4	12.5	0.1	5.5

The measurements were made before and after Ar sputtering at 800 °C.

evaluate the amount of CO molecules adsorbed on the surface during the TPD experiments. The coverage of the sample can be evaluated by comparing this value to the integrated intensity of the desorption peak from the Pt(111) sample, since the behavior of CO on clean Pt(111) surfaces has been studied extensively over the last decades [31,32,33,34,35,36]. For a perfect Pt(111) single crystal the CO saturation coverage is $\theta = 0.68$ [32]. By comparing the integrated desorption peaks we determine a CO saturation coverage of $\theta = 0.54 \pm 0.03$ on Gd/Pt(111). We anticipate that the variations in the measured coverage is mainly a consequence of small variations in the sample position relative to the mass spectrometer.

3.1.2. Simulating a bulk alloy

To simulate the behavior of a bulk alloy, a thick layer of Gd was deposited on a sputter cleaned, annealed Pt(111) surface. A thick layer of (200 ± 50) Å Gd was deposited on a sample heated to a temperature of 800 °C in UHV. This temperature is well above the mobility temperature and hence we anticipate that a platinum overlayer will form instantaneously which will protect the Gd from oxidation. The stoichiometry of the alloy was evaluated using XPS, see Table 2. Traces of oxygen were seen in the XPS spectra, see Fig. 7, indicating the formation of gadolinium oxide. To remove this, the sample was sputtered gently using Ar-ions while the sample was kept at 800 °C.

The amounts of oxygen and gadolinium have decreased significantly after the sputtering, which implies that a layer of gadolinium oxide has been formed on the surface during the evaporation, and that the sputtering procedure has removed this. The stoichiometry of the alloy has been evaluated assuming that the platinum skin consists of a single layer of atomic platinum of thickness $d = 2.28$ Å [30], see Table 2.

From the calculated Gd concentration, it is most likely that the crystal has formed Pt_5Gd, which is the most platinum rich, stable Pt_xGd alloy [37]. The composition of the surface layer was measured using ISS, see Fig. 8. Gd was not seen in the ISS spectrum after the deposition, indicating the formation of a Pt overlayer.

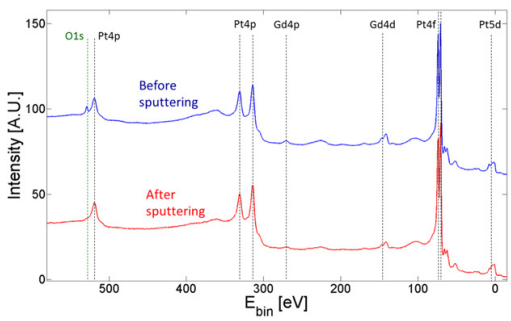

Fig. 7. Blue: XPS overview spectrum made after the deposition of gadolinium at 800 °C. Oxygen can be seen in this spectrum indicating the formation of gadolinium oxide. Red: XPS spectrum made on the sample after a light sputtering at 800 °C. After the sputtering, the oxygen signal is close to the detection limit.

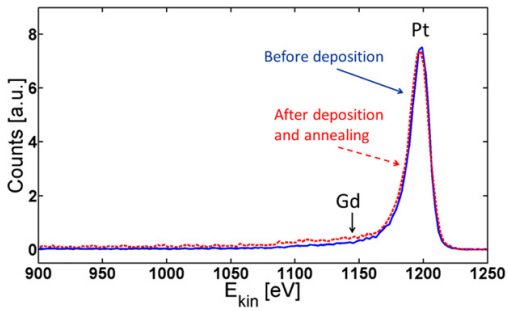

Fig. 8. ISS before and after the deposition. Gd was not seen in the spectrum measured after the deposition, indicating the existence of a Pt overlayer.

The reactivity of this surface was probed using CO TPD experiments using the same experimental conditions as for the thin alloy. The sample was saturated with CO, cooled using liquid nitrogen, and heated using a constant heating rate of 2 °C/s, see Fig. 6. The TPD experiments were repeated several times showing a high degree of reproducibility. From the integrated intensity of the desorption peak the CO saturation coverage of this surface is $\theta = 0.58 \pm 0.02$.

LEED was performed to evaluate the crystal structure of the Gd/Pt(111) sample. This was made on the clean Pt(111) surface before the Gd deposition, and after the deposition and annealing, see

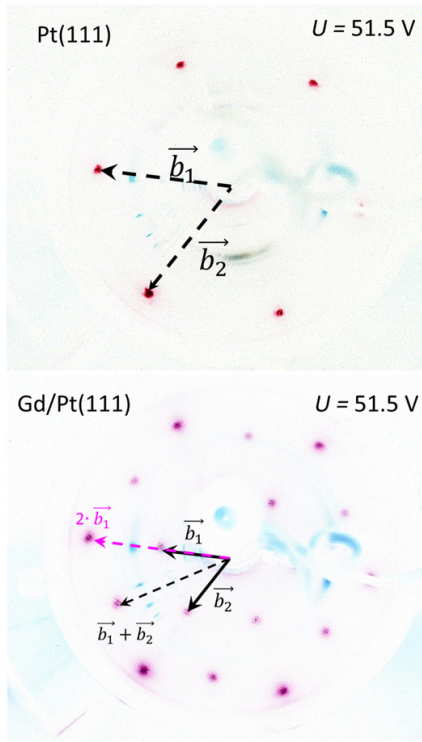

Fig. 9. Top: A LEED pattern made on a sputter cleaned, annealed Pt(111) surface. Bottom: LEED pattern made on the prepared Gd/Pt(111) sample. The colors have been inverted for clarity. The surface structure forms a (1.90×1.90) structure not rotated with respect to the Pt substrate.

Fig. 9. A well-defined diffraction pattern appears after the deposition of Gd, indicating that a well-defined, crystalline surface has been formed. The structure of the Gd/Pt(111) surface is hexagonal and show a (1.90 × 1.90) structure, not rotated with respect to the platinum substrate. The position of the diffraction peak can be estimated within a resolution of 2%. Gd/Pt(111) samples have been prepared using this procedure 5 times. The lattice constant of the observed structures is always the same, but the rotation could vary; the alloy film followed the orientation of the Pt(111) substrate half the time, otherwise it was rotated by 30°, see S.I. Section 1. This indicates that these two configurations are equivalent or extremely close in energy. We will consider this further in the Discussion section.

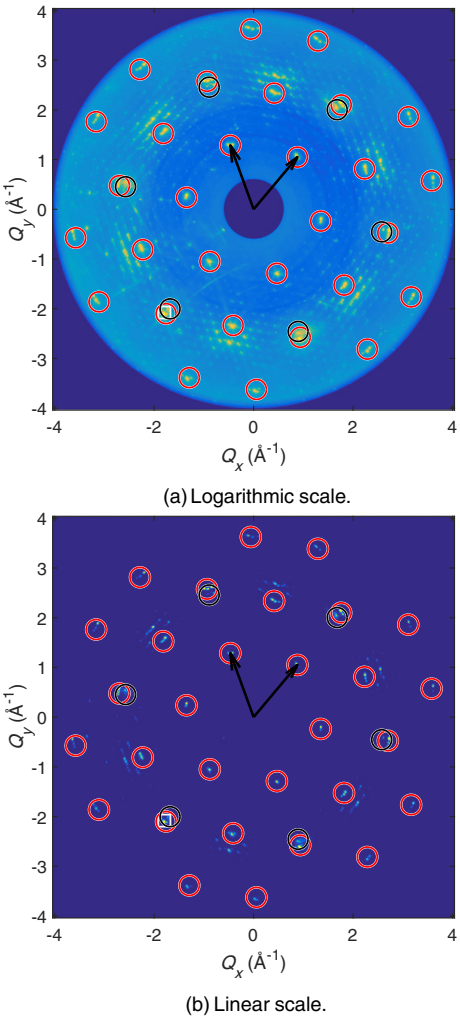

Fig. 10. The XRD intensity integrated along the surface normal, along the L lattice vector. The arrows show the in-plane crystal lattice vectors H and K, the red circles show the diffraction peaks from the Pt_xGd alloy, and the black circles show the diffraction peaks from the Pt(111) substrate. Many super-spots are seen, indicating a high degree of twinning. Furthermore non-merohedral twinning is seen as the spots are split in 3, and this is shown by a zoom of the white square in Fig. 11. In (a) the color scale is logarithmic to show more features, and the intensity ranges 4 orders of magnitude. In (b) the color scale is linear and the maximum is set to 1/4 of the maximum intensity of the peaks.

3.2. X-ray diffraction experiments

The 3-dimensional *Q*-space was investigated, and it was immediately seen that the alloy has a hexagonal symmetry in the plane of the crystal surface. Fig. 10 shows the diffraction pattern integrated along the L-direction, the surface normal. The arrows show the in-plane H and K crystal lattice vectors, and the L lattice vector is perpendicular to the figure plane. The red circles show the diffraction peaks from the Pt_xGd alloy, whereas the black circles show the diffraction peaks from the Pt(111) substrate. The Pt surface monolayer may have a different crystal structure than the rest of the alloy, but the sensitivity of this XRD experiment is not high enough to detect a single monolayer. A large number of super-spots are seen, indicating a high degree of twinning. Besides twinning by merohedry (overlapping diffraction spots) indicated by the super-spots some non-merohedral twins are present, since many of the diffraction spots are split into 3 spots. This peak splitting indicating domains in the alloy is more clearly seen in Fig. 11, showing a zoom of the white square in Fig. 10. This non-merohedral twinning shows a small rotation around the surface normal, and is caused by separate domains in the alloy only, since the Pt(111) substrate does not show any splitting. Unfortunately these non-merohedral twinned peaks are too close to rigorously separate, and in the further data processing they have all been included in a single integrated intensity.

The hexagonal unit cell dimensions were found by fitting a pseudo-Voigt peak shape to the positions of the brightest alloy peaks. These positions in *Q*-space were then calibrated using the Pt(111) substrate diffraction peaks, and small corrections on the order of 1% were made, since the detector positioning method using the LaB_6 sample is not perfect. In the hexagonal unit cell the parameters are $a = 5.3309 \pm 0.0008$ Å and $c = 40.358 \pm 0.012$ Å. Furthermore from the width (full width at half max, FWHM) of the peaks the crystallite sizes are estimated using Scherrer's formula [38], and using a shape factor of 1 the in-plane size is estimated to be 22 nm and out-of-plane size 12 nm. This small crystallite size is consistent with the high number of super-spots seen, since a typical beam coherence length on the order of a μm will illuminate a large number of domains coherently. The broadening of the peaks from the beam coherence

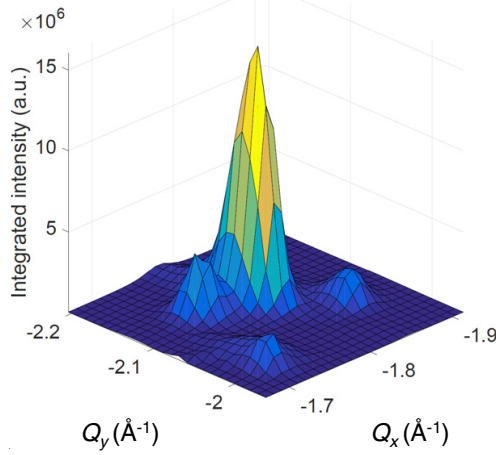

Fig. 11. The alloy splitting in 3 domains is clearly seen in this surface plot, showing a zoom in of the white square in Fig. 10. The 3 large peaks are from the alloy and the weak peak closest is the Pt(111) substrate. The substrate peak does show some broadening in the left-right direction, but there is no splitting as seen in the alloy.

has not been taken into account, since the crystal broadening is much larger.

The main alloy diffraction peaks were indexed, and the intensity was integrated by summing the voxels around each diffraction peak. The noise was assumed to be 10 counts (out of a maximum count of 1,000,000) per voxel. Integrated intensity of the peaks was calculated by summing the intensities in the voxels around the area covering the brightest peak and a depth large enough to cover all 3 domains. Uncertainty on the intensity measurement were estimated as the square root of 10 times the number of voxels contributing to the integrated peak. The range of diffraction peaks in-plane was from (H,K) = (1,0) to (2,1), and the out-of-plane range was L = 1 to 24. Due to the low incidence angle the specular diffraction spots are unavailable, and for the ⟨10L⟩ peaks the maximum L was 21 or 22. This leads to a total of 705 diffraction peaks indexed. The measured intensities and the estimated uncertainties from noise are found in S.I. Tables 1–5, where H and K are multiples of the two reciprocal lattice vectors shown in Fig. 10 and L is multiple of the reciprocal lattice vector pointing out of the plane in the same figure.

Space group determination was done using the program SHELXT, part of the SHELX crystal structure determination and refinement package [39]. The best fit to the presented data is R3m, space-group 160, which has a rhombohedral symmetry. In here, we use the hexagonal axes to represent the rhombohedral lattice to make comparison to the Pt(111) substrate more intuitive. With inspiration from the high temperature Pd_5Ce [40] and Cu_5Ca [22] structures, an initial guess was made. The height of the unit cell (c axis) is consistent with 18 Pt(111) like atomic layers. The rhombohedral symmetry reduces the asymmetric cell to 1/3 c axis height, i.e., 6 Pt(111) like layers. The initial guess for the asymmetric cell is shown in Fig. 12. The lines show the unit cell in-plane, and the *z*-value indicates the relative z-coordinate of the given layer. In this structure three different types of layers are seen. Gd atoms are only located in the 2nd and the 6th layers (H_1 and H_3) and they are ordered with Pt in 2:1 (Pt_2Gd), and 1:2 ($PtGd_2$) ratios. The layers above or below the Gd containing layers, i.e., 1st, 3rd, and the 5th layers, have vacancies in the hexagonal net just above or below the Gd atoms, forming a "kagome" like net (K_1, K_2, and K_3). The 4th layer in the asymmetric cell (H_2) is a Pt only hexagonal net with no vacancies. The atoms in the kagome layers are on a 9b Wyckoff site; whereas the atoms of both types of the hexagonal layers are on a 3a Wyckoff site. There are 12 unique atoms in the asymmetric unit cell with 15 refinable position parameters, and the full unit cell has 54 atoms. Ordering of the Gd atoms and the corresponding vacancies in the adjacent kagome layers presumably helps to accommodate the larger Gd ion.

To optimize the guessed structure the program SHELXL was used, which was used with a least-squared fitting routine. As an input it takes the unique atomic positions and optimizes them against the measured peaks. Out of the 705 measured peaks, 55 unique peaks were found for this space group. The program has an option for handling simple twinning, but it was not possible to get any stable fits considering different kind of twins, both 60° rotated twins and obverse/reverse rhombohedral twinning was attempted. Assuming the trial structure described above, the structure factors for a 60° rotated twin was calculated and all peaks that contribute to this twin were removed from the raw data. A total of 235 diffraction peaks were removed, leaving 470 peaks of which 47 are unique. Because of the complexity of structure and relatively few unique reflections, first set of refinements were performed by fixing the Debye–Waller factors to being isotropic at a value of 0.02 Å^2, and constraining Pt– Pt distances to be approximately equal. In the subsequent refinements, Pt–Pt distance constrains were removed, to achieve a stable refinement with R1 of 0.57 (0 being a perfect fit). To understand the reason for the relatively large R-factor, the calculated and measured structure factors were plotted against the scattering vector Q, see S.I. Fig. 6. The fit is mostly good for the weaker reflections, whereas strong reflections are fitted poorly, and we speculate that perhaps the misfits arise from incomplete separation of intensities from various twins still present in the data.

The fitted structure has the same layers as the initial guess, although the layers have become somewhat disordered. The in-plane structure is not changed due to the symmetry of the special sites.

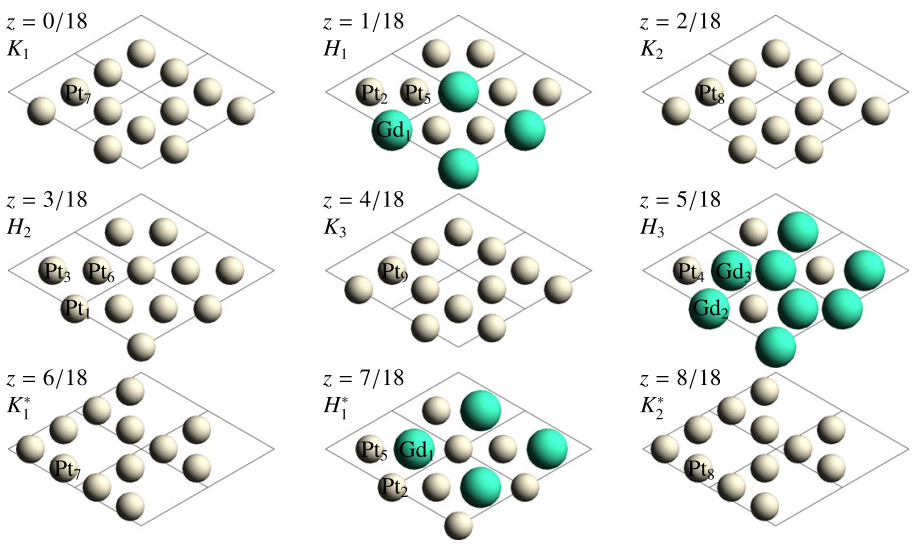

Fig. 12. The first 9 layers out of 18 of the initial structure guess, the grey spheres are Pt and green spheres are Gd. Due to the rhombohdral symmetry the 6 first layers repeat above, but are shifted by one atom, as shown here. The lines show the unit cell in-plane, and the *z*-coordinate gives the relative *z*-position of the given layer. Three types of layers are seen, the first layer is a kagome type layer consisting only of Pt, and it has a void that can accommodate the larger Gd in layer above or below. The other layers are hexagonal and are either pure Pt (H_2) or have a varying Pt–Gd stoichiometry. To distinguish the layers the kagome layers are labeled by *K* and the hexagonal layers are labeled *H*, and the * denotes symmetrically equivalent planes. The unique atoms in the asymmetrical unit cell have been labeled as well.

A side view of the structure is seen in Fig. 13. The structure is seen along the a-axis of the unit cell, and the kagome layers have been shown with black lines. The atomic layers are no longer equidistant, and the structure is more disordered than the initial guess. The hexagonal layers have become significantly buckled, and the Gd atoms have moved closer to the voids in the kagome layers. That also shows as the two neighboring Gd atoms are displaced in opposite directions, just as seen in the Pd_5Ce structure. The Pt atom in the hexagonal layer with the two Gd atoms have moved down very close to the Pt atoms in the kagome layer below, and are unphysically close. A Fourier difference map comparing the measured and calculated electron densities does show that this Pt atom should be higher. Otherwise the rest of the interatomic distances are more reasonable, although varying more than expected. Table 3 sums up the structure with the until cell and atomic positions of the 12 unique atoms.

The fitted structure is somewhat disordered, and in order to understand atomic displacement in great detail anisotropic Debye–Waller factors were fitted while fixing the atomic positions. With the amount of data available these Debye–Waller factors are not expected to represent physical atomic motion, but rather comparing them with Fourier difference maps they can indicate particular disorder and potential broken symmetry. The anisotropic Debye–Waller factors are sketched in Fig. 14, showing an asymmetrical unit cell. It is seen that Pt_1 has a strong disorder along the z-axis, and also that the K_1 layer has a large degree of disorder in-plane, which is shown in Fig. 15.

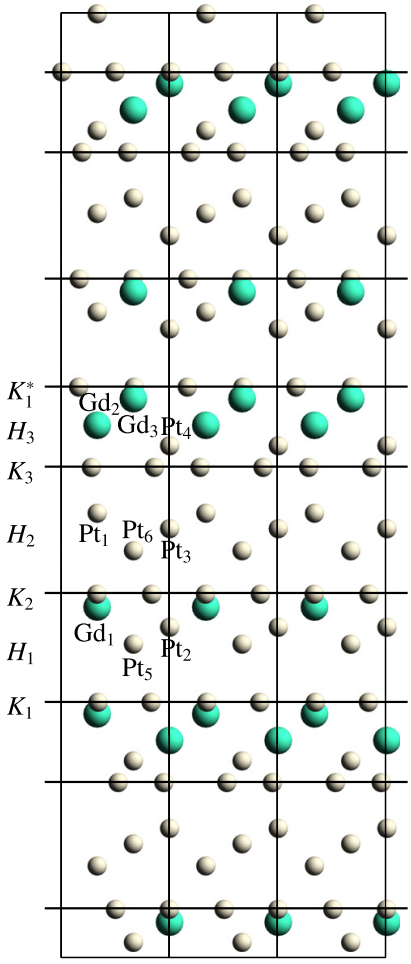

Fig. 13. The final stable structure fit is shown, and the grey spheres are Pt and the green spheres are Gd. The structure is seen along the a-axis, and the black lines are placed on the kagome layers as a guide. Some of the layers have been labeled as in Fig. 12, and the atoms in the hexagonal layers have been labeled as well. It is seen that the kagome layers are no longer equally spaced, and the hexagonal layers have become strongly buckled. The neighboring Gd atoms have displaced in opposite directions, increasing the interatomic distance, just as seen in the Pd_5Ce structure. The Pt in the same hexagonal layer as the two Gd atoms have moved down, and is unphysically close to the other Pt atoms in the kagome layer below. Otherwise the interatomic distances in the rest of the structure are more reasonable.

4. Discussion

In this paper we have studied Gd modified Pt(111) single crystals. Gd has been deposited on a sputter cleaned Pt(111) surface. From the ISS measurements it could be seen that a Pt overlayer forms after annealing the sample to temperatures above 550 °C. By deposition of 200 Å Gd on a sample heated to 800 °C, it was possible to prepare a thick alloy with a stoichiometry close to Pt_5Gd. The crystal structure of the sample was investigated using LEED and surface sensitive X-ray diffraction. It was seen that the alloy was sometimes rotated by 30° compared to the Pt(111) substrate. Based on the crystal structure it is suggested that the interface between the alloy and the Pt(111) substrate is a kagome layer, since the bulk Pt(111) consists of hexagonal layers. We speculate that the energy of rotated or not rotated strained kagome layer on top of a non-strained Pt(111) layer is very similar. From the LEED pattern, it could be seen that the Gd/Pt(111) sample had formed a 1.90 × 1.90 structure, corresponding to a 2 × 2 structure with (5 ± 1)% compressive strain. This is in accordance with powder XRD experiments performed on Pt_5Gd that shows a compressive strain of 4.8% [14]. CO TPDs have been made to evaluate the reactivity of the sample. The shape of the desorption peak becomes more well-defined after the deposition of a thick Gd layer, indicating that a more well-ordered surface has been created. The shape of the desorption peak bares many similarities to CO TPDs made on Y/Pt(111) [15]. The desorption peak is extremely sharp, indicating strong attractive interactions between the CO molecules on the surface. It is beyond the scope of this article to understand the origin of interactions that lead to the shape of this desorption peak. A large downshift in the desorption temperature was observed. The change in the desorption temperature compared to the desorption temperature for the Pt(111) surface is $\Delta T = 200$ °C, see

Table 3
The unit cell parameters and positions of the 12 atomic positions of the final refined structure model.

Space group	a (α)	b (β)	c (γ)
R3 m	5.3309 Å	5.3309 Å	40.358 Å
160	90°	90°	120°
Atom	x	y	z
Gd_1	0	0	0.0380
Gd_2	0	0	0.2302
Gd_3	0	0	0.9250
Pt_1	0	0	0.1372
Pt_2	0	0	0.3500
Pt_3	0	0	0.4542
Pt_4	0	0	0.5520
Pt_5	0	0	0.6654
Pt_6	0	0	0.7642
Pt_7	0.5039	0.0078	0.9373
Pt_8	0.4983	0.9967	0.0516
Pt_9	0.4735	0.9470	0.1857

The atomic coordinates are given in relative units to the unit cell.

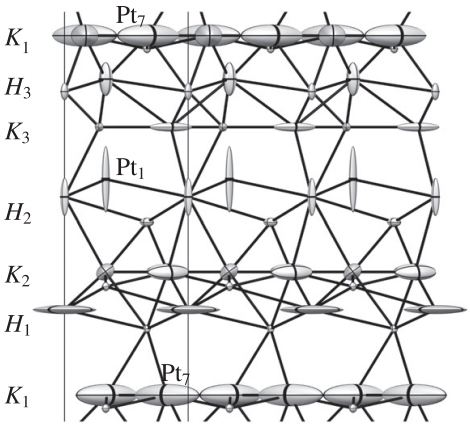

Fig. 14. The anisotropic Debye–Waller factors are sketched in the asymmetrical unit cell. The plot is seen along the a-axis of the structure. Interpreting the Debye–Waller factors as a measure of disorder it is seen that some sites show either disorder in the z-direction or in-plane. As an example Pt_1 shows strong disorder in the z-direction only, whereas Pt_7 shows most disorder in the xy-plane.

Fig. 6. By using the Redheat method the CO desorption energy on the Gd/Pt(111) and Pt(111) surfaces can be evaluated from the desorption temperature [41,42], see Table 4. These calculations have been made under the assumption that the desorption processes were first order.

The CO desorption peak from the Pt(111) is rather broad, and for this surface the high energy limit of the desorption peak has been considered since the CO–CO interactions can be neglected in this temperature limit. This decrease in reactivity is expected for Pt surfaces under compressive strain. A compression of the Pt atoms in the surface will result in a downshift in their d-band center which will cause a weakening of the binding energy of the surface [43,44,45]. The strain seen in the LEED images is in good agreement with the unit cell of the alloy determined by the XRD patterns, and compared to a 2×2 reconstruction the single crystal alloy is compressed by 3.9% in-plane. Furthermore the XRD experiments also reveal that the c-axis is compressed around 1 % compared to 18 layers of pure Pt. It is counterintuitive that the alloy has a closer packing than pure Pt, considering that Gd atoms are significantly larger than Pt atoms. We expect the real structure to have a number of vacancies to accommodate the compression. However, the location of the vacancies could not be determined, they may contribute to the large number of twins. The X-ray diffraction measurements have revealed that the alloy does not behave like an ideal single crystal. The alloy forms a rather complicated stacking sequence, as evidenced by the large c-axis. Furthermore the crystallites are very small, giving a large number of twins. All the measured diffraction peaks have been analyzed, except the superspots, which are expected to appear because of the small crystallites. However, many similar structures could give rise to twinning by merohedry. Other potential structures could also have a different c-axis, being either 2, 3, 6, or 9 atomic layers thick which will give rise to diffraction spots that are completely overlapping with the diffraction peaks from the described structure. This could explain why the fitting procedure underestimates certain diffraction peaks. Nonetheless, since most peaks are described fairly well, this structure is dominant in the alloy. The measuring technique using the rocking scans does not provide the most accurate intensities. Although both factors into the poor structure fit, the twinning is most likely more severe than the measurement error. The strong buckling seen in the hexagonal layers and the inplane rotational disorder, shown in Fig. 15, of the proposed structure may be a way of alleviating the in-plane strain, due to the compression discussed above. The key for the in-plane compression observed in this alloy seems to be the structural motif consisting of a kagome layer stabilized by neighboring Gd atoms; the hexagonal layers are buckling to reduce the strain.

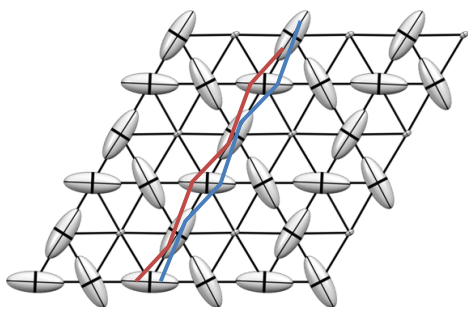

Fig. 15. The anisotropic Debye–Waller factors is sketched for the K_1 kagome type layer. This particular disorder could indicate a broken symmetry in which 1 or 2 of the Pt atoms move closer to the center of the void (in which a Gd atom is seen). Such a symmetry breaking disorder is indicated by the blue and red lines. This might help alleviate the strain within the kagome layer by increasing the Pt–Pt distance, and could also produces a large number of twins.

5. Conclusion

Different amounts of Gd have been deposited on a clean Pt(111) surface in the attempt to create an alloy. The surface has subsequently been characterized in UHV using XPS, ISS, LEED and CO TPD. The crystal structure has been investigated using synchrotron based XRD.

- A thin layer of Gd was deposited on a Pt(111) surface. An alloy terminated by a Pt overlayer was formed after heating the sample to 550 °C.
- A ~63 nm thick single crystal alloy of Pt_5Gd was prepared by depositing a thick layer of Gd on a Pt(111) single crystal heated to 800 °C.
- XPS was used to determine the stoichiometry to be close to Pt_5Gd, and ISS measurements showed that the alloy was terminated by a single atomic layer of Pt.
- Both LEED images and bulk XRD measurements show an in-plane compression of 4–5% of the alloy compared to Pt(111). This value is in good agreement with experimental values reported from Pt_5Gd powders and polycrystalline samples [22,12,14].
- CO TPD experiments showed a downshift in the desorption temperature of 200 °C compared to that of pure Pt(111), indicating a decreased reactivity of the Gd/Pt(111).
- The bulk alloy structure had a high degree of twinning by merohedry and a detailed structure determination was difficult, but a slightly distorted structure was found having a hexagonal unit cell with the parameters $a = 5.3309 \pm 0.0008$ Å and $c = 40.358 \pm 0.012$ Å, and a crystal symmetry of R3 m (space group 160).
- The key to the compressed structure is the combination of kagome type layers stabilized by larger Gd atoms.
- The decreased binding to CO, as probed by TPD, is consistent with the compressive strain we measure using LEED and XRD [43]. Assuming perfect scaling between the intermediates

of oxygen reduction and adsorbed CO, this surface would interact too weakly with OH for optimal activity [17]. However, we do not anticipate that the structure herein is the active phase for oxygen reduction. Gd will dissolve, forming a relaxed pure Pt overlayer with a lower strain value [12]. This alloy is the precursor for the highly active Pt overlayer.

Acknowledgements

For funding of this work we gratefully acknowledge The Danish National Research Foundation's Center for Individual Nanoparticle Functionality (DNRF54). Use of the Stanford Synchrotron Radiation Lightsource, SLAC National Accelerator Laboratory, is supported by the U.S. Department of Energy, Office of Science, Office of Basic Energy Sciences under Contract No. DE-AC02-76SF00515. The Danish Ministry of Higher Education and Science is acknowledged for an EliteForsk travel grant making an extended stay at SLAC possible.

Appendix A. Supplementary data

Supplementary data to this article can be found online at http://dx.doi.org/10.1016/j.susc.2016.02.009.

References

[1] V.R. Stamenkovic, B.S. Mun, K.J.J. Mayrhofer, P.N. Ross, N.M. Markovic, J. Am. Chem. Soc. 128 (2006) 8813.
[2] V.R. Stamenkovic, B. Fowler, B.S. Mun, G. Wang, P.N. Ross, C.A. Lucas, N.M. Markovic, Science 315 (2007) 493.
[3] T. Toda, H. Igarashi, H. Uchida, M. Watanabe, J. Electrochem. Soc. 146 (1999) 3750.
[4] C. Chen, Y. Kang, Z. Huo, Z. Zhu, W. Huang, H.L. Xin, J.D. Snyder, D. Li, J.A. Herron, M. Mavrikakis, M. Chi, K.L. More, Y. Li, N.M. Markovic, G.A. Somorjai, P. Yang, V.R. Stamenkovic, Science 343 (2014) 1339.
[5] I. Spanos, J.J.K. Kirkensgaard, K. Mortensen, M. Arenz, J. Power Sources 245 (2014) 908.
[6] N. Todoroki, Y. Asakimori, T. Wadayama, Phys. Chem. Chem. Phys. 15 (2013) 17771.
[7] R. Srivastava, P. Mani, P. Strasser, J. Power Sources 190 (2009) 40 11th Ulm Electro-Chemical Talks, Neu Ulm, GERMANY, JUN 11-12, 2008.
[8] S. Chen, H.A. Gasteiger, K. Hayakawa, T. Tada, Y. Shao-Horn, J. Electrochem. Soc. 157 (2010) A82.
[9] H.L. Xin, J.A. Mundy, Z. Liu, R. Cabezas, R. Hovden, L.F. Kourkoutis, J. Zhang, N.P. Subramanian, R. Makharia, F.T. Wagner, D.A. Muller, Nano Lett. 12 (2012) 490.
[10] P. Malacrida, M. Escudero-Escribano, A. Verdaguer-Casadevall, I.E.L. Stephens, I. Chorkendorff, J. Mater. Chem. A 2 (2014) 4234.
[11] U. Vej-Hansen, J. Rosmeisl, I. Stephens, J. Schiøtz, Phys. Chem. Chem. Phys. (2015).
[12] M. Escudero-Escribano, A. Verdaguer-Casadevall, P. Malacrida, U. Grønbjerg, B.P. Knudsen, A.K. Jepsen, J. Rossmeisl, I.E.L. Stephens, I. Chorkendorff, J. Am. Chem. Soc. 134 (2012) 16476.
[13] A. Velázquez-Palenzuela, F. Masini, A.F. Pedersen, M. Escudero-Escribano, D. Deiana, P. Malacrida, T.W. Hansen, D. Friebel, A. Nilsson, I.E.L. Stephens, I. Chorkendorff, J. Catal. 328 (2015) 297.
[14] M. Escudero-Escribano, P. Malacrida, M.H. Hansen, U.G. Vej-Hansen, A. Velazquez-Palenzuela, V. Tripkovic, J. Schiøtz, J. Rossmeisl, I.E.L. Stephens, I. Chorkendorff, 2015. (submitted for publication, -)
[15] T.P. Johansson, E.T. Ulrikkeholm, P. Hernandez-Fernandez, M. Escudero-Escribano, P. Malacrida, I.E.L. Stephens, I. Chorkendorff, Phys. Chem. Chem. Phys. 16 (2014) 13718.
[16] A.F. Pedersen, E.T. Ulrikkeholm, M. Escudero-Escribano, T.P. Johansson, P. Malacrida, C.M. Pedersen, M.H. Hansen, K.D. Jensen, J. Rossmeisl, D. Friebel, A. Nilsson, I. Chorkendorff, I.E.L. Stephens, 2016. (submitted for publication, -)
[17] J.K. Nørskov, J. Rossmeisl, A. Logadottir, L. Lindqvist, J.R. Kitchin, T. Bligaard, H. Jonsson, J. Phys. Chem. B 108 (2004) 17886.
[18] J. Rossmeisl, G.S. Karlberg, T. Jaramillo, J.K. Nørskov, Faraday Discuss. 140 (2008) 337.
[19] H.R. Siddiqui, X. Gou, I. Chorkendorff, J.T. Yates, Surf. Sci. 191 (1987) L813.
[20] P.L. Hagans, I. Chorkendorff, J.T. Yates, J. Phys. Chem. 92 (1988) 471 (1896-1996).
[21] N. Baenziger, J.L. Moriarty, Acta Crystallogr. 14 (1961) 946.
[22] W. Bronger, J. Less-Common Met. 12 (1967) 63.
[23] J. Yates, Experimental Innovations in Surface Science: A Guide to Practical Laboratory Methods and Instruments, Aip-Press Series, AIP Press 1998.
[24] 2015, http://www-ssrl.slac.stanford.edu/toneygroup/node/10.
[25] A. Kildemo, A. Juel, S. Raaen, Surf. Sci. 581 (2005) 133
[26] J. Tang, J.M. Lawrence, J.C. Hemminger, Phys. Rev. B 48 (1993) 15342.
[27] A. Ramstad, S. Raaen, N. Barrett, Surf. Sci. 448 (2000) 179.
[28] A. Ramstad, S. Raaen, Phys. Rev. B 59 (1999) 15935.
[29] D. Lide, CRC Handbook of Chemistry and Physics:, CRC-Press 1996.
[30] D. Briggs, P. Seah, Practical Surface Analysis, Auger and X-ray Photoelectron Spectroscopy, Practical Surface Analysis, Wiley 1990.
[31] G. Ertl, M. Neumann, K.M. Streit, Surf. Sci. 64 (1977) 393.
[32] E.K. Vestergaard, P. Thostrup, T. An, E. Laegsgaard, I. Stensgaard, B. Hammer, F. Besenbacher, Phys. Rev. Lett. 88 (2002) –.
[33] J.C. Davies, R.M. Nielsen, L.B. Thomsen, I. Chorkendorff, A. Logadottir, Z. Lodziana, J.K. Norskov, W.X. Li, B. Hammer, S.R. Longwitz, J. Schnadt, E.K. Vestergaard, R.T. Vang, F. Besenbacher, Fuel Cells 4 (2004) 309.
[34] S.R. Longwitz, J. Schnadt, E.K. Vestergaard, R.T. Vang, I. Stensgaard, H. Brune, F. Besenbacher, J. Phys. Chem. B 108 (2004) 14497.
[35] G. Ertl, M. Neumann, K. Streit, Surf. Sci. 64 (1977) 393–410.
[36] P.J. Feibelman, B. Hammer, J.K. Nørskov, F. Wagner, M. Scheffler, R. Stumpf, R. Watwe, J. Dumesic, J. Phys. Chem. B 105 (2001) 4018.
[37] B. Predel, Gd–Pt (Gadolinium–Platinum), Landolt–Börnstein — Group IV Physical Chemistry, 5f. Springer-Verlag 1996.
[38] J.I. Langford, A. Wilson, J. Appl. Crystallogr. 11 (1978) 102.
[39] G.M. Sheldrick, Acta Crystallogr. A: Found. Crystallogr. 64 (2008) 112.
[40] M. Itakura, Y. Hisatsune, H. Sato, N. Kuwano, K. Oki, Jpn. J. Appl. Phys. 27 (1988) 684.
[41] P. Redhead, Vacuum 12 (1962) 203.
[42] I. Chorkendorff, H. Niemantsverdriet, Concepts in Modern Catalysis and Kinetics, Wiley-VCH 2003.
[43] B. Hammer, J.K. Nørskov, Surf. Sci. 343 (1995) 211.
[44] B. Hammer, J.K. Nørskov, Theoretical surface science and catalysis — calculations and concepts, in: B.C. Gates, H. Knozinger (Eds.), Advances in Catalysis, VOL 45: Impact of Surface Science on Catalysis, volume 45 of Advances in Catalysis, 2000. pp. 71–129.
[45] M. Mavrikakis, B. Hammer, J.K. Nørskov, Phys. Rev. Lett. 81 (1998) 2819.

Formation and evolution of the Pt overlayer on Gd/Pt(111) single crystals

Anders F. Pedersen[a], Maria Escudero-Escribano[a,b], Elisabeth T. Ulrikkeholm[a], Daniel Friebel[c], Ifan E. L. Stephens[a], Ib Chorkendorff[a,*].

[a]Department of Physics, Surface Physics and Catalysis, Building 312, Technical University of Denmark, 2800 Lyngby, Denmark

[b]Department of Chemical Engineering, Shriram Center, 443 Via Ortega, Stanford University, Stanford, CA 94305, USA

[c]SLAC National Accelerator Laboratory, 2575 Sand Hill Road, MS31, Menlo Park, CA 94025, USA

***Corresponding author.**

Email address: ibchork@fysik.dtu.dk (Ib Chorkendorff)

***Keywords*: Oxygen reduction, in-situ, Pt(111), XRD**

Abstract

For the oxygen reduction reaction the alloy of Pt and Gd shows significant activity enhancement over pure Pt, both as nanoparticles and extended surfaces. Our previous efforts have shown that upon exposure to the acidic electrolyte a compressed Pt overlayer is formed. Here we measured the strain and correlation lengths of the pure Pt overlayer using in-situ synchrotron X-ray diffraction. We found that the overlayer forms upon exposure to electrolyte under open circuit conditions, and that the compressive strain relaxes slightly upon repeated electrochemical cycling in the range 0.6 V to 1.0 V vs. RHE. On another crystal prepared in the same manner the strain was found to relax strongly when exposing the electrode to 1.20 V vs. RHE, and at potentials above 1.3 V vs. RHE the crystalline thickness of the overlayer increases with potential.

1 Motivation

Fuel cells. Understanding overlayer formation and evolution is important.

2 Methods

2.1 Alloy preparation

UHV Prep

2.2 Synchrotron XRD

The diffraction measurements were performed at SSRL (Stanford Synchrotron Radiation Lightsource) at beam line 7-2. This end station is equipped with a Huber six-circle diffractometer (4S + 2D) and a Pilatus 300K area detector. The beam line has a Si(111) double-crystal monochromator, and we used a photon energy of 11 keV to avoid fluorescence from the Pt by staying below the L3 absorption edge.

When mounting a sample the surface normal was aligned to the ϕ rotation axis using a laser, and the angular accuracy was about 0.1˚. For all the experiments the incidence angle was set to 0.2˚ to optimize surface sensitivity. Furthermore the χ angle was fixed at 90˚, giving a vertical ϕ axis.

For convenience we will refer to the hexagonal unit cell for the Pt(111) surface, which has the lattice parameters: a = b = 2.775 Å, c = 6.797 Å, α = β = 90˚, and γ = 120˚. In this unit cell the a- and b-axis are parallel to the surface and the c-axis is perpendicular to the surface. The area detector was aligned such that the (1,0,1), (0,1,2), and (1,0,4) diffraction spots from the Pt(111) substrate was visible upon correct rotation of the ϕ axis. This also allows the recording of the diffraction from the overlayer once formed, since this has an FCC-like structure [cite: Nano Energy]. To record the entire diffraction peak, the ϕ axis was rocked by ±5˚ during exposure.

Due to the curvature of the Ewald sphere the reciprocal space image on the area detector is distorted, and to correct for this a powder pattern from a LaB_6 crystal was used for calibration. The images were processed using MatLab programs developed by the authors to separate the in-plane and out-of-plane components of the scattering vector, Q.

3. Results

The diffraction measurements show many features from both the substrate Pt(111), the Gd/Pt(111) alloy thin film, and the overlayer itself. Figure 1 shows a representative diffraction pattern from sample 1 showing these features, as well as some Pt powder grains. The image has been corrected and shows the intensity as a function of in-plane (Q_{xy}) and out-of-plane (Q_z) components of the scattering vector, Q. The overlayer diffraction peak is shown inside the white dashed ellipse, and it is immediately recognized that the overlayer is very thin, since the diffraction peak is highly elongated in the z-direction. On this sample the overlayer is not rotated relative to the Pt(111) substrate, which was observed in previous experiments [cite: surface science, nano energy]. Therefore the (1,0,1) diffraction spot is seen inside the red dotted circle next to the overlayer. These two peaks are not overlapping completely, showing that the overlayer is compressed relative to the Pt(111) bulk. The two large arcs in the image is most likely diffraction from randomly oriented Pt grains on the edge of the single crystal. The remaining diffraction is from the Gd/Pt(111) alloy phase.

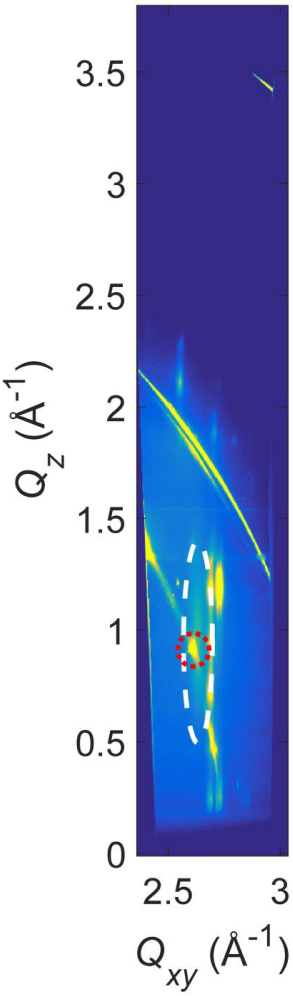

Figure 1: A representative diffraction image from the first single crystal (sample 1), showing the intensity as a function of in-plane (Q_{xy}) and out-of-plane (Q_z) components of the scattering vector, Q. The overlayer peak is seen in the white ellipse next to the (1,0,1) diffraction peak from the Pt(111) substrate, indicating that the overlayer is not rotated from the substrate. The large arcs arise from randomly oriented Pt grains on the edge of the sample. The remaining features are from the Gd/Pt(111) alloy phase.

To quantify the changes in lattice parameter and correlation lengths of the overlayer, the diffraction peaks at different ϕ angles were fitted by a two dimensional pseudo-voigt profile. The position of the overlayer peaks relative to the Pt(111) substrate peaks were used to extract the relative strain of the overlayer, and the peak widths were used to estimate the correlation length. Figure 2 shows the relative strain of the overlayer

compared to bulk Pt as a function of electrochemical treatment. Part (a) shows the in-plane strain evolution, and part (b) shows the out-of-plane strain evolution. Initially the crystal was cycled 0.0-0.6 V vs. RHE, and the diffraction pattern was recorded while keeping the potential fixed at 0.1 V, 0.5 V, and 0.6 V vs. RHE. This was followed by cycling 0.0-0.8 V vs. RHE and XRD recording at 0.1 V, 0.5 V, and 0.8 V vs. RHE. The sample was finally cycled 0.0-1.0 V vs. RHE with XRD recording at 0.1 V, 0.5 V, and 1.0 V vs. RHE. All subsequent cycling was done 0.6-1.0V vs. RHE. During this stability test done at 100 mV/s the cycling was either stopped to do XRD recording at 0.1 V, 0.5 V, and 0.9 V vs. RHE or the XRD recording was done during cycling. At this scan rate a few cycles ran during exposure, and about 80 cycles passed during the entire XRD recording. The last data point was acquired after changing the electrolyte and exposing the electrode surface to air, followed by a few cycles in from 0.0-1.0 V vs. RHE in the new electrolyte. The error bars represent the error in the peak position from fitting, and is representative of the changes seen in the figure. However the combined error in the peak positions of the overlayer peaks and the substrate peaks gives a larger error for the strain that affects each measurement identically, and for the in-plane strain this error is ±0.3% and for the out-of-plane strain it is ±0.5%.

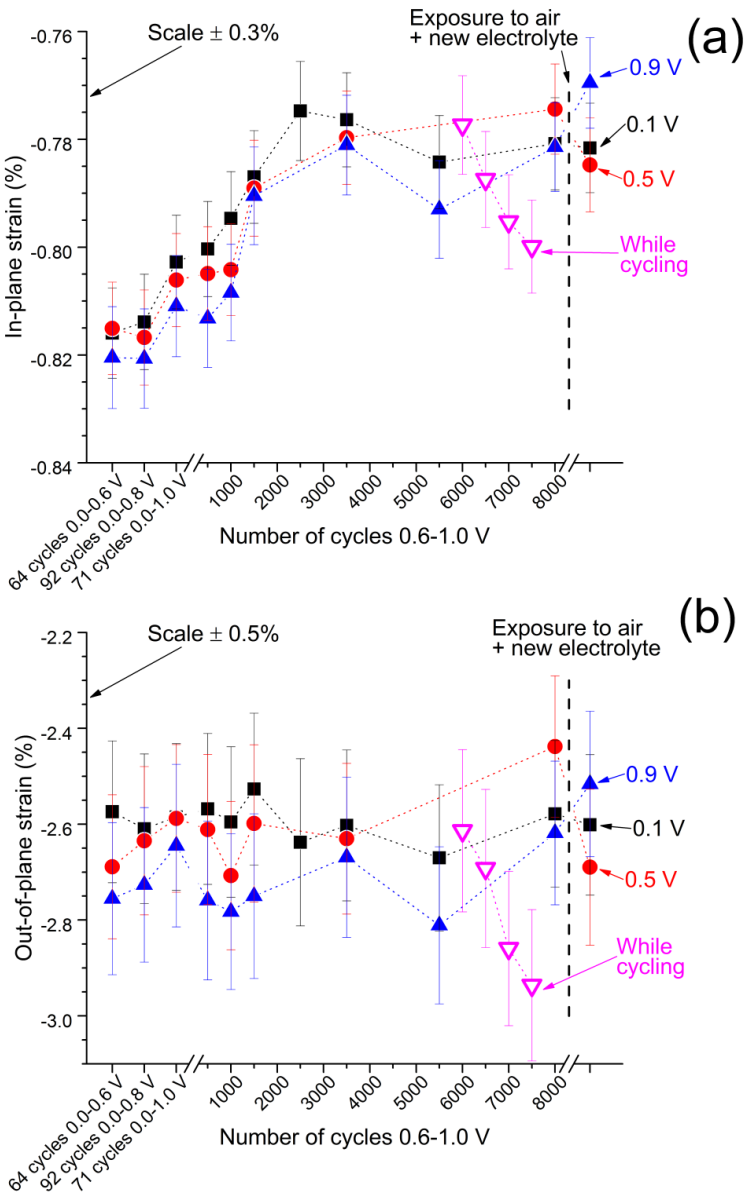

Figure 2: The figure shows the in-plane (a) and out-of-plane (b) components of the strain of the overlayer relative to bulk Pt as a function of electrochemical treatment. Initially the electrode was cycled 0.0-0.6 V, followed by XRD measurements while keeping the potential constant at 0.1 V, 0.5 V, and 0.6 V. Subsequently the electrode was cycled 0.0-0.8 V, the XRD was recorded at 0.1 V, 0.5 V, and 0.8 V, it was cycled 0.0-1.0, and

XRD was measured at 0.1 V, 0.5 V, and 1.0 V. Any subsequent cycling was done in the range 0.6-1.0 V, and the cycling was either stopped to measure the XRD at 0.1 V, 0.5 V, and 0.9 V, or the XRD pattern was recorded during cycling. The last data point was acquired after changing the electrolyte and exposing the crystal to air, and doing a few cycles with the fresh electrolyte. The error bars represent the error in the overlayer peak position from the fitting. However there is a global error in the strain value that comes from the combined uncertainty of the peak position of the overlayer and the Pt(111) substrate. This global strain error is indicated in the figure as ±0.3% for the in-plane strain and ±0.5% for the out-of-plane strain.

Similar to the strain, the correlation length of the overlayer can also be tracked in-situ, as shown in figure 3. Part (a) shows the in-plane correlation length and part (b) shows the out-of-plane part. The electrochemical treatment is described for figure 2. The correlation length was calculated from the full width at half maximum (FWHM) of the pseudo-voigt profile, using Scherrer's formula with a shape factor of K=0.886 [cite scherrer shape]. For the correlation length there is only a single error from the fitting of the peak width.

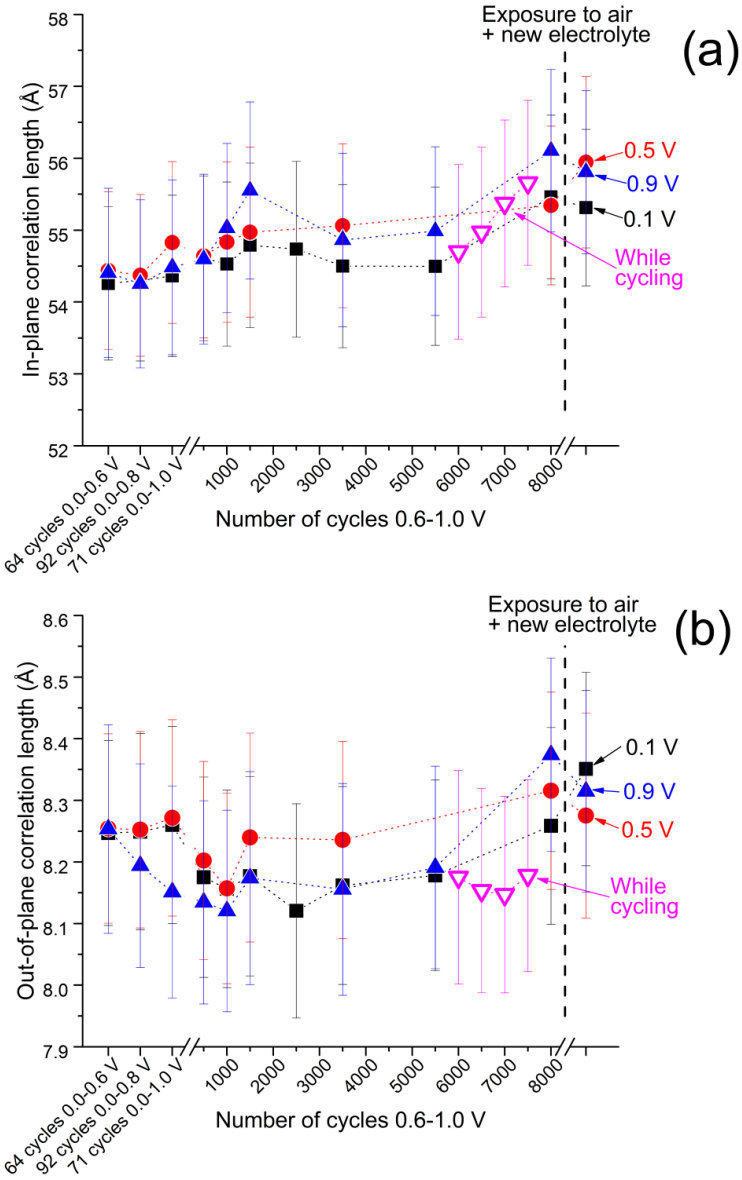

Figure 3: The figure shows the in-plane (a) and out-of-plane (b) correlation length as a function of electrochemical treatment. See figure 2 for a description of the electrochemical treatment. The correlation length has been calculated from the FWHM using the Scherrer's equation. The error is from the fitting of the peak width of the pseudo-voigt profile.

The peak positions of the substrate, alloy, and the overlayer revealed that they their c-axis were all tilted relative to the surface normal. Furthermore, the alloy and overlayer were both tilted more than the Pt(111) substrate, and all tilted in the same direction. The tilt angles are shown in table 1.

	Tilt vs. surface normal (±0.1˚)	Tilt vs. Pt(111) substrate
Pt(111) substrate	1.10˚ ± 0.02˚	-
Gd/Pt(111) alloy	1.28˚ ± 0.001˚	0.18˚ ± 0.02˚
Pt overlayer	1.60˚ ± 0.05˚	0.50˚ ± 0.07˚

Table 1: The c-axis of the Pt(111) substrate, Gd/Pt(111) alloy, and the Pt overlayer were all tilted in the same direction from the surface normal. The amount of tilt was different for the three layers, and this resulted in an angle of the c-axis of the alloy and overlayer relative to the Pt(111) substrate.

For sample 2 the strain and correlation length was quantified in the same way as for sample 1, and the strain as a function electrochemical treatment is shown in figure 4. On this crystal the overlayer turned out to be rotated by 30˚ around the surface normal relative to the Pt(111) substrate, as was observed in our previous study [cite nano energy]. The strain was first measured directly after exposure to electrolyte at open circuit potential, at which point the overlayer had already formed. The potential was then cycled 0.0-1.0 V vs. RHE, after which the XRD was recorded while keeping the potential constant at 0.1 V, 0.5 V, and 0.9 V vs. RHE. This process was repeated after cycling 0.0-1.20 V vs. RHE and 0.0-1.25 V vs. RHE. At every cycling step about 100 cycles were performed. Subsequently the XRD pattern was recorded during cycling in the ranges 0.0-1.3 V, 0.0-1.4 V, 0.0-1.5 V, and 0.0-1.6 V vs. RHE. The strain error bars represent the error from fitting, and the overall strain error is indicated in the figure.

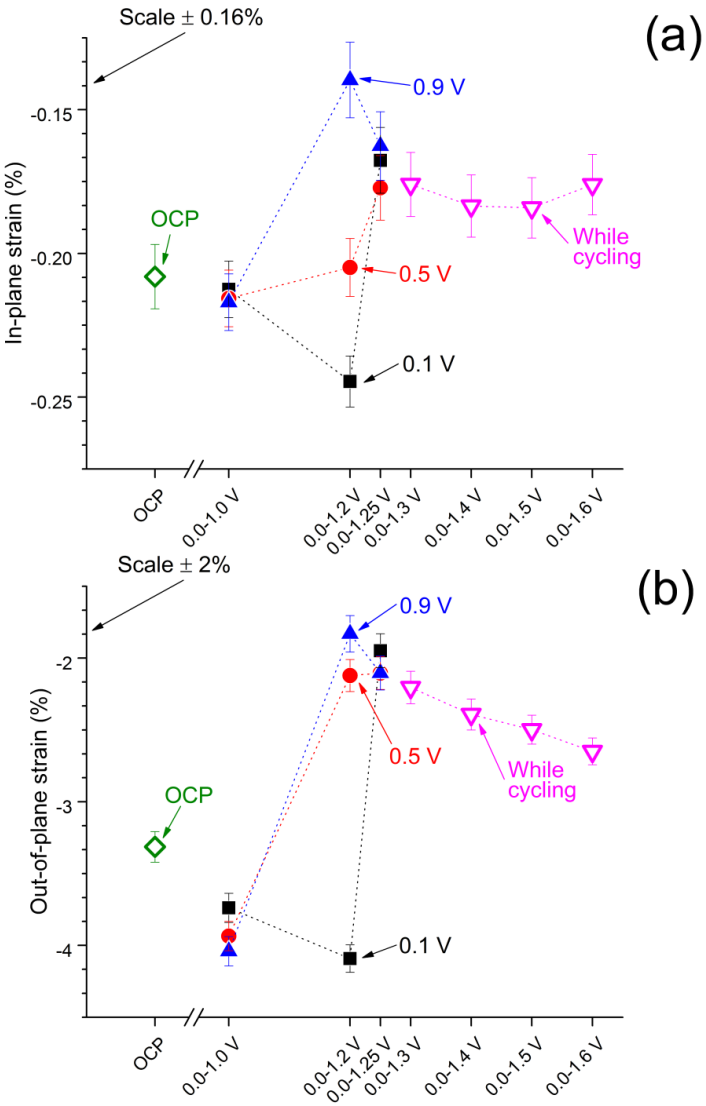

Figure 4: The figure shows the in-plane (a) and out-of-plane (b) components of the strain of the overlayer as a function of electrochemical treatment. On this sample the overlayer was rotated by 30˚ compared to the Pt(111) substrate. The overlayer formed immediately upon exposure to electrolyte at open circuit conditions, which is the first point shown. The electrode was then cycled 0.0-1.0 V, followed by XRD recording under constant potential of 0.1 V, 0.5 V, and 0.9 V. This process was repeated after cycling 0.0-1.20 V and 0.0-1.25 V.

Upon cycling at higher potential the XRD pattern was recorded during the electrochemical cycling in the ranges 0.0-1.3 V, 0.0-1.4 V, 0.0-1.5 V, and 0.0-1.6 V.

Similarly to the strain the correlation length was quantified and is shown in figure 5. The analysis was done in the same manner as sample 1.

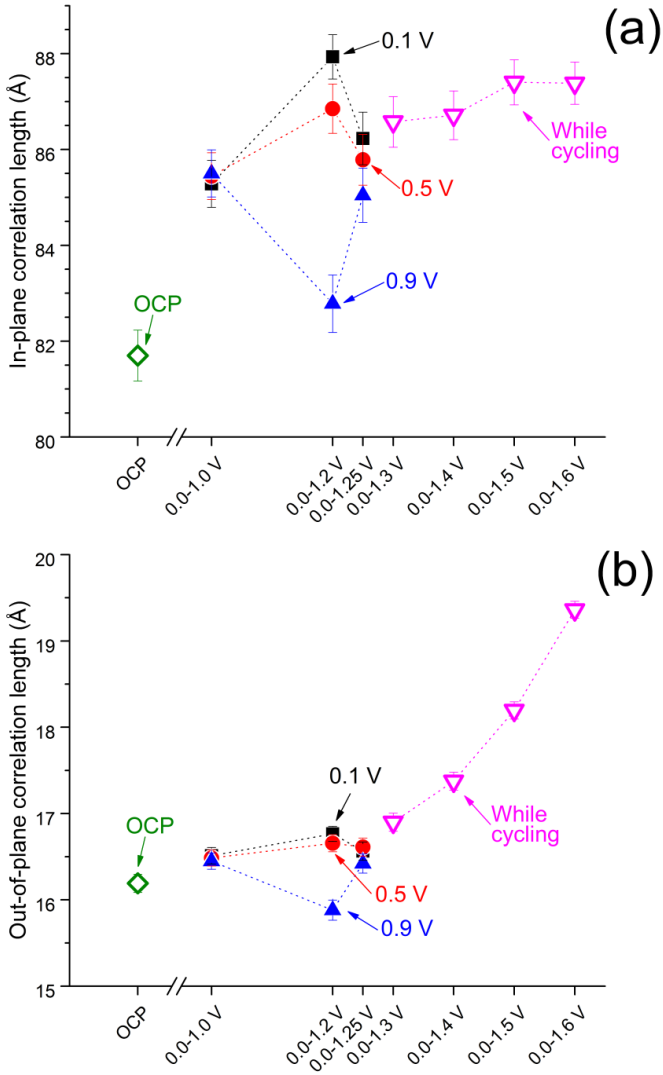

Figure 5: The figure shows the in-plane (a) and out-of-plane (b) correlation lengths on sample 2 as a function of electrochemical treatment.

4. Discussion

Strain and correlation length.

5. Conclusion

Acknowledgments